414 Nicollet Mall
Minneapolis, MN 55401

September 19, 2025

—Via Electronic Filing—

Sasha Bergman
Executive Secretary
Minnesota Public Utilities Commission
121 7th Place East, Suite 350
St. Paul, MN 55101

RE: RIVERSIDE ROOT CAUSE ANALYSIS REPORT
2025 AND 2026 ANNUAL FUEL FORECASTS AND MONTHLY FUEL COST CHARGES
DOCKET NOS. E002/AA-24-63 AND E002/AA-25-63

Dear Ms. Bergman:

Northern States Power Company, doing business as Xcel Energy, submits the enclosed Riverside Root Cause Analysis Report to the Minnesota Public Utilities Commission investigating the primary cause of an outage event that occurred at the Riverside Power Plant Unit 7.

On April 1, 2025, the Riverside steam turbine generator experienced a mechanical failure within the generator and tripped the unit. As a result of the failure, there is internal damage in the generator, and the unit is currently off-line. The Company informally notified the Department of this outage and indicated that we were performing a root cause analysis to determine the likely cause of the failure, which we provide in this filing. The attached report concludes that the failure was caused by a manufacturing flaw. We will provide more information about the outage and its impacts on fuel costs in our March 1, 2026 Fuel True-Up Report providing 2025 actual fuel results in Docket No. E002/AA-24-63.

We appreciate the opportunity to present the Commission with this report. We have electronically filed this document with the Minnesota Public Utilities Commission, and copies have been served on the parties on the attached service lists. Please contact Stephanie Mayers at stephanie.m.mayers@xcelenergy.com or me at allen.krug@xcelenergy.com if you have any questions regarding this filing.

Sincerely,

/s/

ALLEN KRUG
VICE PRESIDENT, REGULATORY AFFAIRS

Enclosure
cc: Service Lists

REPORT NO. 2551958.402
REVISION: 0
PROJECT NO. 2551958.00
July 2025

Root Cause Investigation Report

Riverside Generating Station – Unit 7

Prepared For:

Mr. David F. Motzko
Principal Engineer
Ms. Tara R. Duginske
Assistant General Counsel
Xcel Energy – Riverside Station
3100 Marshall Street NE
Minneapolis, MN 55418
PO No. 4501865510
Prepared by: Date: July 22, 2025

PO No. 4501865510

Prepared by: 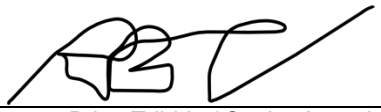 **Date:** 7/22/2025
Brian Tribble / Senior Associate

Reviewed by:  **Date:** 7/22/2025
John Molloy / Senior Consultant

REVISION CONTROL SHEET				
Report Number: 2551958.402				
Title: Root Cause Investigation Report				
Client: Xcel Energy – Riverside Station				
SI Project Number: 2551958.00				
SECTION	PAGES	REVISION	DATE	COMMENTS
All	All	0	[Insert Date]	Initial Issue

1 INTRODUCTION

On April 1, 2025, the Westinghouse steam turbine and generator at Unit 7 of Xcel's Riverside Power Plant, located in Minneapolis, Minnesota, experienced a catastrophic failure. The failure reportedly occurred in a sudden manner while the unit was under normal, full-load operation, with no indications of pending issues (no abnormal vibration trends, no alarms, etc.). After the failure event, operators on-site observed an ensuing fire in the area of the generator, which subsided with no direct action by the responding fire department. When the south (turbine) end of the generator was opened for examination, the retaining ring was found to have failed, and as a result, extensive damage to windings, end coils, generator frame and other components had occurred.

Structural Integrity Associates, Inc., (SI) was hired by Xcel Energy to analyze the cause of the generator failure. SI personnel (Brian Tribble and Clark McDonald) visited the Riverside site on April 17, 2025, and again on May 12 and 13, 2025, to examine components, collect operational data and interview the on-site operators in support of the overall failure investigation. This report provides details regarding history, operational data, operator actions related to the generator and the results from metallurgical testing performed to evaluate the retaining ring, including the damage mechanism associated with the failure (Attachment 1).

2 CONCLUSIONS

In summary, all controls and protective devices functioned as designed before, during and after the failure of the Unit 7 generator south end (turbine end) retaining ring. All appropriate operator actions were taken to minimize plant damage and protect the remainder of the plant, including the Combustion Turbine, HRSG and Steam Turbine. Based on the examinations and testing performed on the failed retaining ring, the failure occurred because of a manufacturing flaw that was present throughout the life of the ring. More detail of the metallurgical evaluation is provided in Attachment 1, Metallurgical Analysis of Failed Retaining Ring.

3 BACKGROUND

The Westinghouse steam turbine and generator were reportedly constructed in the mid-1980's as a repowered unit, with delivery to the Riverside site in approximately 1986. The steam turbine components were fabricated at Mitsubishi (Japan) under a subcontract from Westinghouse, and the generator components were delivered from a Westinghouse plant in Pennsylvania. The nominal capacity of the generator was originally reported as 150 MW.

In 2009, Riverside was converted to a combined cycle plant with Units 9 and 10 being GE 7FA.03 combustion Turbines that are combined with HRSGs to create steam for Unit 7. The output of these units goes to a substation on site that feeds the grid that is in the Midcontinent Independent System Operator (MISO) territory. The operating profile of these units can be considered Intermediate since they come offline routinely (up to several times per week) and when online have a variable output to match load demands from the grid. The load profile changes based on seasonal demands, weather, renewable power availability and other factors.

4 SITE VISITS AND COMPONENT EXAMINATIONS

SI personnel (Brian Tribble and Clark McDonald) visited the Riverside plant site on April 17, 2025, and again on May 12 and 13, 2025. During these visits, various components were

examined and photographed, operational data was collected, operating procedures were reviewed, the operators on site were interviewed, and all previous outage reports were reviewed.

At the time of SI's initial site visit (April 17, 2025), the enclosure at the south end of the generator had been removed to permit direct visual examination of damage to the rotor, stator, and surrounding structural elements. Visible damage included deformed components, destroyed windings, numerous broken cooling fan blades, and a broken retaining ring, which had expanded outward because of the failure event.

At the time of SI's return visit to the Riverside plant site on May 12th and 13th, the generator rotor had been removed from the machine. Details of the condition of the generator and observations are included in Attachment 1, Metallurgical Analysis of Failed Retaining Ring.

5 OPERATIONAL DATA REVIEW

The Unit 7 turbine and generator operational data was retrieved from the unit data historian and reviewed for indications of any conditions that could have contributed to or indicated an imminent failure. The data revealed no condition that could have contributed to the retaining ring failure or gave indication of any operating conditions that indicated a potential failure. Additionally, all observed operating data indicated that the control and protection systems associated with the generator operated and responded as designed and expected, as shown below in the Unit 7 Generator Oscillography Record and Generator Differential Oscillography Record.

Unit 7 Generator Oscillography Record

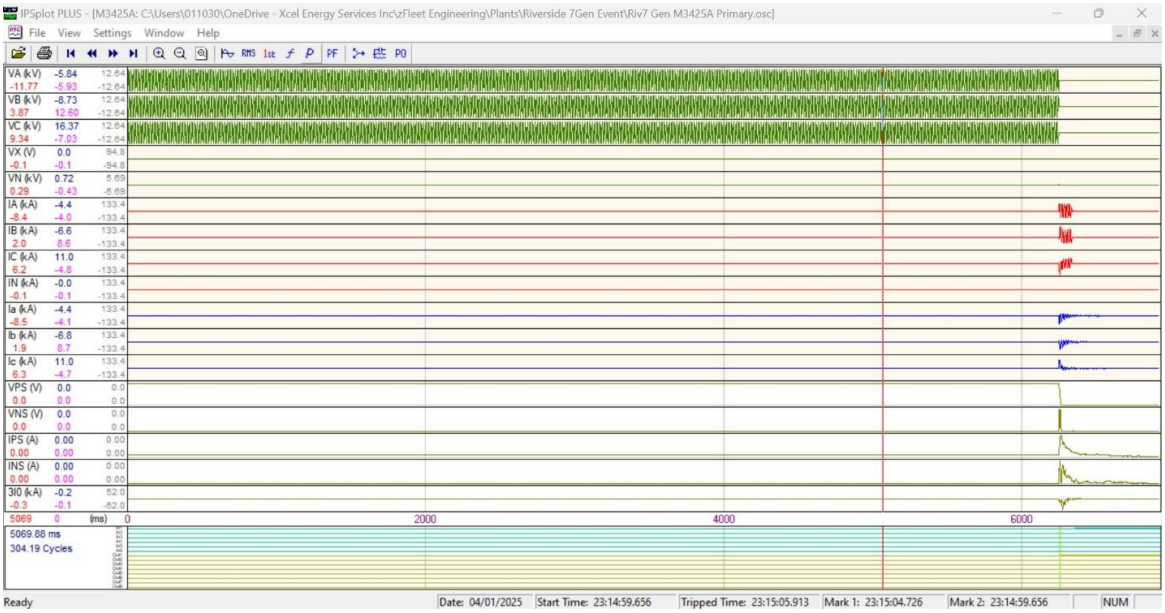

Unit 7 Differential Oscillography Record

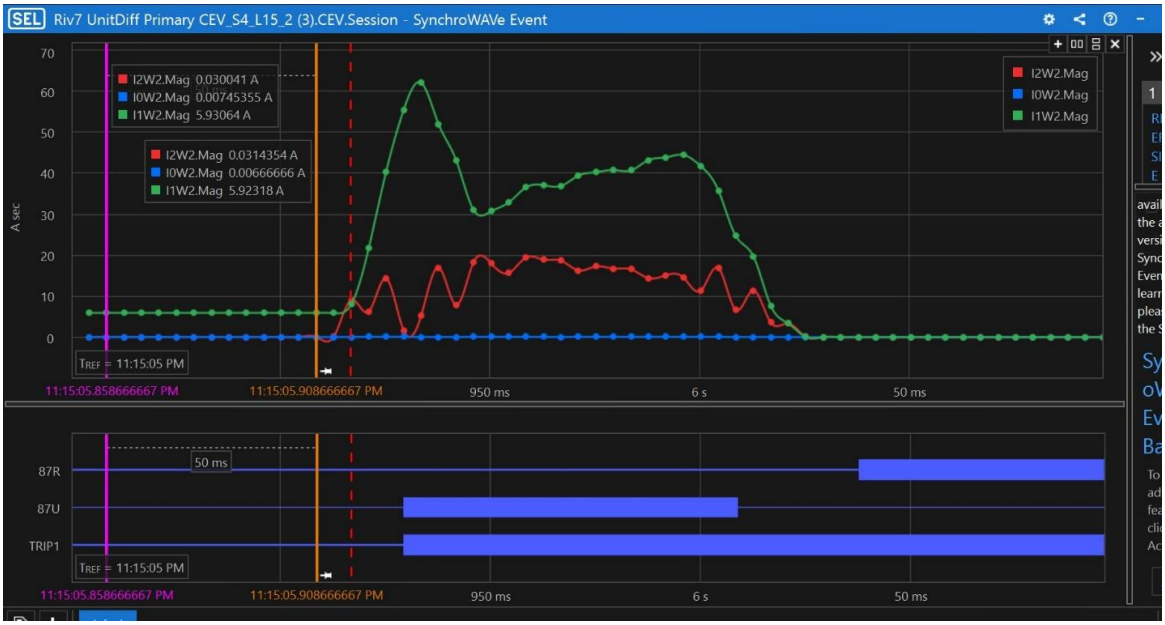

6 MAINTENANCE REPORT REVIEW

The following maintenance reports were reviewed with no findings that could have led to the retaining ring failure. Further, there was no information in these reports to indicate that the retaining ring in question was removed since initial commissioning.

- Riverside Unit #7, HP, LP, Valves, and Generator Inspection Report, May 18, 1990 – July 12, 1990 (with Attachments): RIV7-1990_Turbine,Valves,GeneratorInsp.pdf
- Riverside Unit #7, H2 Cooler Forced Outage Report, December 2001: RIV7-2001_GeneratorH2CoolerInsp.pdf
- Riverside Unit #7, Generator Forced Outage Final Report, November 8 to December 16, 2004 (with Attachments): RIV7-2004_GeneratorInsp (1).pdf
- Riverside Unit Number 7, Customer Final Report (Siemens-Westinghouse), 2004/11/09 to 2004/12/11: RIV7-2004_GeneratorInsp-Siemens (1).pdf
- Riverside Unit #7, Turbine Valves/Generator H2 Seals Minor Inspection Report, September 11 – October 11, 2004 (with Attachments): RIV7-2004_TurbineValves,GeneratorH2Seals MinorInsp.pdf
- Riverside 7, Field Service Report (Covarrubias Enterprises), 2008 Outage: RIV7-2008_ GeneratorRepair-Regenco (1).pdf
- Riverside Unit #7, Major Turbine Generator Inspection, September 8 – December 13, 2008 (with Attachments): RIV7-2008_TurbineGeneratorMajorInsp-MDA (1).pdf
- Riverside Unit Number 7, Generator Frame Vibration Survey – Customer Final Report (Siemens), 2014-12-15 to 2014-12-17 (with Attachments): RIV7-2014_GeneratorFrame VibrationSurvey-Siemens (1).pdf
- Riverside Unit Number 7, Onsite Evaluation – Customer Final Report (Siemens), 2015-02-18 to 2015-02-23 (with Attachments): RIV7-2015_MachineTrainVibrationEvaluation-Siemens (1).pdf
- Riverside Unit 7, Steam Turbine Inspection Report – LP Generator Valve and Auxiliaries Inspection Report (GE Power Services), September 18, 2017, Start Date (with Attachments, including Advanced Steam Path Audit): RIV7-2017-Fall_TurbineGeneratorValveInsp-GE.pdf
- Riverside Unit 7, Generator Major Inspection Report, September 15 – December 20, 2017 (with Attachments): RIV7-2017_GeneratorMajorInsp.pdf

7 OPERATOR INTERVIEWS

The on-site operating crew, including one additional senior operator not scheduled but on site, were interviewed. A discussion of how the equipment was operating before the event occurred revealed that all equipment was operating properly and no relevant alarms were in place. All operating parameters were normal. All shift operators were in the control room when the failure occurred.

In general, the site training process and operational procedures appear to be adequate. All operators were knowledgeable. Operators confirmed that all equipment was operating normally and there were no abnormal conditions or alarms just prior to the event. Operators in the control room felt a brief “vibration” at the time of the unit trip. Units 9 and 10 were manually tripped and placed in a shutdown condition. Steam pressure was bled from the HRSG. Other operators investigated the Unit 7 turbine deck and found heavy smoke. The local fire department was notified. The resultant fire subsequently extinguished itself and no action was required by the fire department.

8 DISCUSSION

At the time of the retaining ring failure, Unit 7 was running at full load and had been for a few days. The time of the trip was approximately 11:14:48 pm on 4/1/2025 Central Time. Note the image below shows 10:14:48 pm because the data server is in Colorado, logging as Mountain time.

Unit Load Historical Data

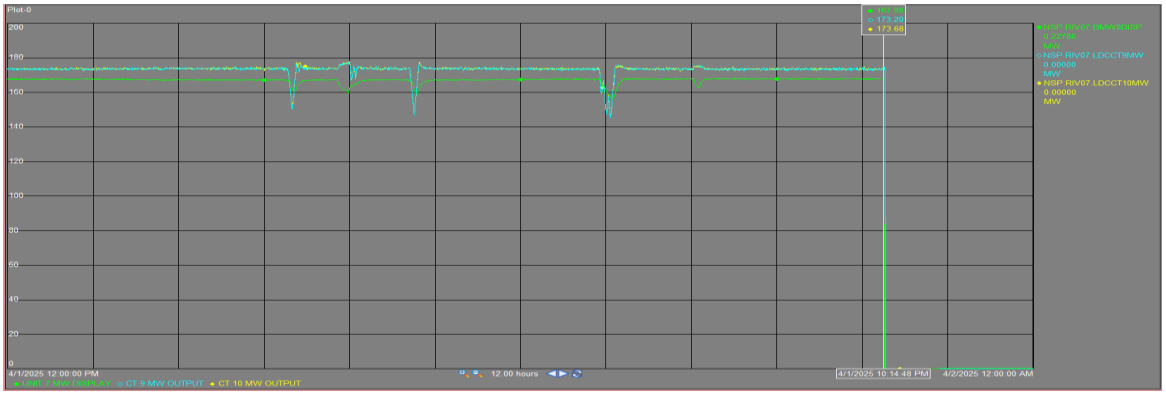

Historical operating data was collected and reviewed. Plant procedures and training processes were reviewed. Plant historical maintenance records were reviewed. Operator knowledge levels and actions were reviewed. Equipment damage was assessed. No evidence was found that operator action, prior maintenance activities, or equipment failure contributed to the event.

At the end of May 2025, the failed retaining ring was shipped to the SI Metallurgical Laboratory in Austin, TX for evaluation. Conclusions from that evaluation indicate the failure initiated because of a manufacturing flaw in one of the cooling holes. This flaw, which was 0.25 inches from the ring's inner surface, eventually led to the initiation of a fatigue crack, which propagated across the retaining ring approximately 2.10 inches, at which point a final overload (burst) failure occurred. Details are discussed and presented in the metallurgical report, which is included as Attachment (1).

ATTACHMENT (1):

REPORT NO. 2551958.401
Metallurgical Analysis of Failed Retaining Ring Riverside Generating Station – Unit 7

Structural Integrity Associates, Inc.®

cmcdonald@structint.com
1825 B Kramer Lane, Suite 500, Austin, TX 78758 | 512-533-9191

REPORT NO. 2551958.401
REVISION: 0
PROJECT NO. 2551958.00
July 2025

Metallurgical Analysis of Failed Retaining Ring

Riverside Generating Station – Unit 7

Prepared For:

Mr. David F. Motzko
Principal Engineer
Ms. Tara R. Duginske
Assistant General Counsel
Xcel Energy – Riverside Station
3100 Marshall Street NE
Minneapolis, MN 55418

PO No. 4501865510

Prepared by: _____ **Date:** July 21, 2025
L. Clark McDonald, Ph.D. / Associate

Reviewed by: _____ **Date:** July 21, 2025
John Molloy / Senior Consultant

REVISION CONTROL SHEET				
Report Number: 2551958.401				
Title: Metallurgical Analysis of Failed Retaining Ring				
Client: Xcel Energy – Riverside Station				
SI Project Number: 2551958.00				
SECTION	PAGES	REVISION	DATE	COMMENTS
All	All	0	7/21/2025	Initial Issue

1 INTRODUCTION

On April 1, 2025, the Westinghouse steam turbine and generator at Unit 7 of Xcel's Riverside Power Plant, located in Minneapolis, Minnesota, experienced a catastrophic failure. The failure event reportedly occurred in a sudden manner while the unit was under normal, full-load operation, with no indications of pending issues (no abnormal vibration trends, no alarms, etc.). Subsequent to the failure event, operators on-site observed an ensuing fire in the area of the generator, which subsided with no direct action by the responding fire department. When the south (turbine) end of the generator was opened for examination, the retaining was found to have failed, and as a result, extensive damage to windings, end coils, and other components had occurred.

Structural Integrity Associates, Inc., (SI) was hired by Xcel Energy to analyze the cause of the generator failure. SI personnel (Brian Tribble and Clark McDonald) visited the Riverside site on April 17, 2025, and again on May 12 and 13, 2025, to examine components and collect information in support of the overall failure investigation. This report provides the results from metallurgical testing performed to evaluate the retaining ring, including the damage mechanism associated with the failure; details regarding operational data and history related to the generator are provided in a separate report. For destructive testing purposes, the failed retaining ring was delivered to SI's Material Science Center on May 28, 2025.

2 CONCLUSIONS

- The examinations and testing performed on the retaining ring from the south (turbine) end of the Xcel Riverside Unit 7 generator revealed that the failure occurred as a result of a manufacturing flaw that was present throughout the life of the ring. More specifically, mechanical gouges with distinct locations of deformed (piled-up) metal were identified within multiple cooling passage holes in the retaining ring, and one of these flaws was situated at the crack origin location. This flaw, which was 0.25 inches from the ring's inner surface, eventually led to the initiation of a fatigue crack, which propagated across the retaining ring approximately 2.10 inches, at which point a final overload (burst) failure occurred.

- The position of the particular damage feature that initiated the fatigue crack was at the side of a cooling passage near the middle of the retaining ring. This is considered to be one of the worst locations for a mechanical damage feature, as the stress concentration caused by the feature coincided with the normal stress concentration associated with the hole.

- A review of historical information regarding the failed retaining ring indicated that it had never been removed from the Riverside generator. The observed damage at the interior of cooling passages was situated in locations very close to the inner (ID) surface of the ring, indicating that the damage was caused from the *inside* of the ring, and was therefore concluded to be a result of original manufacturing or assembly processes. In locations where damage was observed, the gouging and piled up metal were a result of clockwise gouging when looking into the cooling passage from the inside of the retaining ring, which is consistent with damage from a drill-like tool. However, the exact cause of the damage could not be confirmed with the available information.

- The examinations and testing performed on the failed retaining ring indicated that a materials issue did not cause or contribute to the failure.

    - The ring was heavily deformed as a result of the failure event, and the inner surface of the ring exhibited localized ovaling at many of the cooling passages with no induced cracking or tearing. The extent of deformation observed suggested that the material was not embrittled as a result of long-term operation within a hydrogen environment.

    - Mechanical testing performed on material taken from a location near the failure origin revealed appropriate strength, ductility, and impact energy properties, with no indications of material degradation. Although a specification for the failed retaining ring was not available, the mechanical properties obtained from the ring were consistent with ASTM A288 Class 8 material. In addition, the observed microstructure (tempered martensite with scattered non-metallic inclusions) was considered normal for a component of this type.

- For the Riverside ring failure, assessing high cycle fatigue (HCF) versus low cycle fatigue (LCF) based on a "number-of-cycles" approach was not possible, as the number of cycles to failure could not be determined. As an observation, the fracture surface features observed at high magnifications were not entirely consistent with a high cycle fatigue failure. More specifically, small secondary cracks and tears were observed at locations along the crack path, and some locations exhibited cleavage-like features. These fracture characteristics were more consistent with fewer load cycles than with traditional high cycle fatigue.

3 BACKGROUND

The Westinghouse steam turbine and generator were reportedly constructed in the mid-1980's, with delivery to the Riverside site in approximately 1986. The steam turbine components were fabricated at Mitsubishi (Japan) under a subcontract from Westinghouse, and the generator components were delivered from a Westinghouse plant in Pennsylvania. The nominal capacity of the generator was originally reported as 150 MW. A view of the original installation of the generator rotor (in approximately 1986) is provided below:

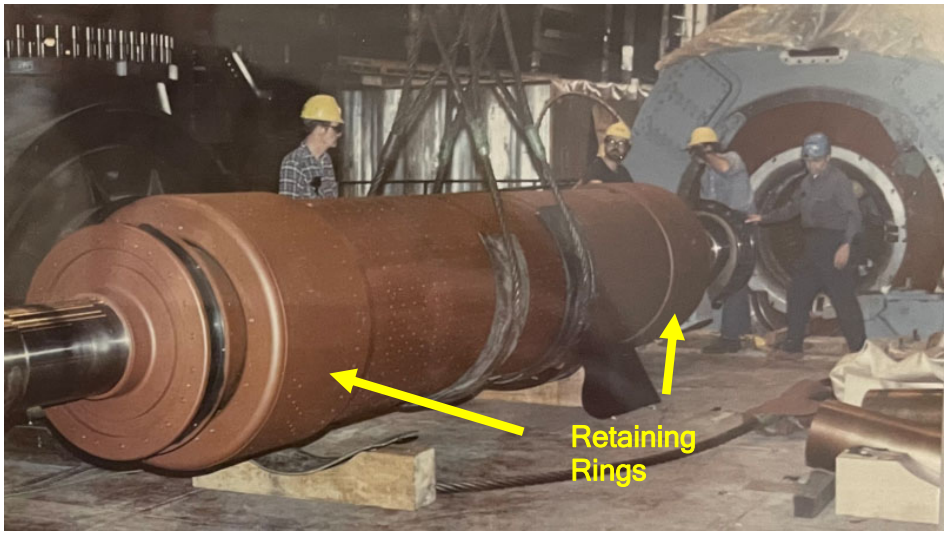

Image of the Original Installation of the Generator Rotor (Xcel Image)

An image of a schematic drawing showing the retaining ring at the collector end of the generator is provided below (taken from Instruction Book 2-1-192 at the Riverside plant site). Although a schematic of the turbine end retaining ring was not included in the book, the ring geometry is presumed to be similar to that shown for the collector end. The rings were reportedly manufactured from martensitic (magnetic) steel, consistent with ASTM A288 (Standard Specification for Carbon and Alloy Steel Forgings for Magnetic Retaining Rings for Turbine Generators). Specified dimensions of the retaining rings were reportedly unavailable, but measurements taken on the failed ring indicated the following approximate dimensions: 132 inch OD x 27-1/4 inch width x 2-5/8 inch thickness.

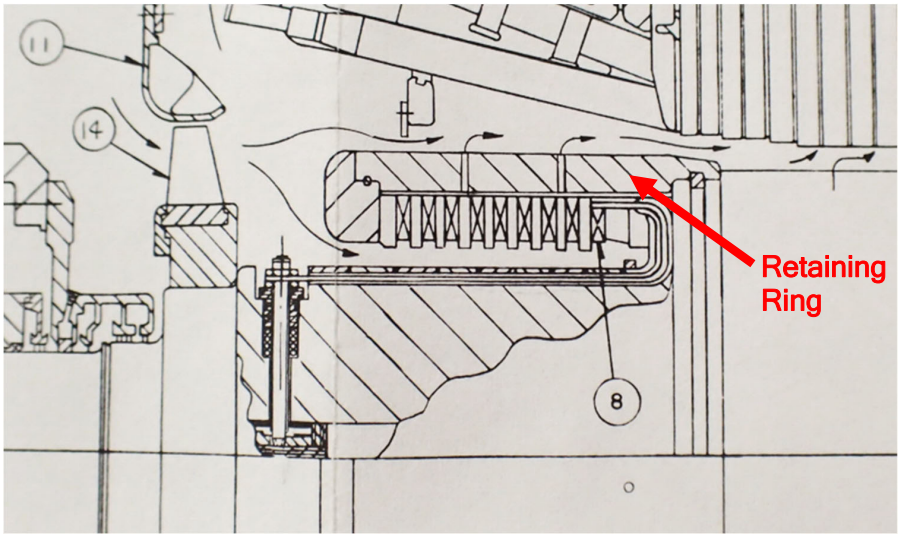

Image of a Generator Rotor Schematic Drawing in Instruction Book 2-1-192

Some history exists regarding the use of magnetic retaining rings for generator service. Early (pre-1969) rings were found to have some history of failure associated with hydrogen assisted cracking, and studies of these identified several key factors that combined to increase the risk of failure. Shortly after the failed (Riverside) retaining ring was manufactured, Operation & Maintenance Memo 089 (Enhancing Operating Reliability of Generator Rotor Magnetic Retaining Rings – October 31, 1988) was issued by Westinghouse. This document summarized that periodic nondestructive examination of magnetic rings did not appear to be a viable tool for assessing the structural reliability of these rings for continued long term operation. The document stated that magnetic rings that have all of the following characteristics have the highest susceptibility to hydrogen assisted cracking:

- Rings operating in a hydrogen environment
- Rings were manufactured prior to 1969 (vacuum degassing of magnetic ring forgings was applied as a requirement for all forgings after 1969)
- Ring material has a Rockwell C hardness greater than 38

The document also included a recommendation for replacement for all magnetic rings that met all three of these requirements. Therefore, the Riverside retaining rings would not have been included in this replacement recommendation (based on the year of manufacture).

Records related to a 2017 Generator Major Inspection for the Riverside Plant – Unit 7 contained information and data that was specific to the generator retaining rings. Attachment A is a copy of hardness test results for both retaining rings (performed using a Proceq Equotip portable tester on October 5, 2017). The test readings indicated average hardness values ranging from 41 to 42 Rockwell C. As discussed above, the slightly high hardness readings (42 Rockwell C versus the desired maximum of 38 Rockwell C) would not lead to a replacement recommendation for rings manufactured after 1969.

4 SITE VISITS AND COMPONENT EXAMINATIONS

SI personnel visited the Riverside plant site on April 17, 2025, and again on May 12 and 13, 2025. During these visits, various components were examined and photographed. The Westinghouse steam turbine and generator at Unit 7 are oriented south-to-north on the turbine deck, with the south (turbine) end of the generator situated on the north side of the steam turbine (Figures 1 and 2). A nameplate on the hydrogen-cooled generator provides capability and rating data, along with information regarding the machine's operation, and serial number (92P0884) (Figures 3 and 4).

At the time of SI's initial site visit, the enclosure at the south end of the generator had been removed to permit direct visual examination of damage to the rotor, stator, and surrounding structural elements (Figures 5 through 9). Visible damage included deformed components, destroyed windings, numerous broken cooling fan blades, and a broken retaining ring, which had expanded outward as a result of the failure event. One of the retaining ring fracture surfaces was visible in the upper part of the generator (Figure 6, upper image). The mating fracture surface was situated in the lower part of the generator, and was partially blocked by debris (Figure 8, upper image). For discussion purposes, these fractures will be referred to as the upper and lower fractures, respectively, throughout this report. Some fractures on the cooling fan blades were also visible, with blade root sections still attached to the rotor (Figure 9).

Closer examination of the upper fracture surface on the retaining ring revealed visible features (texture) that indicated the directions of crack propagation at various positions across the fracture (Figures 10 and 11). The fracture plane coincided with three cooling passages (holes) oriented radially through the ring, and the crack growth directions indicated propagation from the central cooling passage towards the outboard and inboard edges of the rings. As the cracks on either side of the central cooling passage reached the outer cooling passages, new cracks were initiated and continued outside of the outer cooling passages.

The observed texture and surrounding features on the upper fracture surface included Chevron markings, which are characteristic of fast crack propagation. At the edges of the regions containing Chevron markings, angled fracture regions were evident, consistent with ductile shear, mostly along the ring OD and ID surfaces (Figure 12). A flat region of fracture, which exhibited a finer surface texture that was different from other locations on the ring, extended

about two inches towards the inboard edge of the retaining from the central cooling passage. This area also had a very thin shear lip along the outer side of the cooling passage (Figure 13).

Due to uncertainty regarding the ease with which the retaining ring could be removed from the generator, and the potential for damage to occur to the fracture surfaces, fracture surface replications were taken on April 17, 2025, using RepliSet media (Figure 14). As the interior of the generator was considered to be a confined space, the replications were collected by an Xcel Riverside employee under the direction of SI, and preserved for possible future use.

At the time of SI's return visit to the Riverside plant site on May 12th and 13th, the generator rotor had been removed from the machine, and much of the end winding debris had been cleaned up (Figure 15). The interior of the south end of the generator exhibited structural damage as a result of the retaining ring failure (Figure 16).

Components that had been removed from the generator, including the failed retaining ring, were observed to be stored at various locations around the turbine deck (Figure 17). In addition, multiple boxes containing winding pieces and other debris were stored on the turbine deck (Figures 18 and 19). The debris included several components that appeared to include a snap ring and keys that were associated with the retaining ring at the south end of the generator.

The generator rotor was stored in a tented enclosure on a level below the turbine deck (Figures 20 through 22). The enclosure had space heaters at each end to maintain a dry environment for storage. The intact retaining ring was still in place at the north end of the rotor (Figure 20, lower image). At the south end, the centering ring was temporarily blocked into its original position and held in place with tape. The cooling fan wheel was also still attached, along with the root regions of all of the blades (Figure 21, lower image). The fractures on these blade segments were visually examined and appeared to be the result of the overall failure event; no indications of pre-existing cracks were observed. Also, at the south end of the rotor, the end windings were missing from the area beneath the retaining ring location, and damage was visible in some locations around the rotor (in proximity to the snap ring slot that was beneath the inboard edge of the retaining ring) (Figure 23). This damage was consistent with the end windings losing support from the failed retaining ring. The original positions of the components at the south end of the rotor were represented by the undamaged north end (Figure 24).

The failed retaining ring from the generator rotor was stored on the turbine deck with other components (Figures 25 through 29). Visual examination of the locations around the ring ID

surface revealed evidence of deformation (elongation) at the cooling passage holes (e.g., Figure 27, upper image). Snap ring and key slots were also visible on the ID surface at the outboard and inboard edges of the retaining ring (Figures 28 and 29). A location on the outboard edge of the retaining ring had scalloped damage (Figures 30 and 31). Close examination of the features in this location revealed that the damage was caused by impact to the outer edge of the ring, with localized deformation and shear indicating the direction of impact.

The mating fracture surfaces at each end of the deformed ring appeared to be in the same condition as observed inside of the generator during the April 17th site visit (Figures 32 through 37). On the lower fracture surface, the relatively flat region of fracture located adjacent to the central cooling passage exhibited a clear texture that indicted that the crack origin area was located at the cooling passage wall at a location close to the ID surface of the ring (Figures 33 and 34). This apparent origin area was situated at a location where distinct features were visible on the surface of the cooling passage (Figures 35 and 36).

The upper fracture surface exhibited a similar surface texture (as well as a small region with remnant material from the RepliSet sampling effort) (Figures 37). The cooling passage surface at the upper fracture surface also exhibited features (gouges in the metal surface) that coincided with the apparent crack origin area (Figures 38 and 39). The damage at this location included an angled feature with a small amount of metal that appeared to have piled up during the damage process. The observed features were only located close to the ID surface of the ring, and were coarser than the fine machining marks that were visible on the remainder of the cooling passage surface.

The flat region of the fracture extended a couple of inches towards the inboard edge of the retaining from the cooling passage, and within this region were several faint, curved marks that were consistent with beach marks[1] (Figure 40). The beach marks were also consistent with the apparent crack origin, with propagation occurring towards the inboard edge of the ring and towards the ring OD surface.

Other cooling passages on the failed retaining ring were examined from the interior (ID side) of the ring (Figures 41 through 44). While most of the cooling passage holes did not exhibit

[1]Beach marks occur under fatigue crack propagation and indicate the intermittent position of the advancing crack tip. They can occur as a result of changes in loading conditions or environmental conditions, or they can occur due to intermittent pauses in crack propagation.

indications of mechanical damage or coarse features near the ring ID surface, some were identified that had similar features to those observed in the central cooling passage at the crack origin area. In particular, cooling passage holes exhibited damage that included surface gouges near the ID surface of the ring, and angled features at the edges of the gouges with small amounts of deformed (piled-up) metal (e.g., Figures 42 and 44).

Additional parts (and fragments) that appeared to be part of the retaining ring retention components were visually examined during the May site visit. These included a deformed bar that was part of the snap ring, two deformed key-like components, and an additional section of square bar (the source of this item was not clear) (Figure 45). The ends of the square bar were flat, with no indications of fracture (Figure 46). One end of the snap ring bar was fractured and deformed, and the other end was damaged (Figures 47 and 48). The key-like components were deformed, and one exhibited a cracked edge that appeared to be associated with localized bending or impact during the failure event (Figure 49).

5 RETAINING RING EXAMINATION AND TESTING

5.1 As-Received Examination

The retaining ring was subsequently transported to SI's metallurgical testing laboratory in Austin, Texas (Figures 50 and 51). The ring was visually examined and appeared to be in the same condition, including the central areas of the upper and lower fractures, as when it was stored on the Riverside turbine deck (Figure 52).

5.2 Hardness Testing

Prior to cutting efforts, hardness testing was performed at seven locations around the ring OD surface. Testing was performed using a portable hardness tester with both ultrasonic contact impedance (UCI) and rebound probes at locations prepared by light grinding to a clean metal surface with a 240 grit finish. For the UCI measurements, five readings were taken at each location, and for the rebound method, two readings were taken at each location. A schematic of the approximate test locations and results are provided below. Locations 1 and 2 were approximately 6 and 12 inches, respectively, from the upper fracture surface, and locations 6 and 7 were approximately 12 and 6 inches, respectively, from the lower fracture surface.

Initial efforts to cut the upper fracture region from the intact retaining ring were made using a high-amperage plasma cutter. During this cutting process, the metal temperature was monitored in the area near the cut; metal temperatures within one to two inches from the plasma cut were generally in the 200°F to 300°F range, whereas temperatures farther away from the plasma cut (towards Location 2) were less than 200°F. As this cutting process was nearing completion, the plasma cutter failed, so a subsequent cut was made using a bandsaw at a location father away from the upper fracture surface (Figure 53). Metal temperatures were also monitored during cutting with the bandsaw, and did not exceed approximately 125°F (Figure 54).

Subsequent to the removal of the upper section of retaining ring, hardness testing was repeated at Locations 1 and 2, with results as indicated in the tabulated data below. The results obtained after the major cuts were completed confirmed that the retaining ring hardnesses were not affected by heat from cutting. Prior to cutting, the overall hardness of the ring ranged from about 38 to 42 Rockwell C, as measured using a UCI probe, and from 37 to 40 Rockwell C as measured using a rebound probe. Subsequent to the major cuts, the hardness testing indicated similar hardnesses (38 to 40 Rockwell C) at Locations 1 and 2.

Approximate Hardness Test Locations at Retaining Ring OD Surface

Test Method	Test Location – Measurements Prior to Plasma Cutting						
	1	2	3	4	5	6	7
UCI	39	40	40	41	40	42	42
	37	41	42	40	41	41	40
	37	43	41	39	41	41	40
	38	42	42	39	41	42	40
	39	42	42	42	42	41	39
Ave	38	42	41	40	41	41	40
Rebound	37	39	37	40	38	39	39
	38	39	37	40	38	39	39
Ave	**38**	**39**	**37**	**40**	**38**	**39**	**39**

Test Method	Test Location – Measurements After Plasma Cutting						
	1	2	3	4	5	6	7
UCI	38	39	-	-	-	-	-
	38	40	-	-	-	-	-
	38	40	-	-	-	-	-
	37	40	-	-	-	-	-
	37	39	-	-	-	-	-
Ave	38	40	-	-	-	-	-
Rebound	38	39	-	-	-	-	-
	38	37	-	-	-	-	-
Ave	38	38	-	-	-	-	-

Pre- and Post-Cut Hardness Test Results from Retaining Ring

5.3 Upper Fracture Examination and Testing

A portion of the upper fracture surface, which included the central cooling passage, was removed for further examination (Figure 55). This removed section exhibited similar features to those observed when the retaining ring was examined on the turbine deck, including mechanical damage to the cooling passage surface, and beach marks on the flat region of fracture adjacent

to the cooling passage (Figures 56 and 57). One beach mark that was aligned with ductile shear zones at the OD and ID surfaces appeared to represent the position of the crack tip when the final fast rupture occurred (Figure 57, lower image). At a location aligned with the crack origin, this beach mark was approximately 2.05 inches from the origin area, and at a location aligned with the center of the cooling passage length, this beach mark was approximately 2.15 inches from the cooling passage.

A smaller segment of the upper fracture was removed to facilitate further examination (Figure 58). The crack origin area and adjacent cooling passage damage were documented prior to cleaning using a digital microscope (Figures 59 through 62). The crack origin area, which was identified through small ridges emanating from the cooling passage surface, was coincident with mechanical gouges within the cooling passage. At higher magnifications, the fracture surface features and cooling passage surface were covered with a thin film of slightly oily grime and debris, possibly including residue or soot from the failure event.

Close examination of the region of piled up metal that was visible on the cooling passage surface revealed that the shape of this feature was similar to the shape of the crack origin area (Figure 61). In addition, the mechanical gouges generally appeared to be a result of a tool rotating clockwise as it moved into the cooling passage hole from the ID side of the retaining ring (Figure 62).

The ring segment containing the crack origin area was cleaned in an ultrasonic bath with a mild Alconox solution, then rinsed with acetone and dried (Figure 63). The cleaning process did not remove the RepliSet residue or the dark deposits that were present at a location close to the ring ID surface and within the cooling passage, but otherwise the cleaning removed much of the deposits and debris that were on the sample surfaces. In the crack origin area, the cleaned surface exhibited faint beach marks, and a brighter thumbnail feature that was centered around the origin area (Figure 64).

On the cooling passage surface, the cleaning process revealed a bluish tint in locations where mechanical damage was present (Figure 65). On the ring ID surface adjacent to the cooling passage, arc-shaped scratches were visible after the cleaning process (Figure 66).

The cleaned crack origin area was also examined and documented using a digital microscope (Figures 67 through 70). The origin area was located approximately 0.25 inches from the ID surface of the ring, and the radius of the brighter “thumbnail feature” around the origin area was

approximately 0.20 inches. In proximity to the crack origin, the fracture surface exhibited ridges radiating outward (Figure 67, lower image, and Figure 68). These features were consistent with ratchet marks, which occur when incipient fatigue cracks form in close proximity, but on slightly different (nearly colinear) planes. As the incipient cracks propagate, they combine onto a single fracture plane and the ridges end.

Examination of the cleaned features in the cooling passage revealed circumferential gouges, along with the piled-up metal feature, additional light scratches that were aligned with the cooling passage axis, and dark deposits on the cooling passage surface near the interior of the ring (Figures 69 and 70). A comparison of the cleaned sample to images of the ring prior to removal from the generator revealed that the dark deposits at this location were present prior to the ring removal (lower image of Figure 13).

5.4 Scanning Electron Microscope Examination

The cleaned sample containing the crack origin area from the upper fracture surface was examined using a scanning electron microscope. Eleven different areas of the sample were documented at various magnifications (Figure 71).

In Area 1, which represented the upper portion of the crack origin area, the crack initiation site was clearly associated with the gouging at the cooling passage surface (Figures 72 through 74). The mechanical gouges appeared to be significantly deeper than the machine marks that were from the original fabrication of the cooling passage hole. At higher magnifications, the ridges were evident, extending away from the cooling passage. These were surrounded by areas with angular features that were probably influenced by the microstructure. In addition, at higher magnifications, features that were consistent with fatigue striations were observed, although these were not widespread (Figure 74). Fatigue striations are approximately parallel features that are associated with the positions of an advancing crack under cyclic or vibrational loading.

In Area 2, which represented the lower portion of the crack origin area, additional ridges were evident, extending away from the cooling passage surface (Figure 75). Higher magnifications revealed similar fracture texture as Area 1, with angular features and some indications of secondary cracks or tears (Figure 76).

Area 3, which was situated approximately half way across the brighter thumbnail region, exhibited a slightly blockier surface texture, also with indications of secondary cracks or tears (Figures 77 and 78). Some features in this area were consistent with localized cleavage fracture,

with possible influence of the hydrogen environment on the crack growth process. Areas 4, 5, and 6, situated approximately at the edge of the bright thumbnail region and slightly beyond the edge of the thumbnail (e.g., Area 6 was about 0.5 inches from the crack origin area), respectively, were similar to Area 3, with only slight variations in fracture appearance (Figures 79 through 82).

Area 7, which was situated just to the right of the final beach mark prior to the final failure (approximately 1.95 inches from the crack origin), exhibited an even blockier appearance, with mostly cleavage and some dimpled rupture, and with larger secondary cracks or tears (Figure 83). Dimpled rupture is characteristic of localized ductile (overload) failure. Area 8, situated on the other side of the final beach mark (approximately 2.2 inches from the origin area), exhibited mostly dimpled rupture features, along with localized indications of cleavage fracture (Figures 84 and 85). This location exhibited fewer indications of secondary cracks or tears.

Area 9 was situated farther into the fast (final) fracture region (approximately 2.75 inches from the cooling passage, and approximately 0.6 inches from the large beach mark at the transition to fast fracture). At this location, the fracture surface exhibited a coarse, blocky appearance with a mixture of cleavage and dimpled rupture, along with secondary cracks or tears (Figure 86).

Features within the cooling passage (Area 10) were also examined (Figures 87 and 88). The piled up metal at the leading edge of one of the gouges was clearly evident, along with smeared metal in nearby locations. The original parallel machine marks were also evident on the cooling passage surface. One region exhibited relatively shallow scratches that were oriented approximately parallel to the cooling passage hole, and other features within the gouged region exhibited separated areas of smeared metal, possibly caused by smearing in two different directions.

Area 11, situated relatively close to the cooling passage, and also closer to the interior of the retaining ring, was also examined in the SEM. In this region, the surface texture had indicated that localized crack propagation was upward and slightly towards the left (when viewing the fracture surface with the ring ID oriented down). The fracture surface at this location exhibited a slightly blocky appearance with indications of cleavage and secondary cracks or tears visible at higher magnification (Figure 89).

During the SEM examinations, locations on the cooling passage surface were analyzed using energy dispersive spectroscopy (EDS[2]) to evaluate the elemental composition of locations on the sample surface. An area identified as EDS 1 was located in a blue-tinted region of surface damage, and EDS 2 was located at an adjacent location with no surface damage (Figure 90, upper image). There was no discernible distinction between the blue-tinted surface and the adjacent machined surface. EDS 3 was performed at a separate location of machined surface, and EDS 4 was within an adjacent region with dark deposits (Figure 90, lower image). The analysis of the dark deposits revealed mostly carbon and oxygen, and the adjacent clean metal was similar in composition to the EDS 1 and 2 locations.

5.5 Metallographic Examination

Two metallographic cross sections were removed from the previously cleaned section of ring. These samples were prepared using standard laboratory methods, and examined and documented, unetched and etched, using digital and metallographic microscopes. The cross section locations included one section through the cooling passage at a location close to the crack origin and one section through the fast fracture region (Figure 91). The location close to the crack origin was selected adjacent to the gouges within the cooling passage, and this cross section included a portion of the fast fracture on the opposite side of the cooling passage.

Examination of the prepared samples using a digital microscope revealed a variable grain size that resulted in a patchy appearance (Figures 92 through 94). In the fatigue fracture region, the crack path was relatively straight (flat), with a slightly jagged appearance at higher magnifications (Figure 92). The fast fracture region on the opposite side of the cooling passage exhibited a coarser (more jagged) fracture morphology (Figure 93). Similarly, the cross section through the fast fracture away from the crack origin was jagged in appearance (Figure 94).

Examination of the fatigue fracture region using a metallographic microscope revealed a similar crack morphology, with a slightly jagged appearance across the sample (Figures 95 through 97).

---

[2] EDS provides qualitative elemental analysis of materials based on the characteristic energies of X-rays produced by the SEM electron beam striking the sample. Using a light element detector, EDS can identify elements with atomic number 5 (boron) and above. Elements with atomic number 13 (aluminum) and higher can be detected at concentrations as low as 0.2 weight percent; lighter elements are detectable at somewhat higher concentrations. As performed in this examination, EDS cannot detect the elements with atomic numbers less than 5 (beryllium, lithium, helium or hydrogen). The relative concentrations of the identified elements are determined using semiquantitative, standardless quantification (SQ) software. SQ electronically analyzes the EDS data, thereby lowering the detection limit to about 0.1 weight percent. Note that values for carbon, when reported, are not considered accurate and are for comparative purposes only.

At higher magnifications, some locations exhibited short secondary cracks or tears that extended up to about 3 mils (0.003 inches) into the sample from the primary crack path. Small inclusions were present throughout the sample, with no indications of internal cracks or fissures.

Etching the sample revealed a tempered martensite microstructure with more pronounced inclusions (emphasized by the etching process) (Figures 98 through 101). Although the grain size was variable within the sample, there was no correlation of microstructural variations with the crack path.

The fast fracture region on the opposite side of the cooling passage was more jagged in appearance with very few secondary cracks or tears (Figures 102 and 103). Dispersed small inclusions were present in the sample, with no indications of internal cracks or fissures.

In the etched condition, the fast fracture region revealed no correlation of microstructural variations with the crack path (Figures 104 and 105). The etching process highlighted many of the inclusions as dark spots, as well as a larger dark feature that was an artifact of the etching process (i.e., not associated with an inconclusion).

The remote fast fracture region in the unetched condition also exhibited a jagged fracture morphology, but with a higher number of secondary cracks or tears (Figures 106 through 109). Some of these were up to about 5 or 10 mils (0.005 to 0.010 inches) in length (e.g., Figure 107, lower image). Dispersed inclusions were present in the ring metal, but no internal cracks or fissures were observed.

After etching, the remote fast fracture region exhibited a variable microstructure with a patchy appearance, but with no correlation between the grain structure and crack path (Figures 110 through 113). The etching process also highlighted many of the inclusions throughout the sample.

Overall, the typical microstructure of the retaining ring consisted of tempered martensite with scattered non-metallic inclusions (Figures 114 and 115). The density of inclusions seemed to vary, with some locations exhibiting many small, round features in the same general area. However, the observed microstructural features did not appear to have any correlation with the crack path within the retaining ring.

5.6 Microhardness Testing of Metallographic Cross Section

The metallographic cross section through the cooling passage was used to perform microhardness testing at locations near the drilled hole. For this testing, an automated LECO hardness tester was used, with readings taken in a Vickers scale (HV, 500g load) and converted to Rockwell C. The measured values are shown in the images below for the locations where each test was performed; two rows of eight readings were taken along lines extending inward from the surface of the cooling passage, and one row of five readings was taken at a location closer to the fracture surface. The hardness readings were all between 37 and 39 Rockwell C, with no indications of variations near the cooling passage surface.

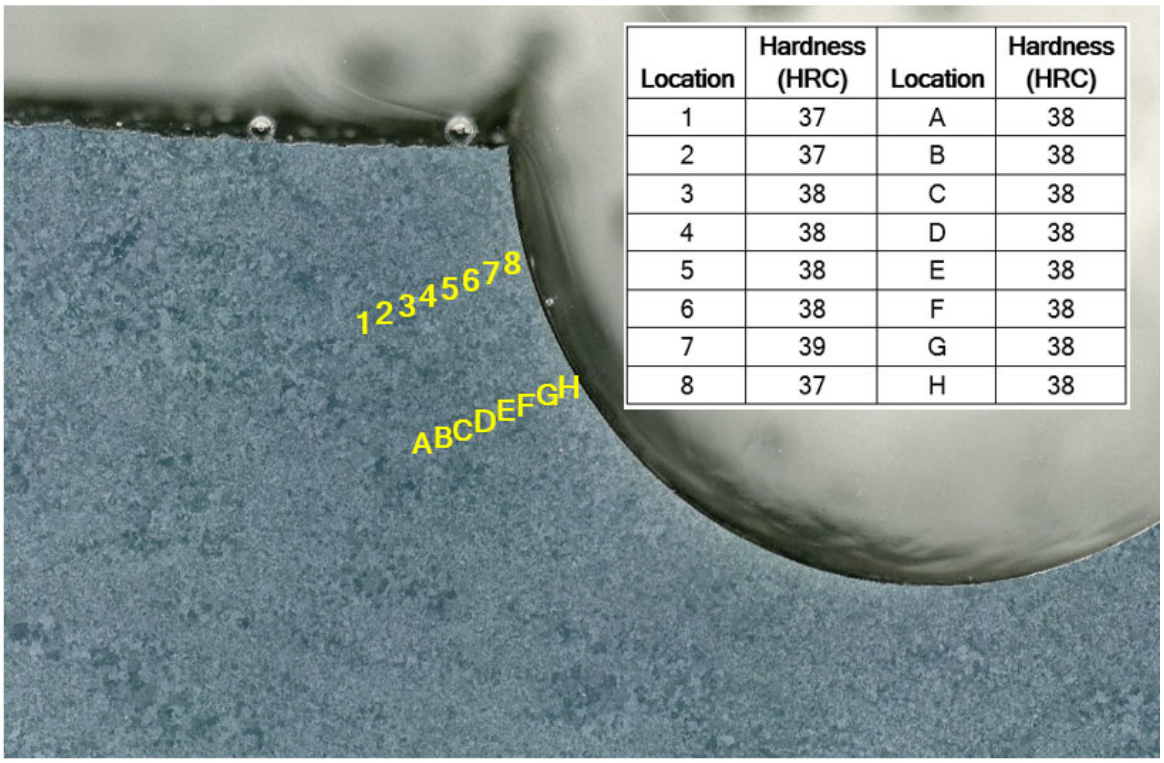

Location	Hardness (HRC)	Location	Hardness (HRC)
1	37	A	38
2	37	B	38
3	38	C	38
4	38	D	38
5	38	E	38
6	38	F	38
7	39	G	38
8	37	H	38

Hardness Data for Two Rows of Eight Readings Near the Cooling Passage Hole

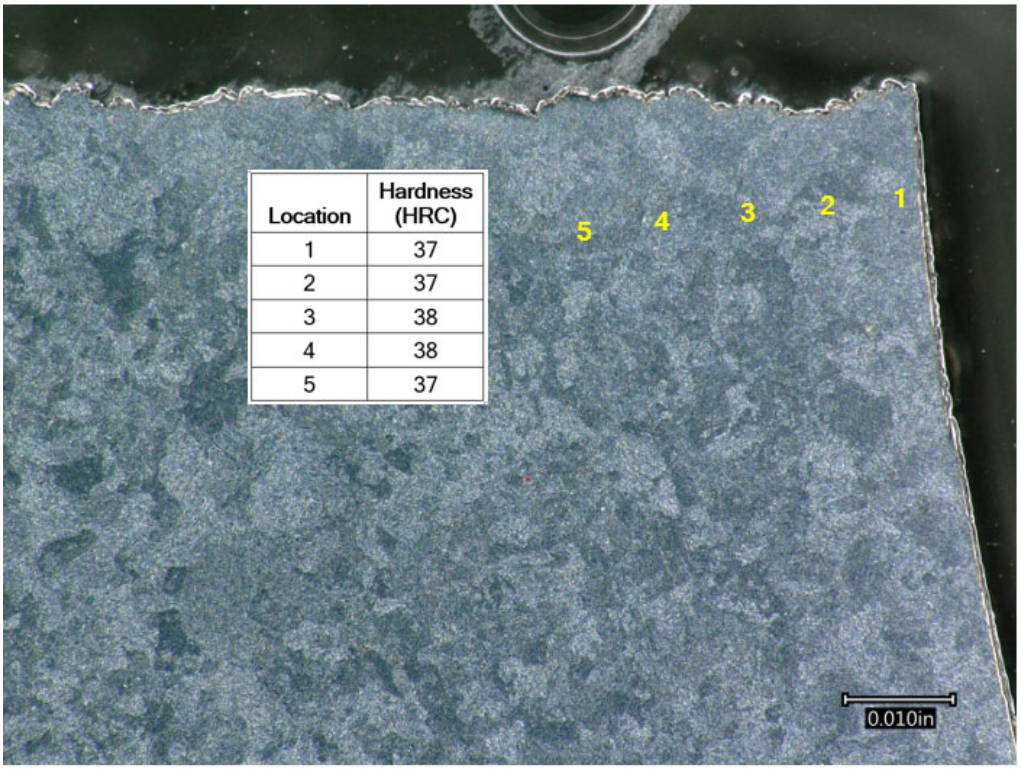

Hardness Data for One Row of Five Readings Near the Fracture Surface

6 COMPOSITIONAL AND MECHANICAL TESTING

A section of the retaining ring situated near the crack origin area at the upper fracture surface was submitted for chemical composition analysis and mechanical testing of the retaining ring material; this region is indicated by the rectangular box in the image below. Tensile and Charpy impact test samples were oriented circumferentially on the retaining ring (parallel to the long axis of the marked rectangular area). For reference, and noting that a material specification for the Riverside retaining rings was not available, mechanical properties are listed in Table 1 for ASTM A288, Standard Specification for Carbon and Alloy Steel Forgings for Magnetic Retaining Rings for Turbine Generators (data taken from the 1991 Edition, reapproved in 2013).

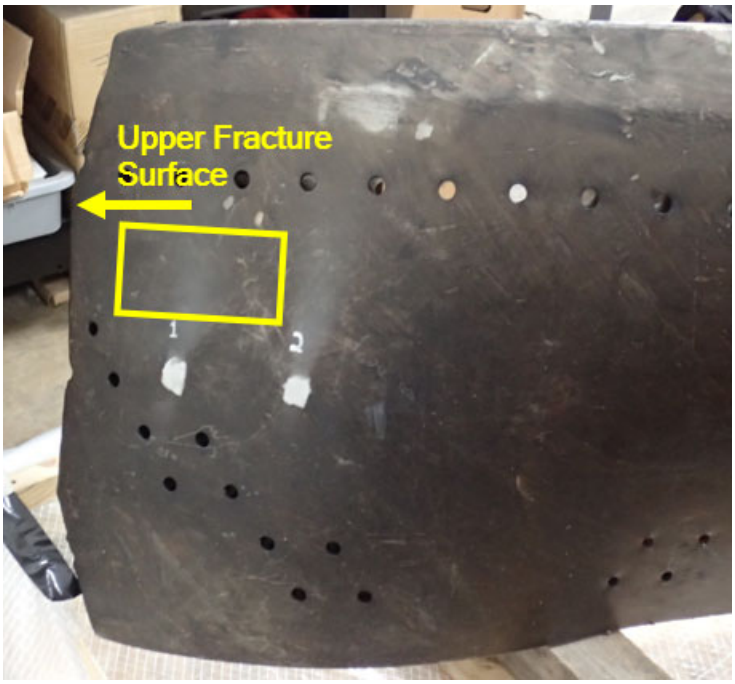

Image Showing Approximate Material Section Used for Material Property Assessment

Table 1. Mechanical Property Requirements for ASTM A288 (1991 Edition)

Class	Min Tensile Strength (ksi)	Yield Strength (0.2% Offset)	Min Elongation (%)	Min Area Reduction (%)	Min Room Temp Charpy Impact Strength (ft-lbs)
1	70	45	18	40	15
2	90	65	20	50	25
3	110	80	18	50	20
4	120	95	18	45	35
5	130	110	16	40	30
6	140	125	14	40	30
7	150	135	13	35	25
8	165	150	12	35	25

6.1 Chemical Composition of Retaining Ring

Chemical composition analysis was performed using atomic emission spectroscopy, with results as listed in Table 2. Table 2 also includes compositional requirements listed in ASTM A288 (1991 Edition, reapproved in 2013). The results from the testing indicated that the retaining ring was similar to material Classes 4 through 8, although the measured values for chromium, nickel, and silicon were out of range. The concentrations of chromium and nickel were higher than the specification limits, and the concentration of silicon was below the limit.

Table 2. Chemical Analysis Results for Retaining Ring (weight percent)

Element	Retaining Ring	Requirements for ASTM A288		
		Class 1	Classes 2 and 3	Classes 4 through 8
Aluminum	0.002	NS[A]	NS	NS
Boron	0.0010	NS	NS	NS
Carbon	0.32	0.50 max	0.45 max	0.45 max
Cobalt	0.010	NS	NS	NS
Chromium	1.50	NS	0.70 - 1.25	0.70 - 1.25
Copper	0.044	NS	NS	NS
Iron	balance	NS	NS	NS
Manganese	0.38	0.60 - 1.00	0.60 - 1.00	1.00 max
Molybdenum	0.45	NS	0.15 min	0.20 min
Nickel	3.68	NS	[B]	1.65 - 3.50
Phosphorus	0.006	0.025 max	0.025 max	0.025 max
Sulfur	0.010	0.025 max	0.020 max	0.020 max
Silicon	0.08	0.15 - 0.30	0.15 - 0.35	0.15 - 0.35
Titanium	0.001	NS	NS	NS
Vanadium	0.12	NS	optional	0.07 - 0.12

[A] NS indicates the element is Not Specified.
[B] For Class 3 rings with wall thickness over 2½ in. (63.5 mm) drawing size, the nickel content shall be 0.85-2.0%.

6.2 Tensile Testing Results from Retaining Ring

Room temperature tensile tests were performed on two samples oriented circumferentially with respect to the retaining ring (such that the tensile fractures were in the same orientation as the retaining ring fracture plane). The results from this testing are provided in Table 3. In comparison to the values listed in Table 1 (for ASTM A288 material), the tensile and yield strengths were consistent with Class 8 material. In addition, the elongation and area reduction values exceeded the minimum requirements for Class 8 material.

Table 3. Room Temperature Tensile Test Results for Retaining Ring

Sample ID	Tensile Strength (ksi)	Yield Strength (0.2% Offset)	Elongation (%)	Area Reduction (%)
1	182	171	12.0	43
2	177	122	15.5	44
Average	**180**	**147**	**14**	**44**

6.3 Charpy Impact Test Results from Retaining Ring

The material submitted for mechanical testing included a request for room temperature Charpy impact testing on one set of three samples, in accordance with ASTM E23, Standard Test Methods for Notched Bar Impact Testing of Metallic Materials. The results, which are provided in Table 4, indicated that the average impact energy for the three test samples was 44 ft-lbs. As indicated in Table 1, the ASTM A288 standard lists minimum impact energy requirements for each Class of material (1 through 8), with the highest energy requirement being 35 ft-lbs (for Class 4 material). The measured impact energy of the retaining ring material exceeded all of the minimum values required by ASTM A288 (1991 Edition).

Table 4. Room Temperature Charpy Impact Test Results for Retaining Ring

Sample ID	Energy (ft-lbs)	Lateral Expansion (inches)	Shear (%)	Specimen Size
1	43	0.021	100	10mm x 10mm
2	45	0.024	100	10mm x 10mm
3	44	0.024	100	10mm x 10mm
Average	**44**	-	-	-

7 DISCUSSION

Based on the examinations and testing performed on the retaining ring from the south end of the Xcel Riverside Unit 7 generator, the failure occurred as a result of a manufacturing flaw that was present throughout the life of the ring. More specifically, mechanical gouges were identified within multiple cooling passage holes in the retaining ring, and these appeared to have been caused by a mechanical tool, such as a drill bit, reamer, or similar cutting tool. The observed damage to the cooling passage surfaces, which eventually led to the initiation of a fatigue crack, included circumferentially oriented scrapes and gouges, with distinct, angled features where small amounts of piled-up metal were present.

The crack origin location for the overall failure was situated at one of these angled features. Further, the position of the particular feature at the crack origin location was at the side of a cooling passage situated at the middle of the retaining ring. This is considered to be one of the worst locations for a mechanical damage feature, as indicated by the schematic diagram below. As the generator rotates during operation, hoop stresses are generated within the retaining ring as it tries to expand outward (stresses from the shrink fit are likely present as well, but are presumed to be much lower). For a solid retaining ring (without cooling passages), the hoop stresses would normally be relatively evenly distributed across the retaining ring. For large components under stress, a drilled hole is normally estimated to result in a local stress concentration that magnifies the surrounding stress by a factor of up to about 3x. The orientation of this estimated stress concentration (for the retaining ring) would be at the sides of the hole, towards the outboard and inboard edges of the ring. For the failed ring, the mechanical damage was at this same orientation, and produced an added stress concentration at the location of highest stress, which eventually led to the initiation of a fatigue crack in the retaining ring.

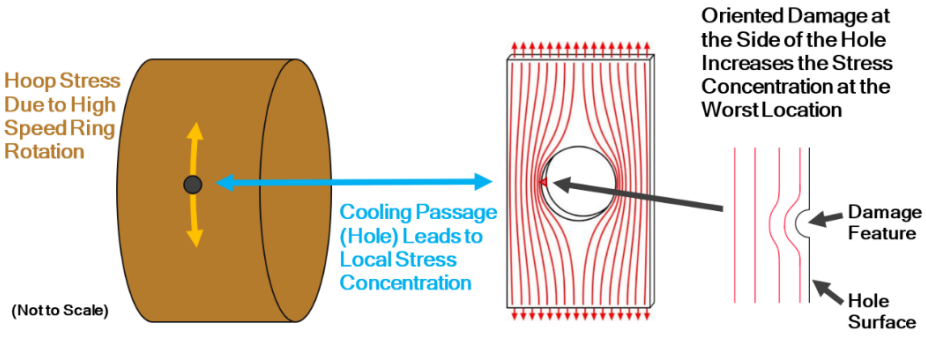

Schematic Showing Stress Concentrations Near a Damaged Hole in a Rotating Ring

Based on historical information regarding the failed retaining ring, Xcel personnel reported that it had never been removed from the Riverside generator. The observed damage at the interior of cooling passages was situated only in locations very close to the inner (ID) surface of the ring, indicating that the damage was caused from the *inside* of the ring, and was therefore concluded to be a result of original manufacturing or assembly processes. With regard to the cause of the identified damage in the cooling passages, several possibilities were considered. First, consideration was given to the use of threaded rods or bolts (e.g., eye bolts) to lift or move the ring. Inserting a bolt through a cooling passage hole could provide for a location to connect a lifting device to move a ring (e.g., within a shop environment). However, the internal damage was not consistent with either an unthreaded or threaded rod or bolt having been used in this manner. In addition, using a rod or bolt within a cooling passage would have produced damage at each end of the cooling passage and on the opposite sides of the hole. This type of damage was not present.

A second consideration was given to the possibility that the damage occurred as a result of drilling of the fiberglass liner that was installed at the inside of the retaining ring. Like the retaining ring, the fiberglass liner was manufactured with cooling passages that were intended to index and align with the holes in the retaining ring. This was confirmed through visual examination of the intact retaining ring at the north end of the generator. Further, the mechanical damage observed in the holes was generally consistent with having been caused by a coarse drill bit with a discernible helix angle at the outer corner, with multiple locations of “piled-up” metal exhibiting the same angle and shape. If the holes in the fiberglass liner were drilled from the inside with the liner in place within the retaining ring, drilling tools extending through the liner and into the inner part of the cooling passages could potentially produce mechanical damage such as that which was observed in the ring.

Alternatively, if the holes in the fiberglass liner were drilled prior to inserting the liner into the ring, further drilling could have been applied to the holes in the fiberglass liner to ensure that the cooling passages in the fiberglass properly aligned with the cooling passages in the retaining ring. In this case, the holes in the fiberglass could have been further drilled (or shaped) using a tool with similar characteristics as a drill bit (or with a similar drill bit). In locations where damage was observed inside of the cooling passages, the gouging and piled up metal were a result of clockwise gouging when looking into the cooling passage from the inside of the retaining ring, which is consistent with damage from a drill-like tool. However, the exact cause of the damage could not be confirmed with the available information.

The examinations and testing performed on the failed retaining ring indicated that a materials issue did not cause or contribute to the failure. The ring was heavily deformed as a result of the failure event, with portions of the ring that were significantly straightened from the originally round condition. In addition, the inner surface of the ring exhibited localized deformation near many of the cooling passages (i.e., severe ovaling of the holes) with no induced cracking or tearing. The extent of deformation observed suggested that the material was not embrittled as a result of long-term operation within a hydrogen environment. Further, mechanical testing performed on material taken from a location near the failure origin revealed appropriate strength, ductility, and impact energy properties, with no indications of material degradation. Although a specification for the failed retaining ring was not available, the mechanical properties obtained from the ring were consistent with ASTM A288 Class 8 material, which is the strongest class designation within that standard. Further, the ring hardness (approximately 39 Rockwell C) was consistent with the measured tensile strength (approximately 180 ksi), and the observed microstructure (tempered martensite with scattered non-metallic inclusions) was considered normal for a component of this type.

A concern with retaining rings operating in a hydrogen environment is that material embrittlement can occur as hydrogen diffuses into the metal over time, leading to premature failure as a result of hydrogen assisted cracking. As discussed in Section 3 of this report, a 1988 Westinghouse publication stated that magnetic rings having all three of the following characteristics have the highest susceptibility to hydrogen assisted cracking and should be replaced:

- Rings operating in a hydrogen environment
- Rings manufactured prior to 1969 (vacuum degassing of magnetic ring forgings was applied as a requirement for all forgings after 1969)
- Ring material having a Rockwell C hardness greater than 38

Based on the Westinghouse document, the Riverside retaining rings would not have been recommended for replacement (based on the year of manufacture). More importantly, the mechanical properties determined through testing of the failed ring indicated that embrittlement had not occurred with the failed ring, and confirming that a material degradation issue did not cause or contribute to the Riverside failure event.

The mechanism associated with the ring failure was fatigue crack propagation, with initiation occurring as a result of the mechanical damage at the cooling passage surface. The origin area

was located approximately 0.25 inches from the inner surface of the ring, and the fatigue crack propagated approximately 2.10 inches from the cooling passage (and through the ring's thickness) prior to the final overload (burst) event. Fatigue failure is a process by which a crack initiates, typically at a metallographic or geometric feature either within the component or at the component surface, and then propagates under cyclic loading conditions until a final catastrophic (overload) failure occurs. The loading conditions that drive crack propagation can be simple or complex, and the stress cycles can result from changes in mechanically applied loads, thermally induced stresses (e.g., during operational transients), or (for pressured systems) changes in internal pressures. In some cases, high stresses associated with vibrational loads can also contribute to crack propagation.

The appearance of fatigue failures, and the nature of loading and stress cycles that a failed component might have been exposed to, often leads to the consideration of high cycle fatigue (HCF) versus low cycle fatigue (LCF) as specific modes of failure. Assessing HCF versus LCF from a strictly "number-of-cycles" approach is often not feasible. Nonetheless, a common approach has been to attribute failures after more than 10,000 load cycles as HCF, and failures after less than 10,000 cycles as LCF. When the actual number of load cycles cannot be assessed through physical evidence (which is most often the case), the fracture surface features (characteristics) can become more important in trying to assess HCF versus LCF, with a distinction occurring due to the nature of loading and the material behavior (such as elastic versus plastic deformation) at the tip of the propagating crack.

For components that are exposed to consistent cyclic loading in service, a simplified rule of thumb is that high cycle fatigue crack initiation occurs approximately 90 percent into the fatigue life of the component. In other words, over the first 90 percent of the component life, atomic level damage accumulates in the material without initiating a crack. At the end of this process, a fatigue crack is initiated, and the remaining 10 percent of component life involves the process of crack propagation, under cyclic loading, to the point of final failure. For components that undergo operational changes that significantly impact the applied cyclic loads (stresses), this simple rule would not apply, and the crack initiation and propagation processes would be more dependent on the applied stress levels (e.g., LCF versus HCF).

For the Riverside retaining ring failure, assessment of the source(s) of loading that might have caused or contributed to the failure are beyond the scope of this report. However, it is noted that this failure event occurred after more than 35 years of service (i.e., more than 50 billion

rotational cycles at 3600 rpm). As an observation, the fracture surface features observed on the failed ring (at high magnifications) were not entirely consistent with a high cycle fatigue failure. More specifically, fracture coarseness (at higher magnifications) and small secondary cracks and tears were observed at locations along the crack path, and some locations exhibited cleavage-like features. While the secondary cracks and tears were not substantial in depth (most were a couple of mils or less), they could be an indication of a lower cycle failure process, with slightly higher stress levels occurring at the tip of the propagating crack. In addition, some of the observed features were likely influenced by the tempered martensite microstructure, which is considered normal. The observed fracture characteristics were more consistent with fewer load cycles than with traditional high cycle fatigue, but an evaluation of the number of cycles to failure was not possible with the available information.

8 REFERENCES

- Riverside Unit #7, Original Installation Report, 1987 (with Attachments): RIV7-1987_OriginalInstallation-Westinghouse (1).pdf
- Riverside Unit #7, HP, LP, Valves, and Generator Inspection Report, May 18, 1990 – July 12, 1990 (with Attachments): RIV7-1990_Turbine,Valves,GeneratorInsp.pdf
- Riverside Unit #7, H2 Cooler Forced Outage Report, December 2001: RIV7-2001_GeneratorH2CoolerInsp.pdf
- Riverside Unit #7, Generator Forced Outage Final Report, November 8 to December 16, 2004 (with Attachments): RIV7-2004_GeneratorInsp (1).pdf
- Riverside Unit Number 7, Customer Final Report (Siemens-Westinghouse), 2004/11/09 to 2004/12/11: RIV7-2004_GeneratorInsp-Siemens (1).pdf
- Riverside Unit #7, Turbine Valves/Generator H2 Seals Minor Inspection Report, September 11 – October 11, 2004 (with Attachments): RIV7-2004_TurbineValves,GeneratorH2Seals MinorInsp.pdf
- Riverside 7, Field Service Report (Covarrubias Enterprises), 2008 Outage: RIV7-2008_ GeneratorRepair-Regenco (1).pdf
- Riverside Unit #7, Major Turbine Generator Inspection, September 8 – December 13, 2008 (with Attachments): RIV7-2008_TurbineGeneratorMajorInsp-MDA (1).pdf
- Riverside Unit Number 7, Generator Frame Vibration Survey – Customer Final Report (Siemens), 2014-12-15 to 2014-12-17 (with Attachments): RIV7-2014_GeneratorFrame VibrationSurvey-Siemens (1).pdf
- Riverside Unit Number 7, Onsite Evaluation – Customer Final Report (Siemens), 2015-02-18 to 2015-02-23 (with Attachments): RIV7-2015_MachineTrainVibrationEvaluation-Siemens (1).pdf
- Riverside Unit 7, Steam Turbine Inspection Report – LP Generator Valve and Auxiliaries Inspection Report (GE Power Services), September 18, 2017 Start Date (with Attachments, including Advanced Steam Path Audit): RIV7-2017-Fall_TurbineGeneratorValveInsp-GE.pdf
- Riverside Unit 7, Generator Major Inspection Report, September 15 – December 20, 2017 (with Attachments): RIV7-2017_GeneratorMajorInsp.pdf

Figure 1. North (upper image) and west (lower image) views of the Westinghouse steam turbine at Xcel Riverside Station.

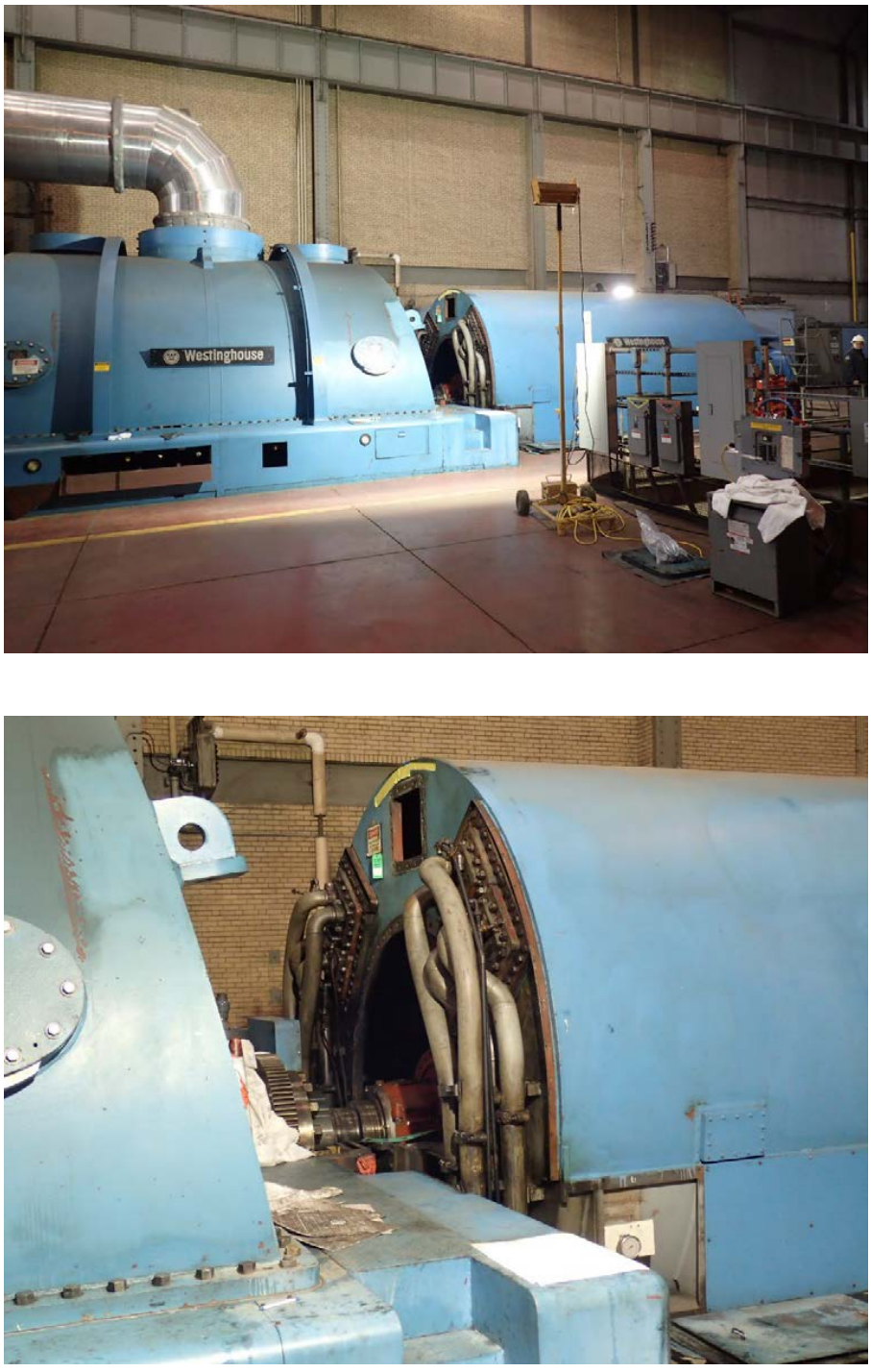

Figure 2. Northwest views of the generator and the damaged end of the generator (lower image) adjacent to the steam turbine. Some components have been removed to permit visual examination of the interior of the generator.

Figure 3. Views of the Westinghouse nameplate on the west side of the generator.

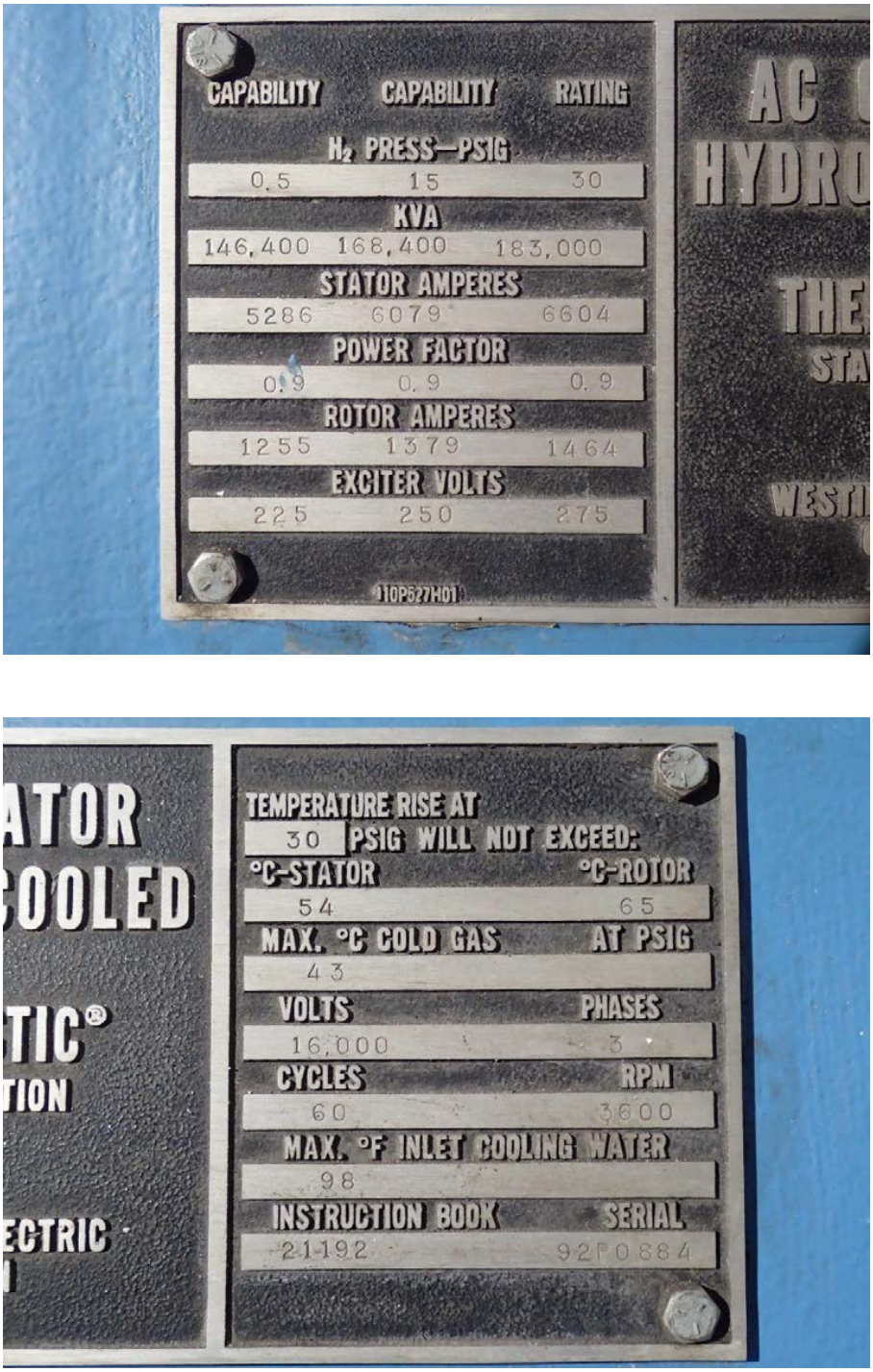

Figure 4. Closer views of the generator nameplate.

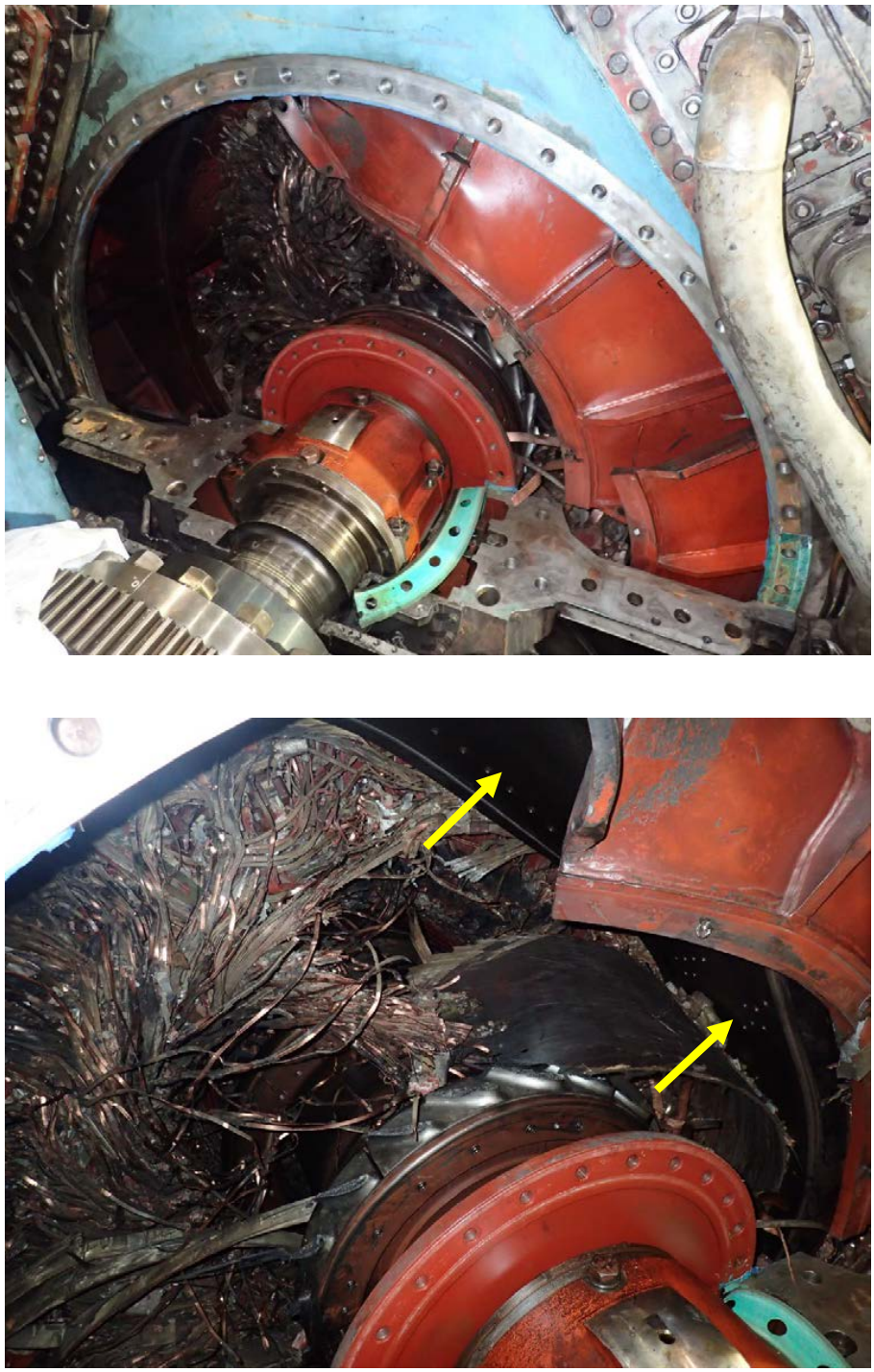

Figure 5. Views of the south (turbine) end of the generator showing damage that occurred during the failure event. Note that some outer components have been removed to permit visual examination of the interior of the generator. The ID surface of the retaining ring is indicated by the arrows in the lower image.

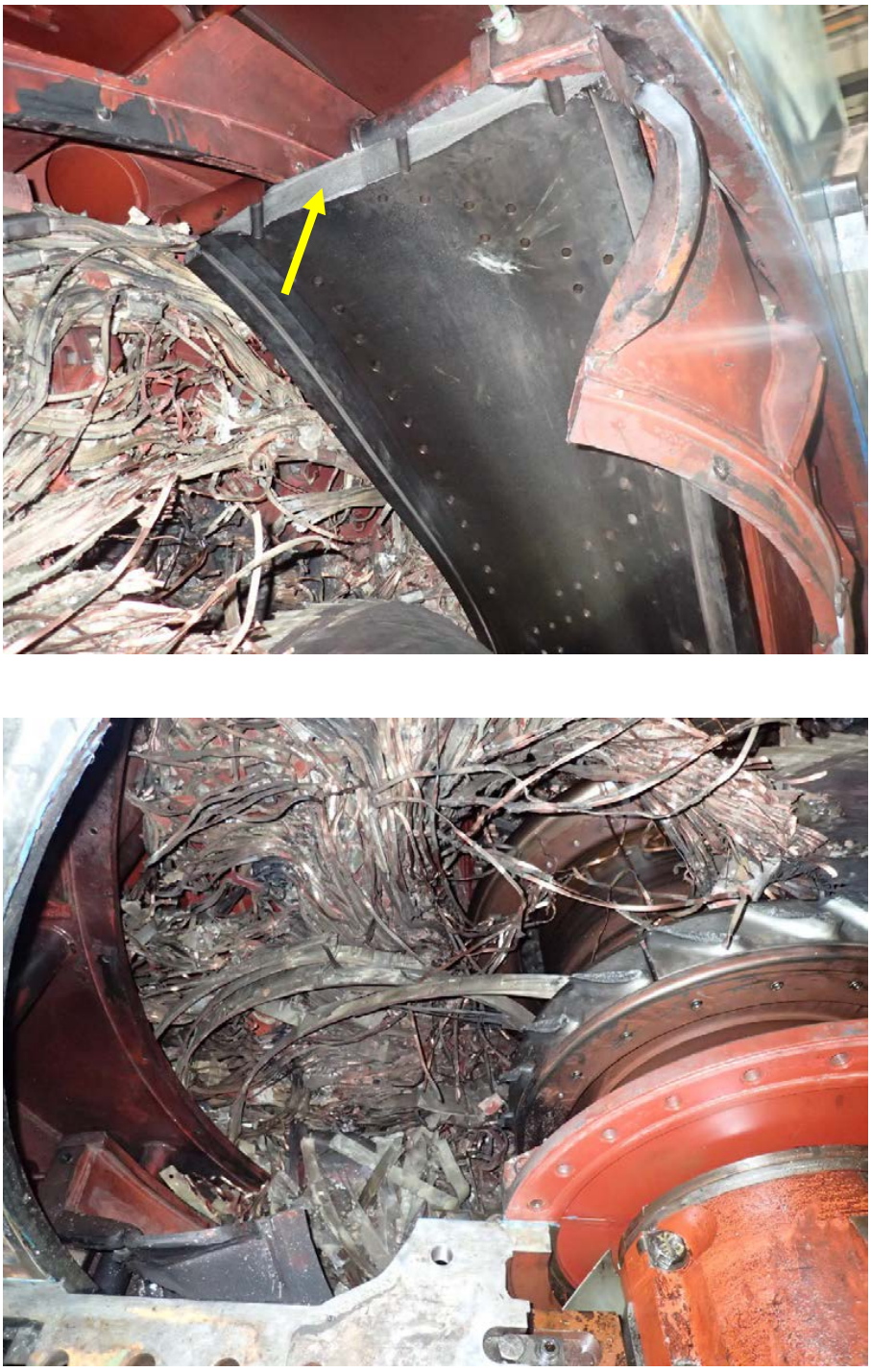

Figure 6. Additional views of the south end of the generator. The upper image shows one of the fractures on the retaining ring (arrow), and the lower image shows damaged windings, broken blades on the hydrogen cooling fan, and other damaged and displaced components.

Figure 7. Closer views of the ID surface and outboard (south) edge of the retaining ring. These images also show portions of the fiberglass liner that was situated just on the inside of the retaining ring prior to the failure event.

Figure 8. Views of the fracture surface at the lower end of the retaining ring (situated beneath the rotor) (arrow). The lower image is a view of the outboard side of the lower fracture. Debris was blocking clear views of much of the lower fracture surface.

Figure 9. Views of representative blade roots on the hydrogen cooling fan adjacent to the retaining ring.

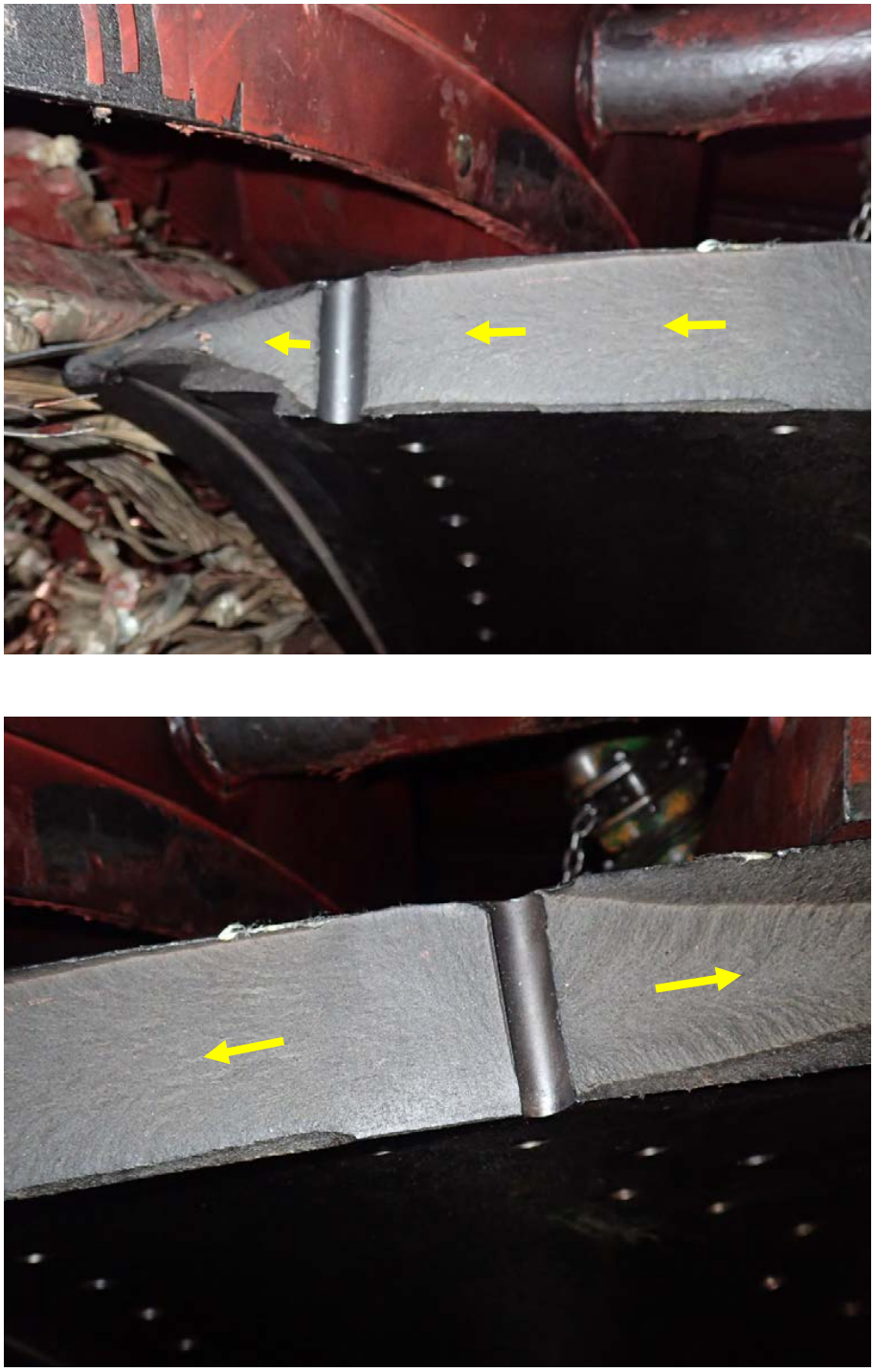

Figure 10. Views of the upper fracture surface on the retaining ring; the upper image is the inboard side of the fracture, and the lower image is the central part of the fracture. Both images include locations where the overall fracture path coincided with hydrogen cooling passages (radial holes) in the retaining ring. Chevron markings are visible on the fracture surfaces, indicating the crack growth directions (indicated by arrows).

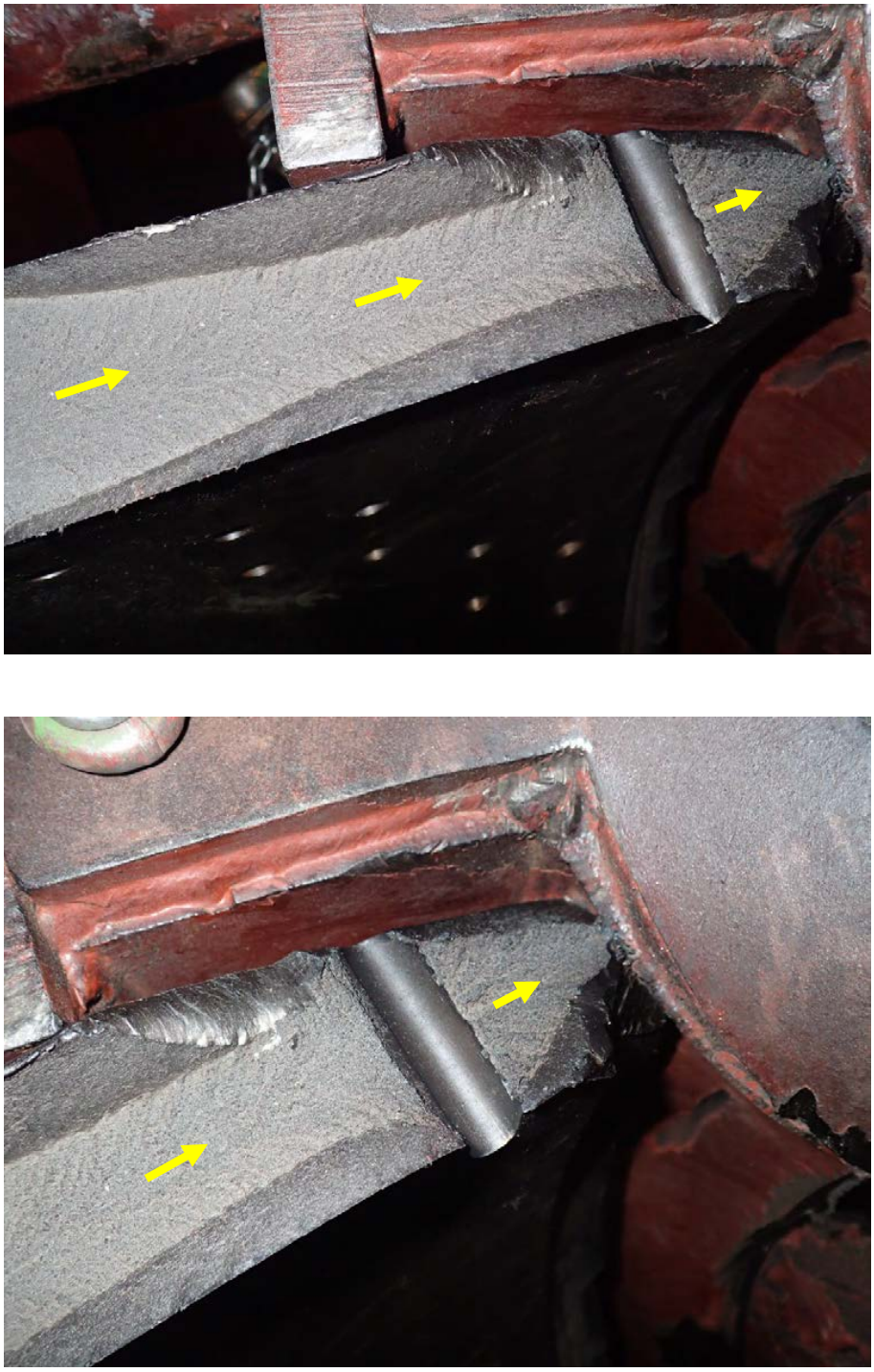

Figure 11. Views of the outboard side of the upper fracture surface on the retaining ring. Both images include a location where the overall fracture path coincided with a hydrogen cooling passage (radial hole) in the retaining ring. Chevron markings are visible on the fracture surfaces, indicating the crack growth directions (indicated by arrows).

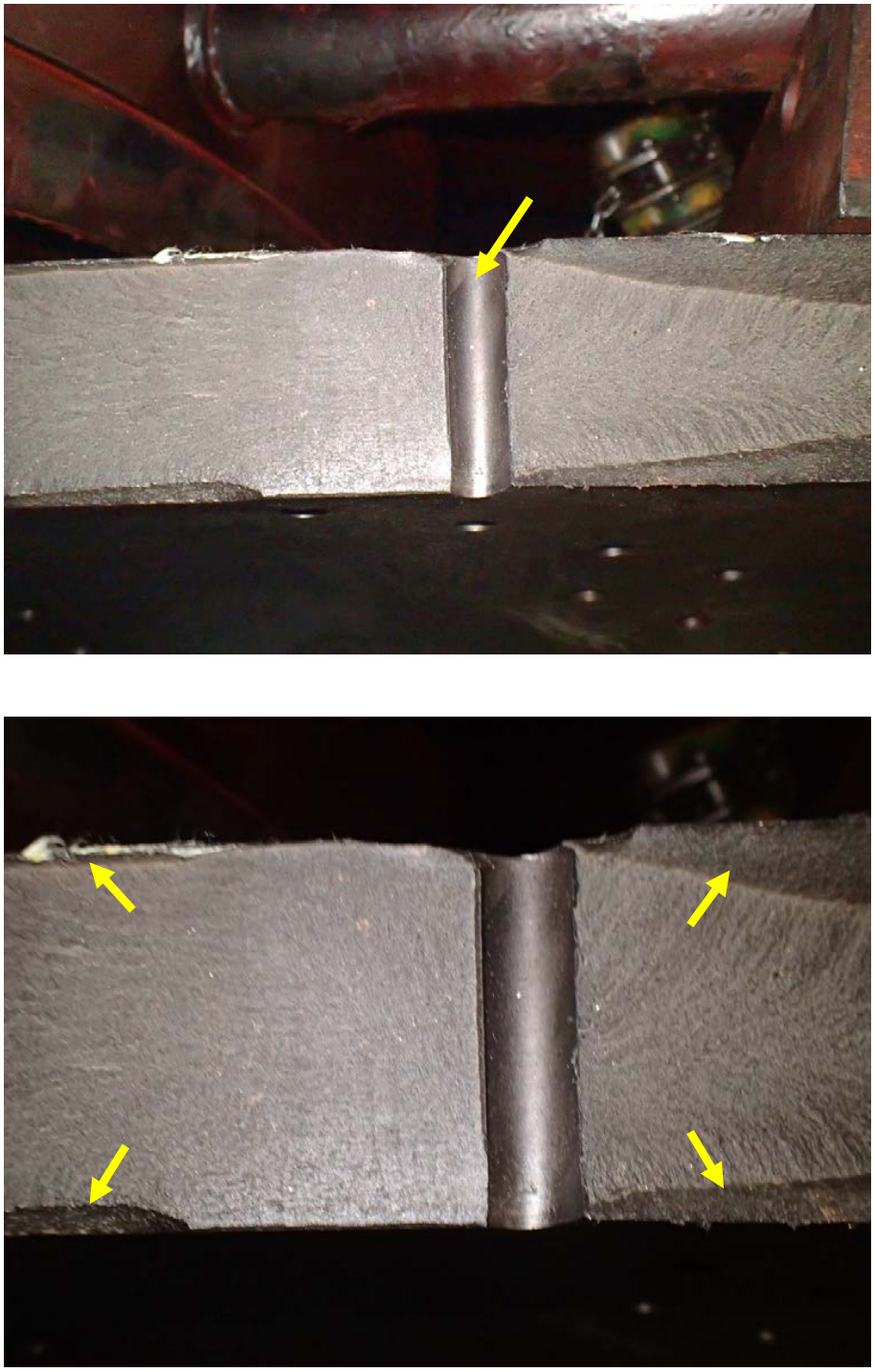

Figure 12. Closer views of the central part of the upper fracture surface on the retaining ring, including one of the cooling passage holes (upper arrow). The ring OD surface is facing up in each image. Note that shear lips are present at the ring OD and ID surfaces from the cooling hole towards the right, and at a distance of a couple of inches from the cooling hole and towards the left (lower arrows).

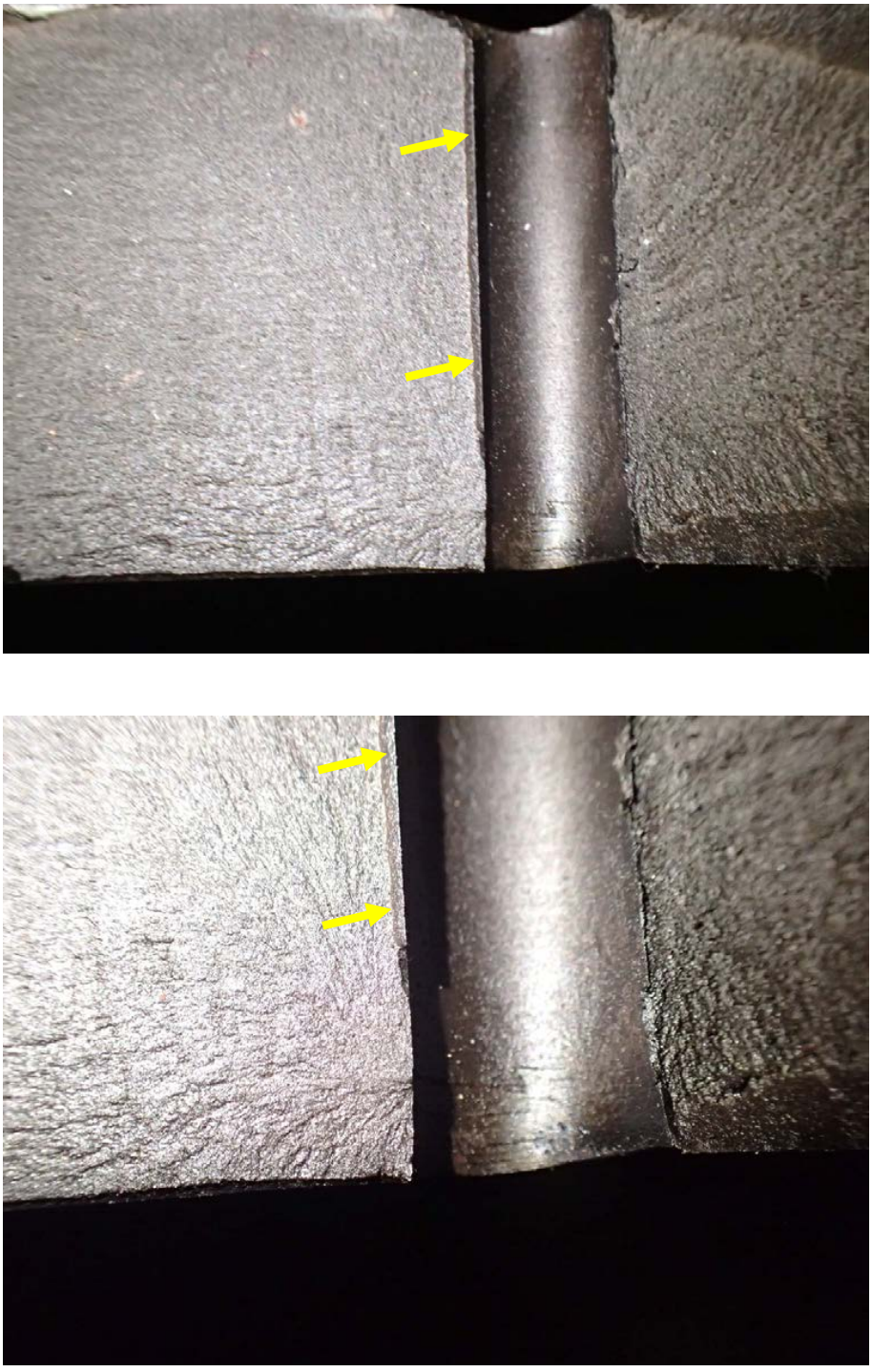

Figure 13. Closer views of the visible fracture surface texture close to the cooling passage hole shown in Figure 12. A thin shear lip is visible along most of the left edge of the hole (arrows).

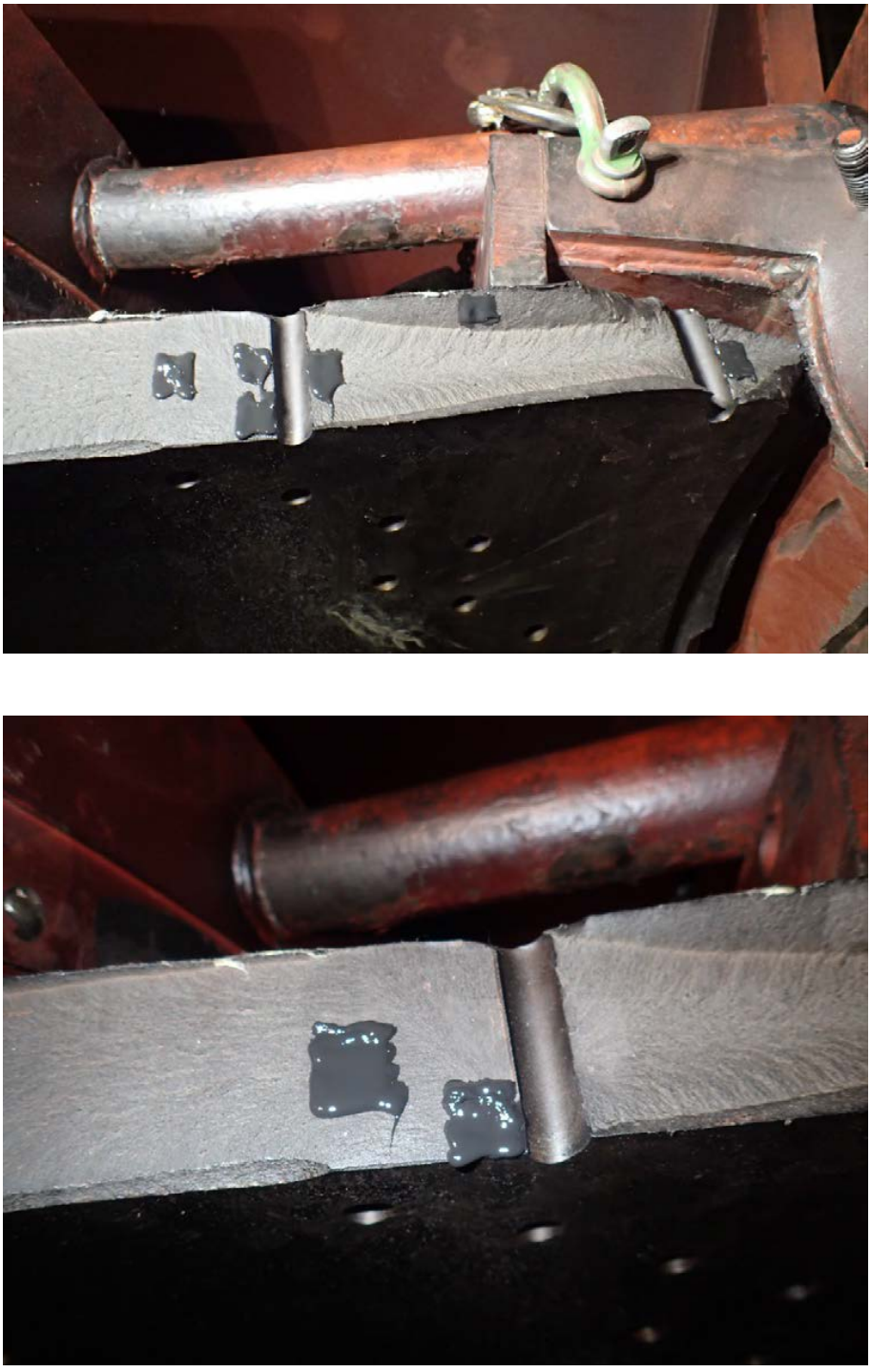

Figure 20. Views of the upper fracture surface on the retaining ring during collection of fracture surface replications (using RepliSet media).

Figure 15. Views of the south (turbine) end of the generator after broken parts, windings, and debris have been cleared out of the machine. Note in the top right corner of the upper image that one of the hydrogen coolers is still in the generator; this cooler could not be removed due to mechanical damage from the failure event.

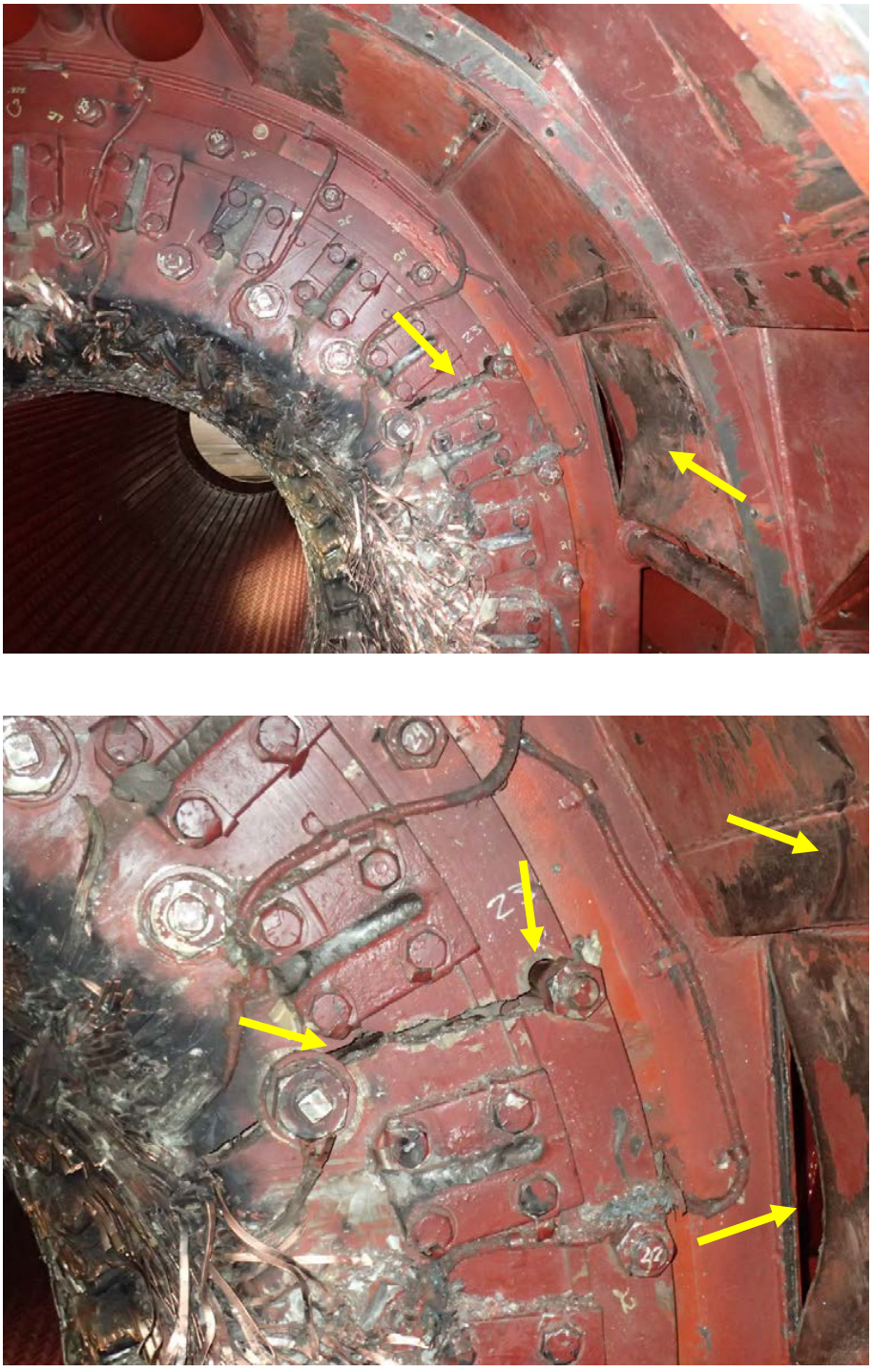

Figure 16. North views of the upper right area of the stator in the area of the failure. These images show cracks and deformed metal (arrows) that occurred as a result of the failure event.

Figure 17. Views of the various components from the generator, temporarily stored on the turbine deck. The lower image also shows the failed retaining ring in the foreground.

Figure 18. Views of multiple wooden boxes containing fragments of windings and other debris cleaned out of the generator.

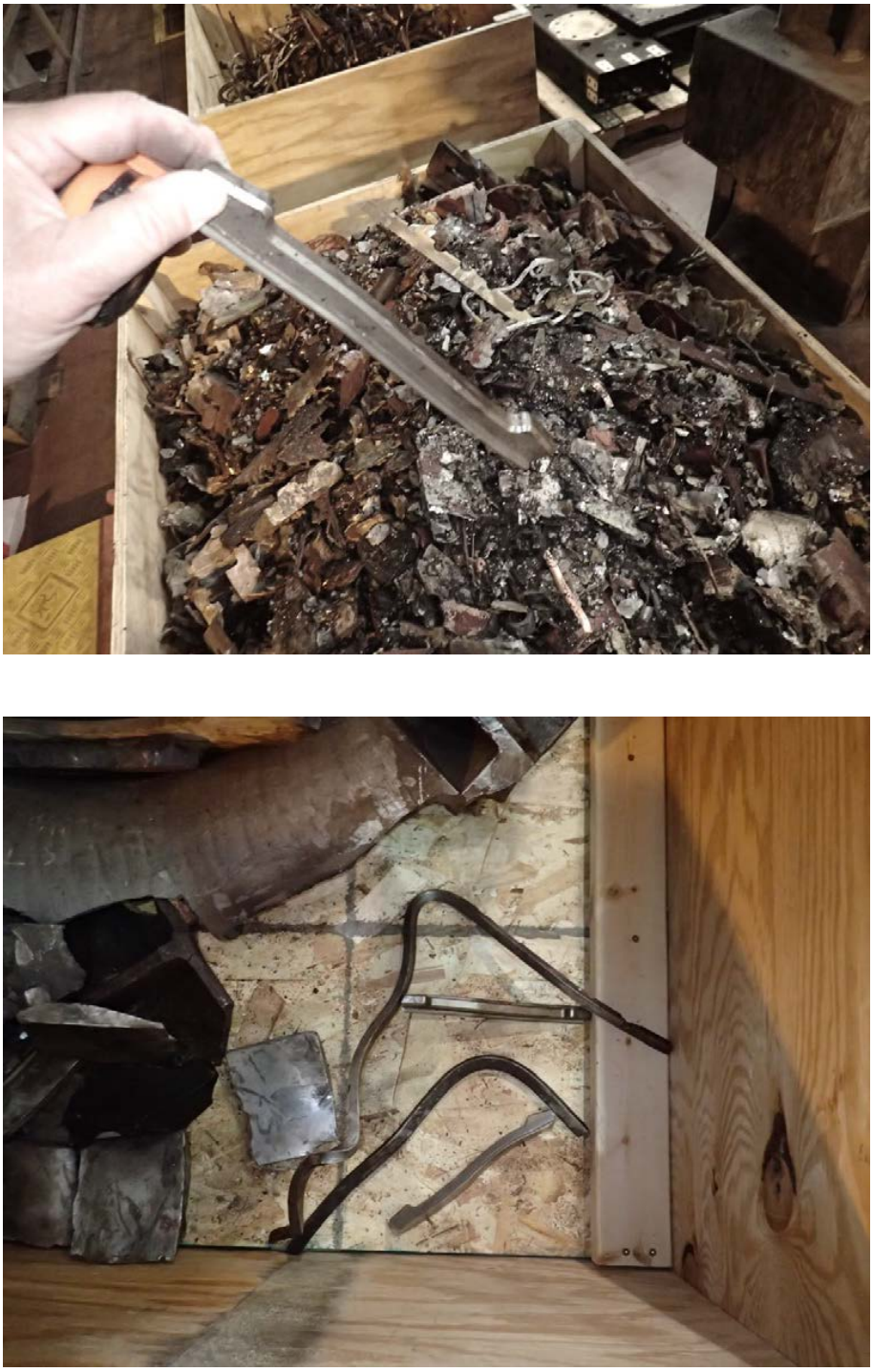

Figure 19. Views of some of the collected debris, which included a snap ring and keys that were associated with the retaining ring at the south end of the generator.

Figure 20. Views of the stored generator rotor, which was tented to maintain a dry storage environment. The lower image shows the intact retaining ring (arrow) at the north (collector) end of the rotor.

Figure 21. Views of the south end of the generator rotor. The arrow in the upper image indicates the approximate location where the retaining ring was attached, between the centering ring and the end of the rotor, and on the outside of the end windings. The arrow in the lower image shows the location of the hydrogen cooling fan.

Figure 22. Closer views of the centering ring, which is temporarily supported by wooden blocks and tape.

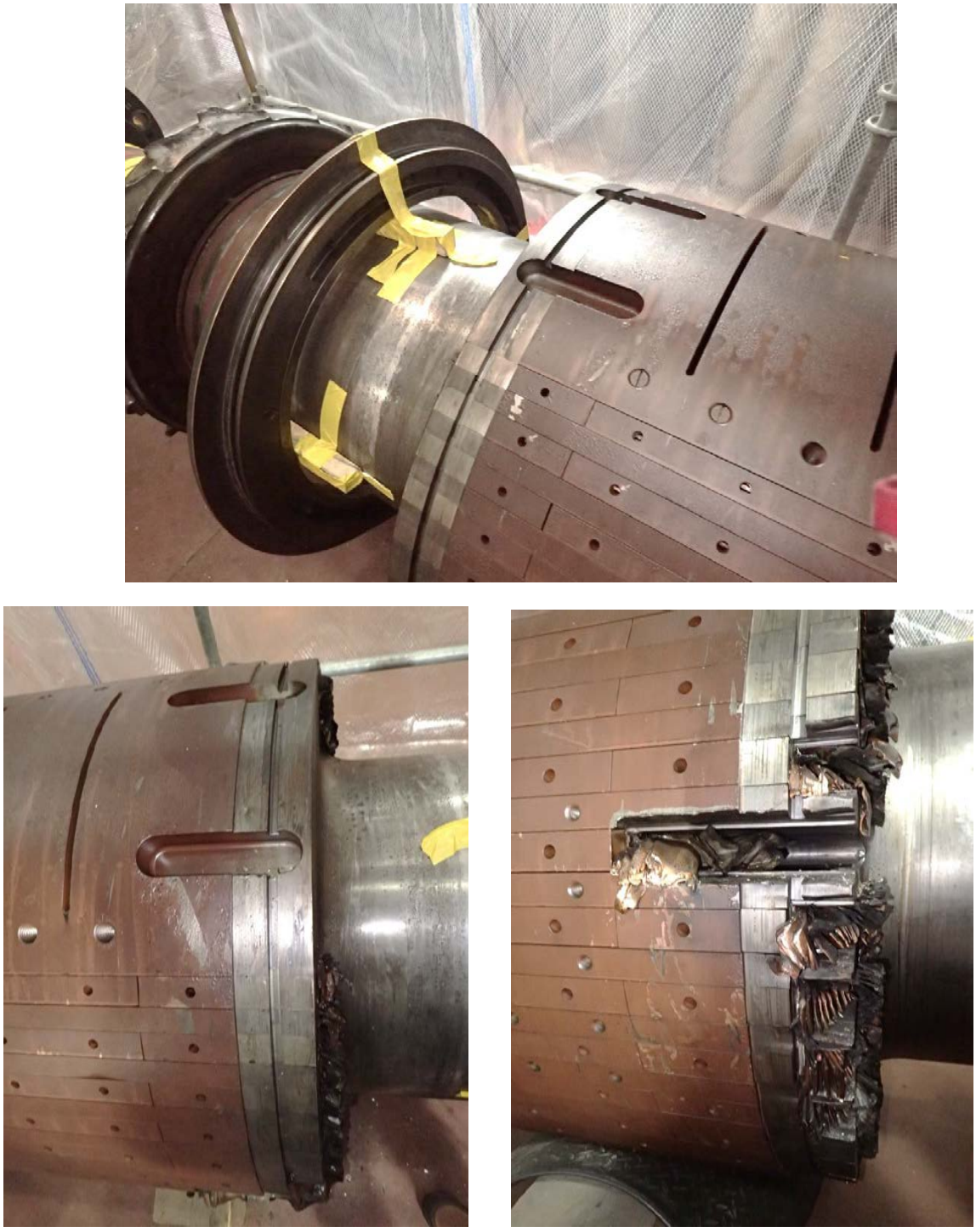

Figure 23. Additional views of the centering ring (upper image) and rotor windings in proximity to the snap ring slot. Localized damage to the rotor is visible in the lower-right image.

Figure 24. Views of the intact retaining ring and centering ring at the north end of the generator rotor. The pattern of cooling passages in the retaining ring are a result of the positions of end winding components and cooling pathways between or through components inside of the retaining ring. Note that in the lower image, the cooling fan (ring) is near the centering ring , but the blades have been removed.

Figure 25. Views of the OD surface of the retaining ring from two different positions. For discussion purposes, the "upper fracture surface" (indicated by the arrows) will reference the fracture surface that was situated at the upper part of the generator in the as-found condition.

Figure 26. Views of the ID surface of the retaining ring showing the lower fracture surface (arrow) and a location near the lower fracture surface (lower image). The outboard edge of the retaining ring is oriented down in these images.

Figure 27. Additional views of the ID surface of the retaining ring, including the upper fracture surface (arrow). In the upper image, visible light variations around the cooling passage holes are due to deformation (elongation) of the ring metal in the areas around the holes.

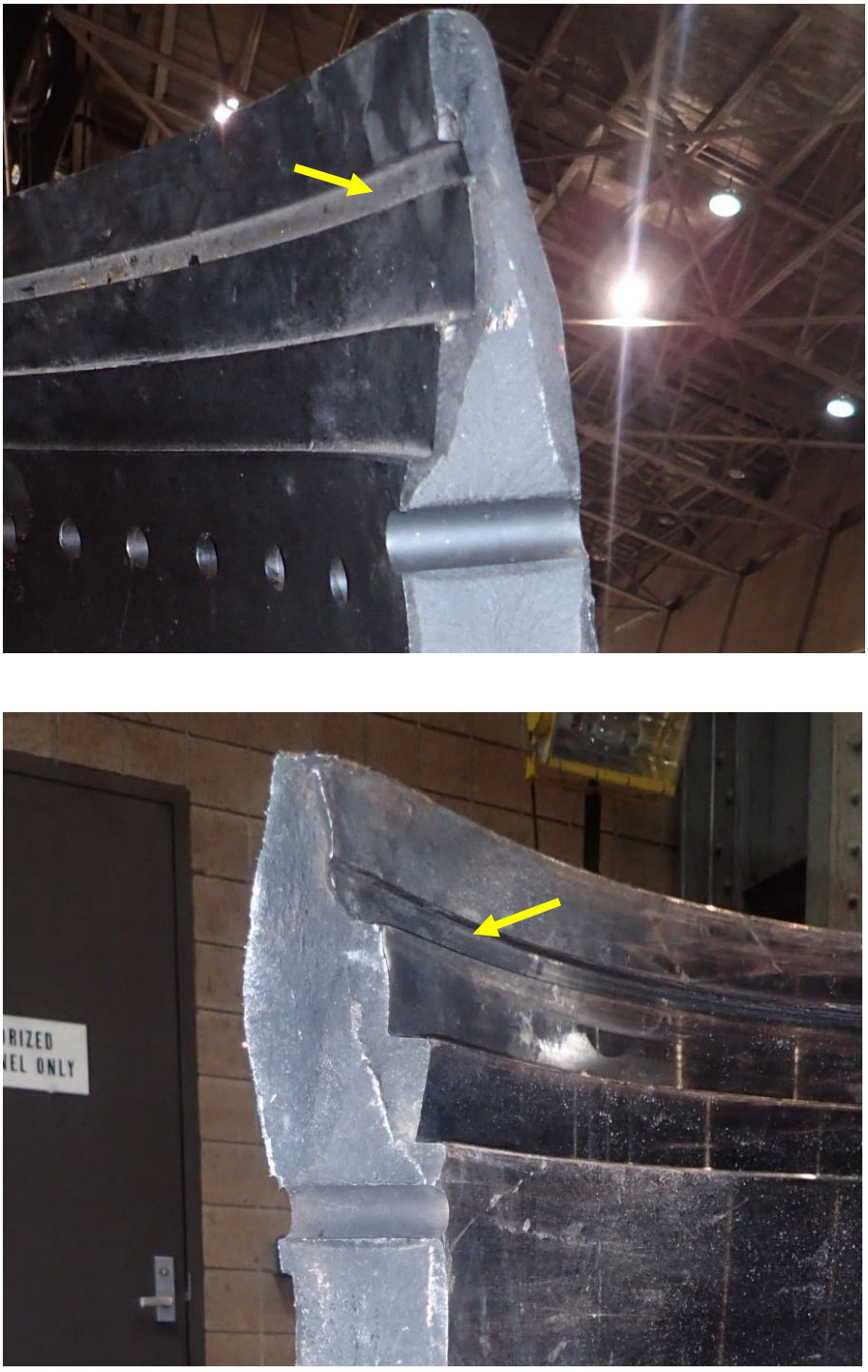

Figure 28. Views of the ID surface profile at the inboard edge the ring (taken at the upper fracture surface (upper image) and lower fracture surface (lower image). The ID slot for the snap ring is indicated by the arrows in each image.

Figure 29. Views of the ID surface profile at the outboard edge the ring (taken at the lower fracture surface (upper image) and at a location between the fractures (lower image). An intermittent keyway slot is indicated by the arrows in each image.

Figure 30. Views of a location of mechanical damage at one of the keyways along the outboard edge of the retaining ring.

Figure 31. Close views of the mechanical damage at the outboard edge of the retaining ring. These features were along one side of one of the intermittent slots, and exhibited deformation and sheared metal (indicated by the arrows) that indicated mechanical impact from the outside toward the inside.

Figure 32. Views of the lower fracture surface on the retaining ring. The upper right image is a closer view of the area near the central cooling passage, and the lower image is a closer view of the same area (rotated 90 degrees clockwise) with side lighting to highlight the fracture surface texture.

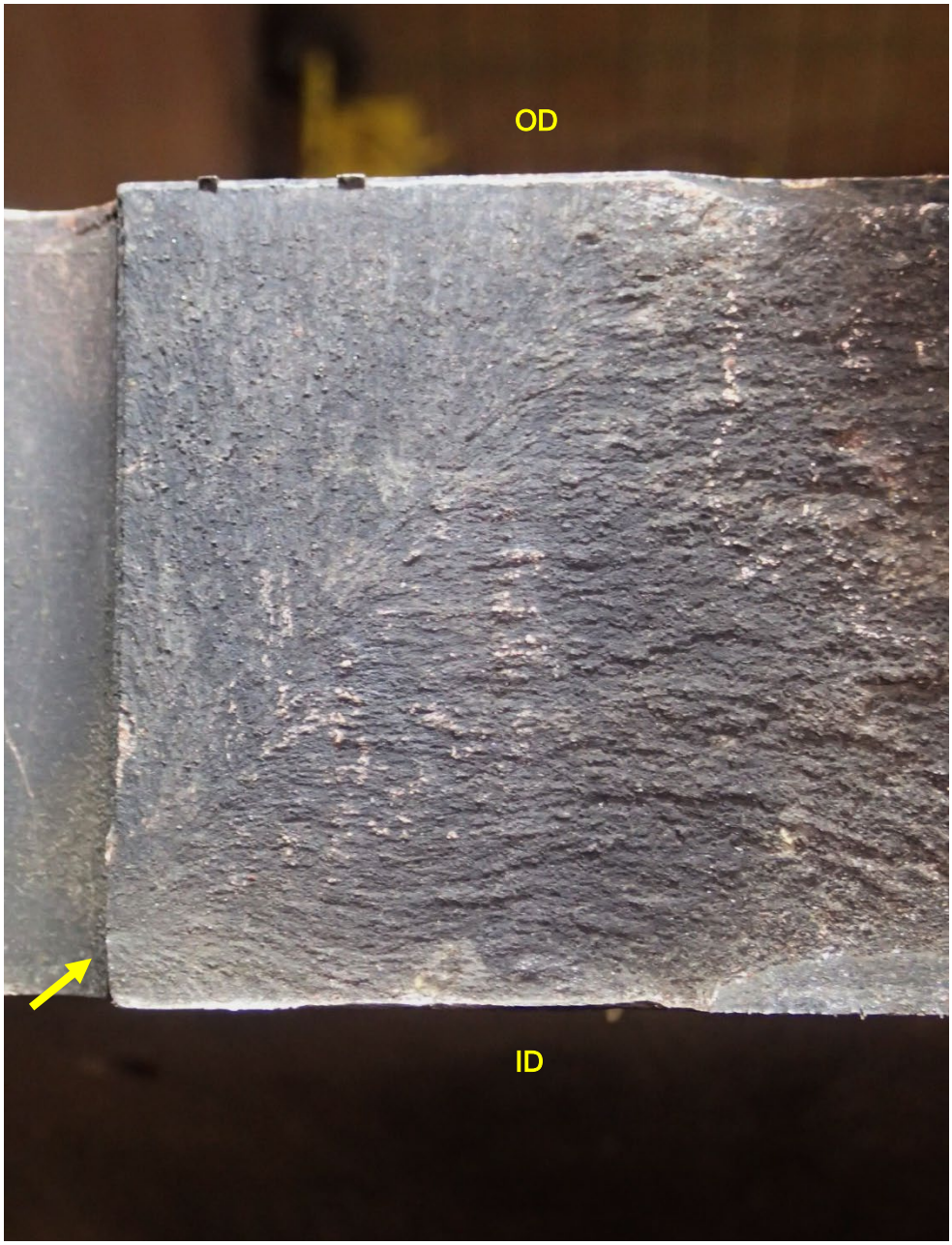

Figure 33. Closer view of the area shown in the lower image of Figure 32. The visible fracture surface texture suggests an origin area at the edge of the cooling passage hole.

Figure 34. Closer view of the area shown in Figure 33, with side lighting to highlight the fracture surface features. The visible fracture surface texture suggests an origin area at the edge of the cooling passage hole.

Figure 35. Alternate view of the area shown in Figure 34, with side lighting to highlight surface features. Features that are visible on the cooling passage surface (arrows) coincide with the apparent crack origin area at the edge of the cooling passage hole. Fine debris (mostly fiberglass particulate) is visible on the cooling passage surface.

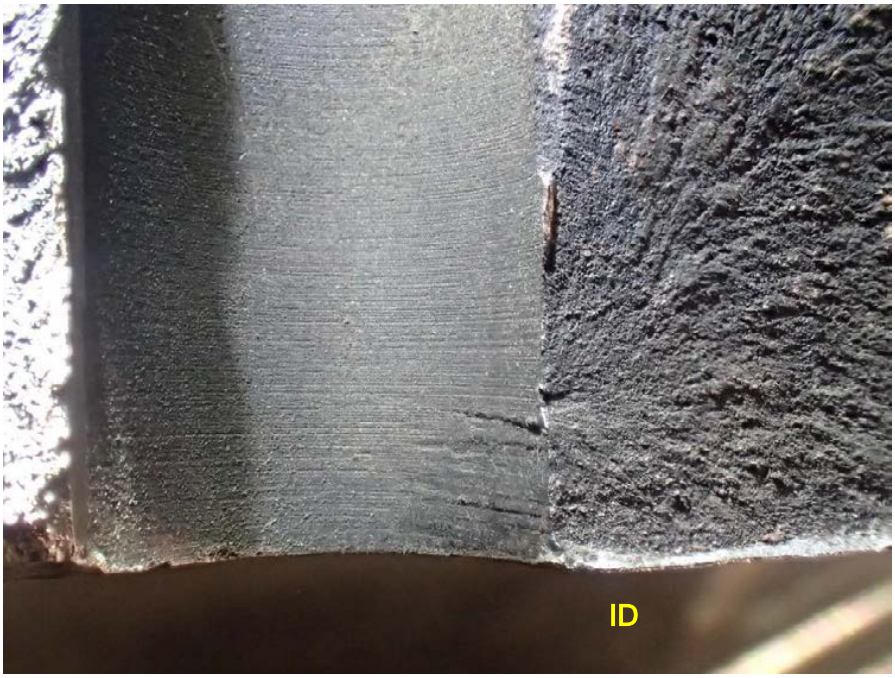

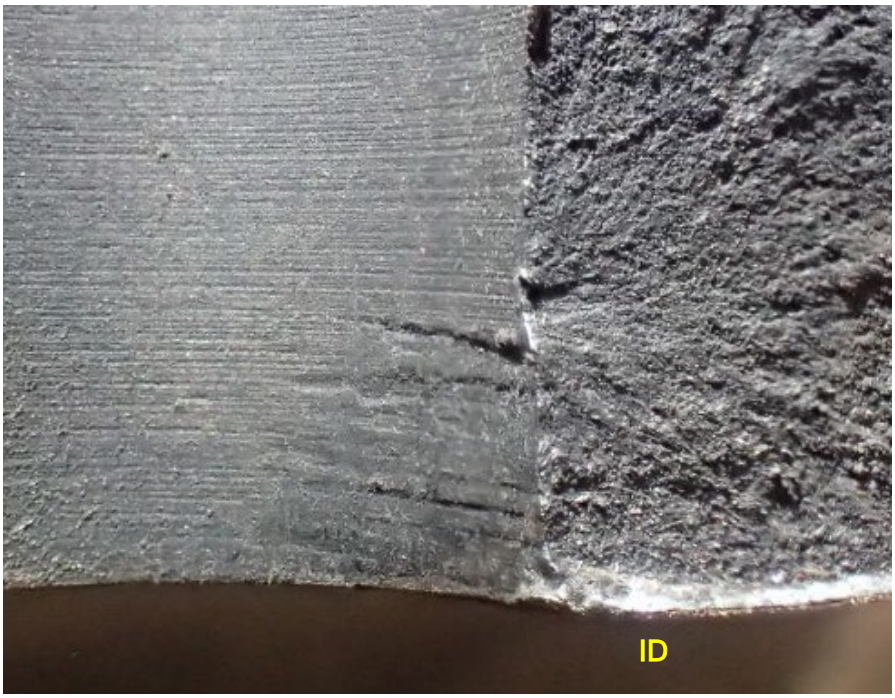

Figure 36. Closer views of the area shown in Figure 35 after blowing off the fiberglass particulate with air.

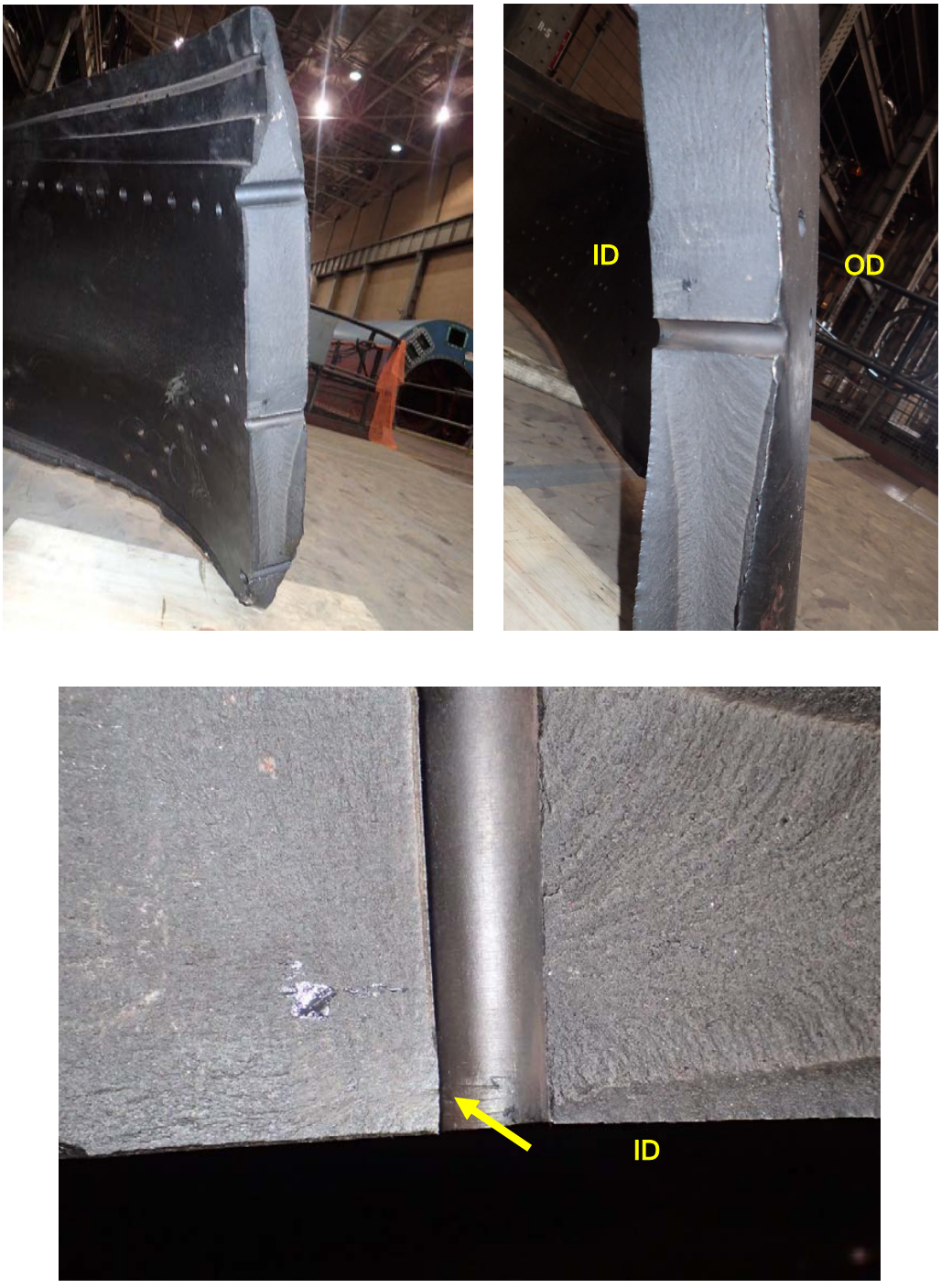

Figure 37. Views of the upper fracture surface on the retaining ring. The upper right image is a closer view of the area near the central cooling passage, and the lower image is a closer view of the same area (rotated 90 degrees counterclockwise); the shiny spot in the lower image is remnant material from the RepliSet sampling. The apparent origin area at the edge of the cooling passage hole is indicated by the arrow.

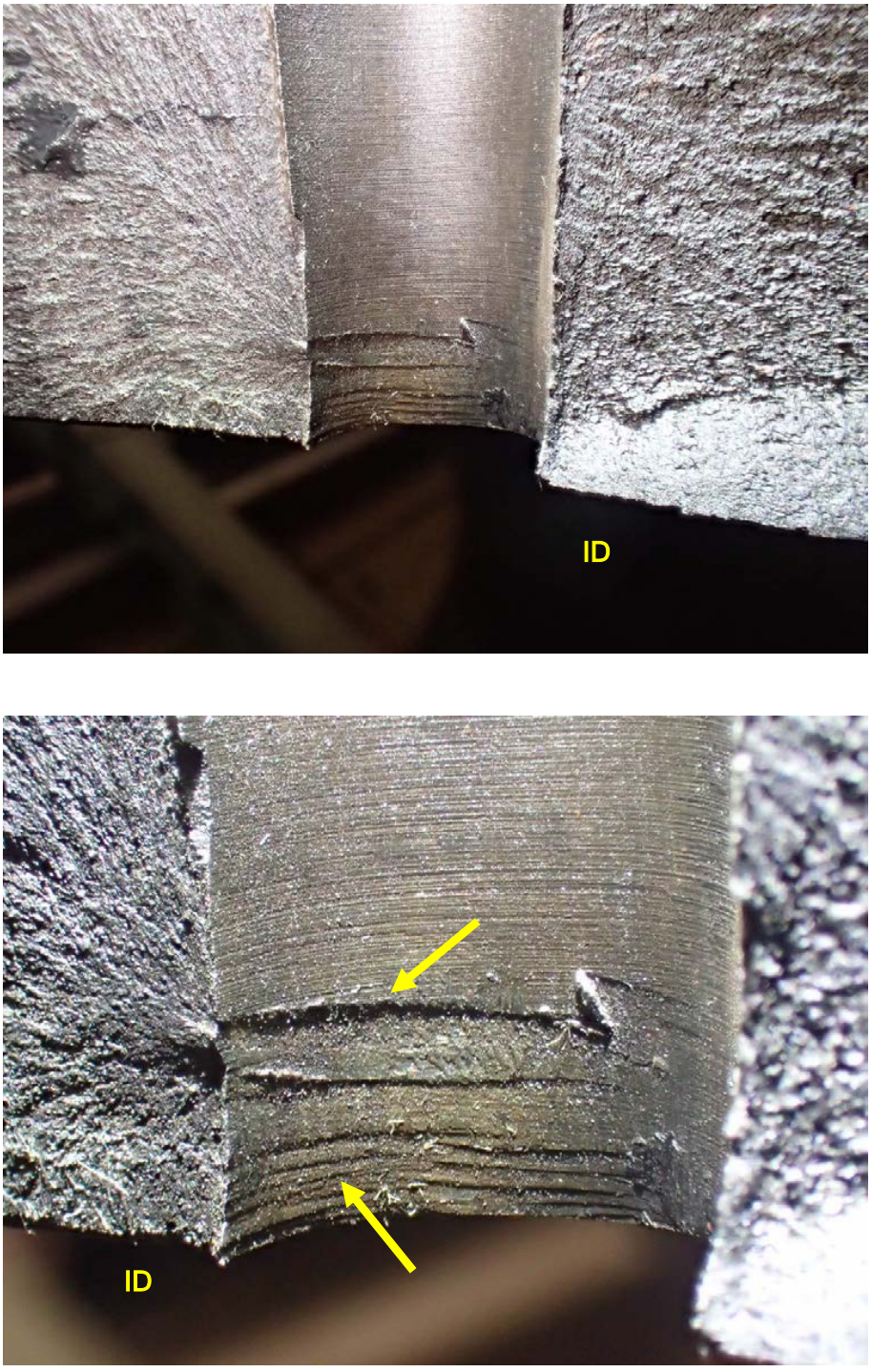

Figure 38. Closer views of the area shown in the lower image of Figure 37, with side lighting to highlight surface texture. Features that are visible on the cooling passage surface (arrows) coincide with the apparent crack origin area at the edge of the cooling passage hole.

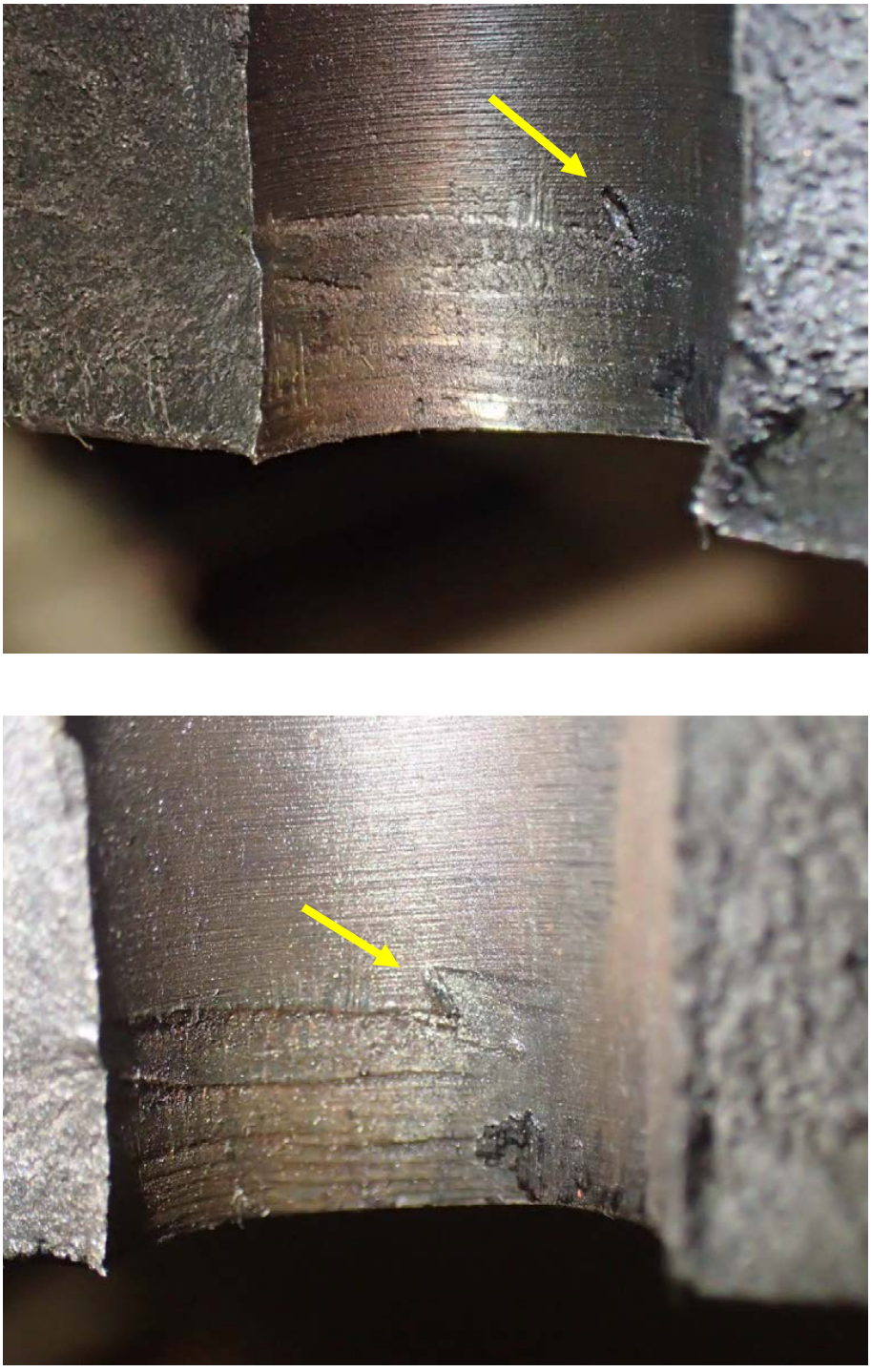

Figure 39. Additional close views, under more direct lighting, of features on the cooling passage surface in proximity to the apparent crack origin area. The visible surface damage included an angled mound of metal that appeared to have been "piled up" during the damage process (arrows).

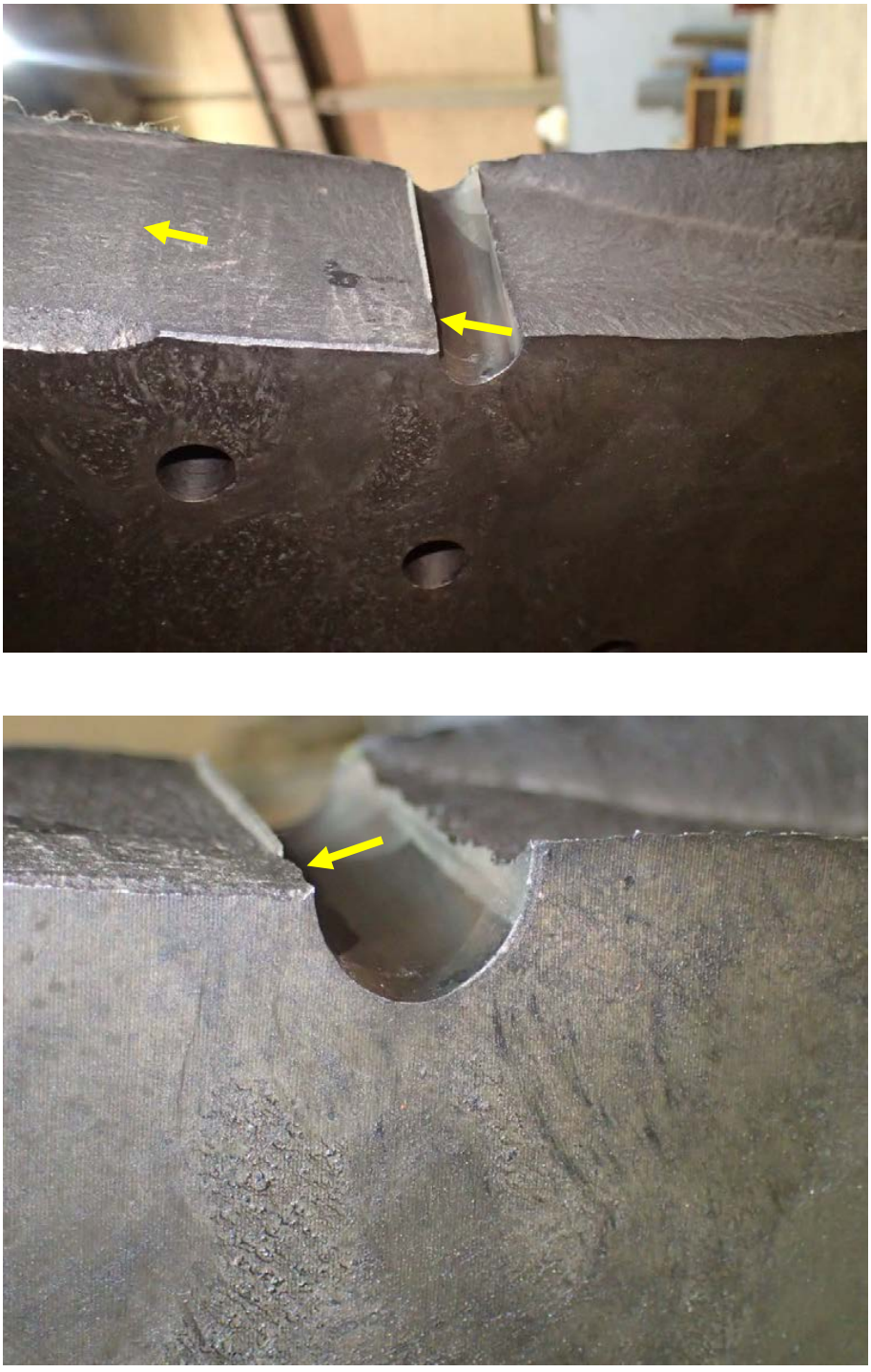

Figure 40. Alternate views of the central cooling passage hole at the upper fracture surface. The ID surface of the retaining ring is visible in each image. In the upper image, the right arrow indicates the crack origin area and the left arrow indicates the location of an apparent beach mark; other possible beach marks are visible between the left and right arrows. The arrow in the lower image also indicates the location of the apparent crack origin.

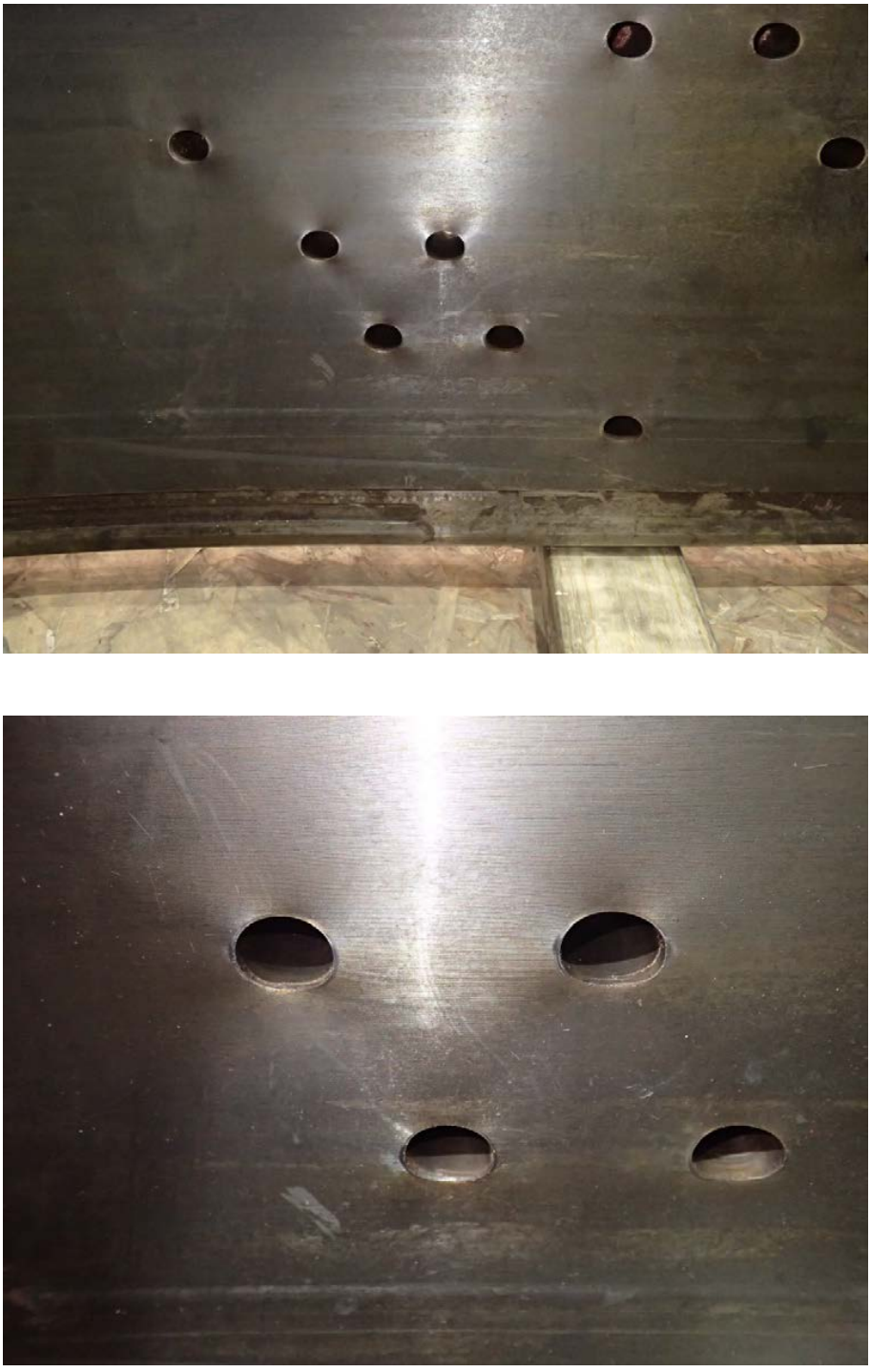

Figure 41. Views of a group of four cooling passage holes that were elongated (consistent with the opening or straightening of the retaining ring, and also exhibited indicates of mechanical damage at the hole ID surfaces near the ring ID surface.

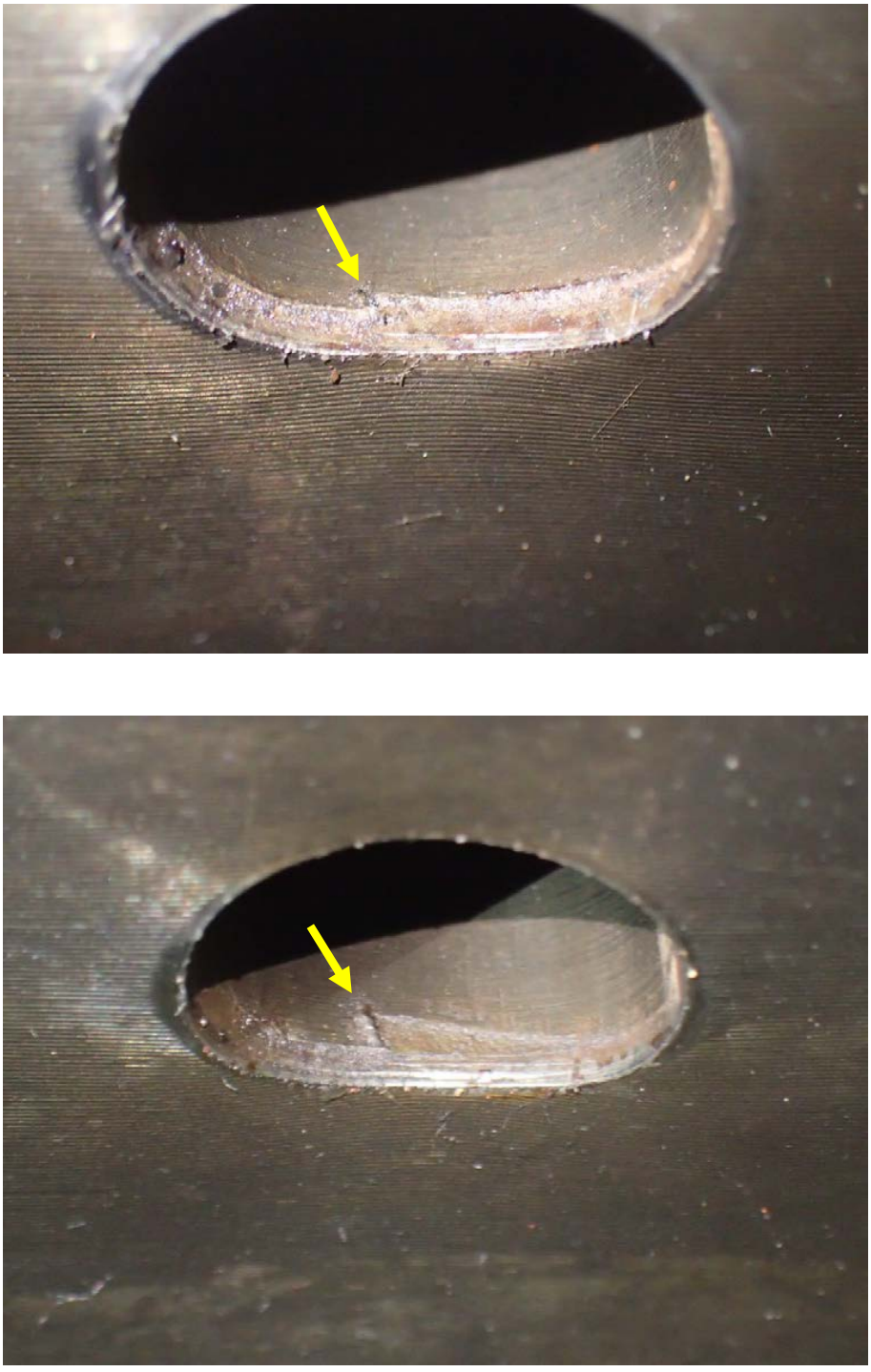

Figure 42. Close views of the interior of two of the elongated cooling passage holes in Figure 41. The arrows indicate the locations where internal surface damage is visible. Both of these locations also exhibited an angled featured with a small amount of piled up metal that was similar to that observed in the cooling passage at the crack origin area (arrows).

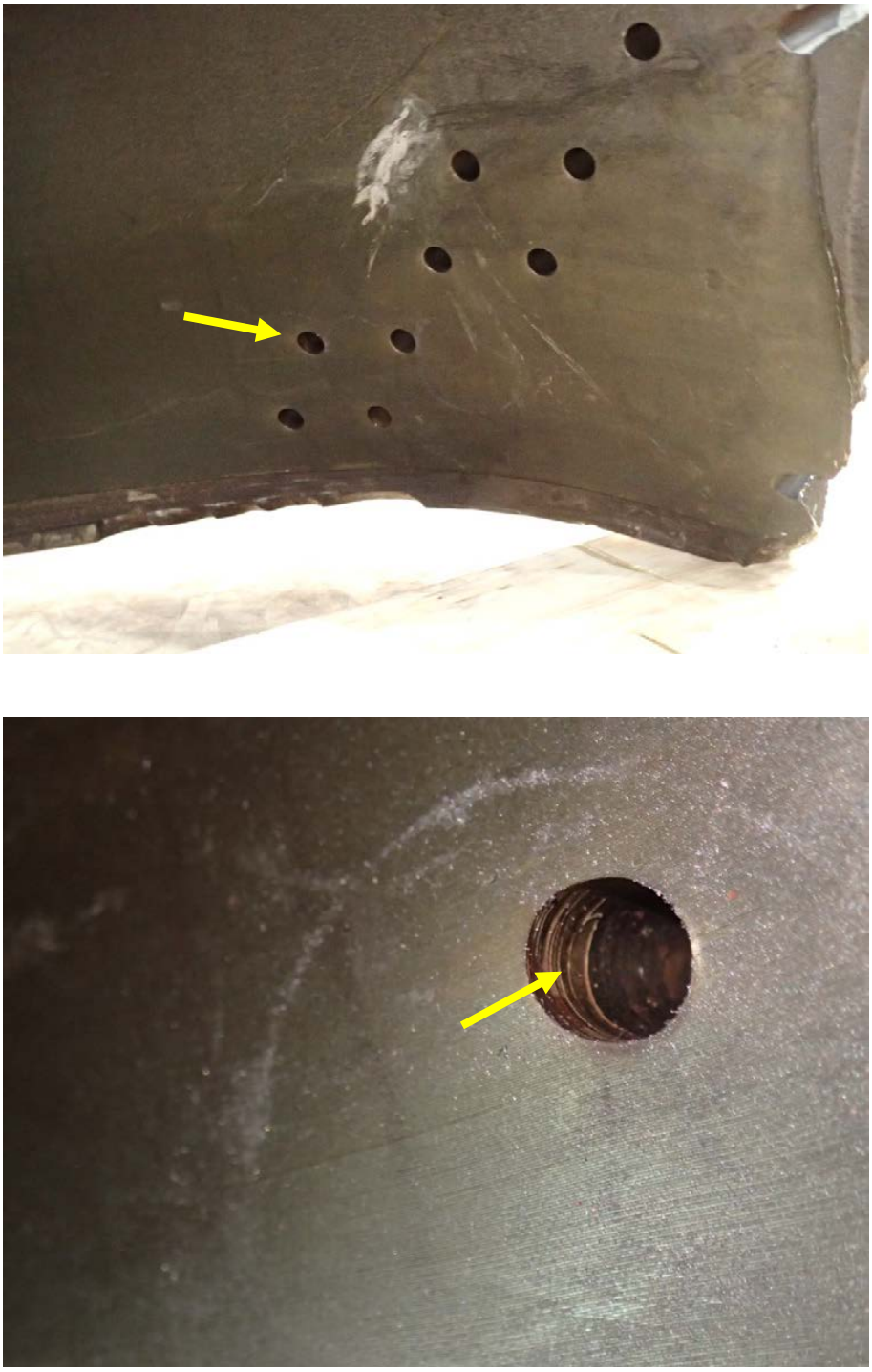

Figure 43. Additional views of a cooling passage hole with internal damage near the ring ID surface (arrow). The area shown is close to the upper fracture surface, which is toward the right in each image.

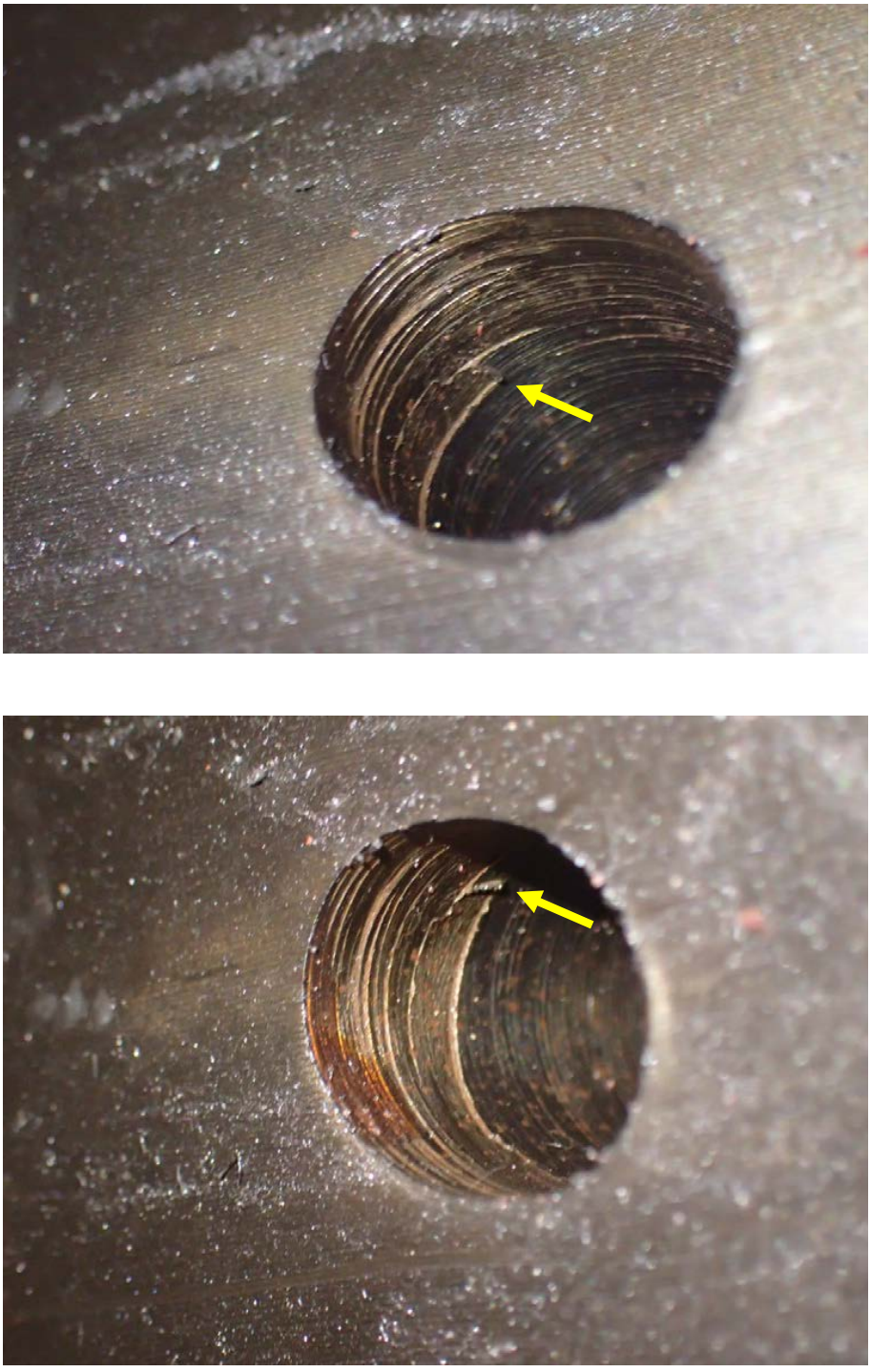

Figure 44. Closer views of the hole ID surface damage shown in Figure 43. This location also exhibited an angled featured with a small amount of piled up metal that was similar to that observed in the cooling passage at the crack origin area (arrows).

Figure 45. Views of the parts and fragments of material that appeared to be part of the ring retention snap ring and keys. The parts were deformed to various degrees and one of the ends of the snap ring was fractured.

Figure 46. Close views of the end of the deformed bar shown in Figure 45.

Figure 47. Close views of one end of the snap ring shown in Figure 45.

Figure 48. Close views of the other end of the snap ring shown in Figure 45. This end was damaged but not fractured, and the tool fitting has broken off at the location of the pins (visible in the upper image).

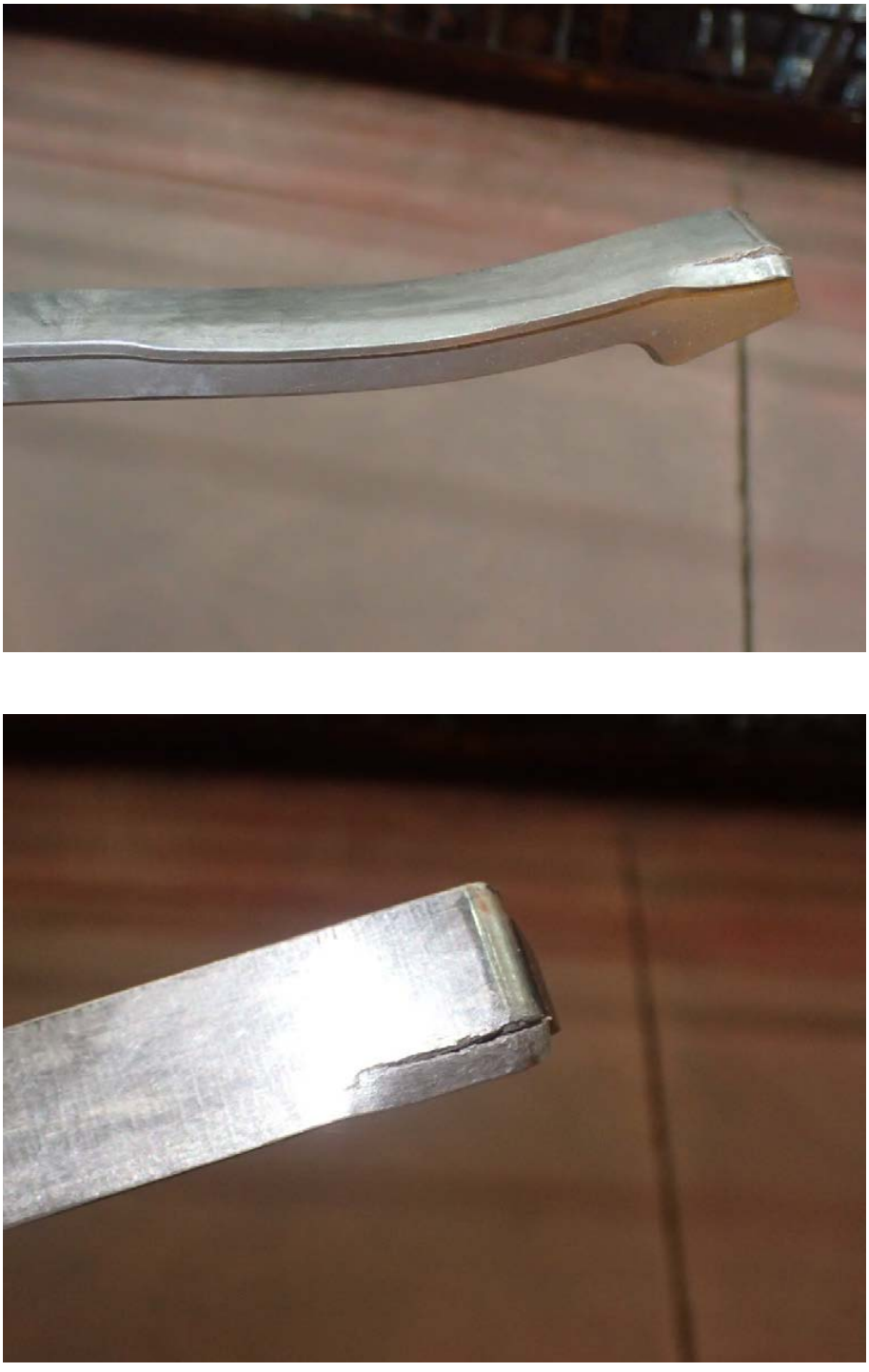

Figure 49. Views of deformation and damage on a ring attachment (key) component.

Figure 50. Views of the retaining ring in the as-received condition at SI's metallurgical laboratory. The ring was enclosed in a crate, which has been disassembled.

Figure 51. Additional views of the retaining ring in the as-received condition at SI's metallurgical laboratory.

Figure 52. Views of the central cooling passage on the upper (upper image) and lower (lower image) fracture surfaces of the retaining ring, in the as-received condition.

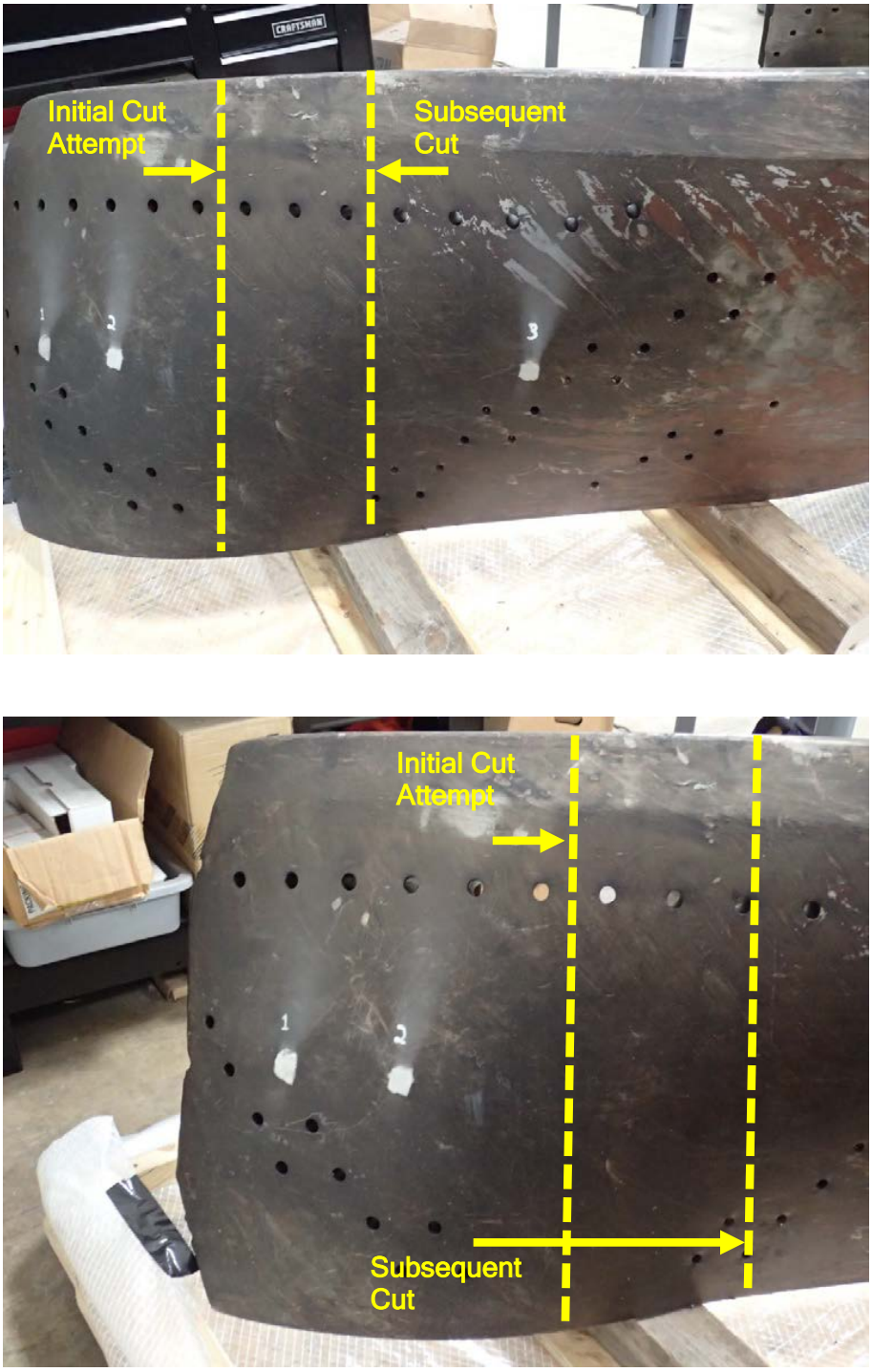

Figure 53. Views of the OD surface of the retaining ring near the upper fracture. The cleaned spots (numbered 1, 2, and 3) are locations where hardness testing was performed, and the dashed lines indicate the approximate locations where an initial cut attempt (via plasma cutter) was made, and where the complete cut was made to remove the upper fracture (and adjacent material) from the retaining ring.

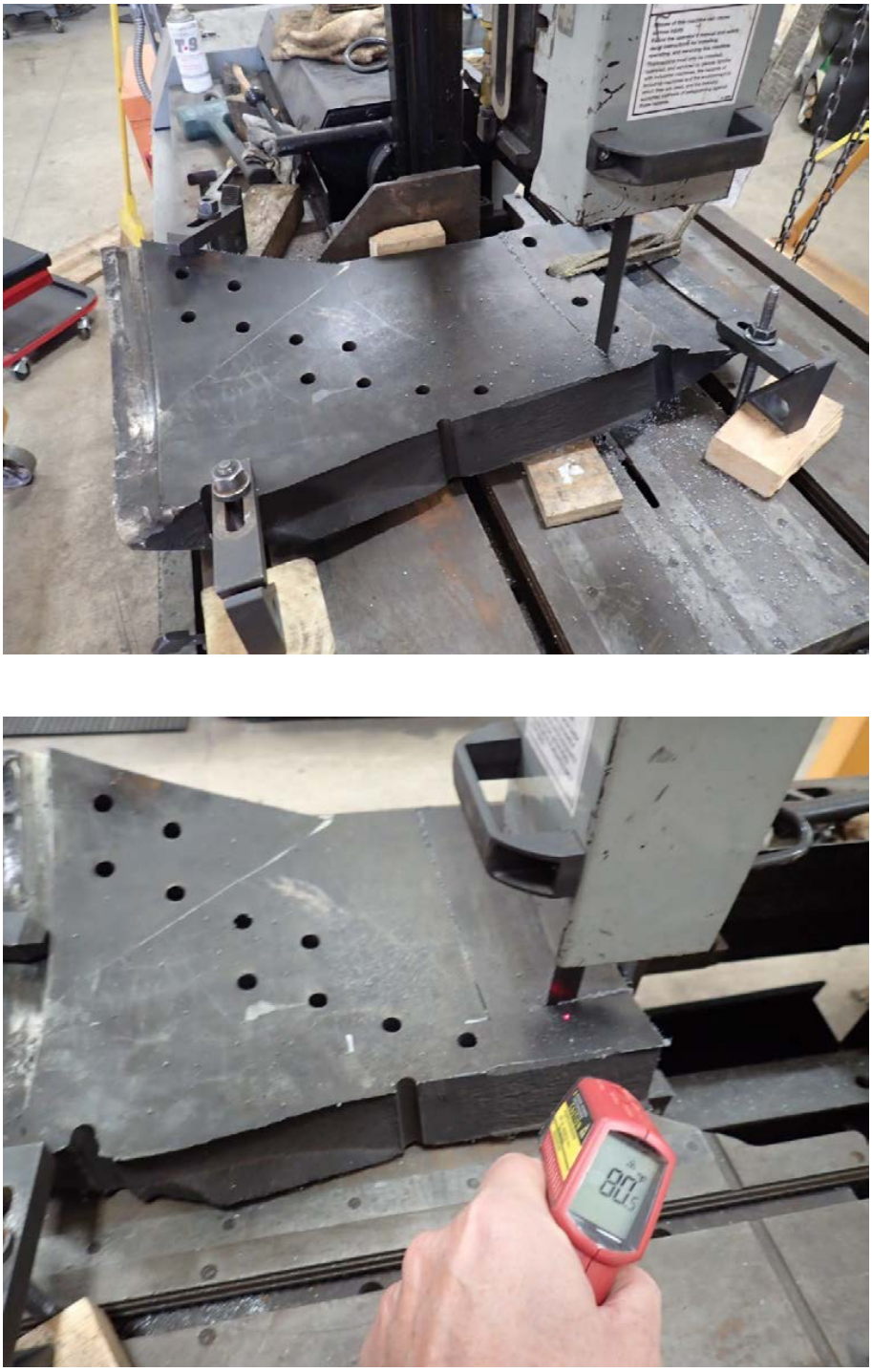

Figure 54. Views of the dry (bandsaw) cutting process during sectioning of the upper end of the ring. The metal temperature was monitored during cutting to ensure that no significant heating occurred.

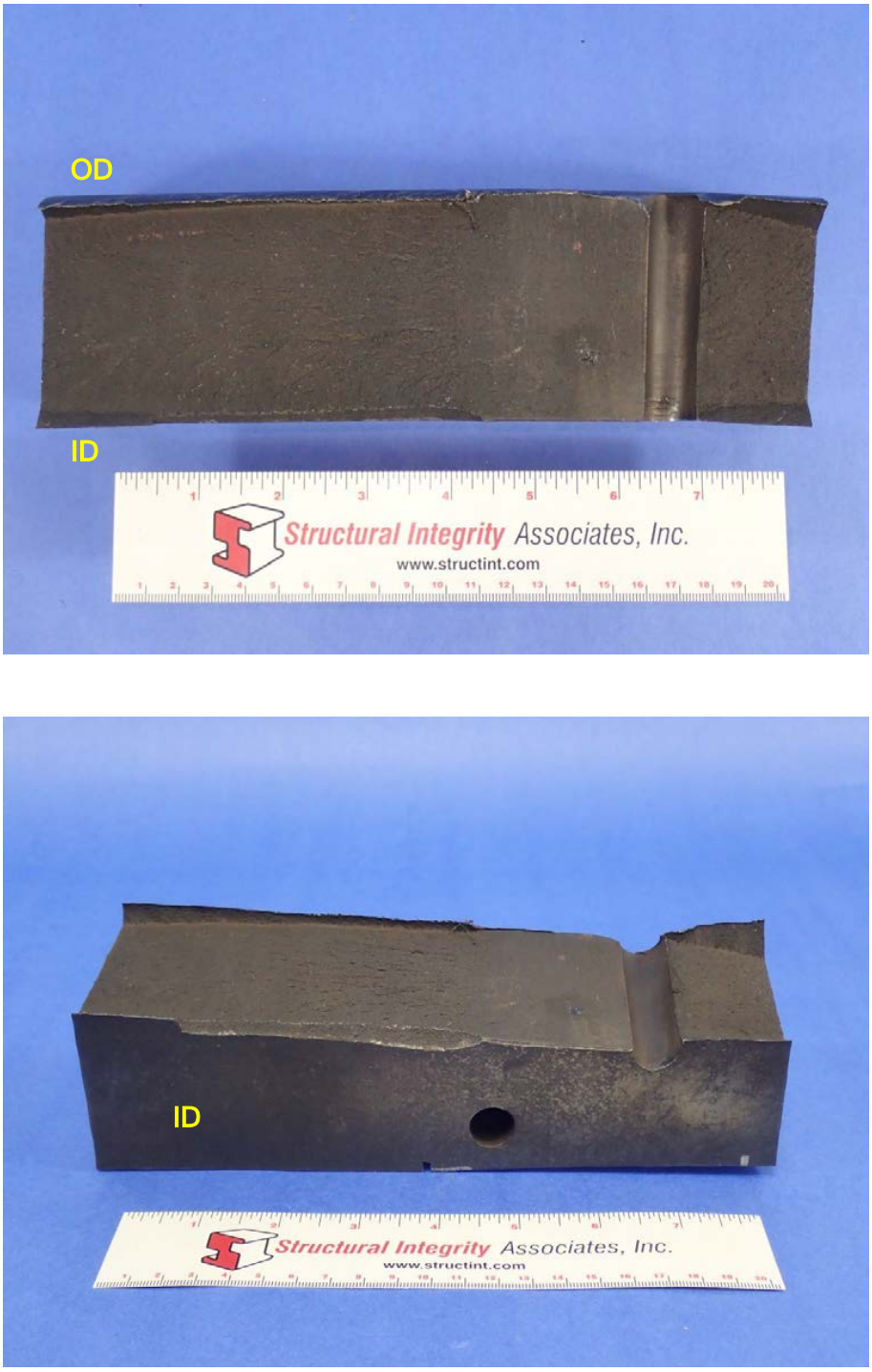

Figure 55. Views of the fracture region of interest (adjacent to the central cooling hole on the upper fracture surface) after removal from the retaining ring.

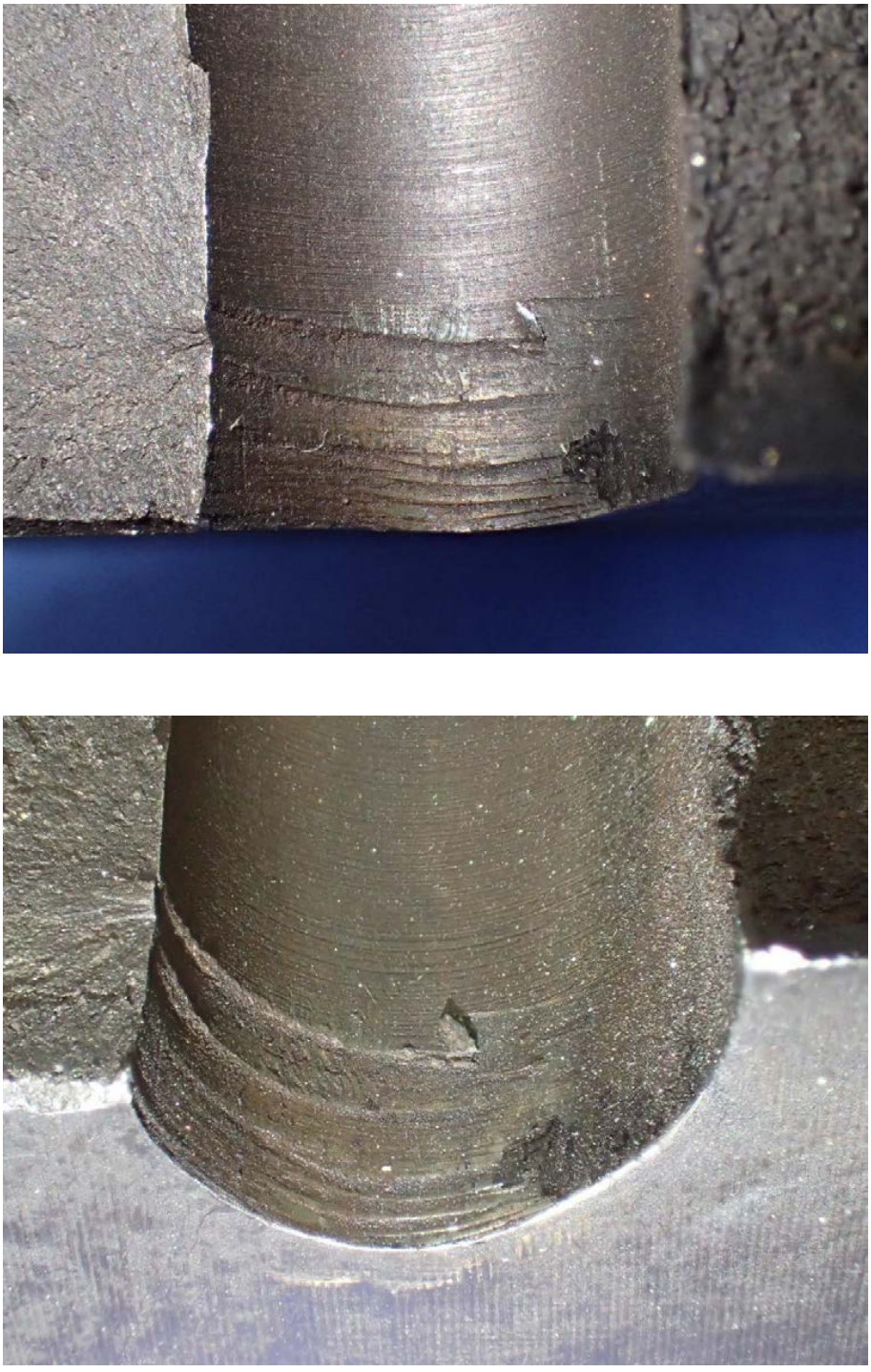

Figure 56. Close views of the central cooling passage and adjacent fracture surface, on the section shown in Figure 55.

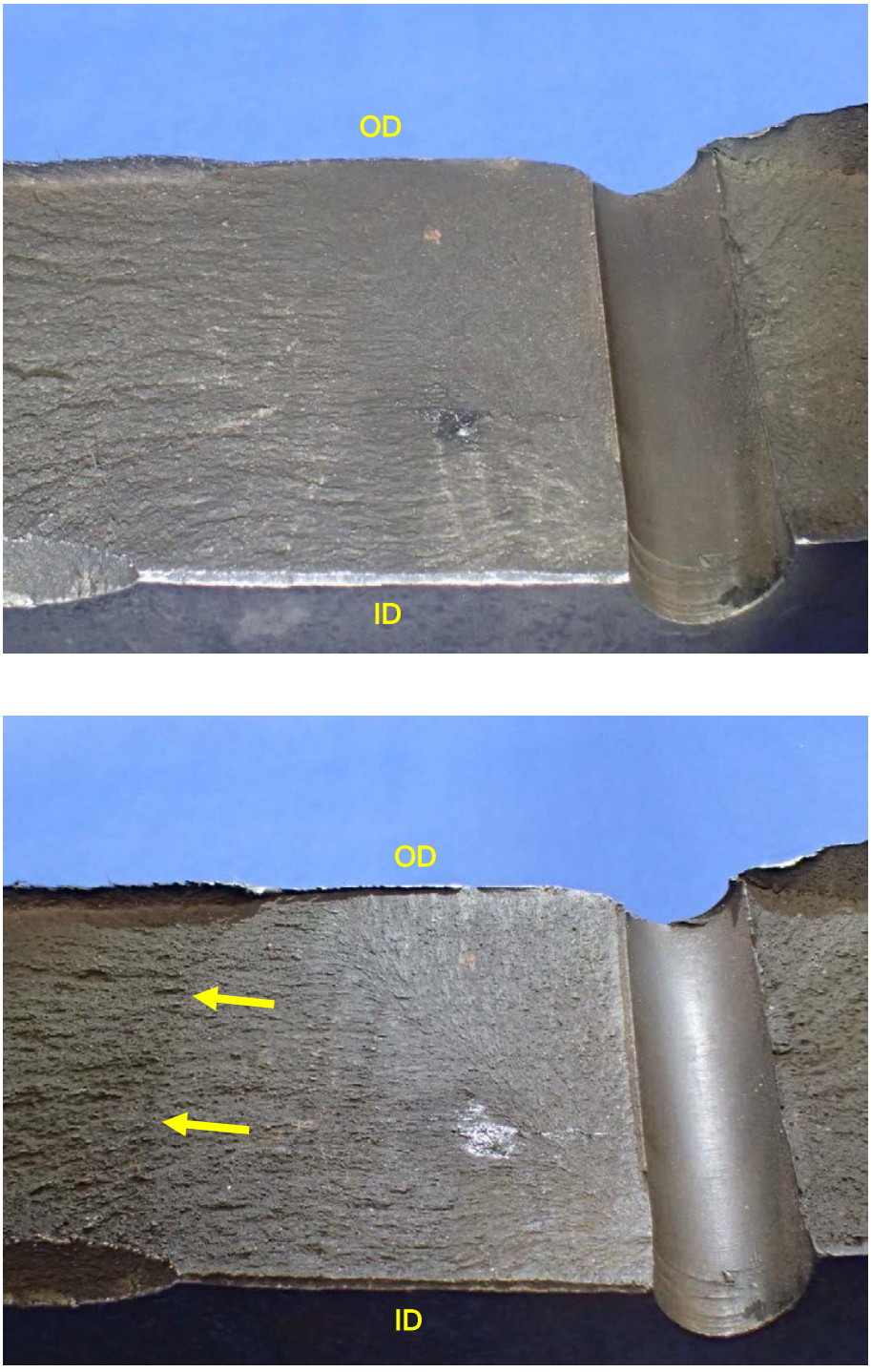

Figure 57. Views of the flat fracture region on the removed ring section shown in Figure 55. The lower image was taken with alternate lighting to highlight the fracture surface texture. The arrows in the lower image indicate the apparent position of the crack tip when the final fast rupture occurred. The localized area with remnant RepliSet material is also visible in both images (gray in the upper image and shiny in the lower image).

Figure 58. Views of a reduced section that was cut from the sample shown in Figure 55. The dashed line shows the location where this sample was cut to remove the area of interest near the retaining ring ID surface.

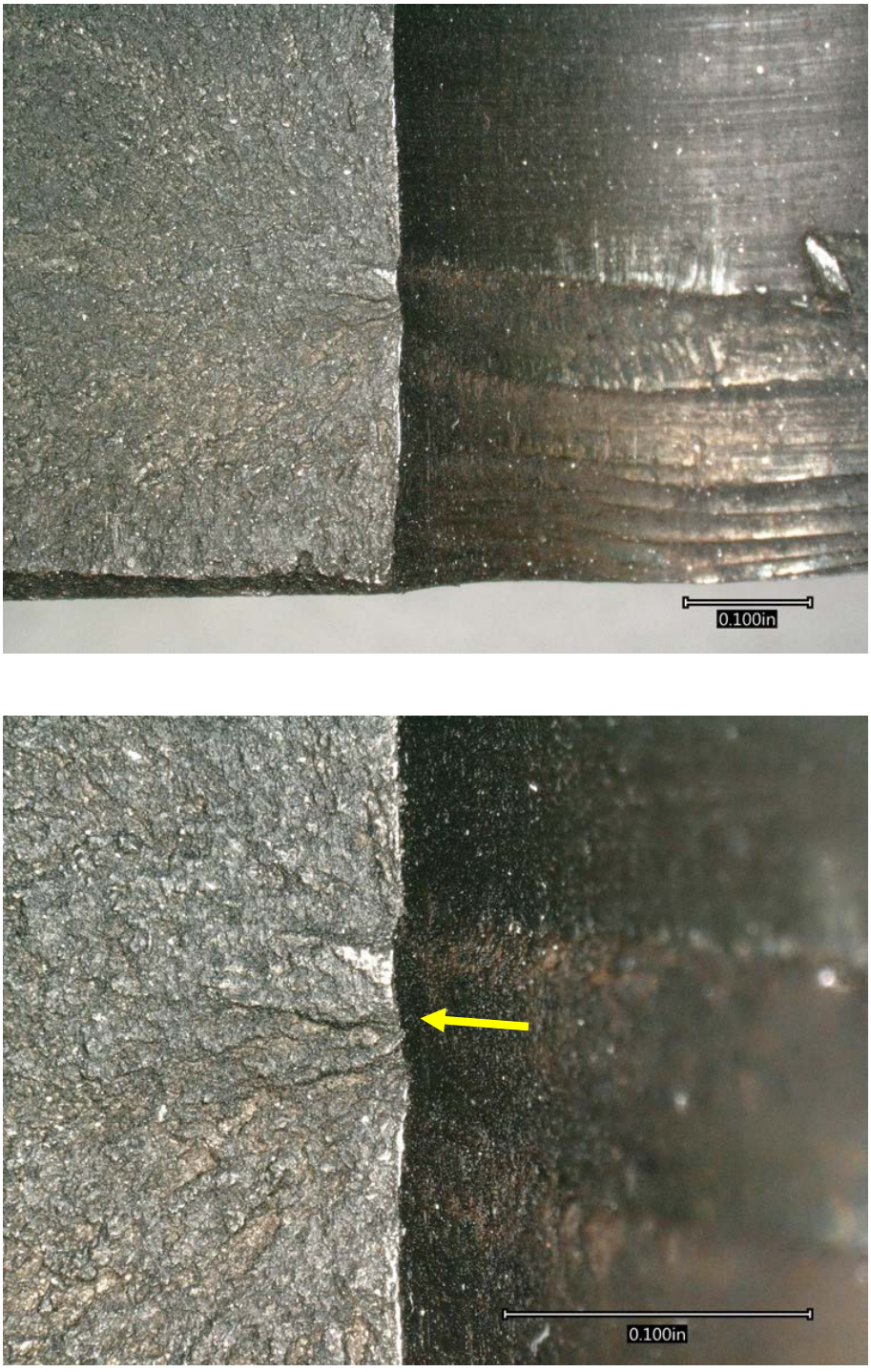

Figure 59. Digital microscope images of the central cooling passage and adjacent fracture surface, on the extracted section shown in Figure 58. Damage to the cooling passage surface is visible adjacent to the crack origin identified by the fracture surface texture (arrow).

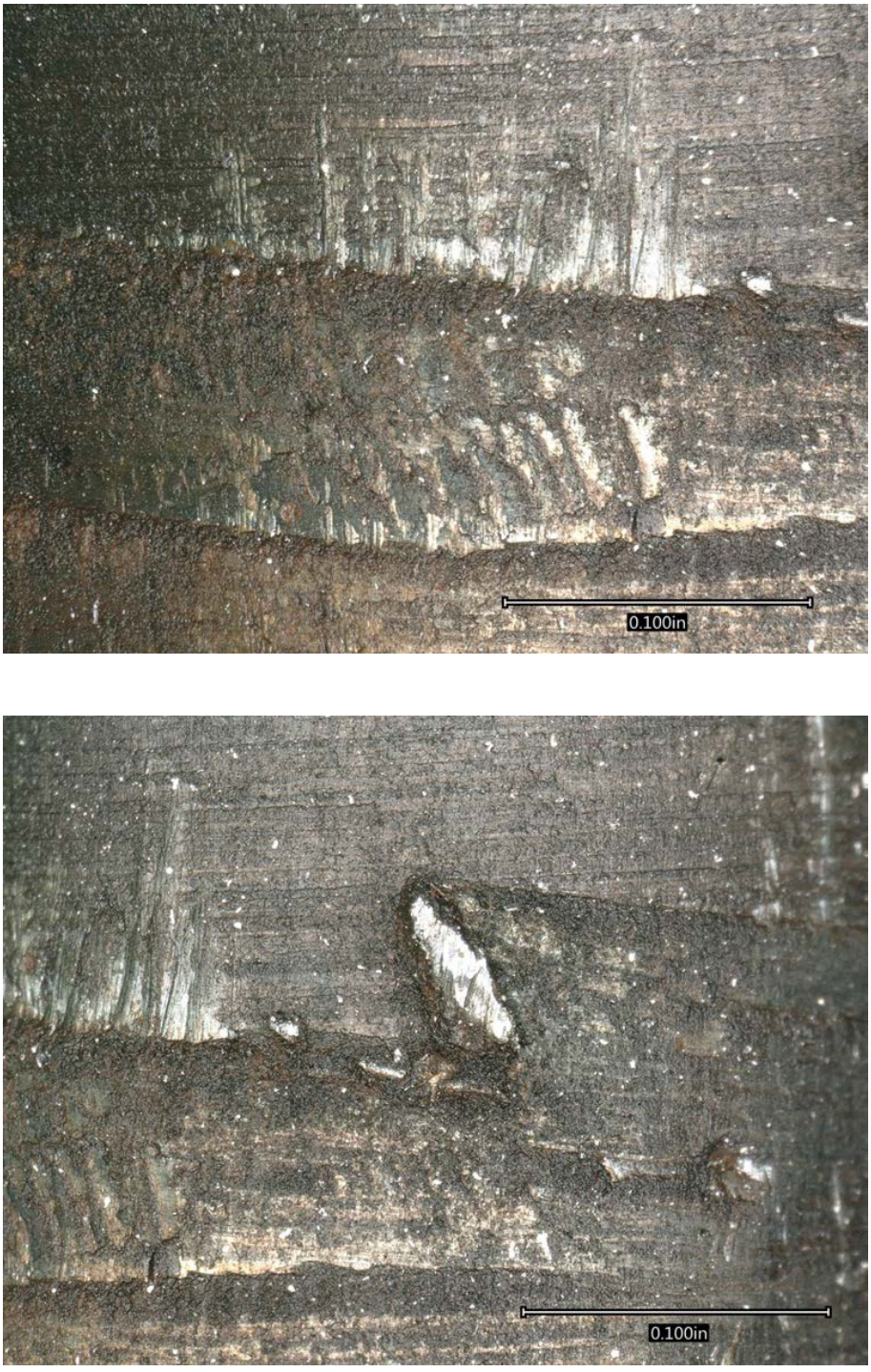

Figure 60. Additional close images of damage at the cooling passage surface. The lower image shows a close view of an angled feature with metal that has been piled up at the edge of the gouge.

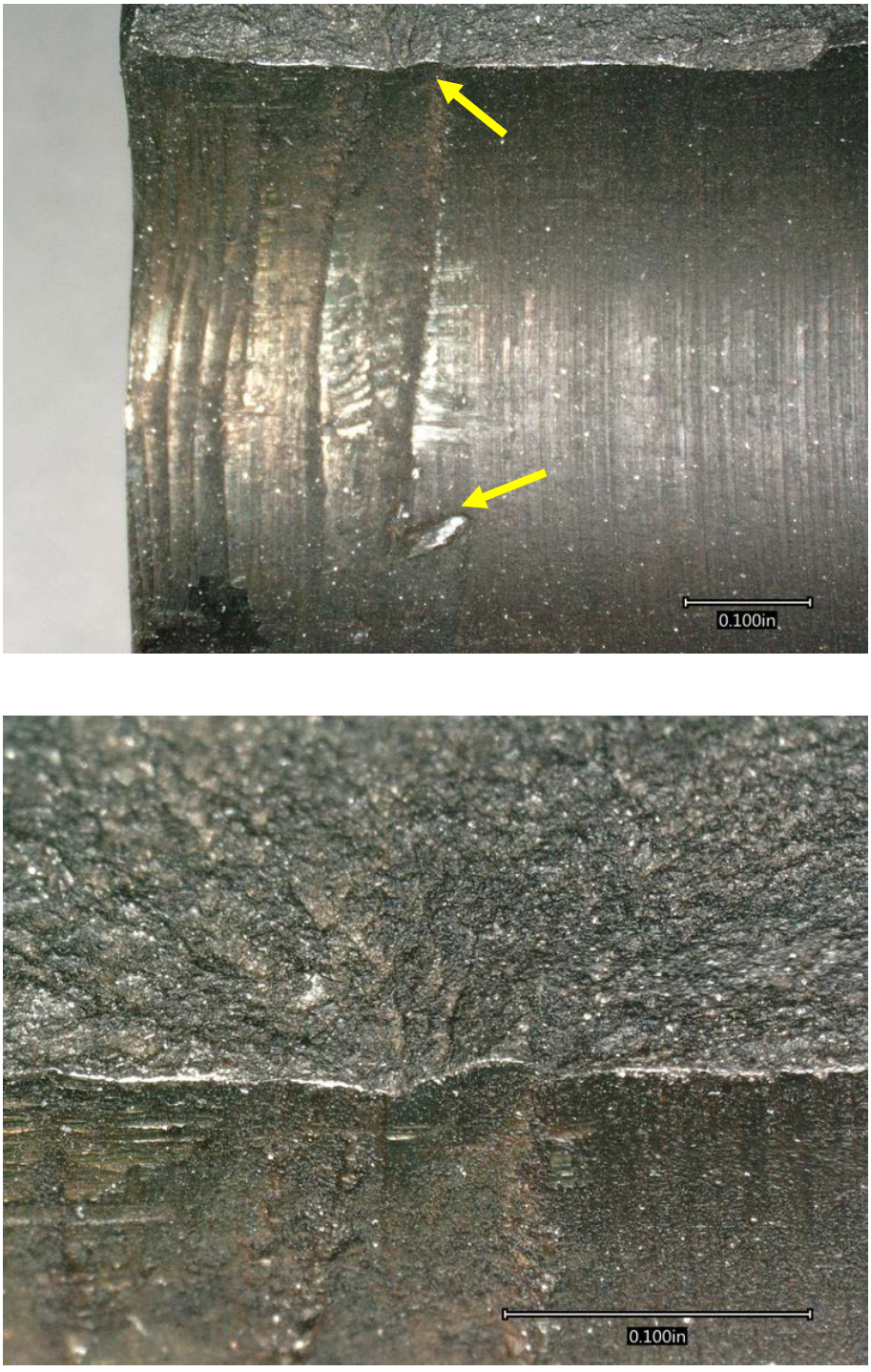

Figure 61. Additional views of the cooling passage and crack origin area (in these views, the sample has been rotated 90 degrees from the images shown in Figure 60). In the upper image, note that the edge of the piled up metal is similar in shape to the crack origin area (arrows).

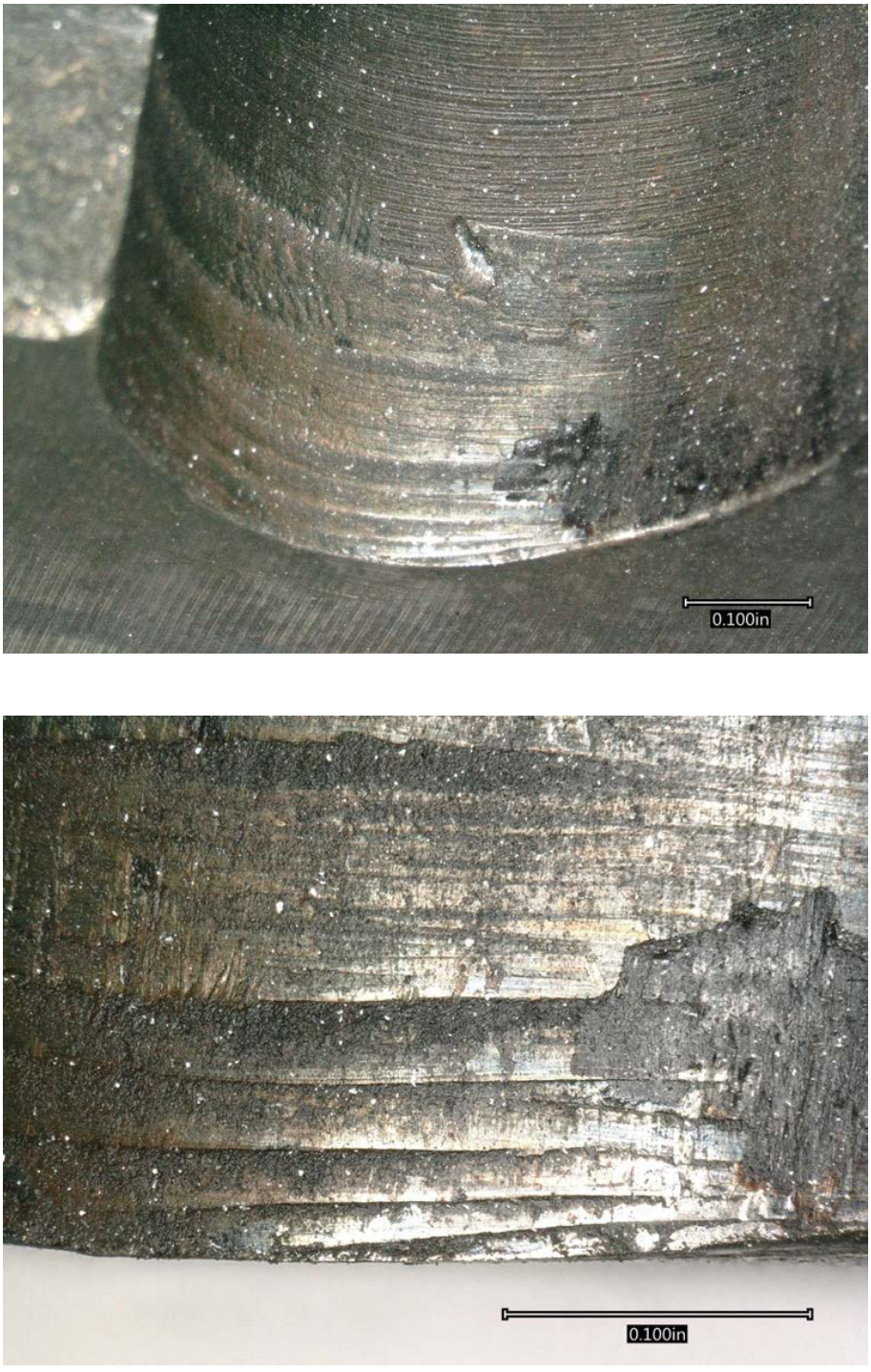

Figure 62. Additional digital microscope images of the damaged cooling passage and features near the ID surface of the retaining ring.

Figure 63. Views of the fracture surface section from the location below the dashed line in the upper image of Figure 58. The removed section is shown after cleaning in an ultrasonic bath with a mild Alconox solution.

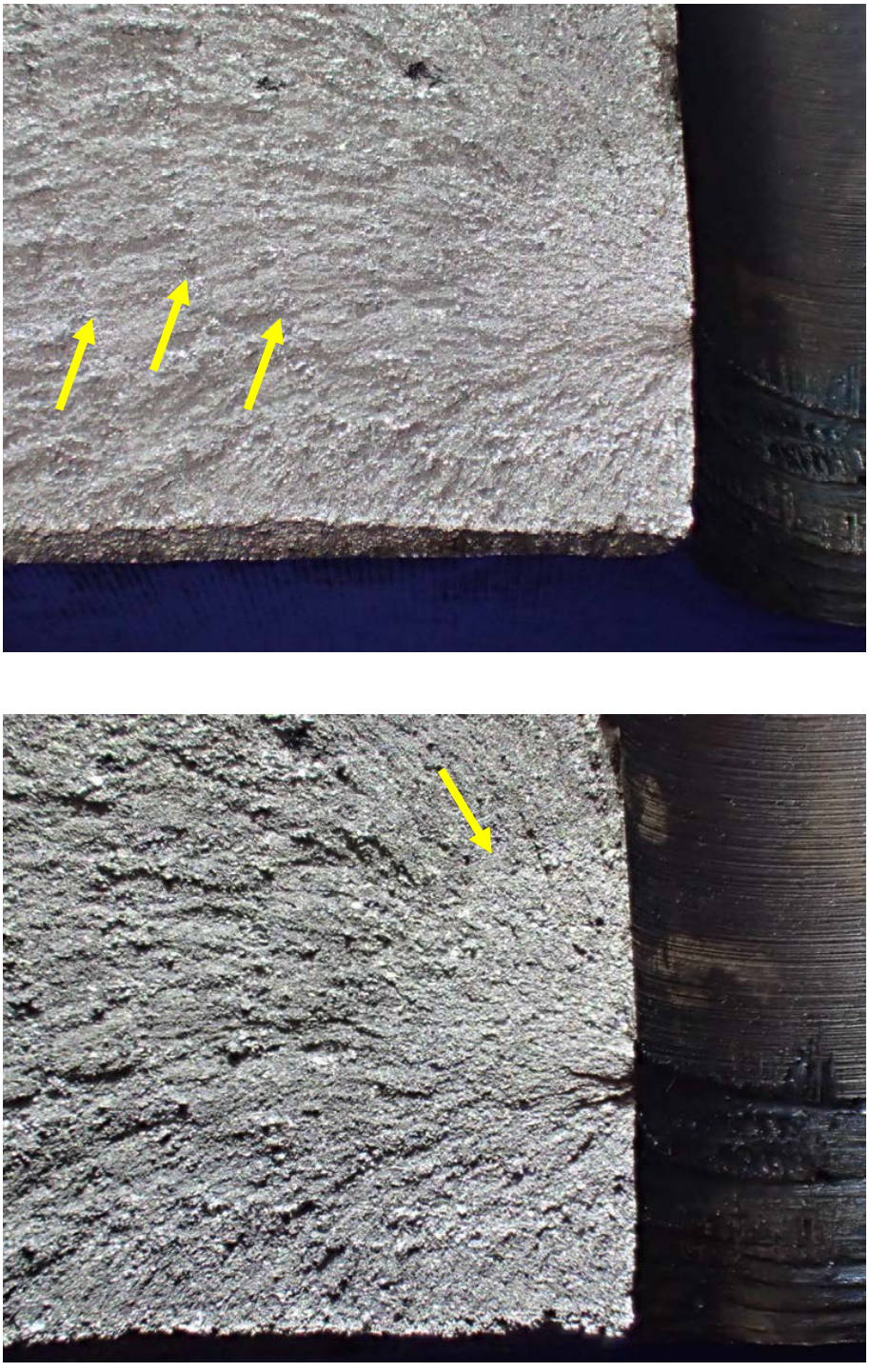

Figure 64. Close views of the crack origin area after cleaning the sample. The upper arrows show the locations of faint beach marks that are visible on the surface, and the lower arrow shows a thumbnail feature that is lighter in color than the surrounding fracture surface.

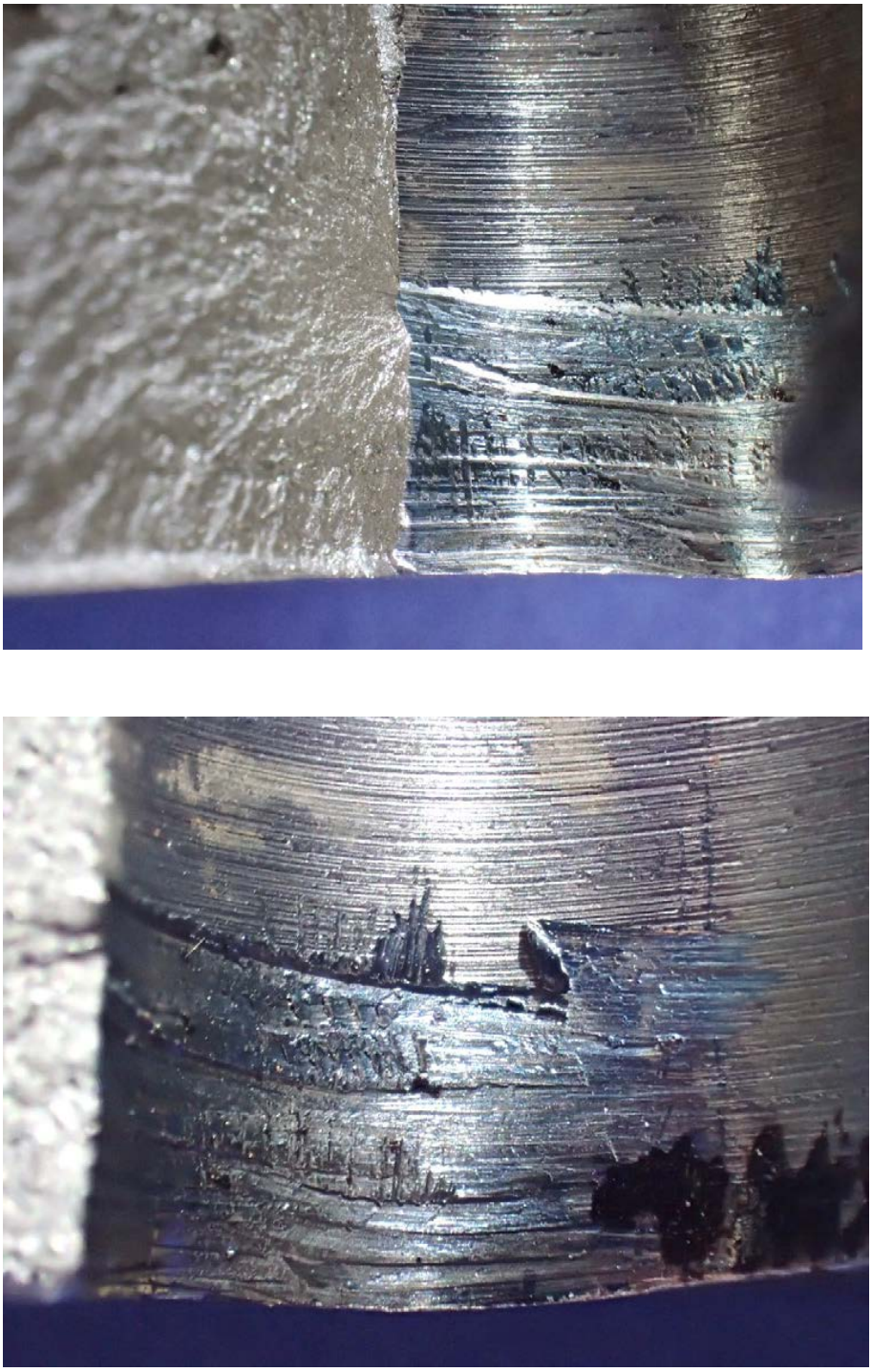

Figure 65. Close views of the cooling passage near the ring ID surface, after cleaning in an ultrasonic bath. Locations with mechanical damage exhibited a bluish tint after cleaning.

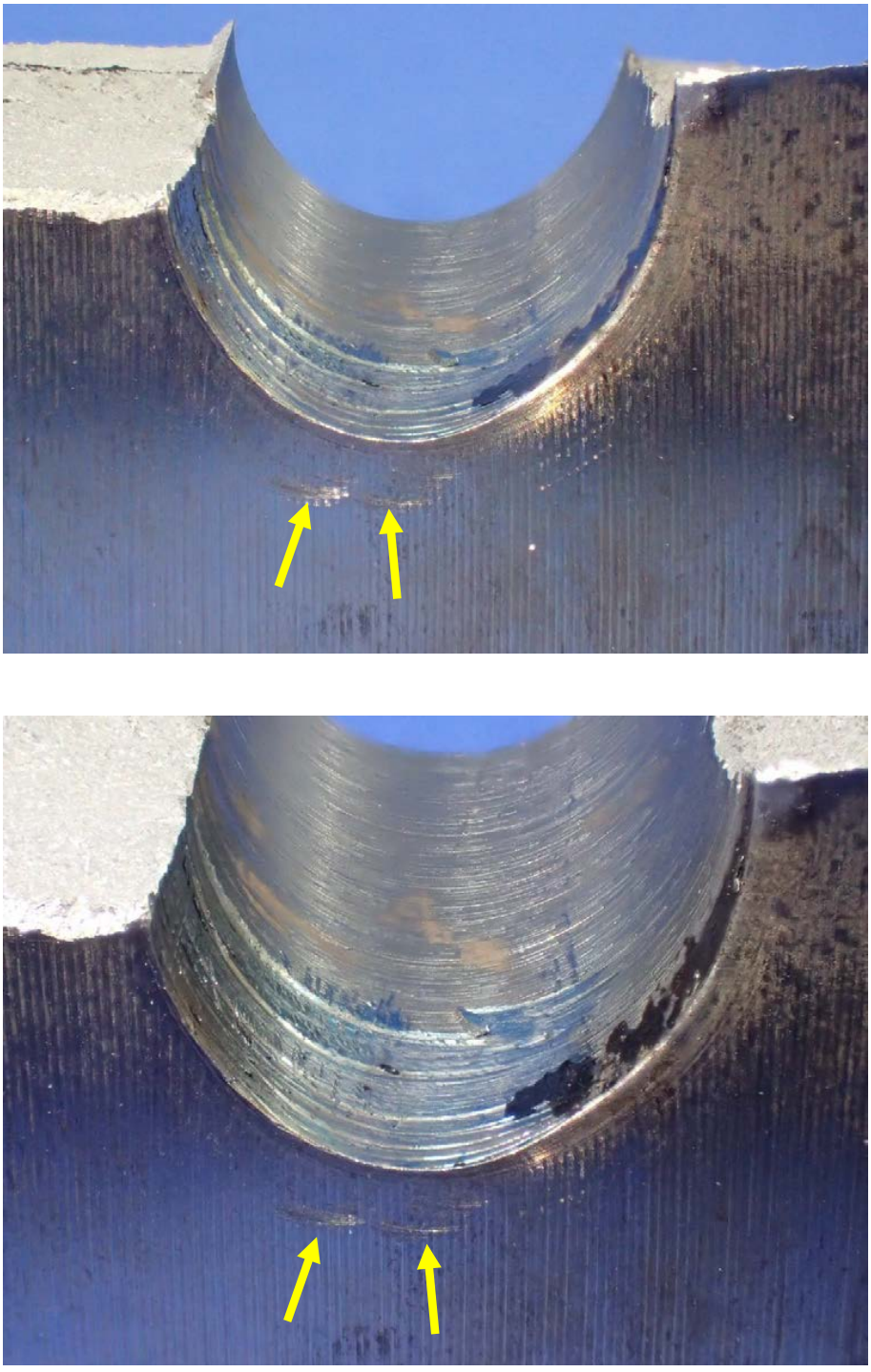

Figure 66. Alternate views of the cooling passage near the ring ID surface, after cleaning in an ultrasonic bath. Arc-shaped markings were visible on the ring ID surface in locations near the cooling passage hole (arrows)

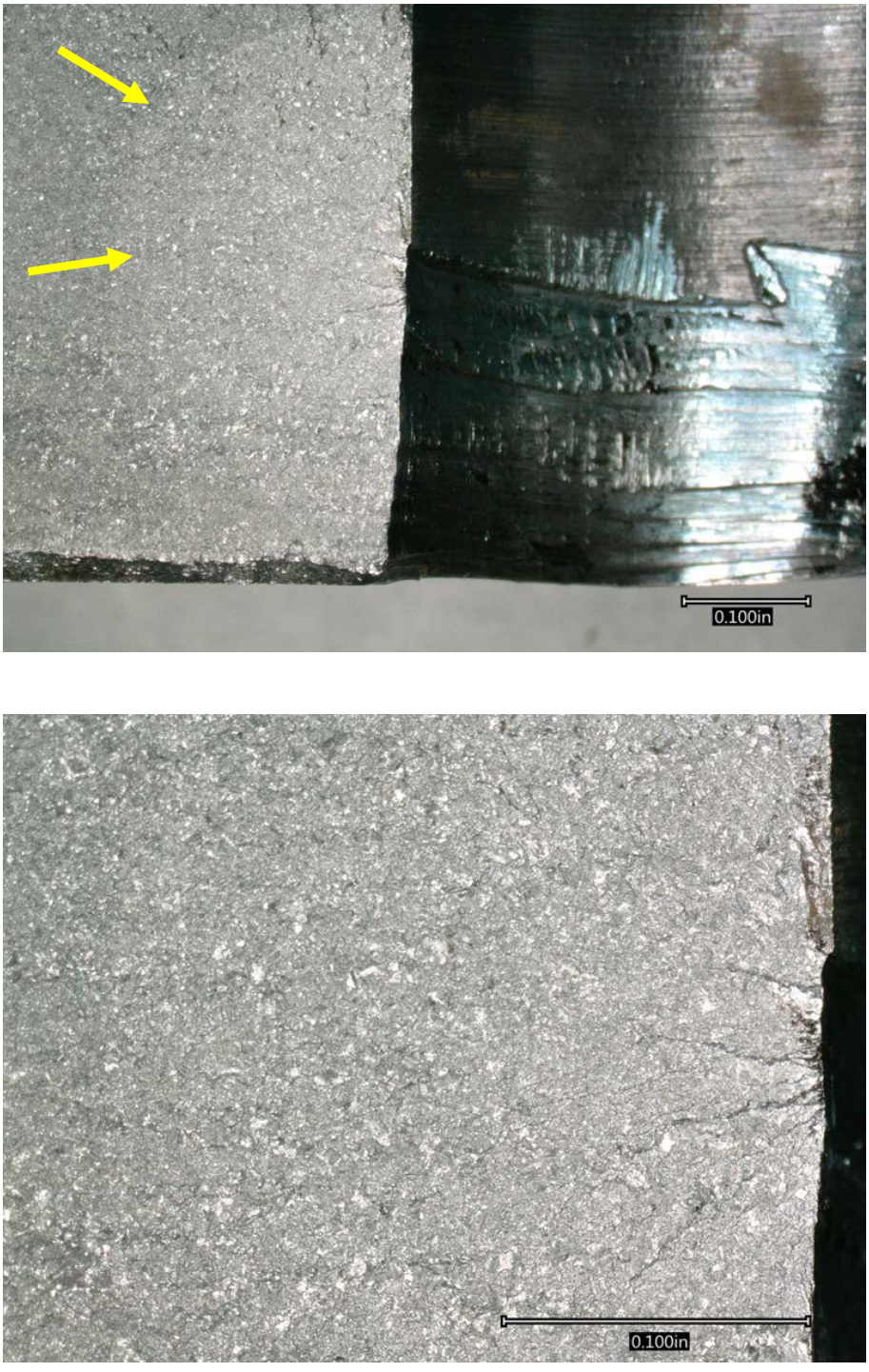

Figure 67. Digital microscope images of the cleaned crack origin area. The lighter thumbnail feature is visible in the upper image (arrows), and the lower image is a closer view of the origin at the cooling passage. Ridges (ratchet marks) extending outward from the origin area are approximately 50 mils (0.050 inches) in length.

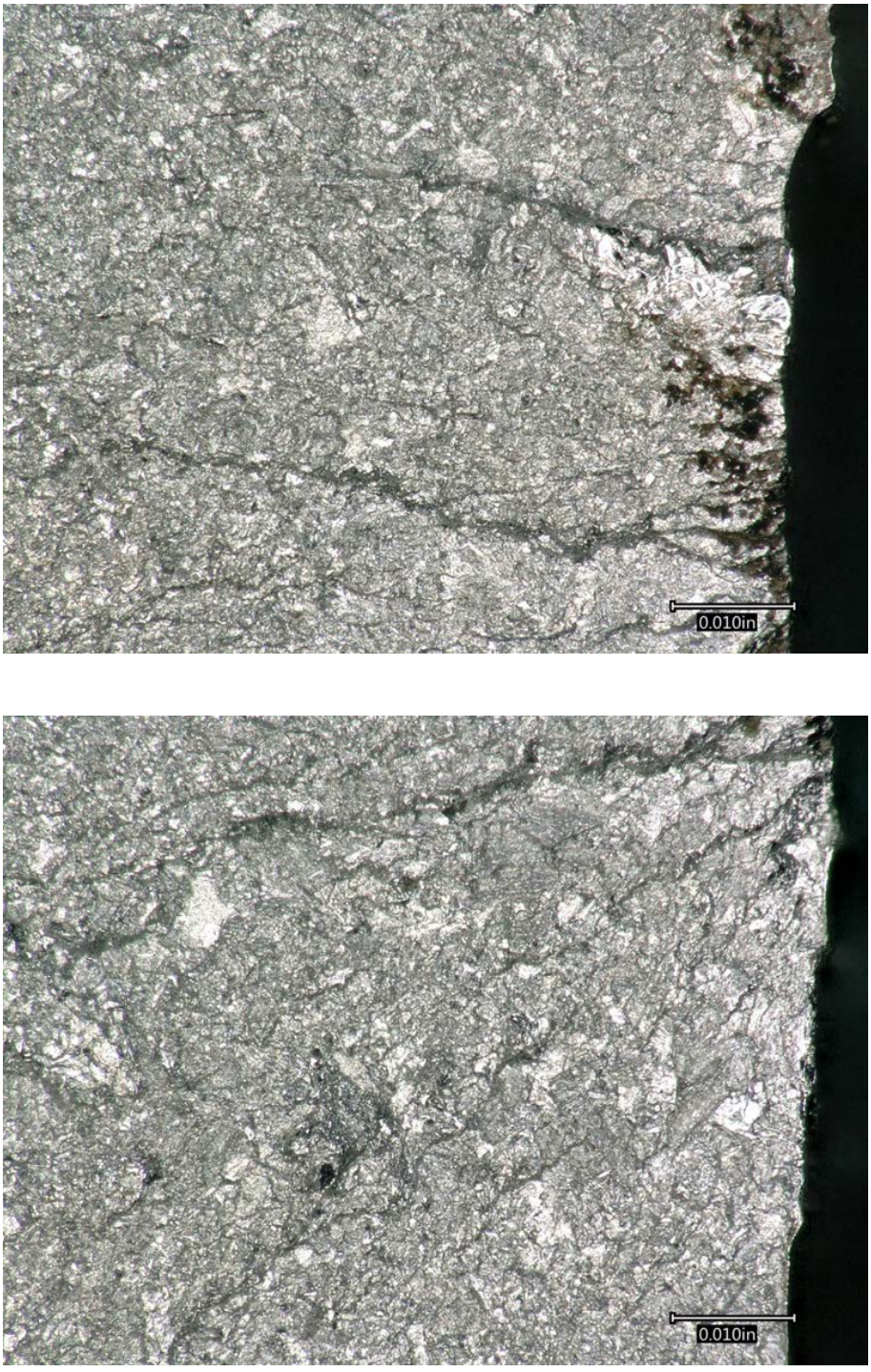

Figure 68. Higher magnification images of the crack origin area on the cleaned sample. Ridges extending to the left from the edge of the cooling passage are consistent with fatigue crack origin sites, where initial cracks are nearly coplanar and propagate together into one crack plane.

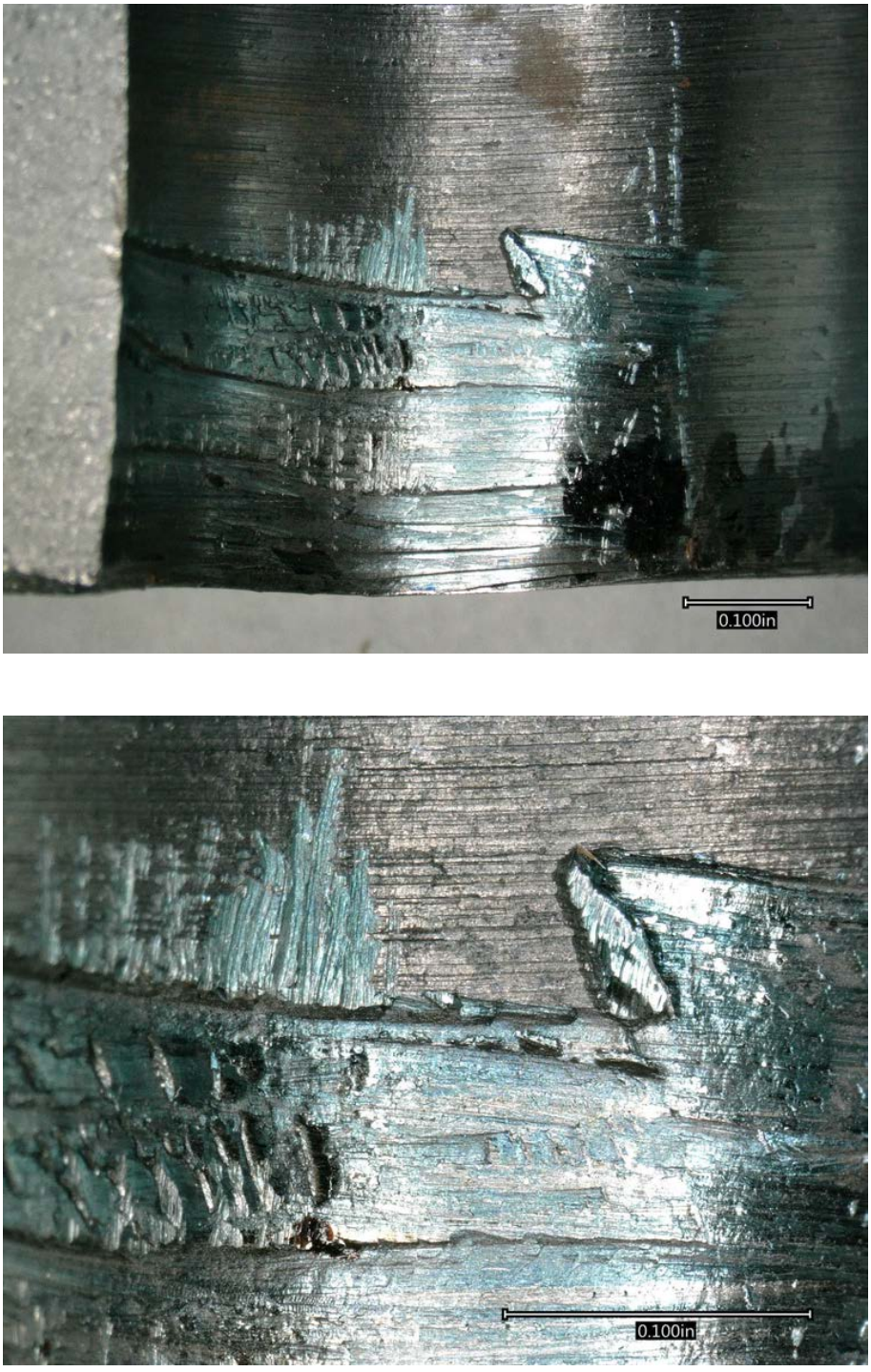

Figure 69. Digital microscope images of the cleaned sample showing damage features at the cooling passage surface. After cleaning in an Alconox solution, the damaged surfaces exhibited a bluish tint. The piled up metal on the cooling passage surface was approximately 60 mils (0.060 inches) in length.

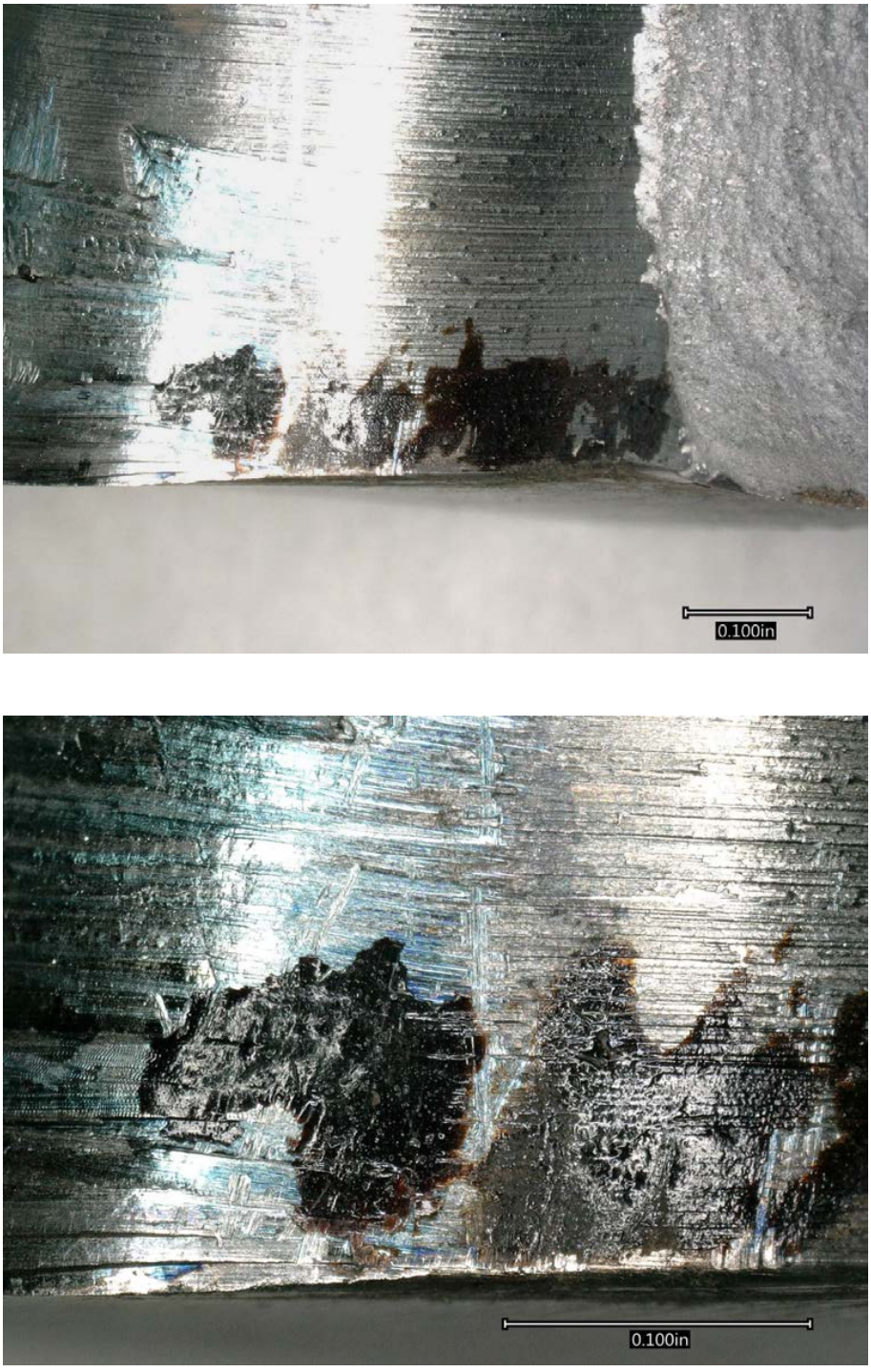

Figure 70. Additional digital microscope images of the cleaned sample showing dark deposits near the retaining ring ID surface. These deposits were also visible on the retaining ring prior to removal from the generator (see lower image of Figure 13).

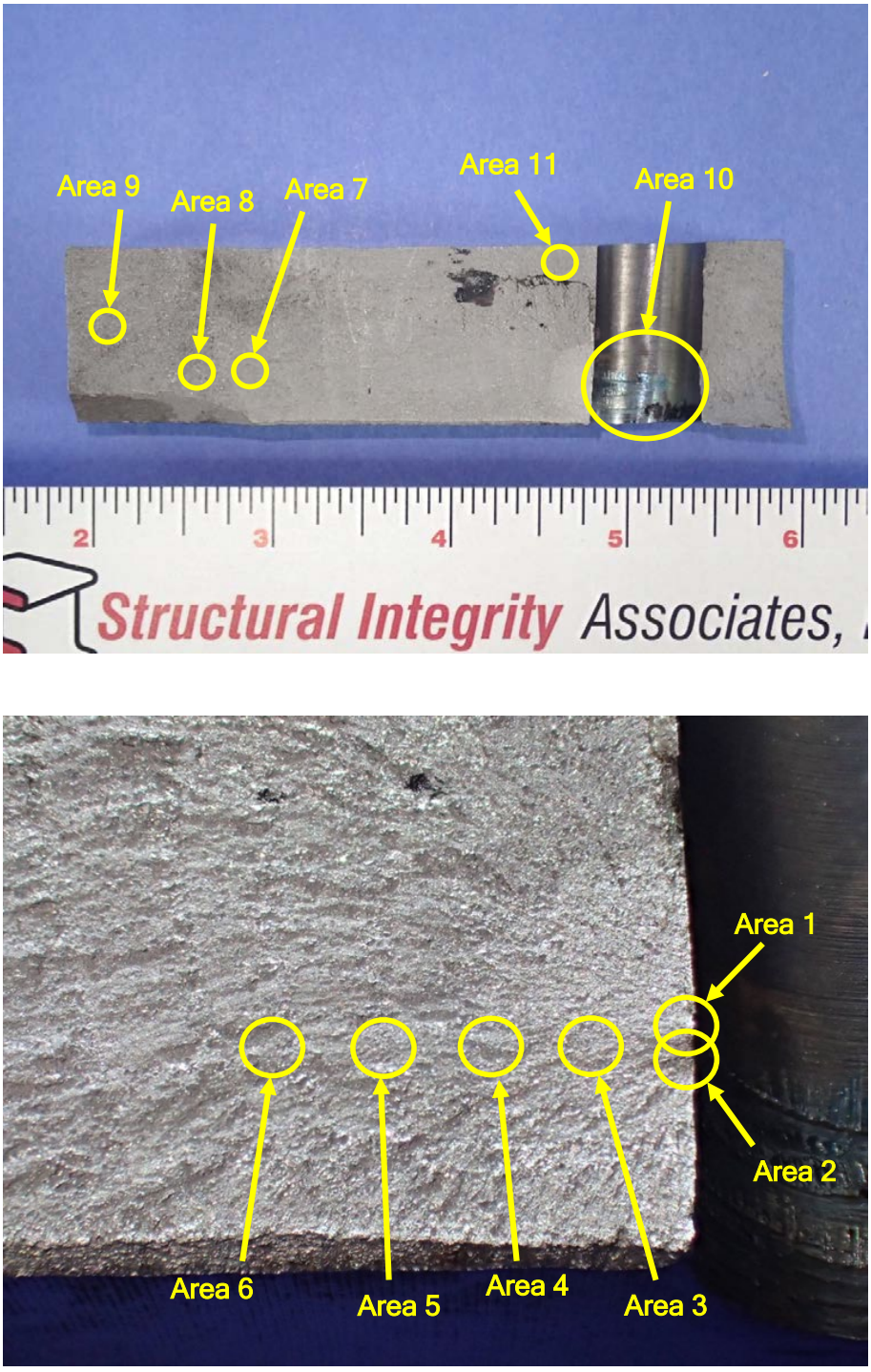

Figure 71. Labeled images showing the approximate locations that were examined using a scanning electron microscope (SEM). These individual areas are referred to, as-labeled, in the following figures.

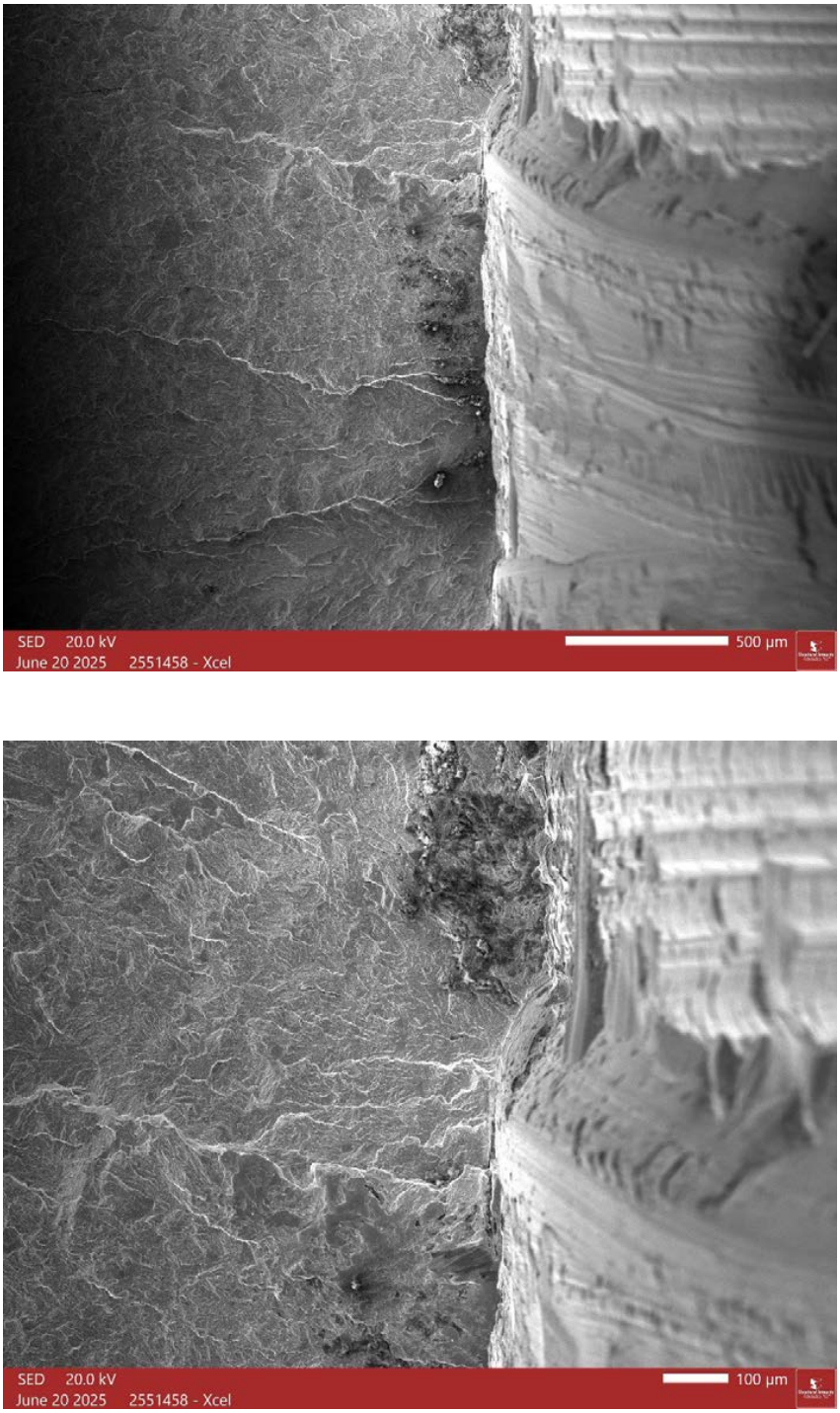

Figure 72. Scanning electron microscope (SEM) images of Area 1 in Figure 71. These images show the crack origin area at the edge of the mechanical gouge at the cooling passage surface. Original machining marks are visible above the gouge in the cooling passage.

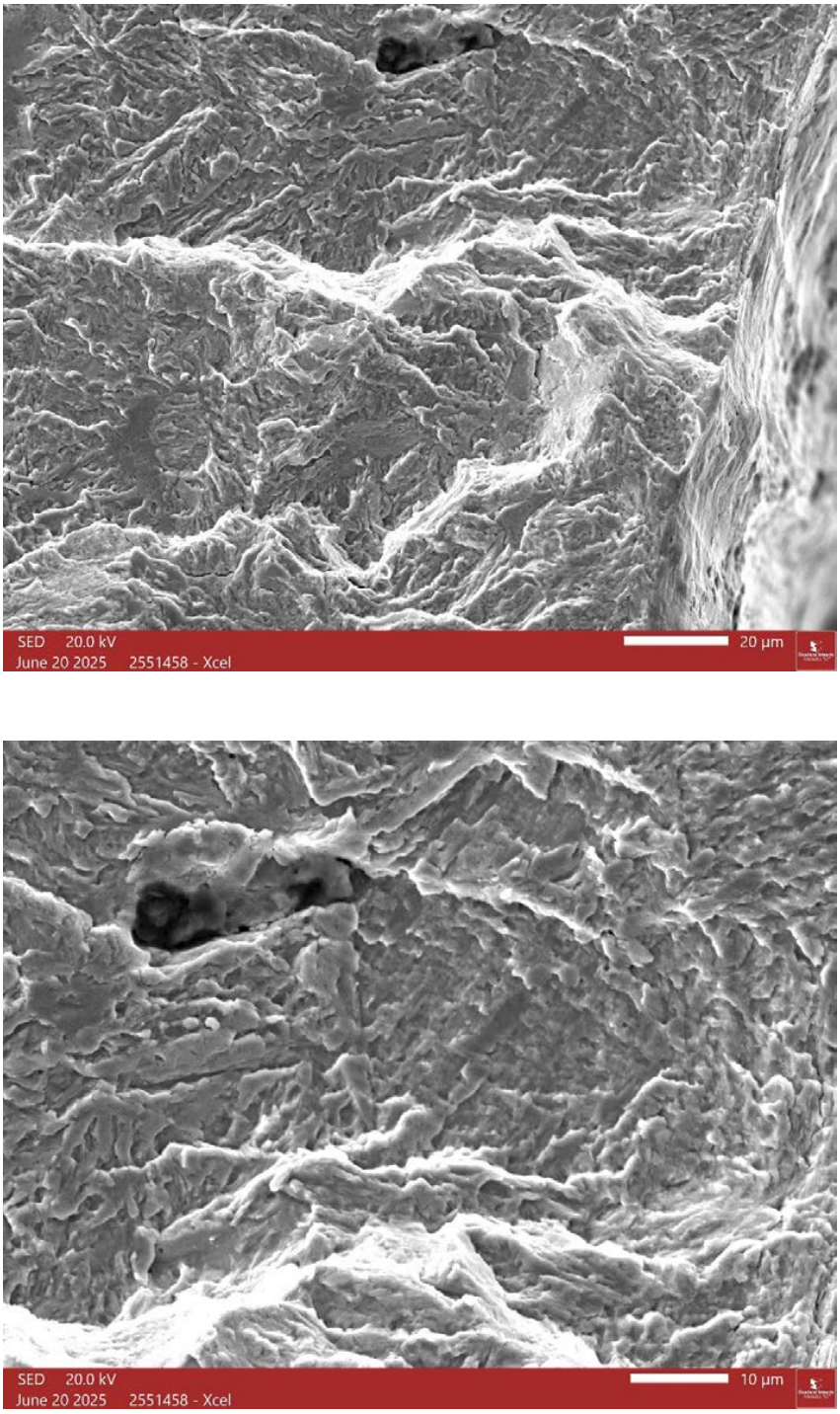

Figure 73. Additional SEM images of Area 1 in Figure 71. In the lower image, the crack propagation direction is approximately lower-right to upper-left.

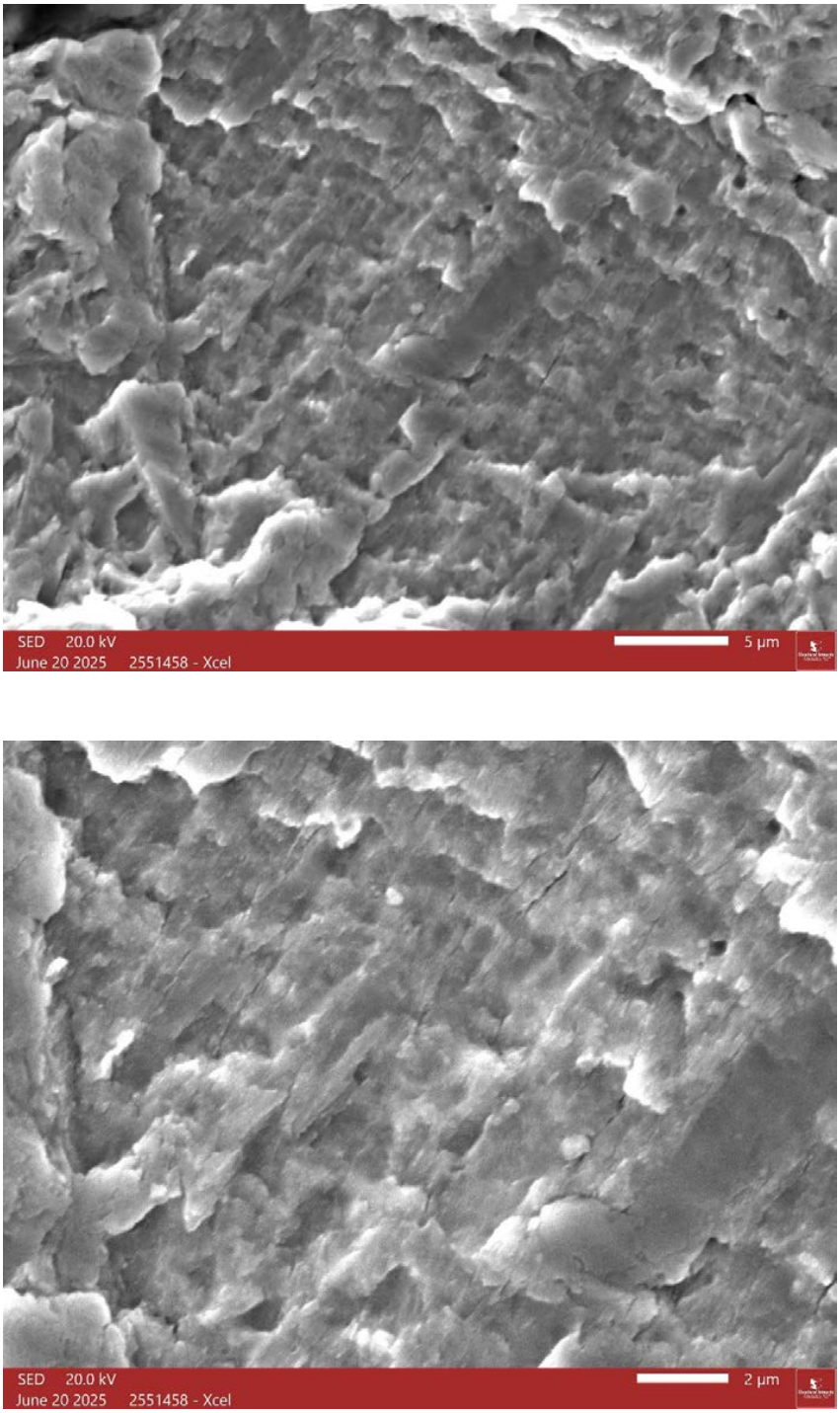

Figure 74. Higher magnification SEM images of Area 1 in Figure 71. In these images, the crack propagation direction is approximately lower-right to upper-left.

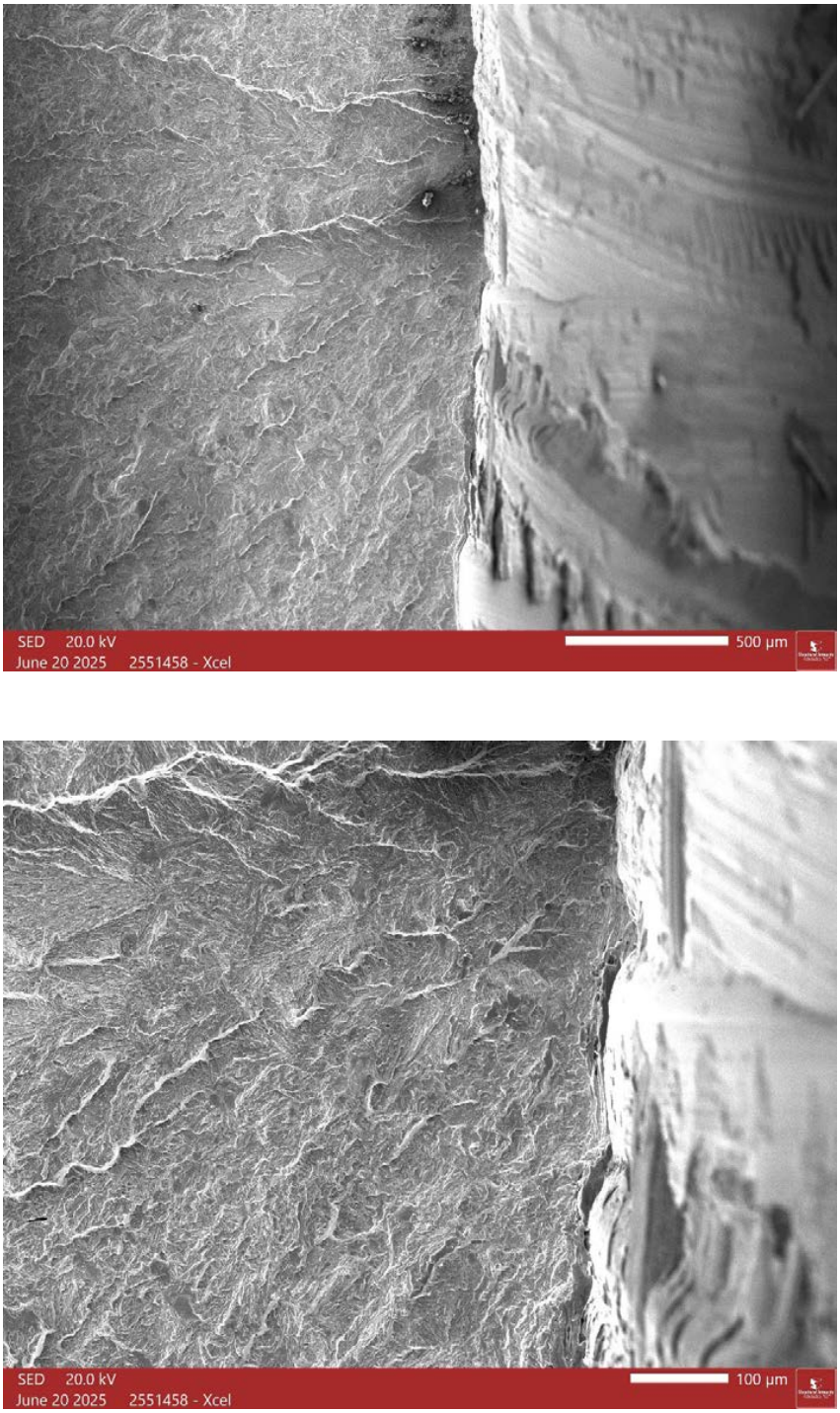

Figure 75. SEM images of Area 2 in Figure 71. These images show the crack origin area at the edge of the mechanical gouge at the cooling passage surface.

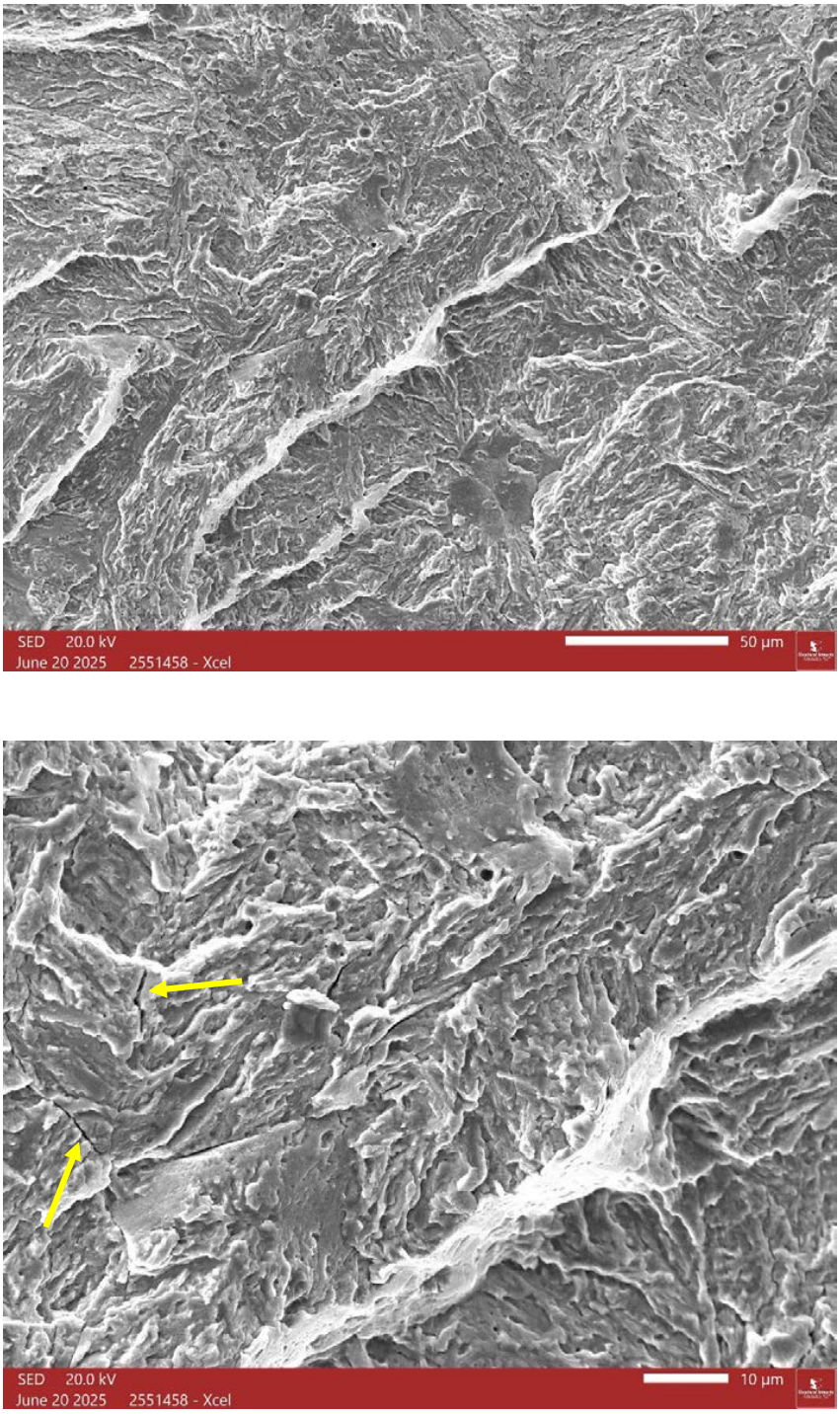

Figure 76. Additional SEM images of Area 2 in Figure 71. In these images, the crack propagation direction is approximately upper-right to lower-left. Indications of secondary cracks or tears are also evident in the lower image (arrows).

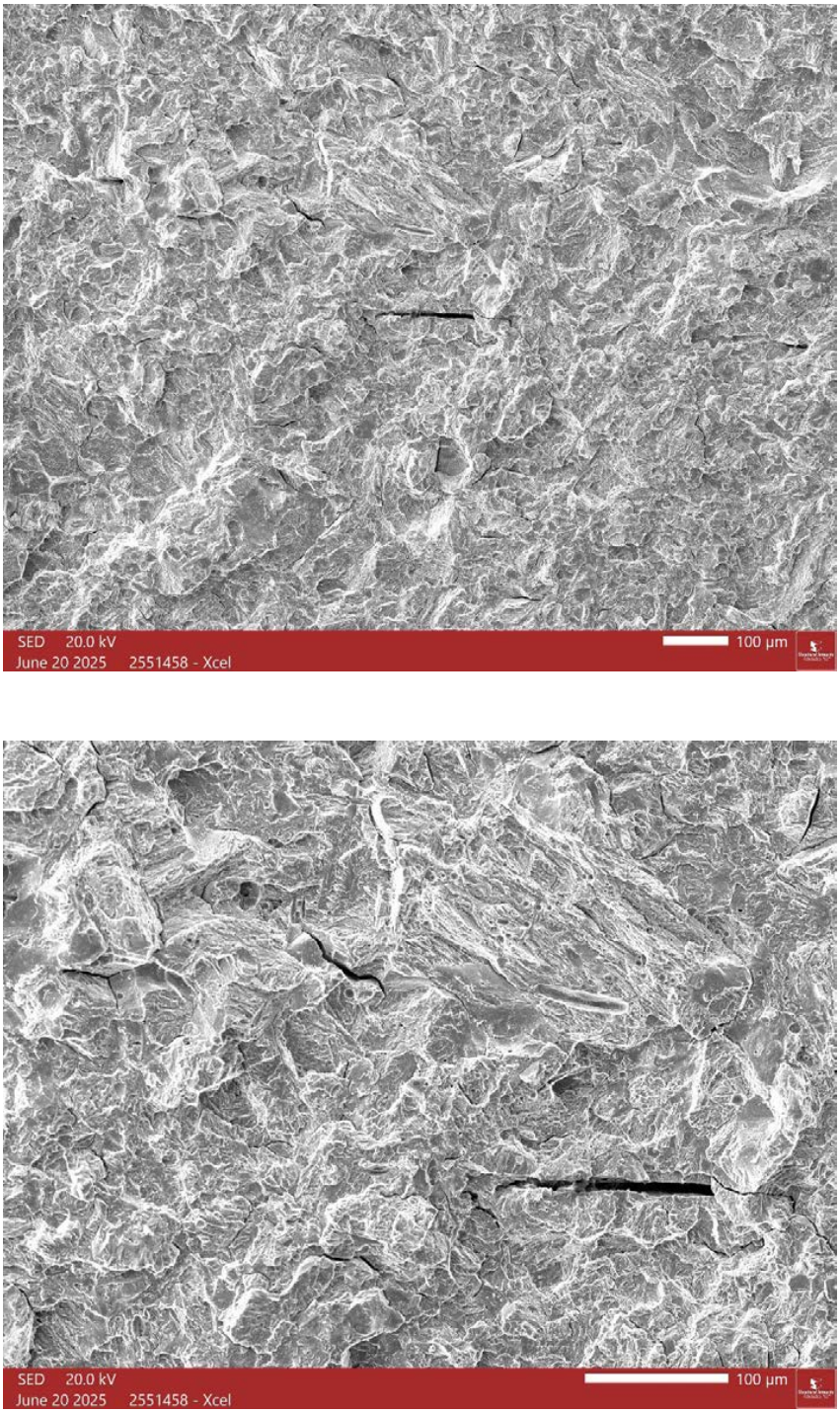

Figure 77. SEM images of Area 3 in Figure 71. This location is approximately at the middle of the bright thumbnail region (see Figure 67, upper image). In these images, the crack propagation direction is approximately right to left.

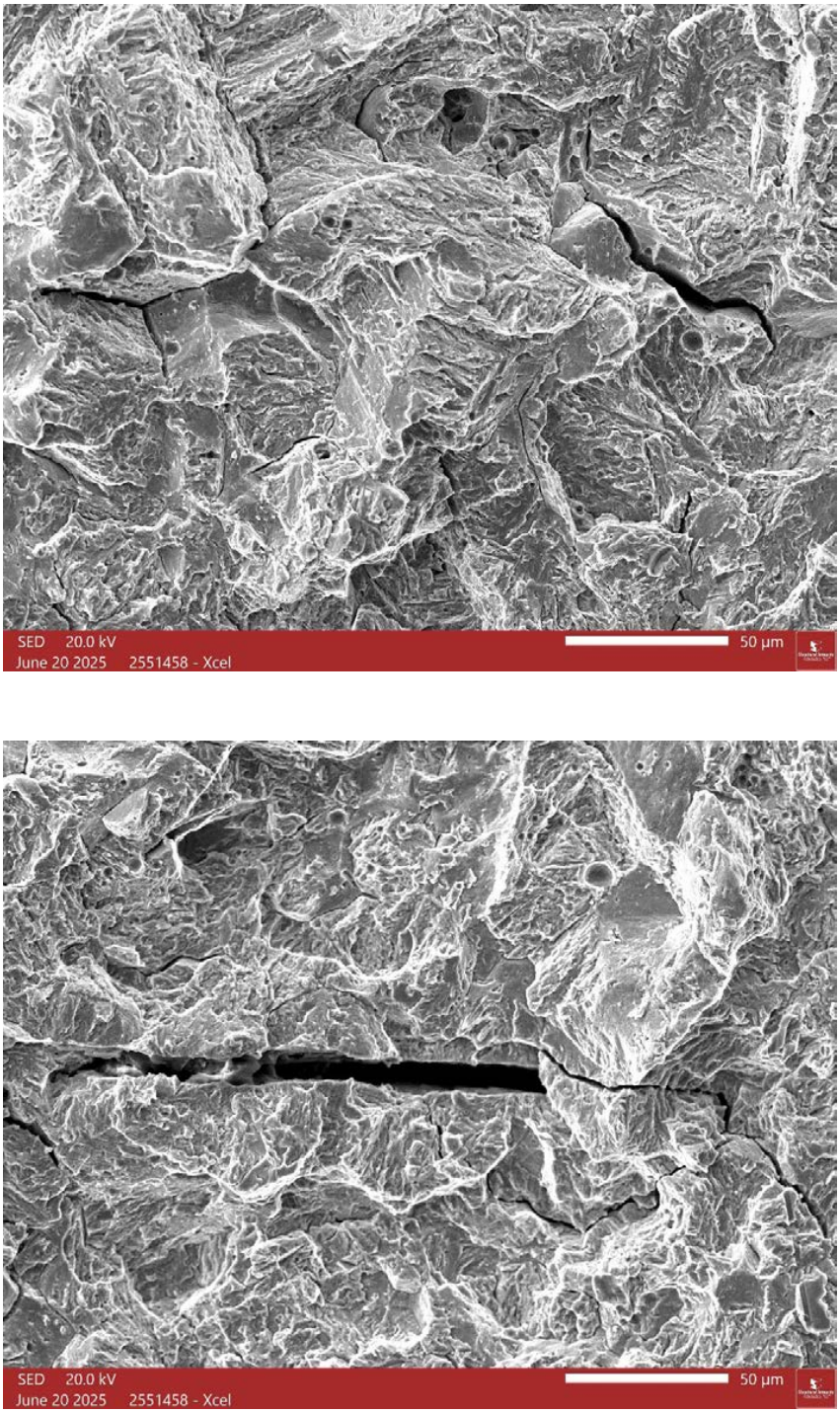

Figure 78. Higher magnification SEM images of Area 3 in Figure 71. In these images, the crack propagation direction is approximately right to left.

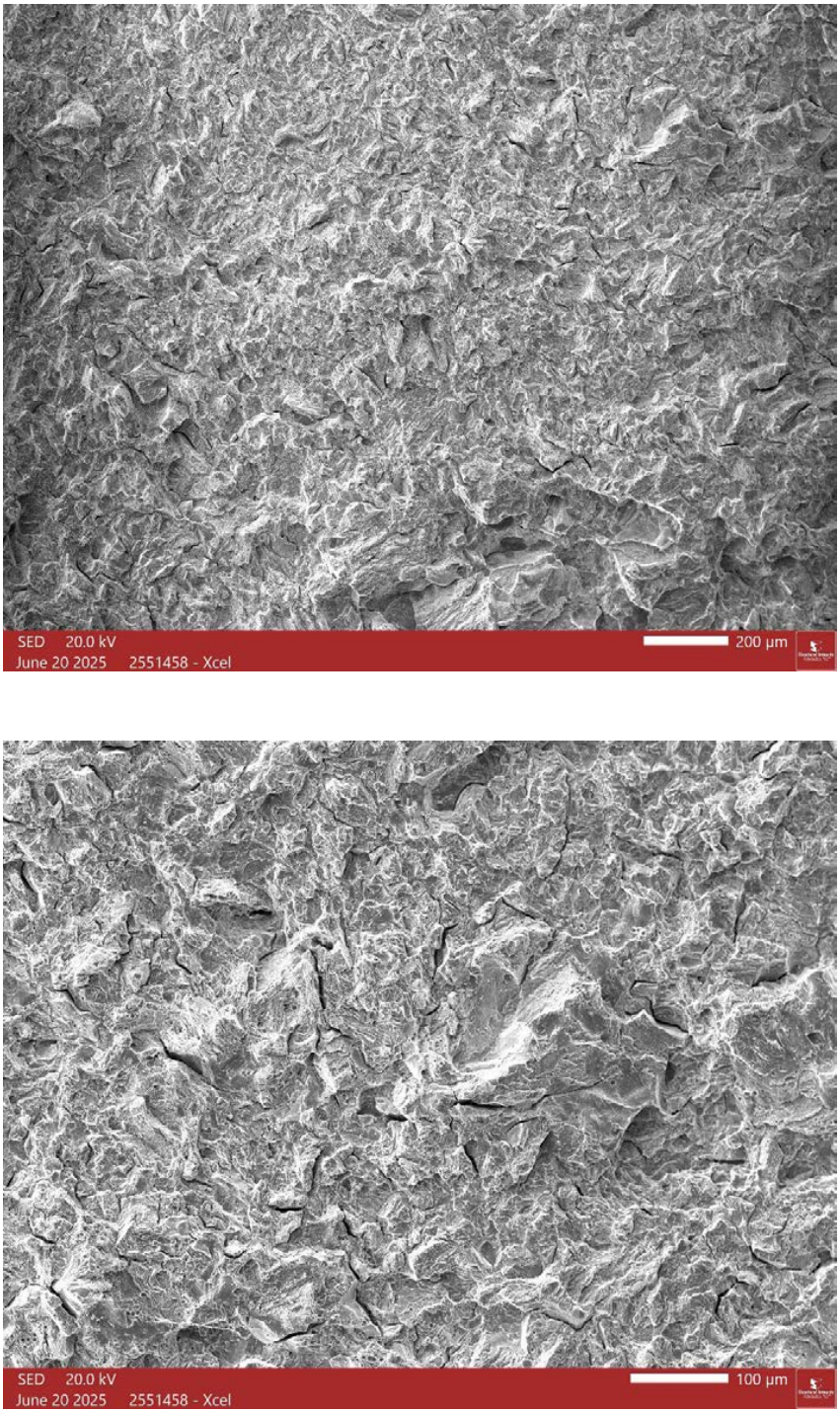

Figure 79. SEM images of Area 4 in Figure 71. This location is approximately at the edge of the bright thumbnail region (see Figure 67, upper image). In these images, the crack propagation direction is approximately right to left.

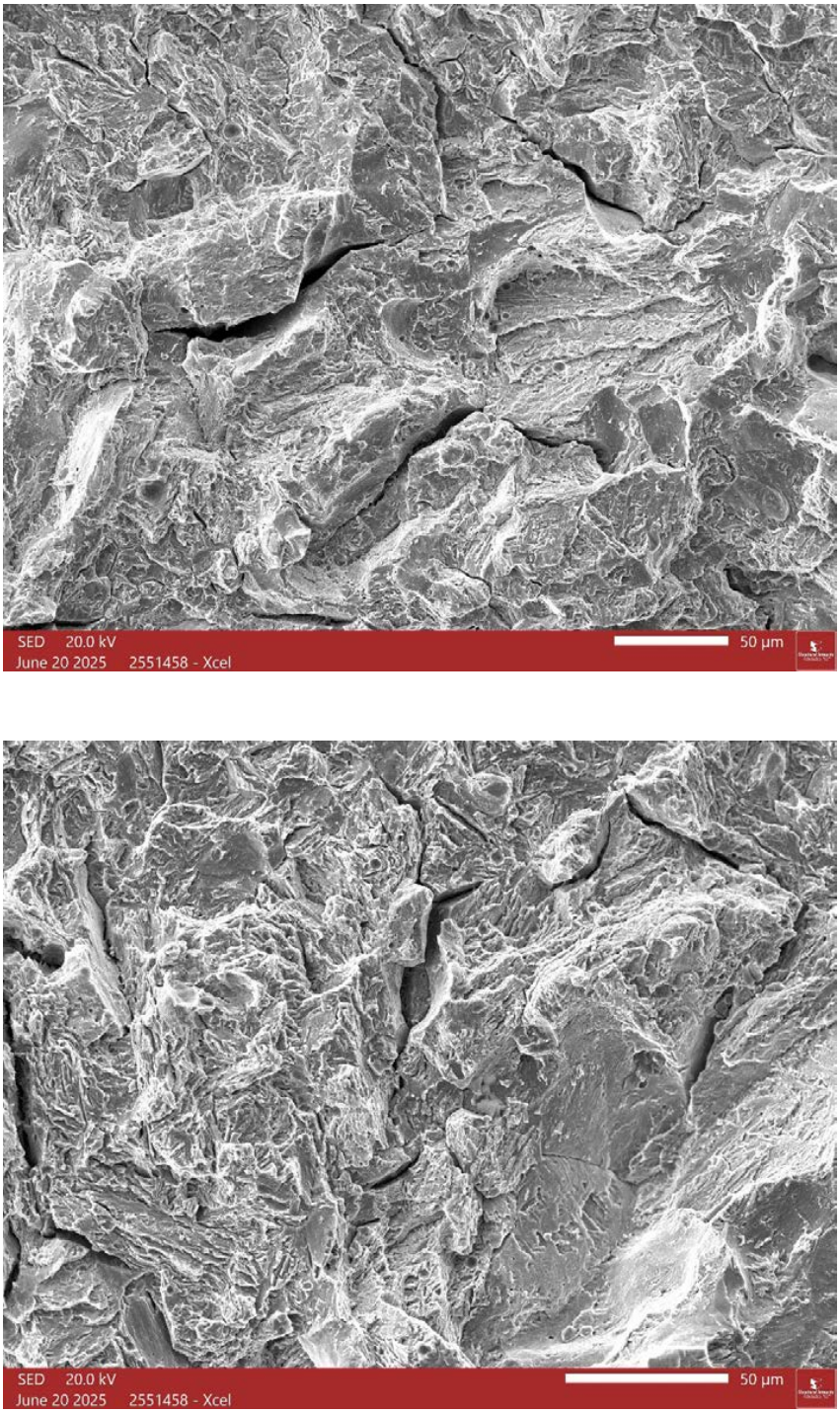

Figure 80. Higher magnification SEM images of Area 4 in Figure 71. In these images, the crack propagation direction is approximately right to left.

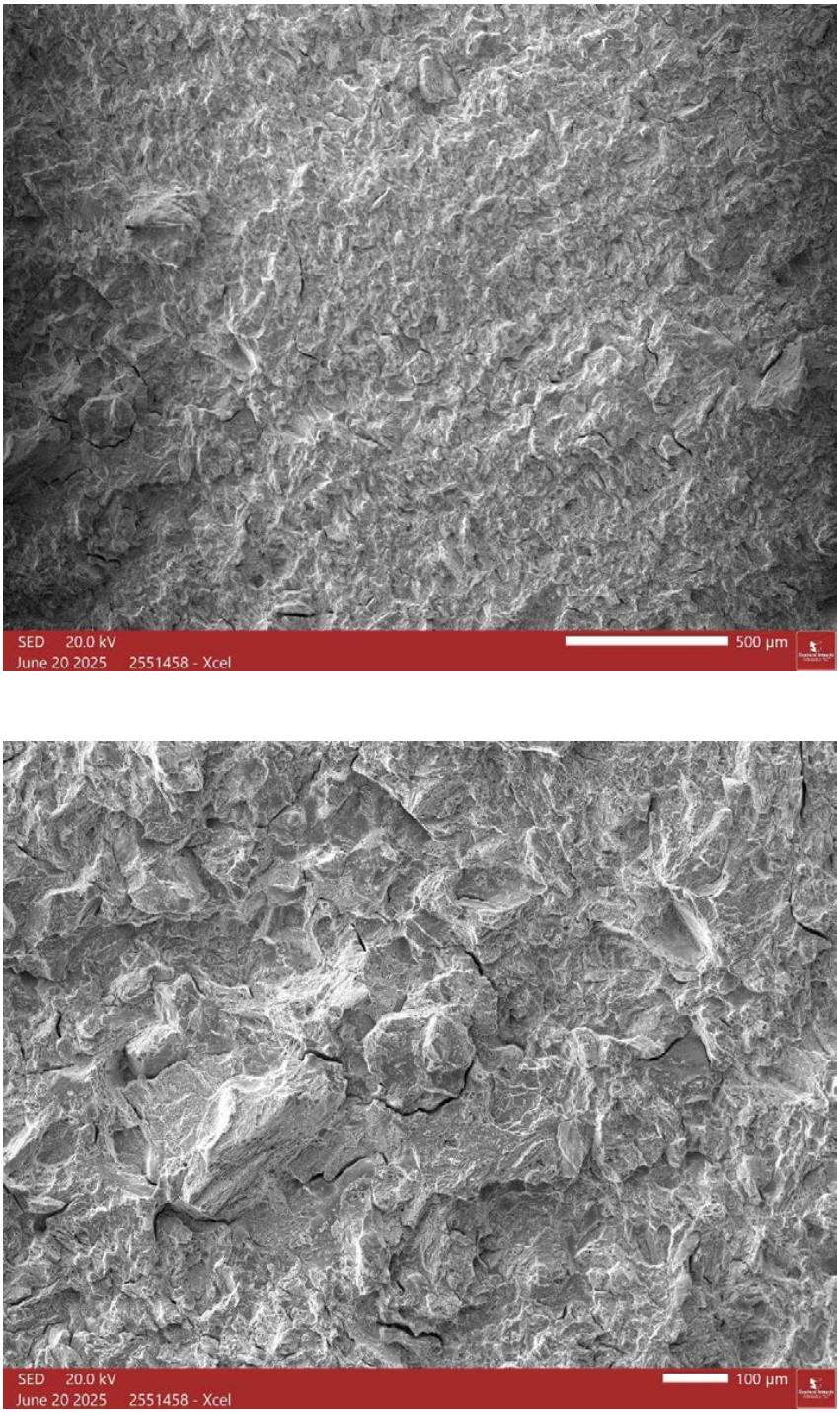

Figure 81. SEM images of Area 5 in Figure 71. In these images, the crack propagation direction is approximately right to left.

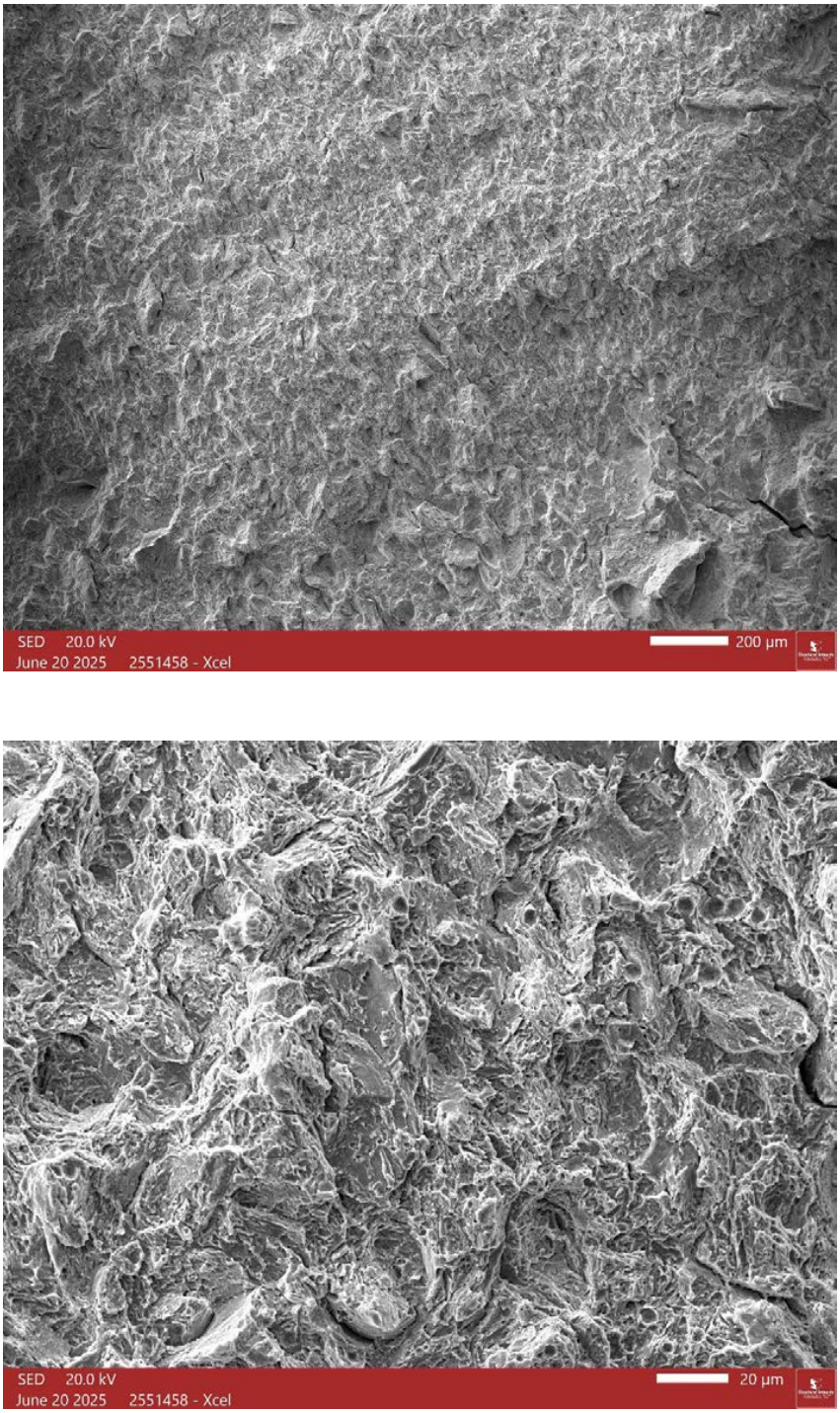

Figure 82. SEM images of Area 6 in Figure 71. In these images, the crack propagation direction is approximately right to left.

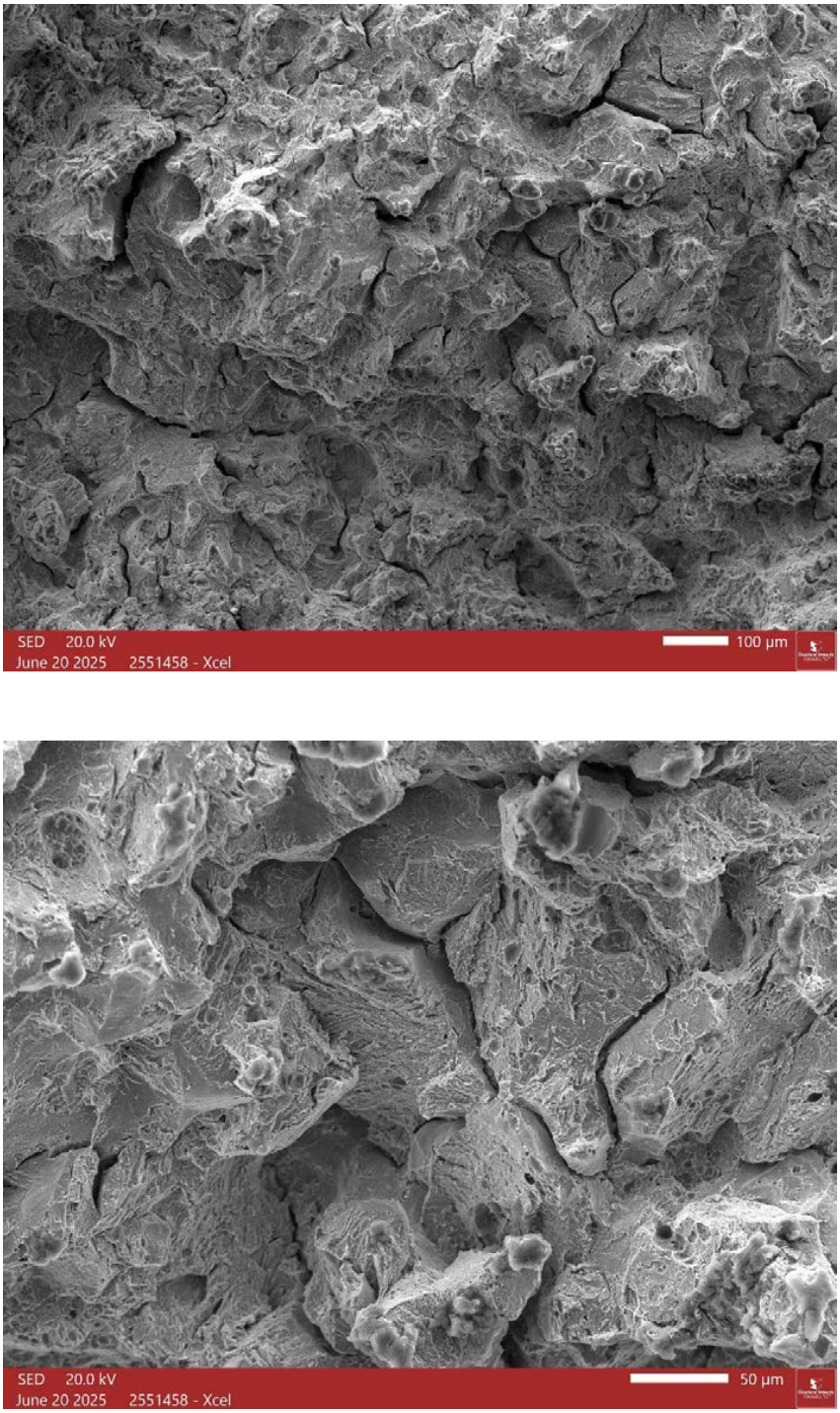

Figure 83. SEM images of Area 7 in Figure 71. This location is just to the right of the beach mark indicated in the lower image of Figure 57. In these images, the crack propagation direction is approximately right to left, and features exhibited a blocky appearance with mostly cleavage and some dimpled rupture, along with larger secondary cracks or tears.

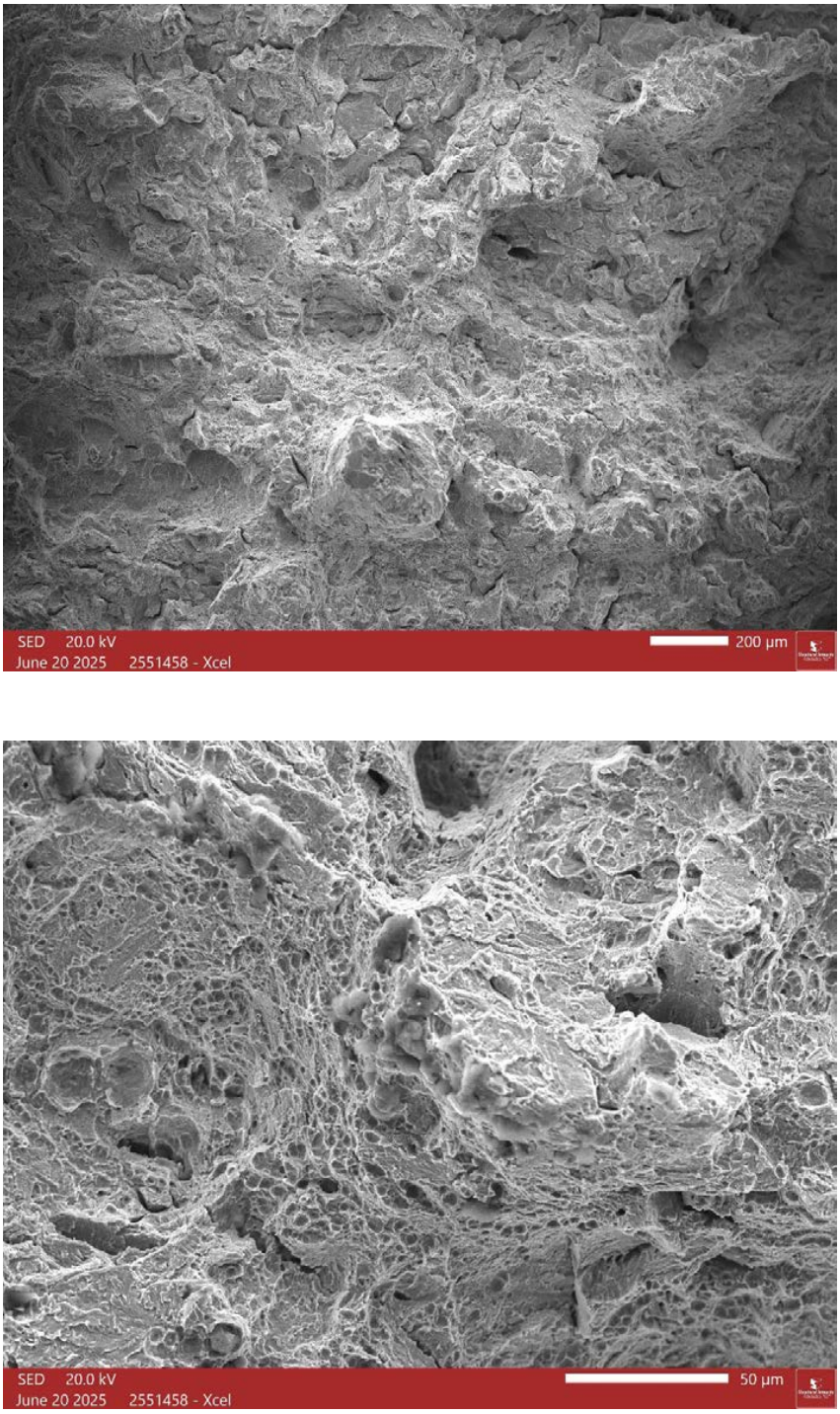

Figure 84. SEM images of Area 8 in Figure 71. This location is just to the left of the beach mark indicated in the lower image of Figure 57. In these images, the direction of cracking is approximately right to left, and features consistent with dimpled rupture mixed with cleavage fracture are present.

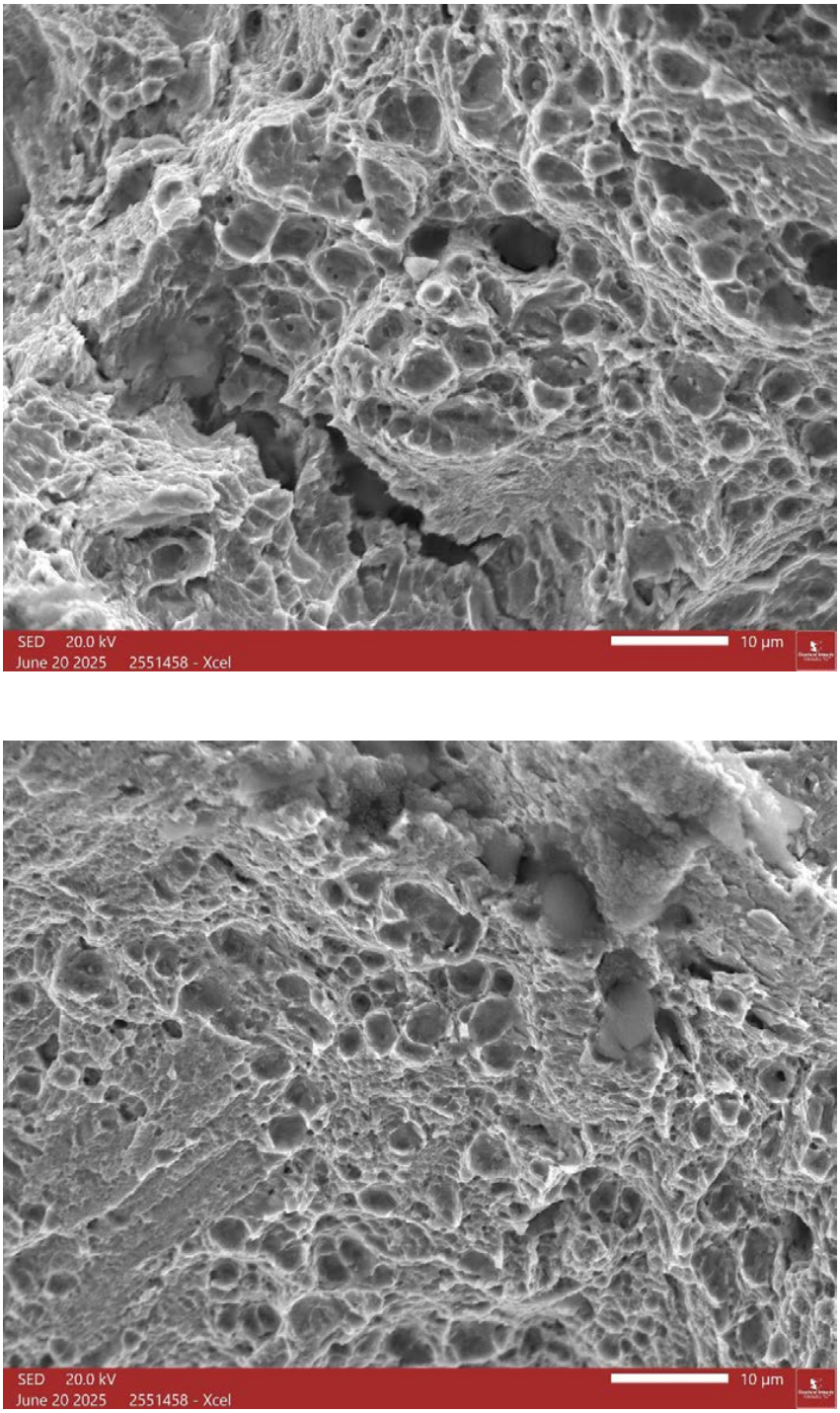

Figure 85. Higher magnification SEM images of Area 8 in Figure 71. In these images, the direction of cracking is approximately right to left, and features consistent with dimpled rupture are present.

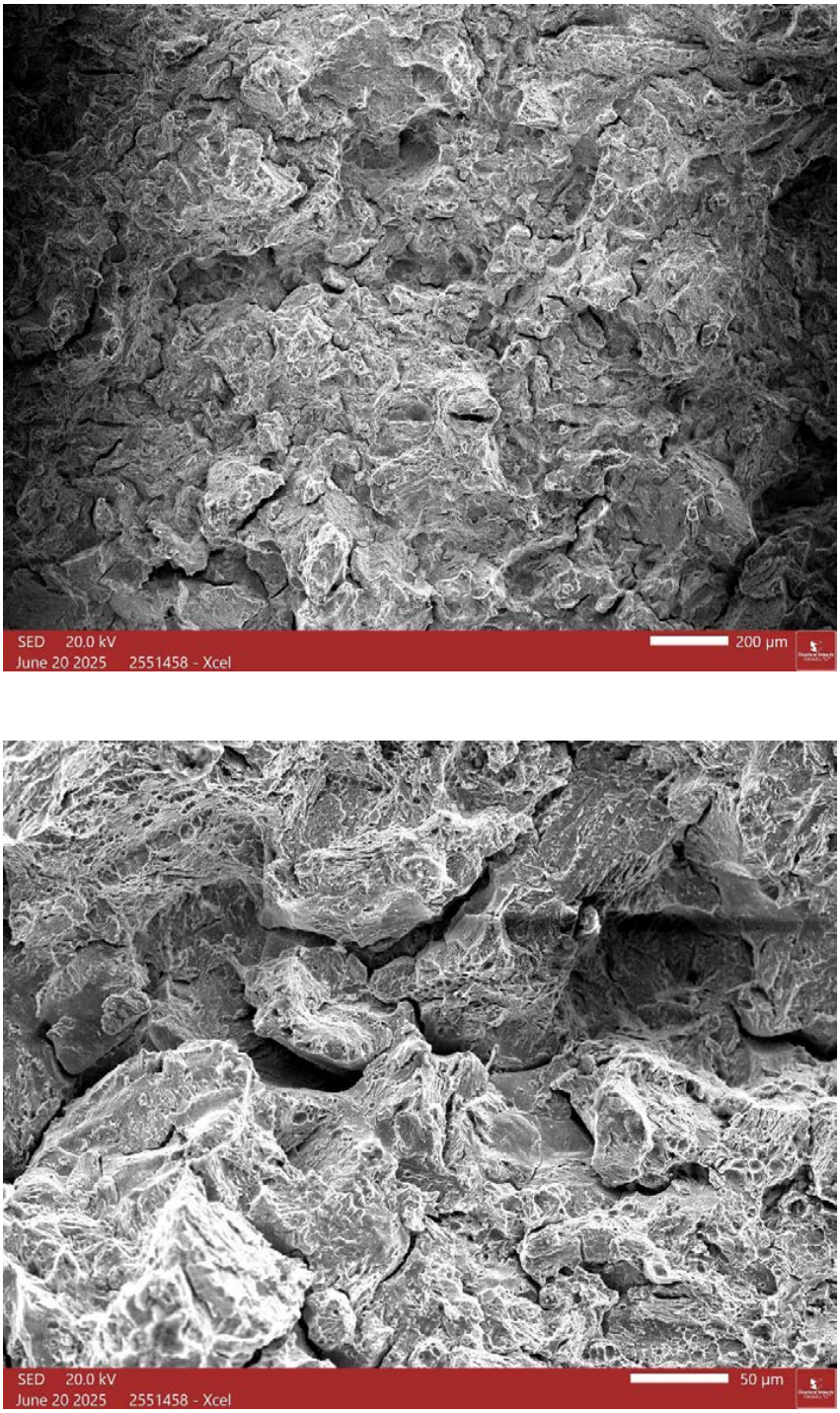

Figure 86. SEM images of Area 9 in Figure 71. In these images, the direction of cracking is approximately right to left. The fracture surface at this location exhibited a coarse, blocky appearance with a mixture of cleavage and dimpled rupture, along with secondary cracks or tears.

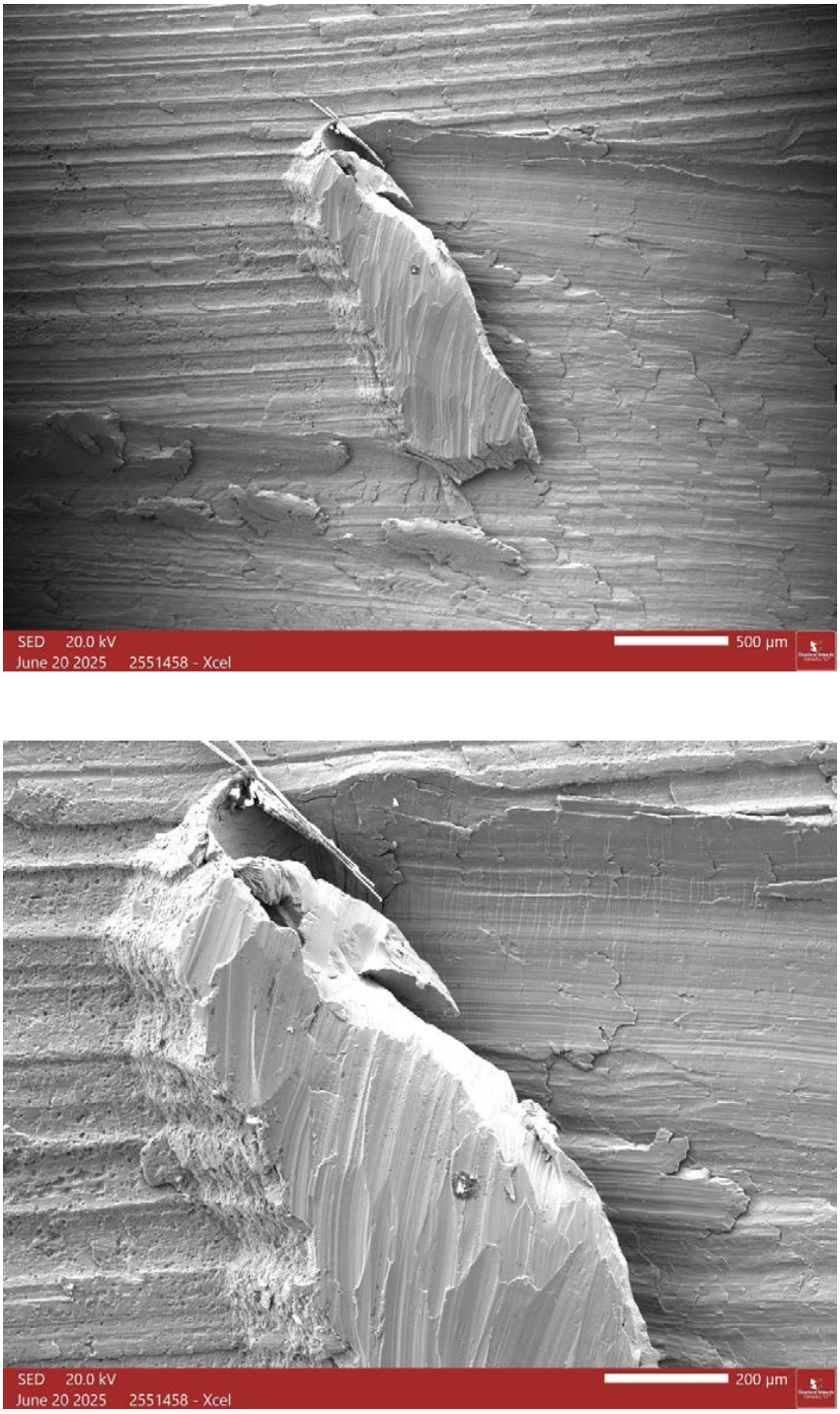

Figure 87. SEM images of Area 10 in Figure 71. These images show the piled up metal at the edge of one of the mechanical gouges on the cooling passage surface.

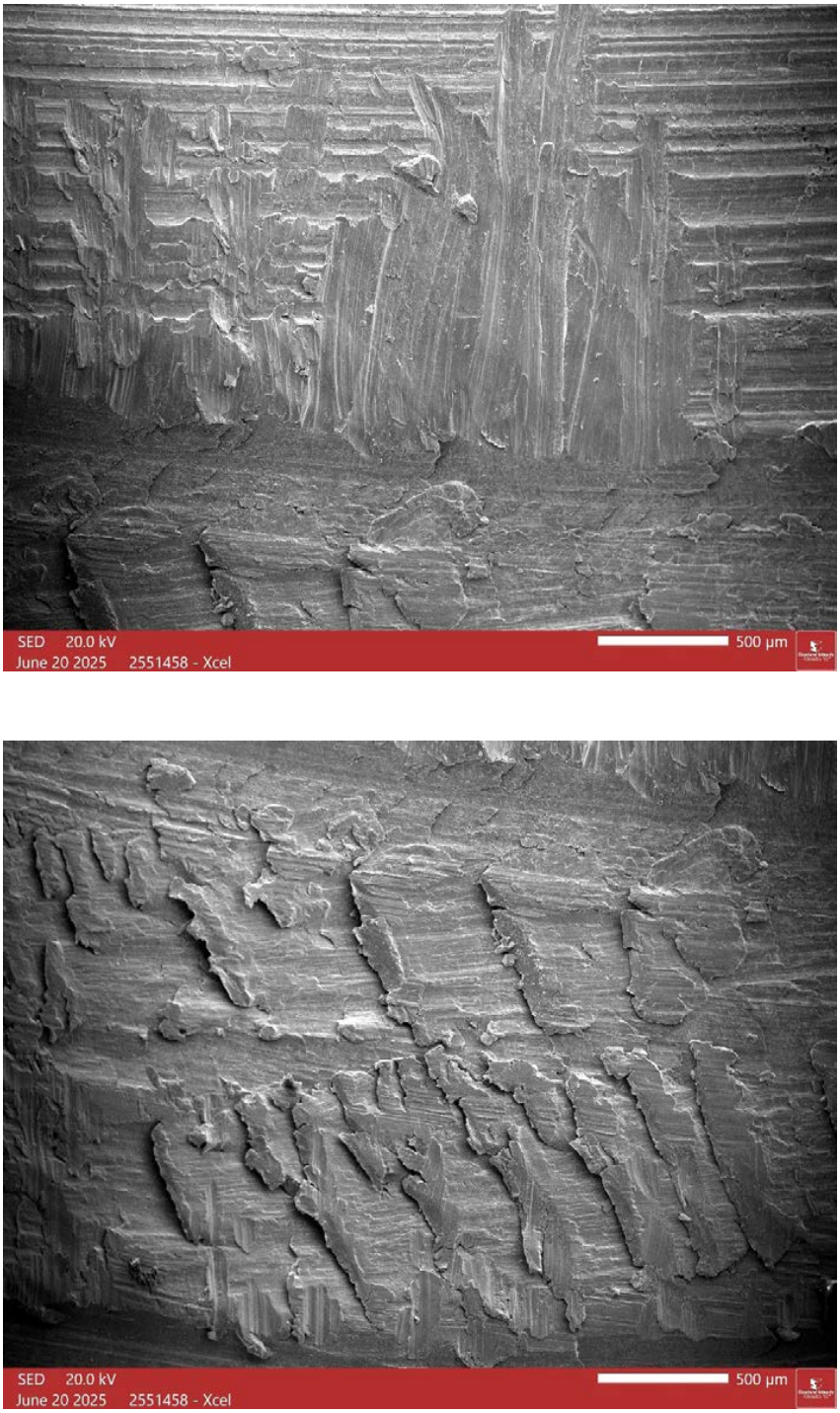

Figure 88. Additional SEM images of Area 10 in Figure 71. These images show various scratches and smeared metal on the cooling passage surface.

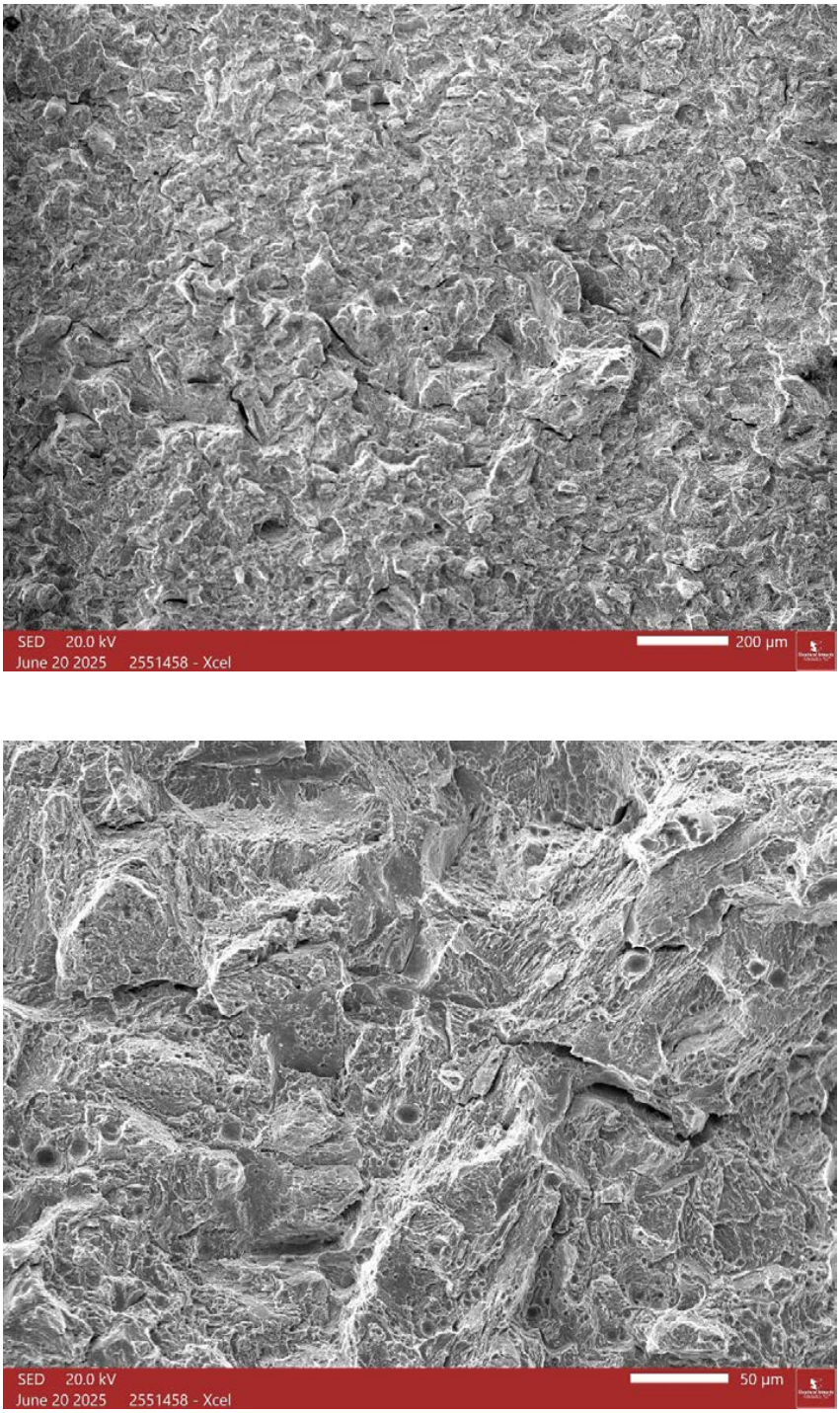

Figure 89. SEM images of Area 11 in Figure 71. In these images, the direction of crack propagation is approximately lower-right to upper-left, and the surface exhibited a slightly blocky appearance with indications of cleavage and secondary cracks or tears.

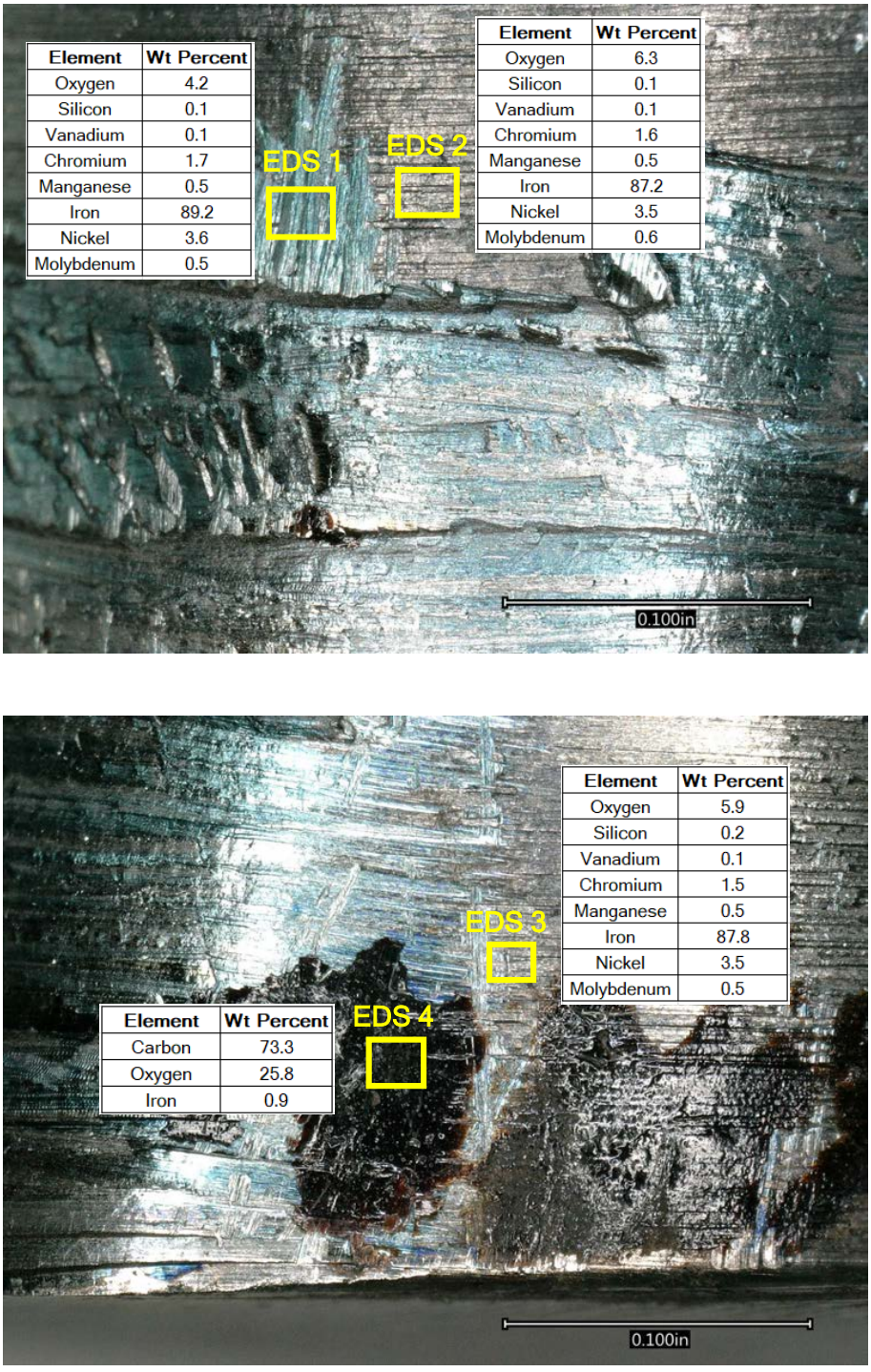

Figure 90. Images of the features in the cooling passage where energy dispersive spectroscopy (EDS) was performed to analyze the elemental compositions at the sample surface.

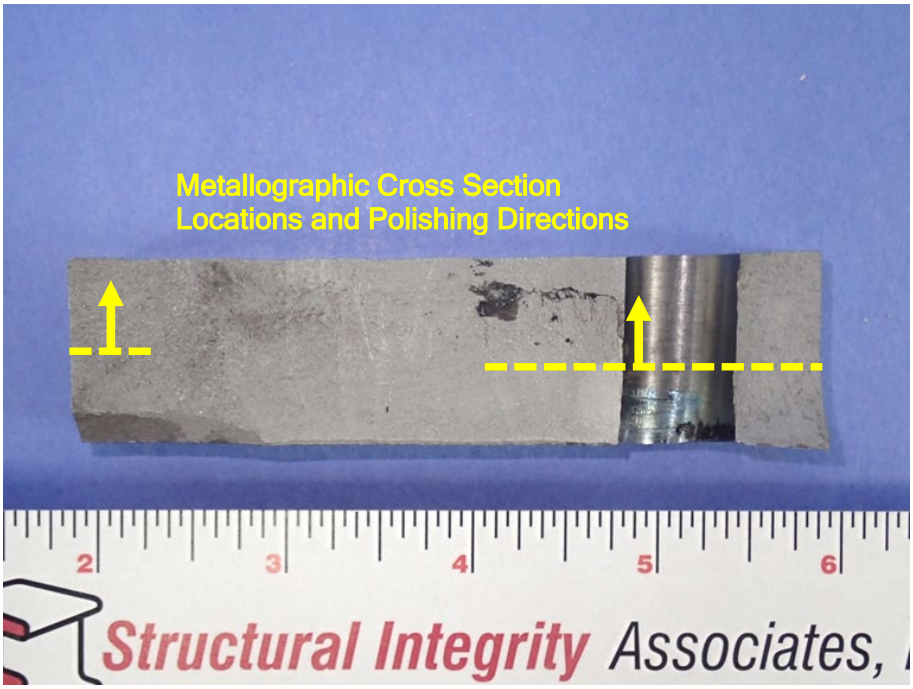

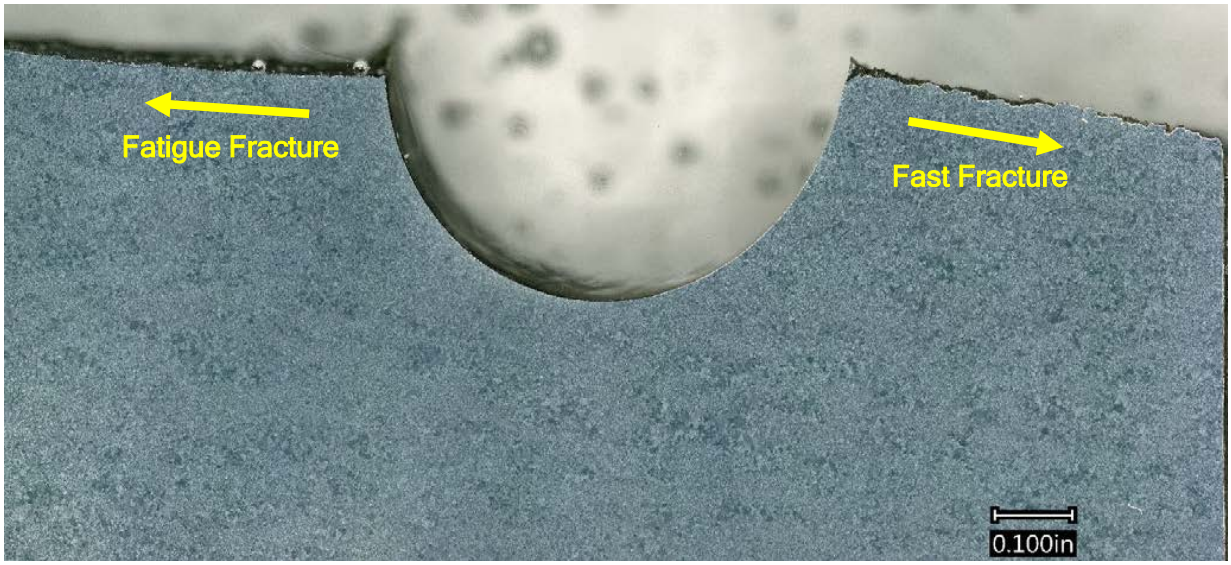

Figure 91. Upper image showing the locations where metallographic cross sections were removed from the ring sample. The cross section at the right side is just above Area 1 in Figure 71, and the cross section at the left side is situated in Area 9 of Figure 71. The lower image is a digital microscope image showing the prepared cross section on the right side of the upper image, with labels indicating the fatigue fracture and fast fracture sides of the cooling passage. (Etchant: Nital)

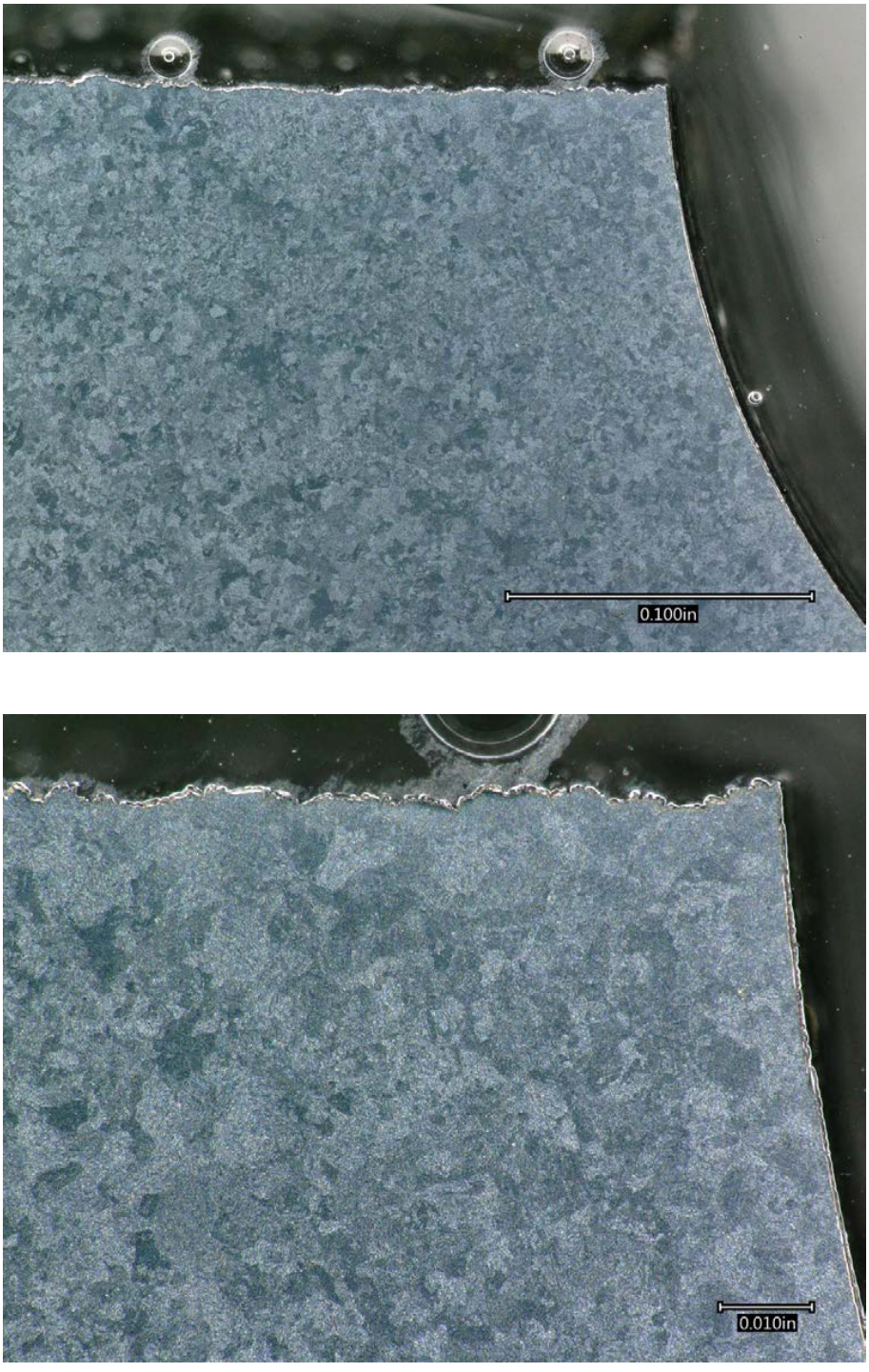

Figure 92. Additional digital microscope images of the fatigue fracture region on the cross section shown in Figure 91. The crack path is relatively straight, and slightly jagged at higher magnifications. In these images, variations in the grain size are evident across the polished sample surface. (Etchant: Nital)

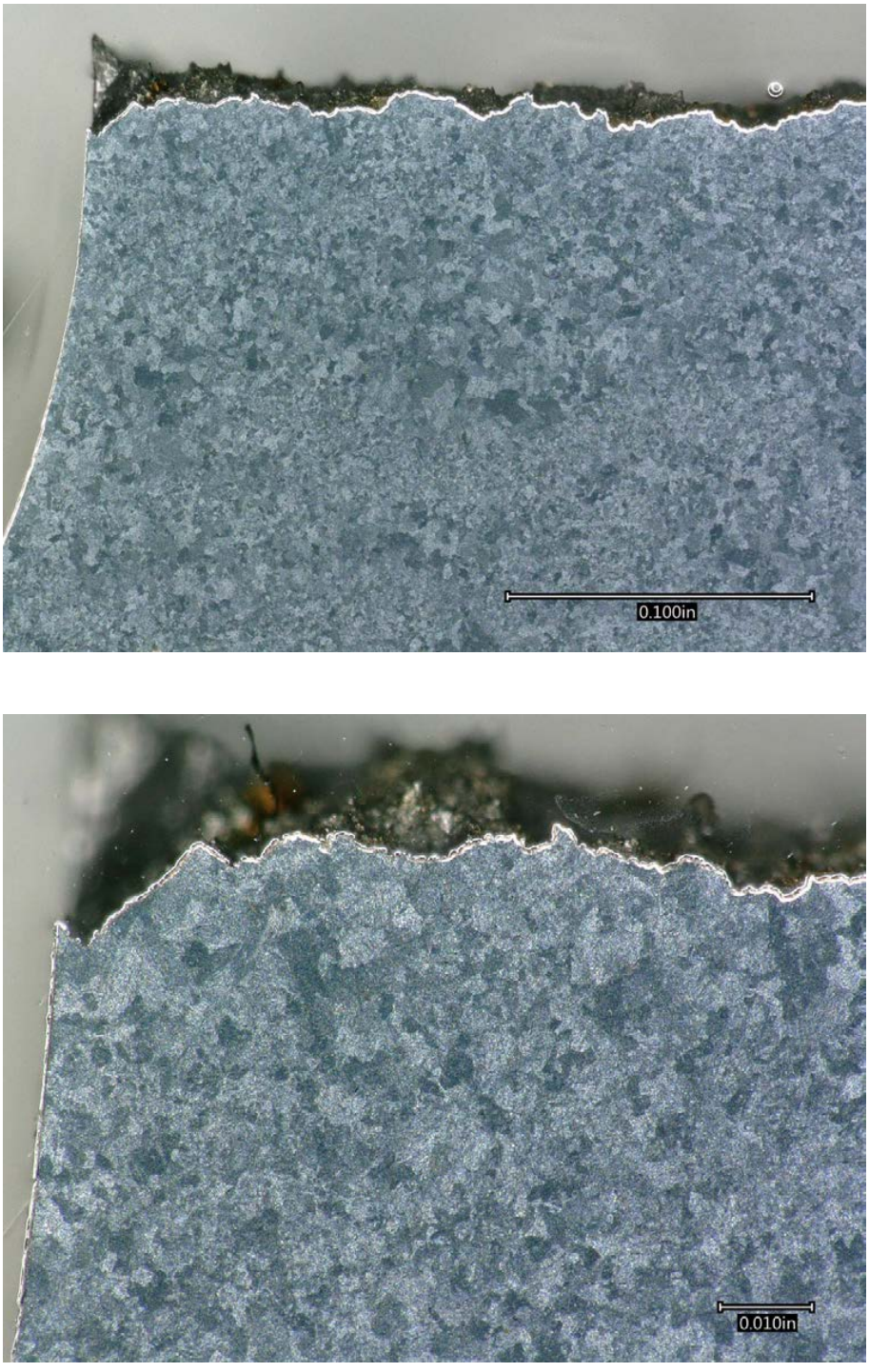

Figure 93. Additional digital microscope images of the fast fracture region on the cross section shown in Figure 91. At this location, which is on the opposite side of the cooling passage from the crack origin area, the crack path is relatively jagged. In these images, variations in the grain size are evident across the polished sample surface. (Etchant: Nital)

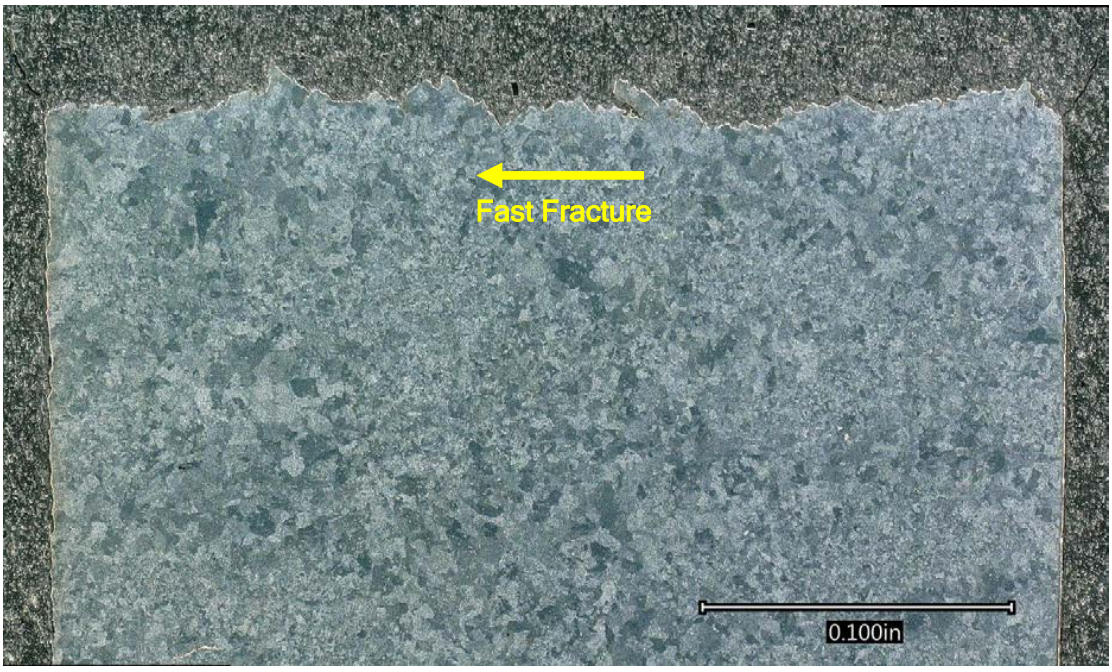

Figure 94. Digital microscope images of the prepared cross section on the left side of the upper image of Figure 91. The crack path was relatively straight and jagged in appearance. In these images, variations in the grain size are evident across the polished sample surface. (Etchant: Nital)

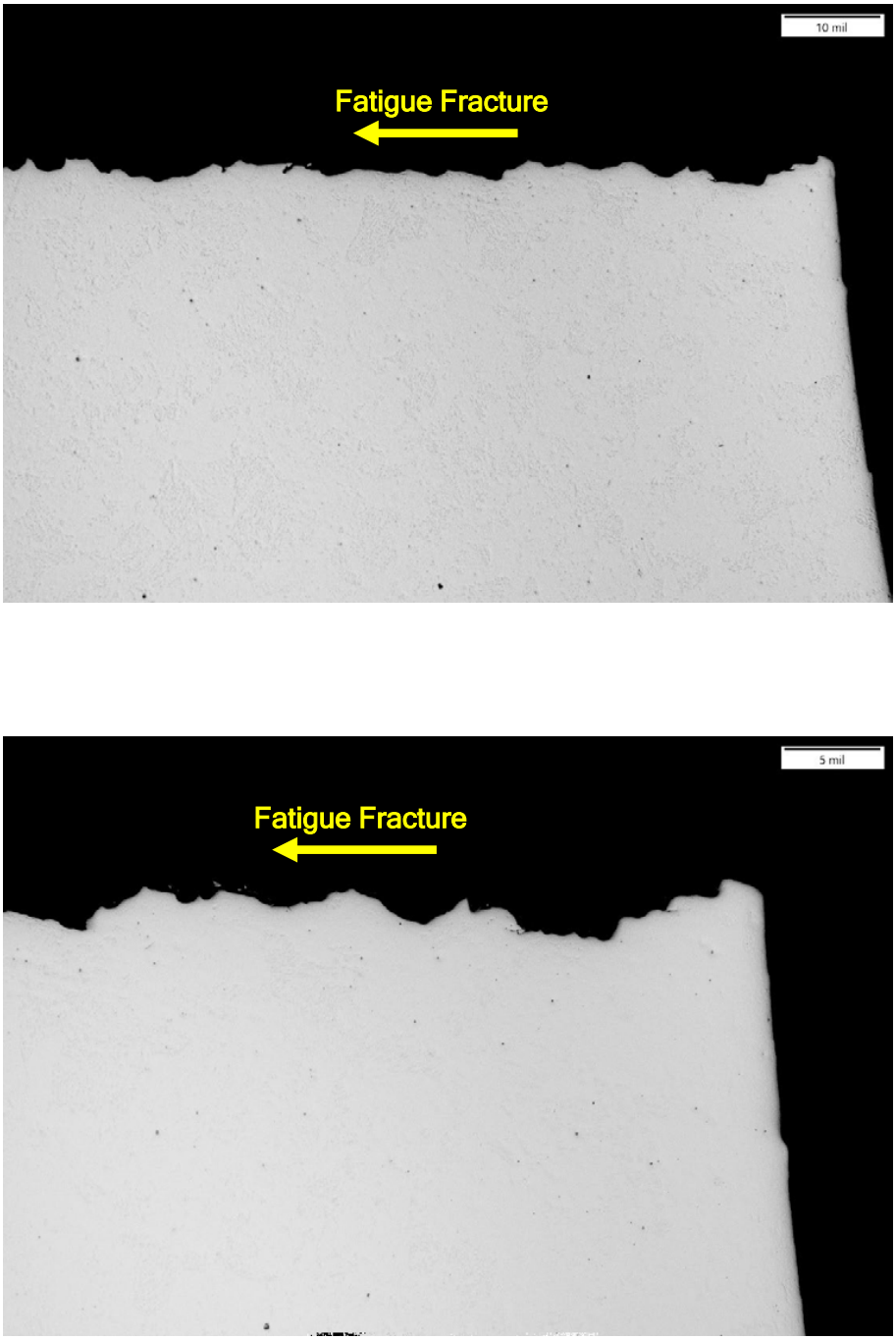

Figure 95. Metallograph images of the fatigue fracture region near the cooling passage, which is visible at the right side. The crack path is relatively straight, and slightly jagged at higher magnifications. (Unetched)

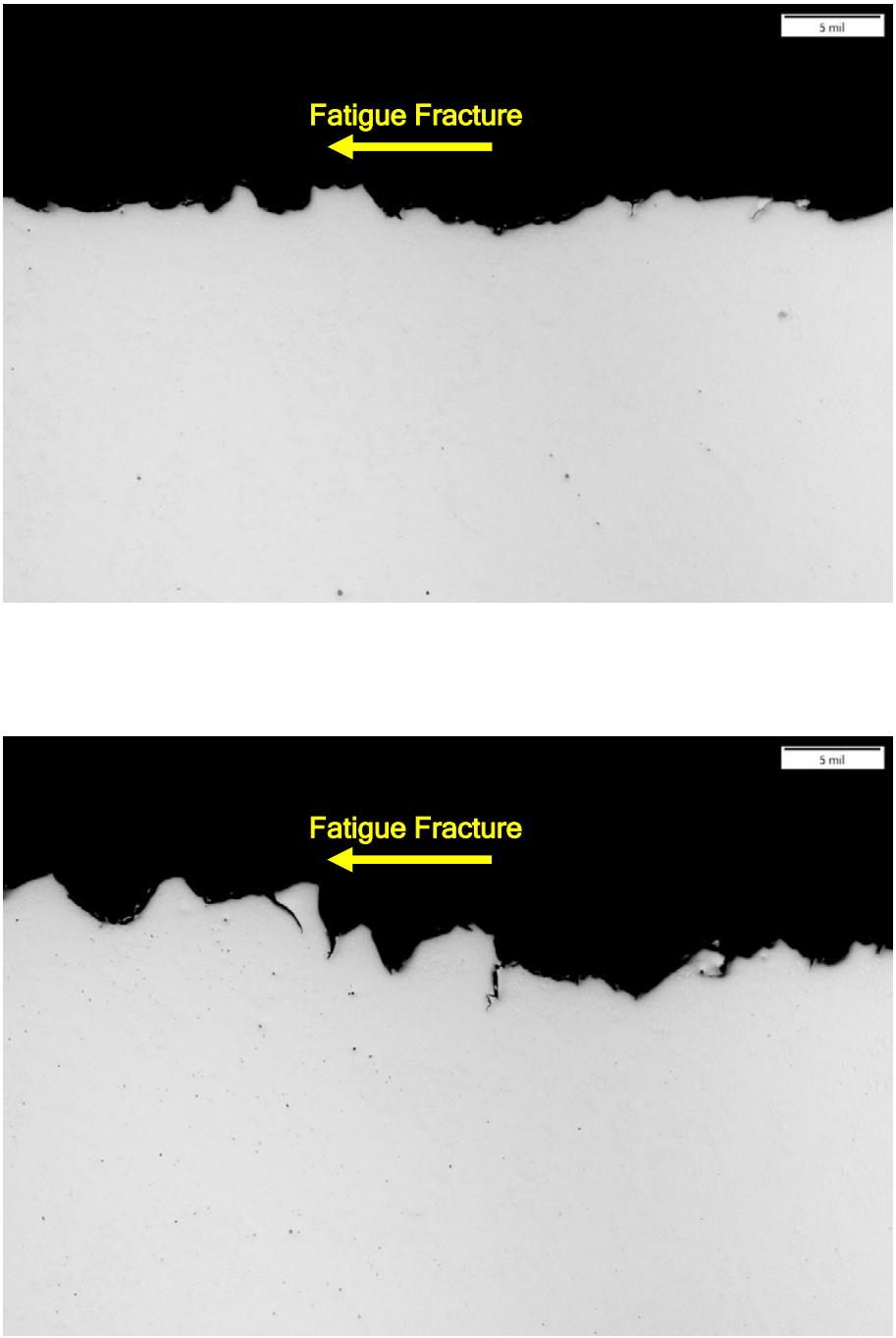

Figure 96. Higher magnification metallograph images of the fatigue fracture at locations along the crack path. In some locations, short secondary cracks or tears are evident. (Unetched)

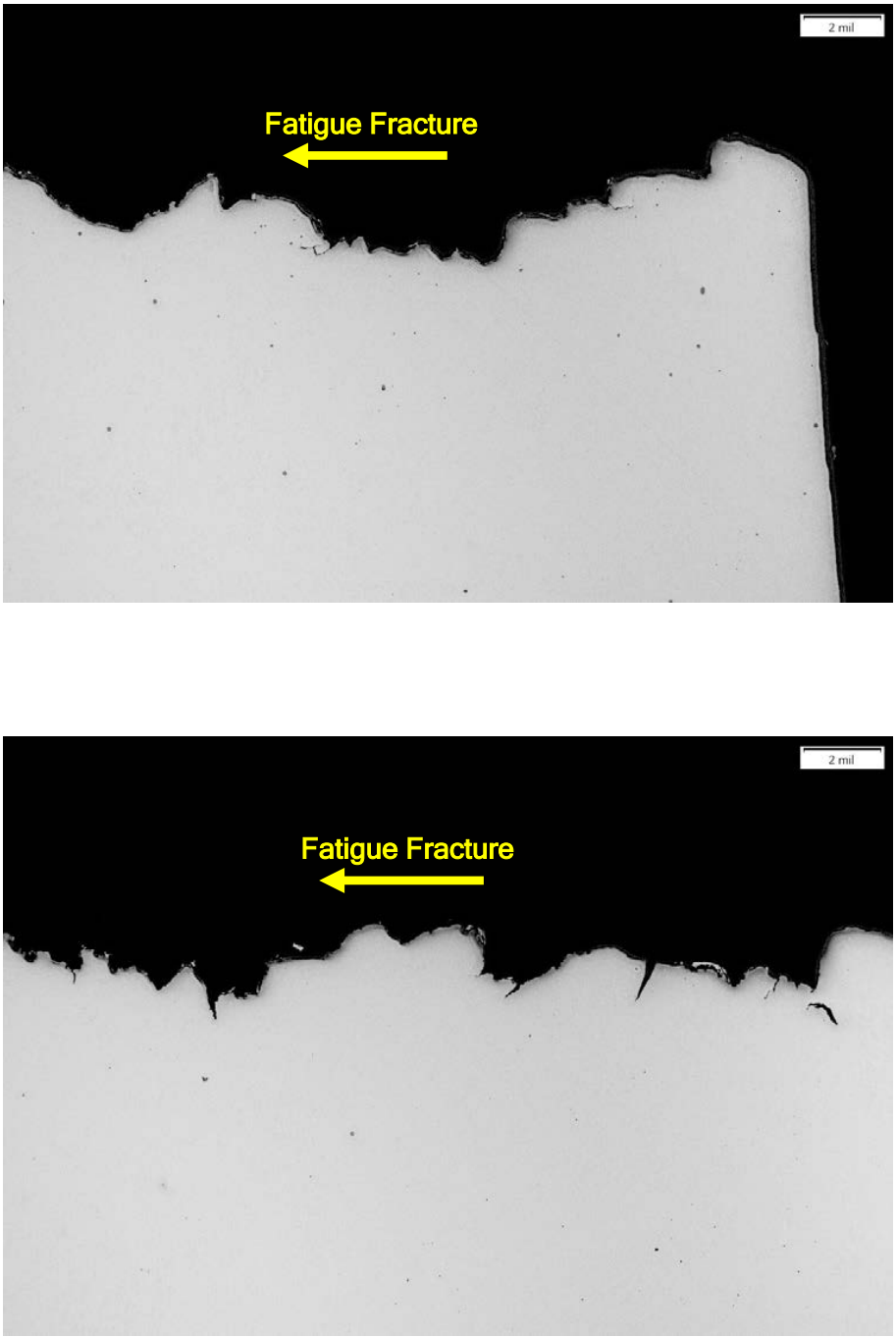

Figure 97. Higher magnification metallograph images of the fatigue fracture at locations adjacent to the cooling passage (upper image) and along the crack path (lower image). In some locations, short secondary cracks or tears are evident. (Unetched)

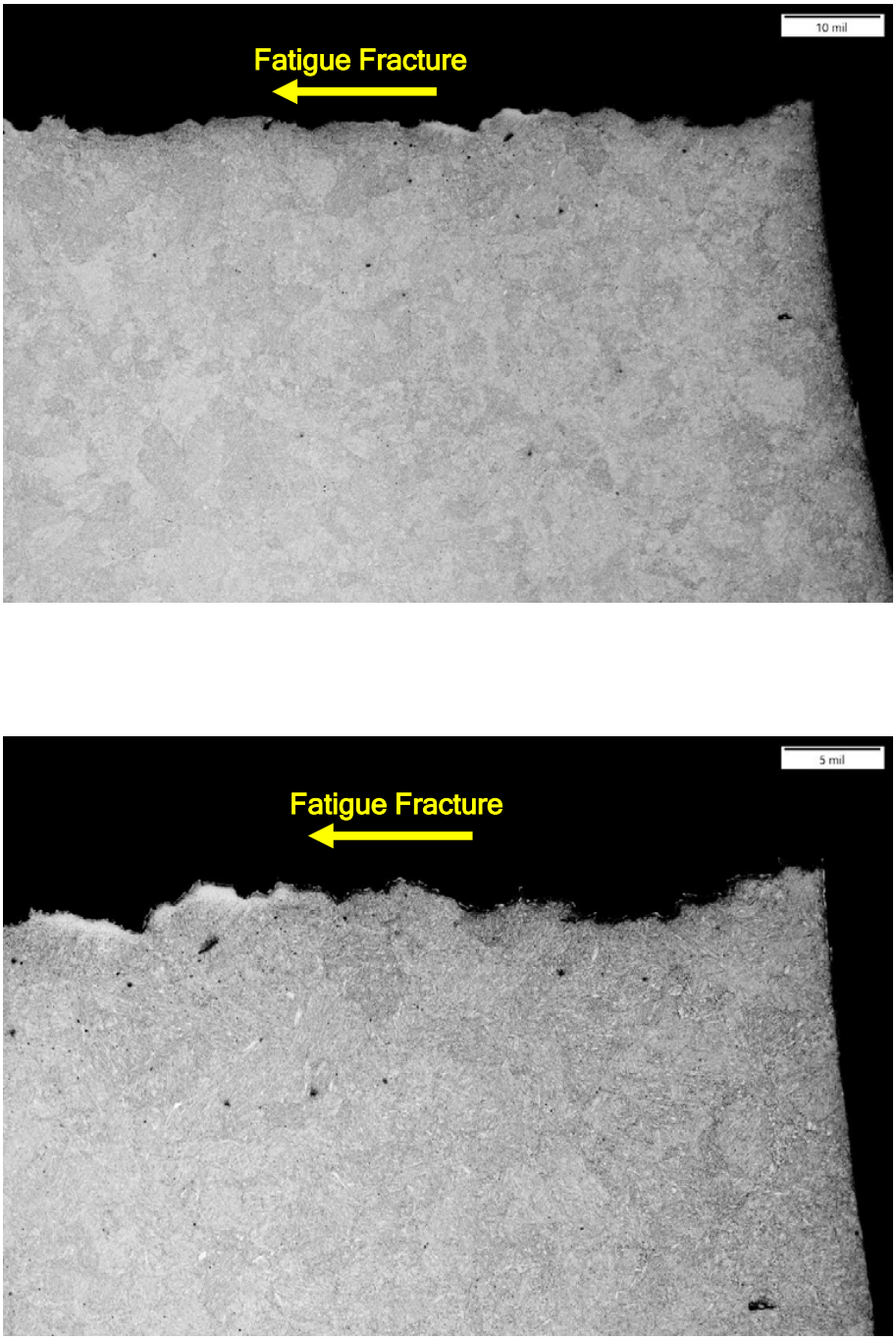

Figure 98. Metallograph images of the fatigue fracture region near the cooling passage, after etching to reveal the microstructure. The crack path is relatively straight, and slightly jagged at higher magnifications. Etched inclusions are also evident as dark features. (Etchant: Nital)

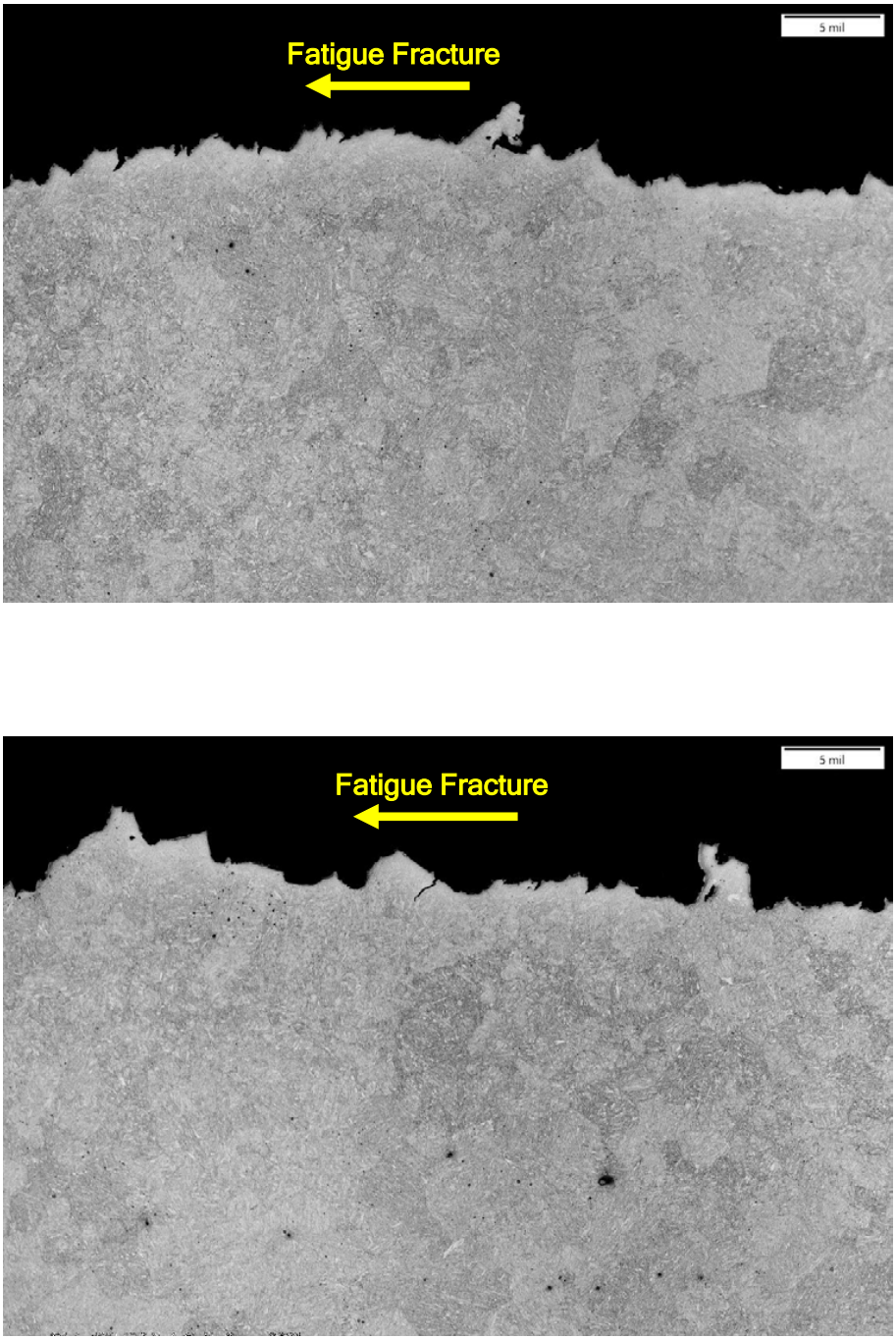

Figure 99. Higher magnification images of features along the fatigue crack path. Etched inclusions are also evident as dark spots. (Etchant: Nital)

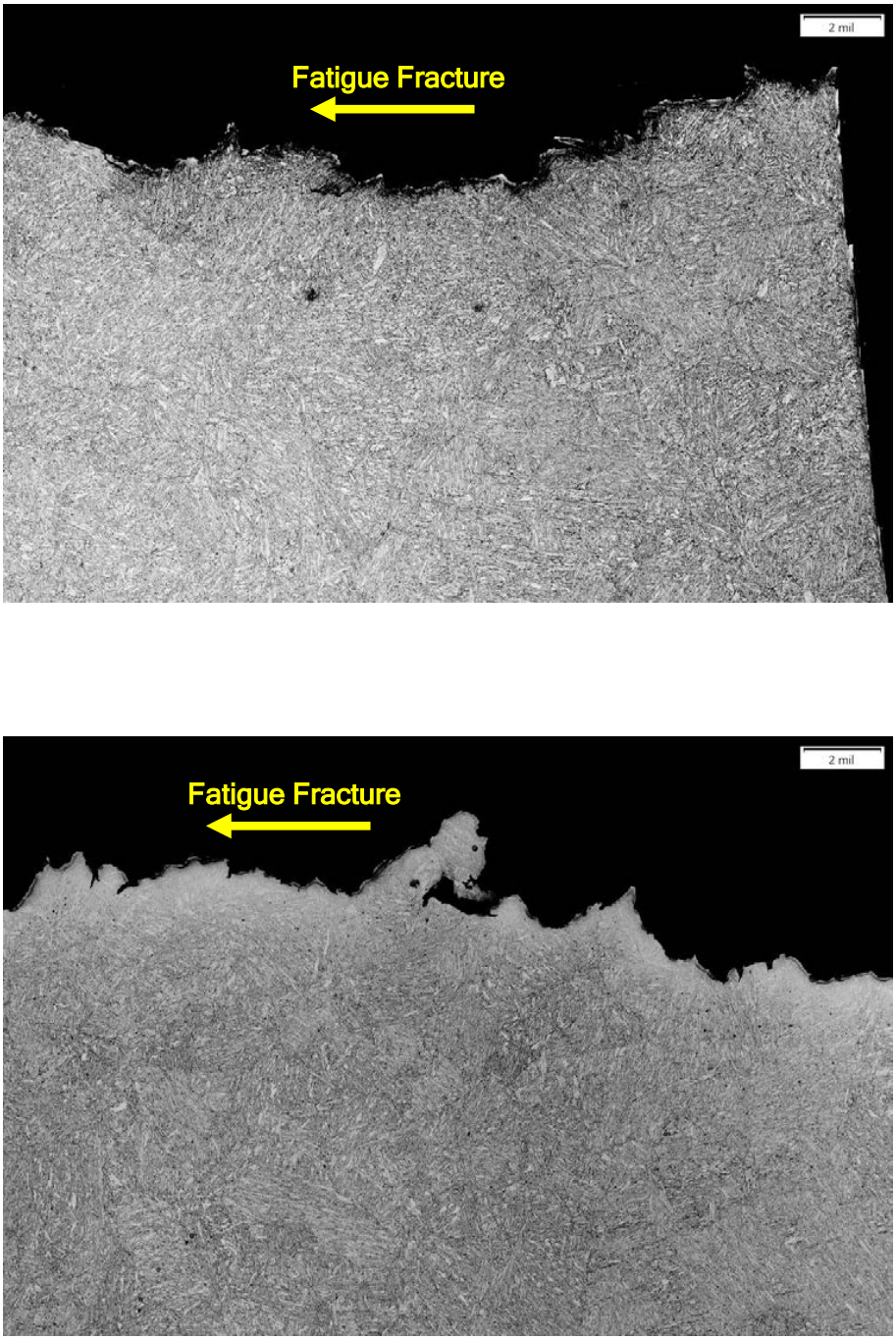

Figure 100. Higher magnification images of features near the cooling passage (upper image) and along the fatigue crack path (lower image). (Etchant: Nital)

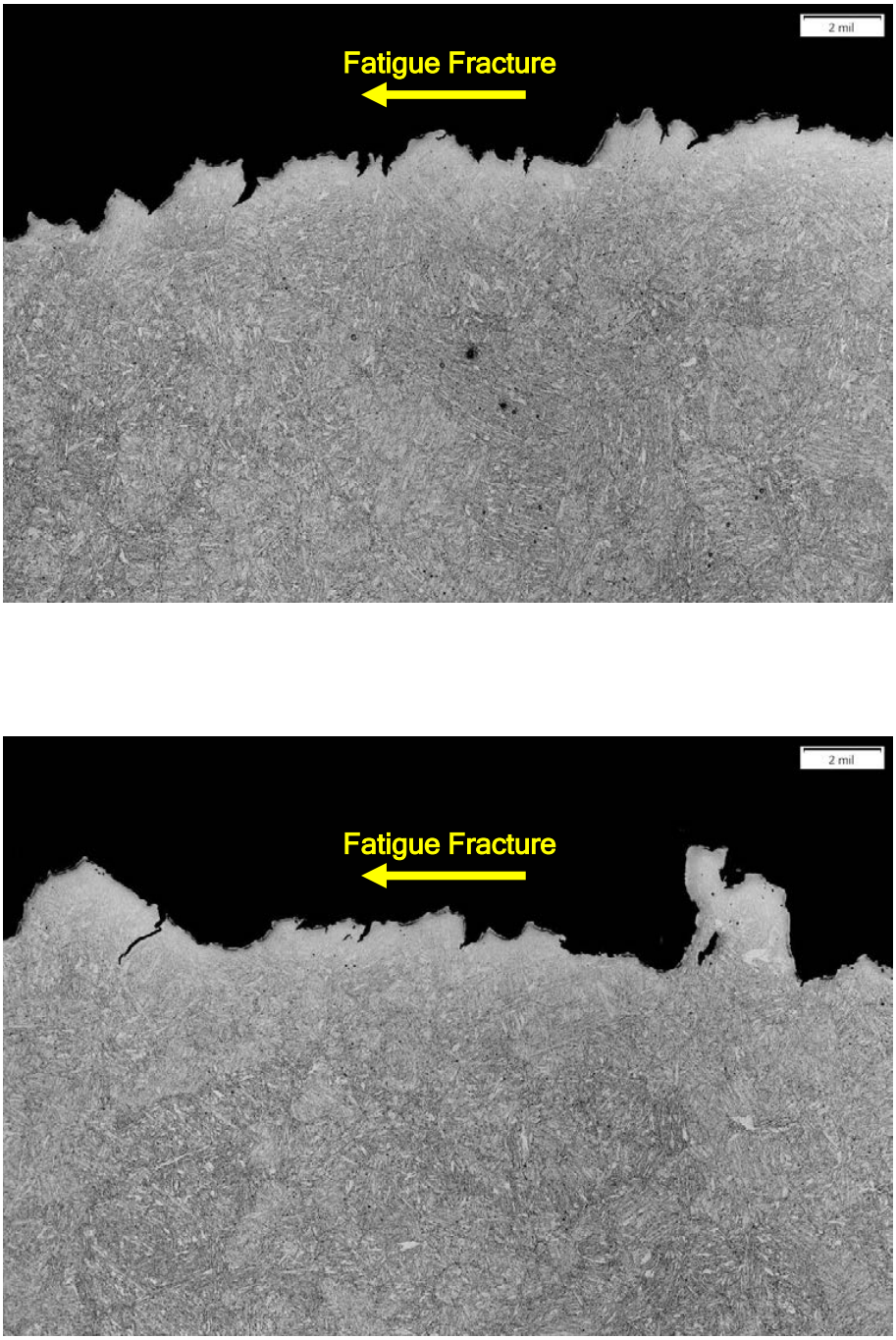

Figure 101. Additional higher magnification images of features along the fatigue crack path. (Etchant: Nital)

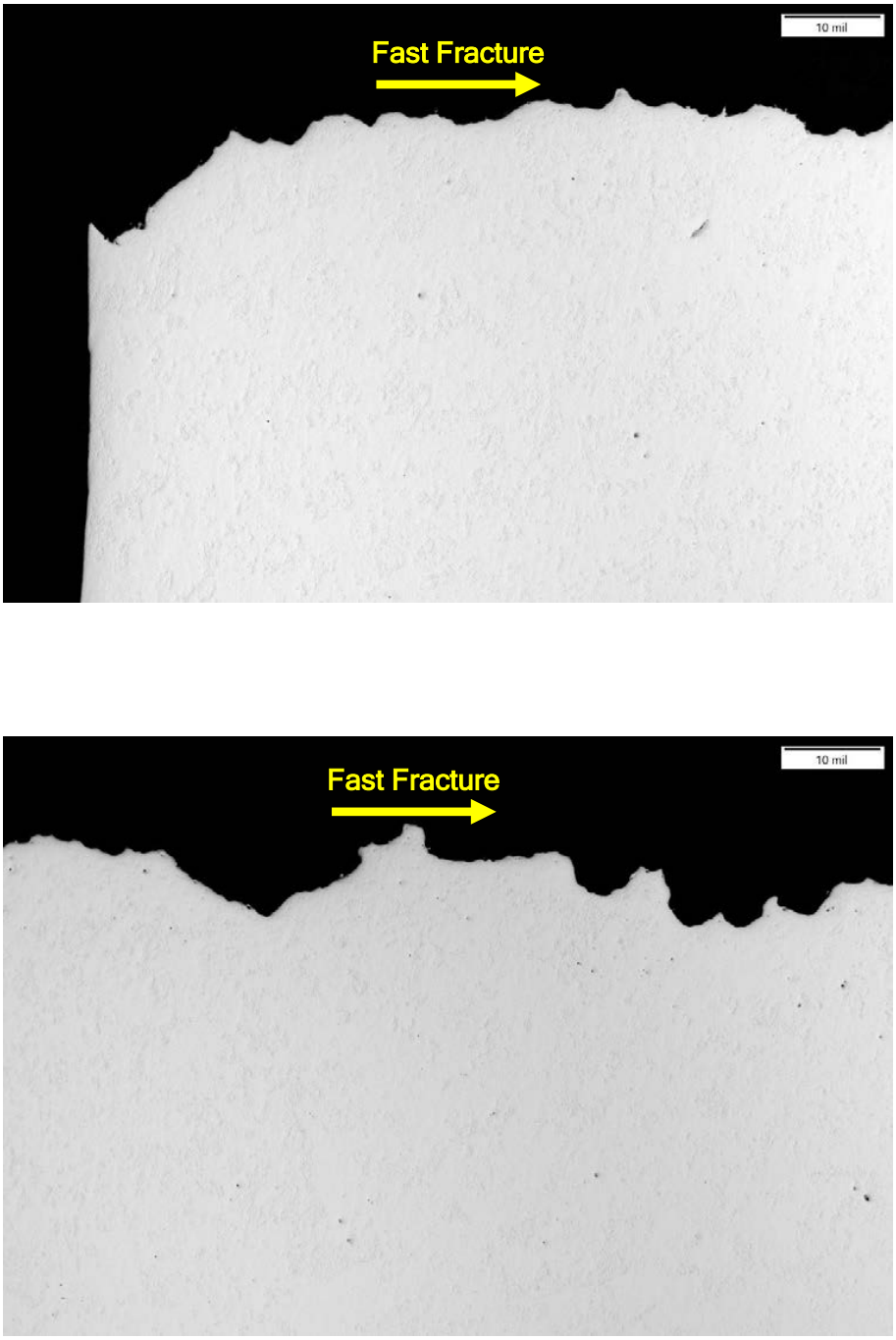

Figure 102. Metallograph images of the fast fracture region on the opposite side of the cooling passage from the crack origin area. The crack path is relatively jagged in appearance. (Unetched)

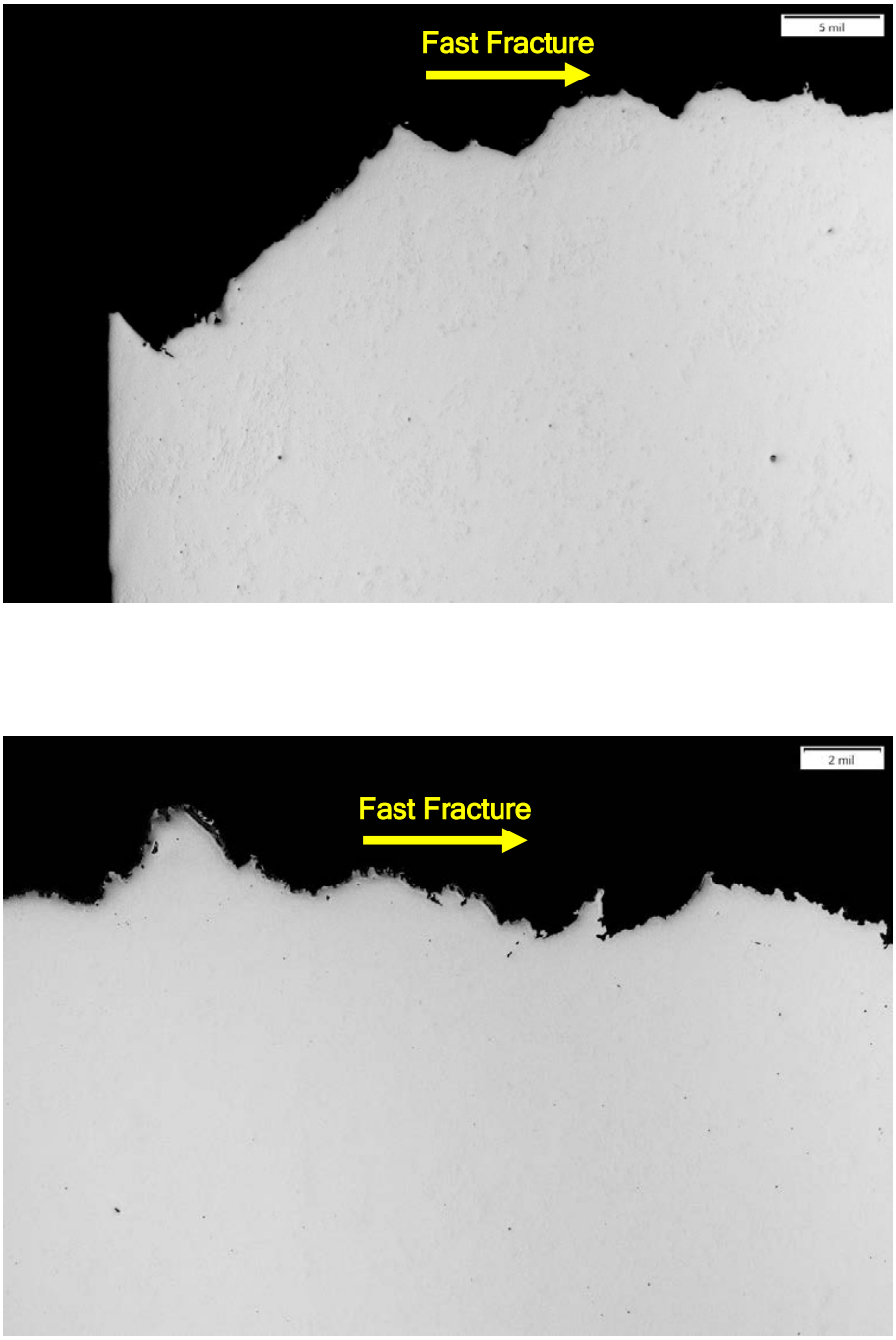

Figure 103. Higher magnification images of the fast fracture region on the opposite side of the cooling passage from the crack origin area. (Unetched)

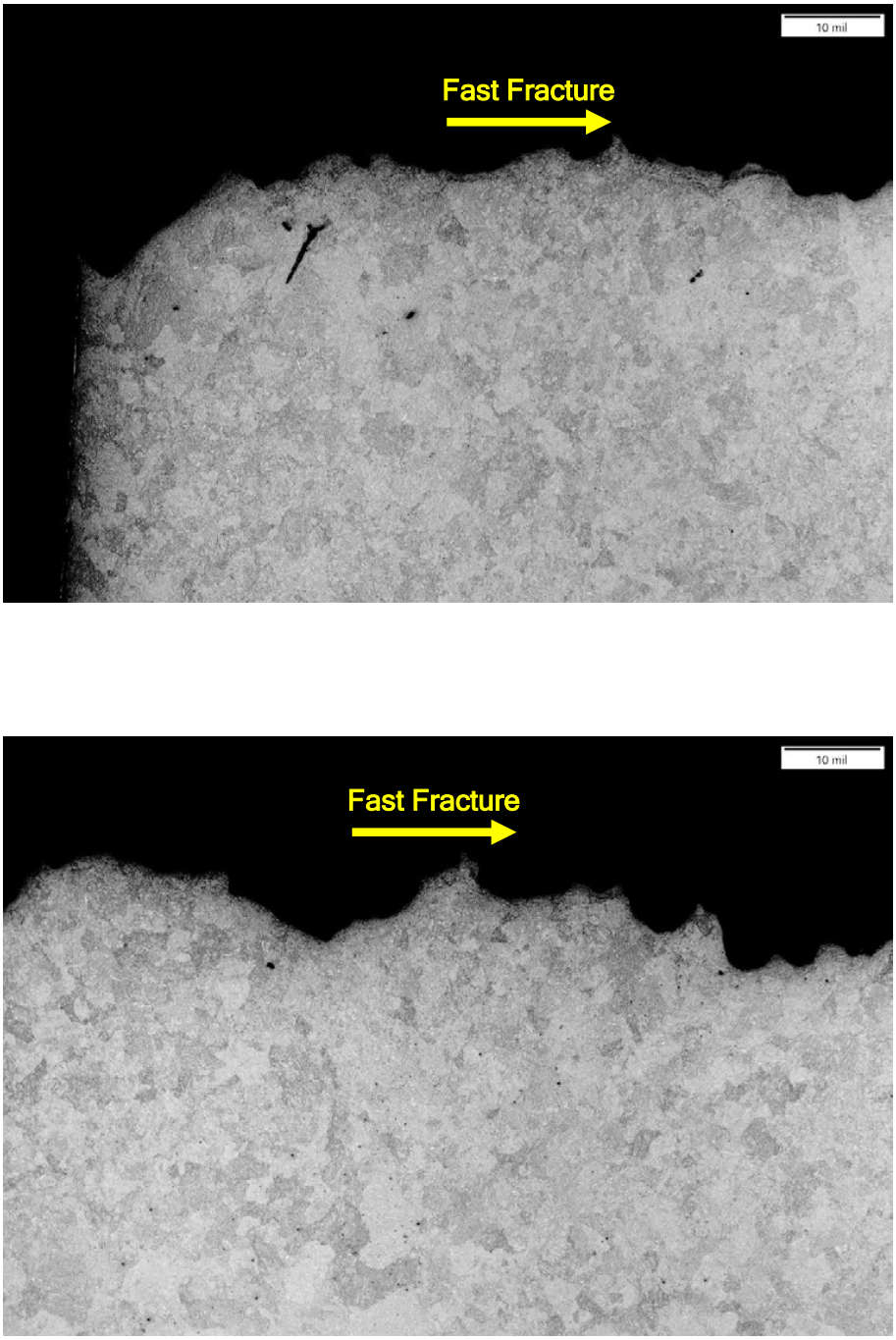

Figure 104. Views of the fast fracture region near the cooling passage, after etching to reveal the microstructure. The crack path is relatively jagged in appearance. The dark feature in the upper image is an artifact of the etching process. (Etchant: Nital)

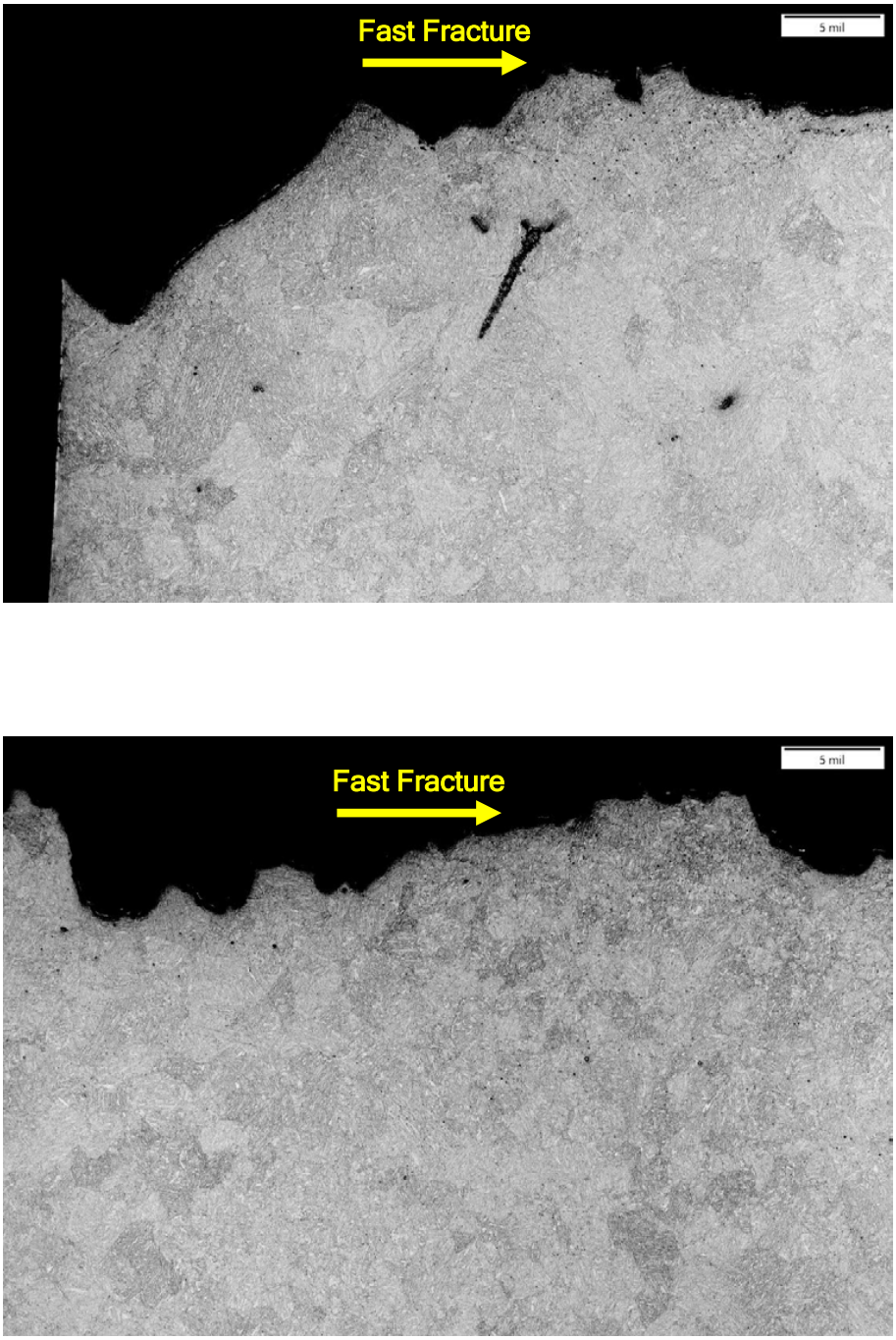

Figure 105. Higher magnification images of the fast fracture region on the opposite side of the cooling passage from the crack origin area. The dark feature in the upper image is an artifact of the etching process. (Etchant: Nital)

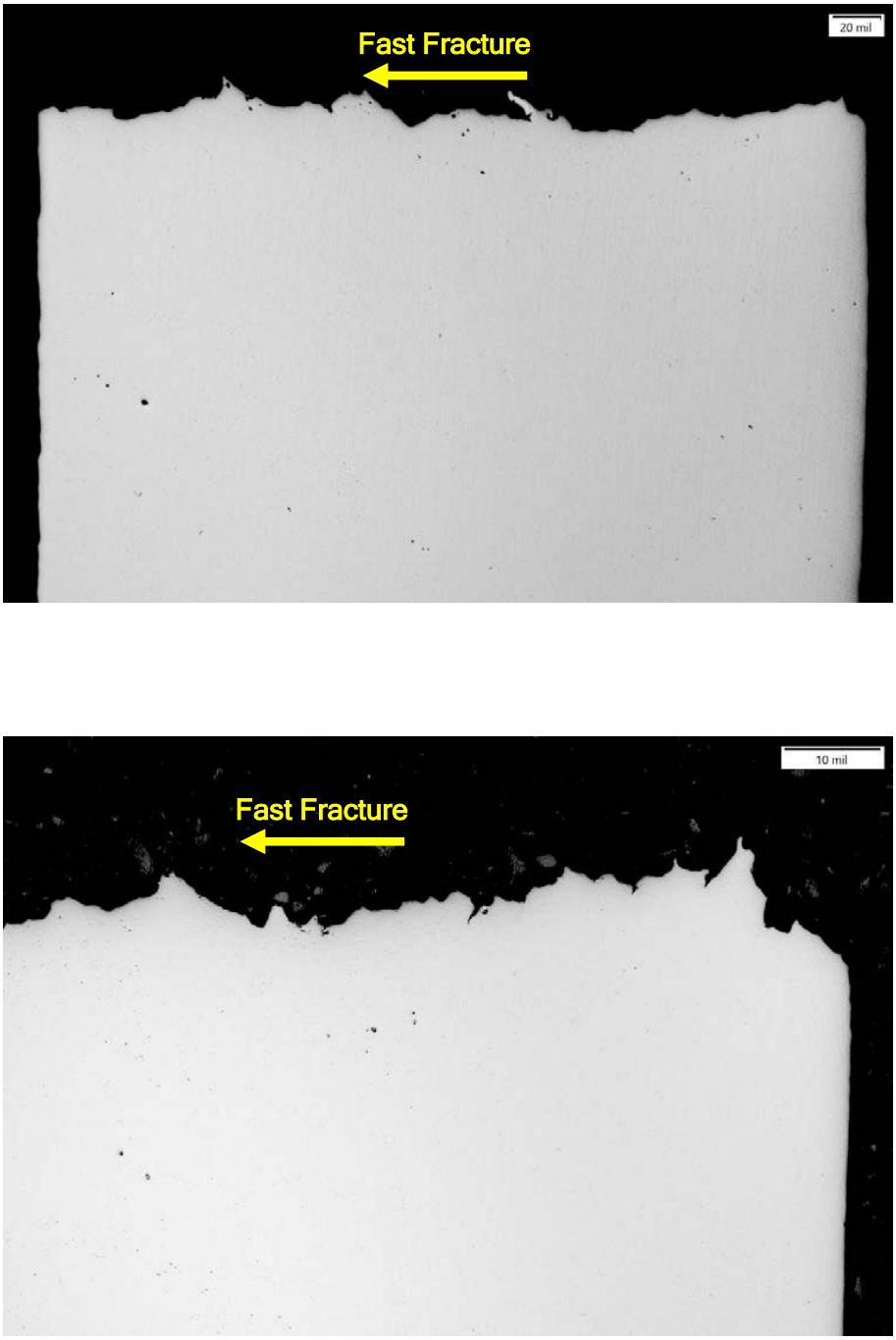

Figure 106. Metallograph images of the fast fracture region shown at the left side of the upper image of Figure 91. The crack path is relatively jagged in appearance. (Unetched)

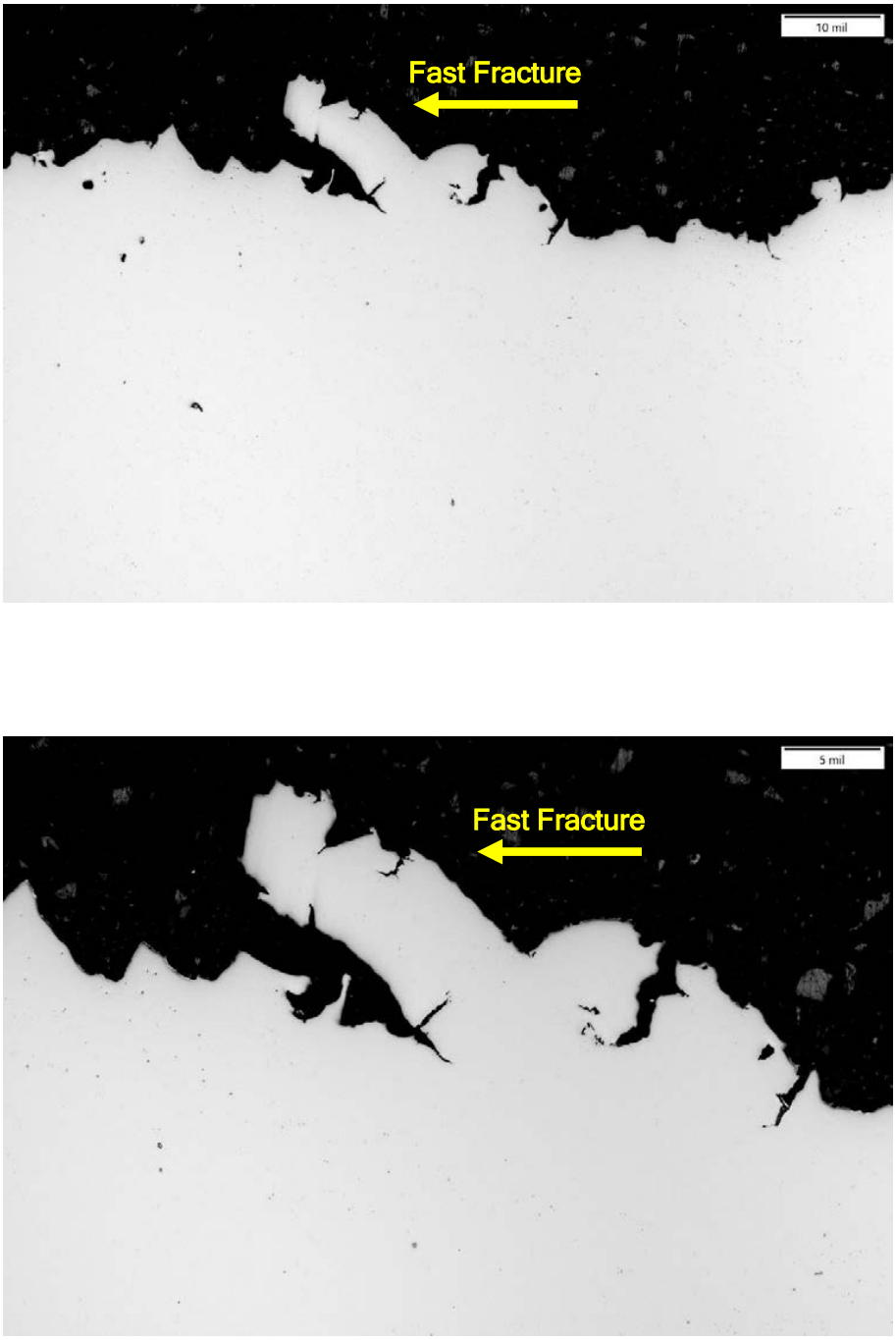

Figure 107. Additional metallograph images of features along the crack path shown in Figure 106. (Unetched)

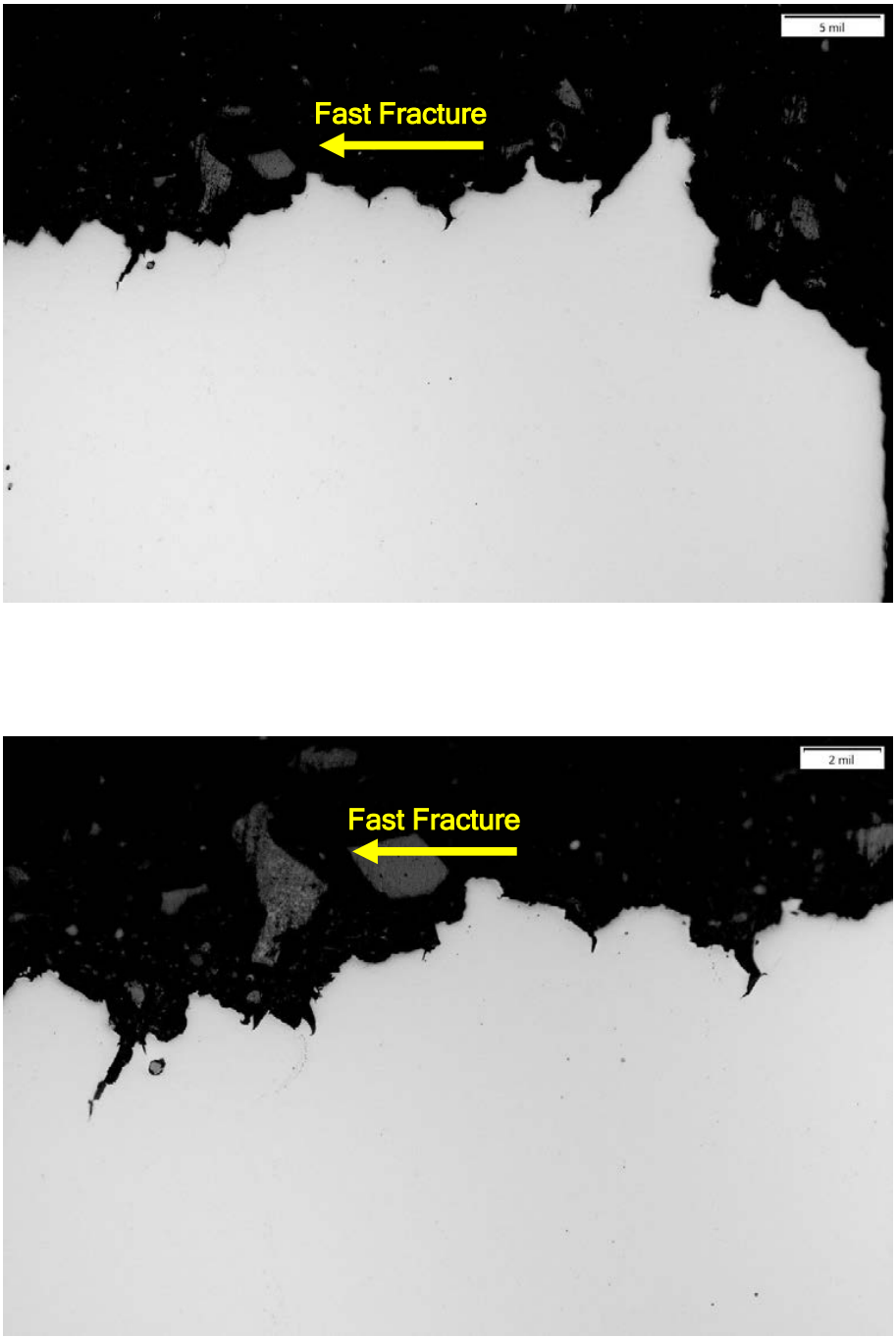

Figure 108. Additional metallograph images of features along the crack path shown in Figure 106. (Unetched)

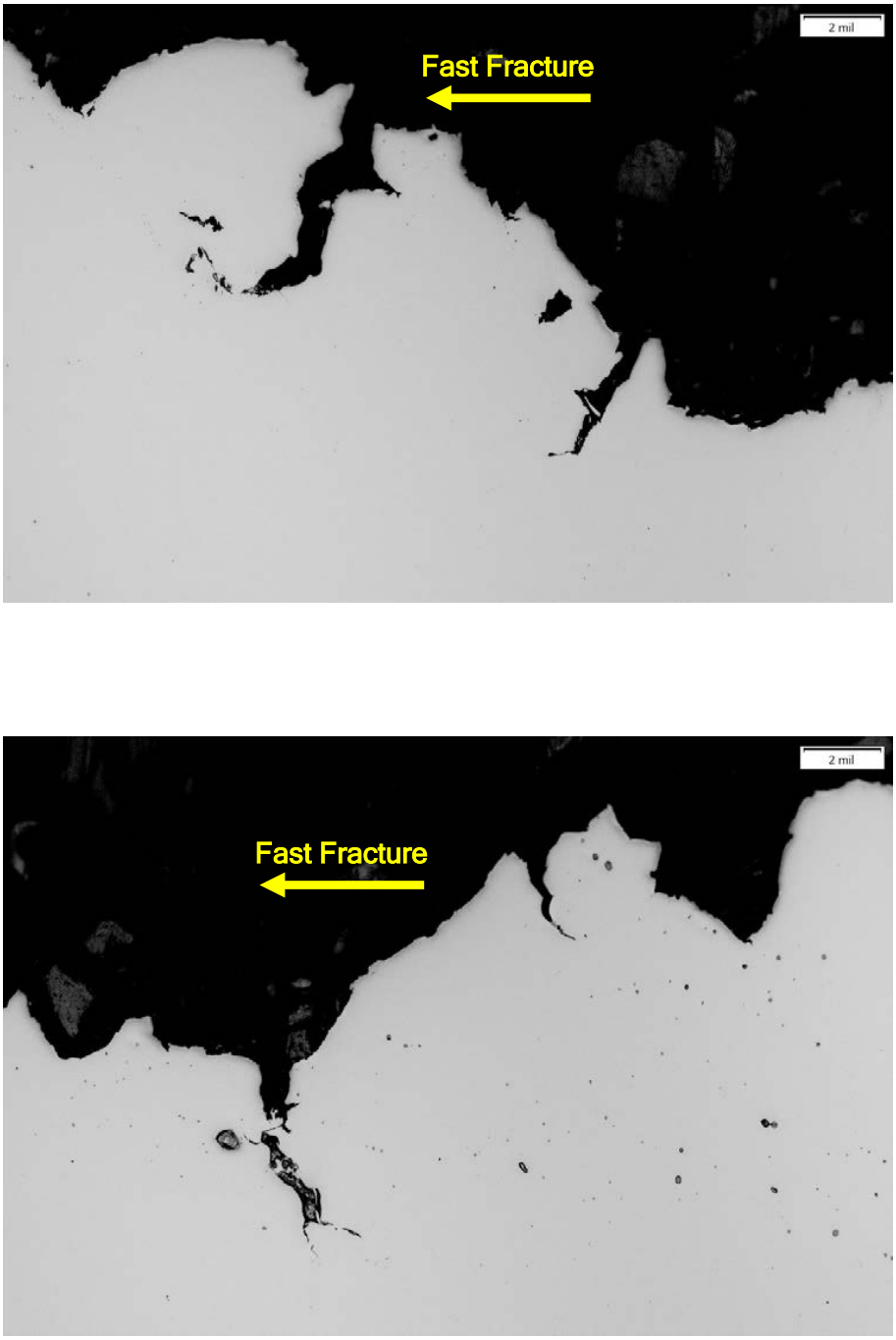

Figure 109. Higher magnification images of features along the crack path shown in Figure 106. (Unetched)

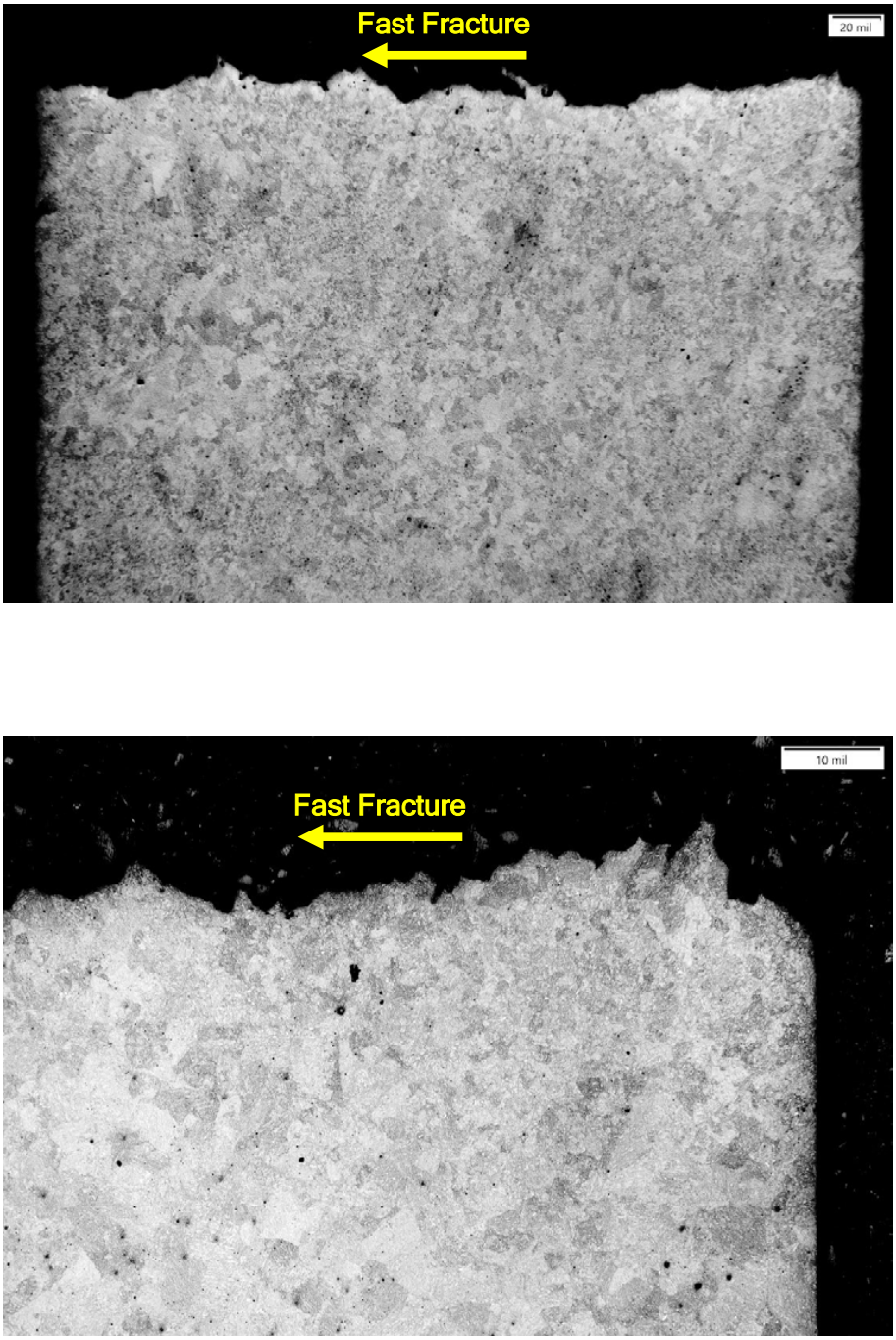

Figure 110. Metallograph images of the fast fracture region shown at the left side of the upper image of Figure 91, after etching to reveal the microstructure. The crack path is relatively jagged in appearance. Etched inclusions are also evident as dark features. (Etchant: Nital)

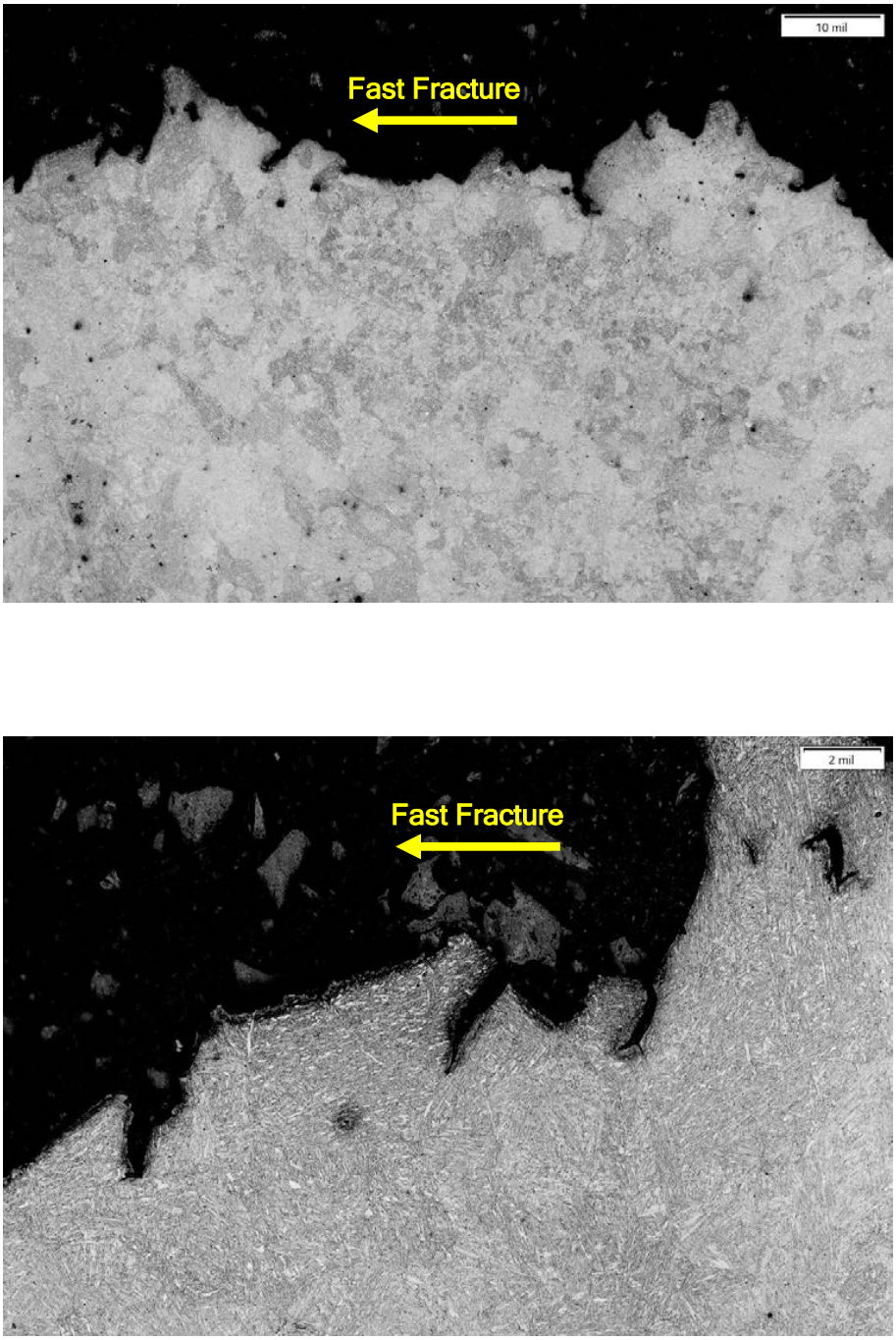

Figure 111. Additional metallograph images of features along the crack path shown in Figure 110. Etched inclusions are also evident as dark features. (Etchant: Nital)

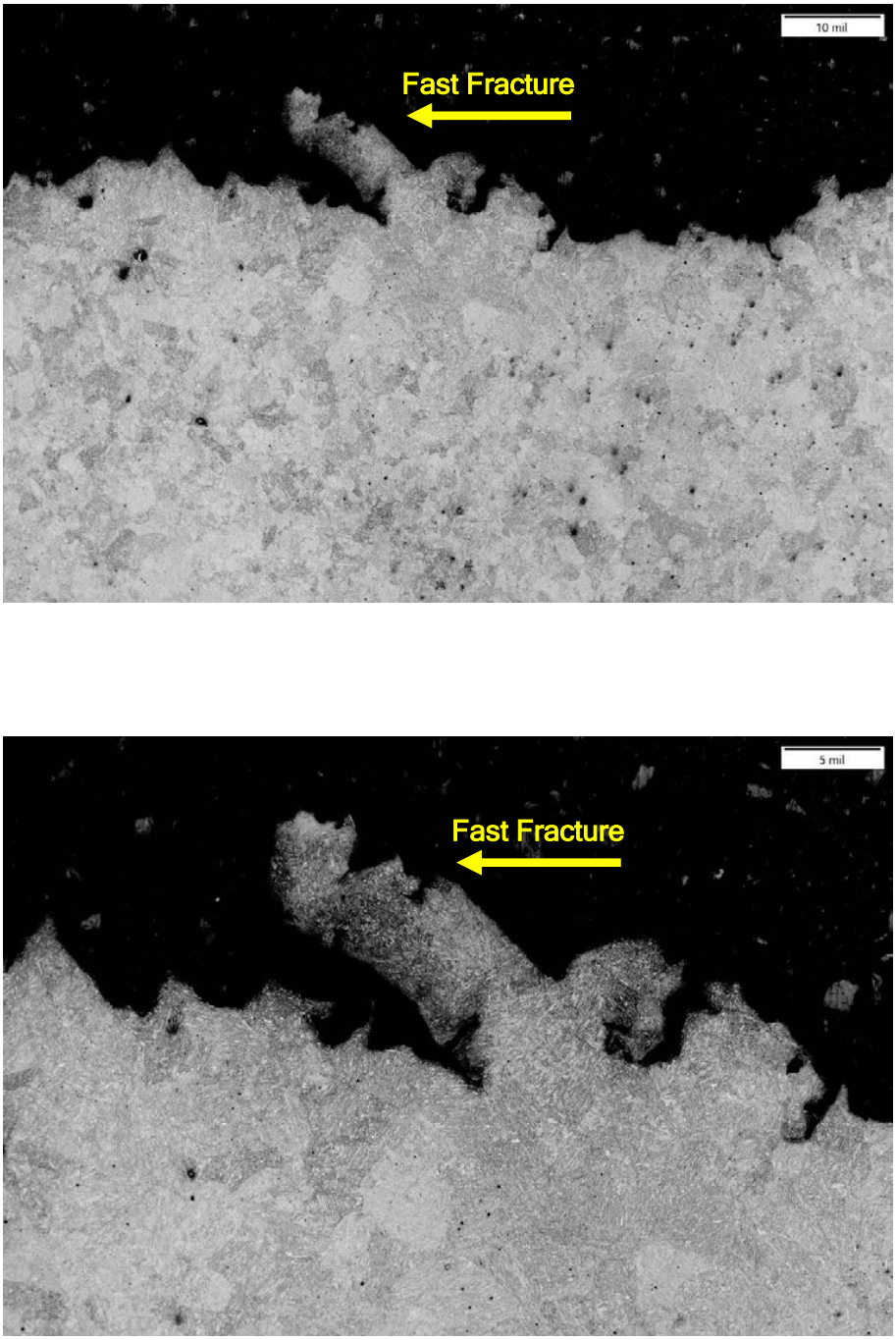

Figure 112. Additional metallograph images of features along the crack path shown in Figure 110. Etched inclusions are also evident as dark features. (Etchant: Nital)

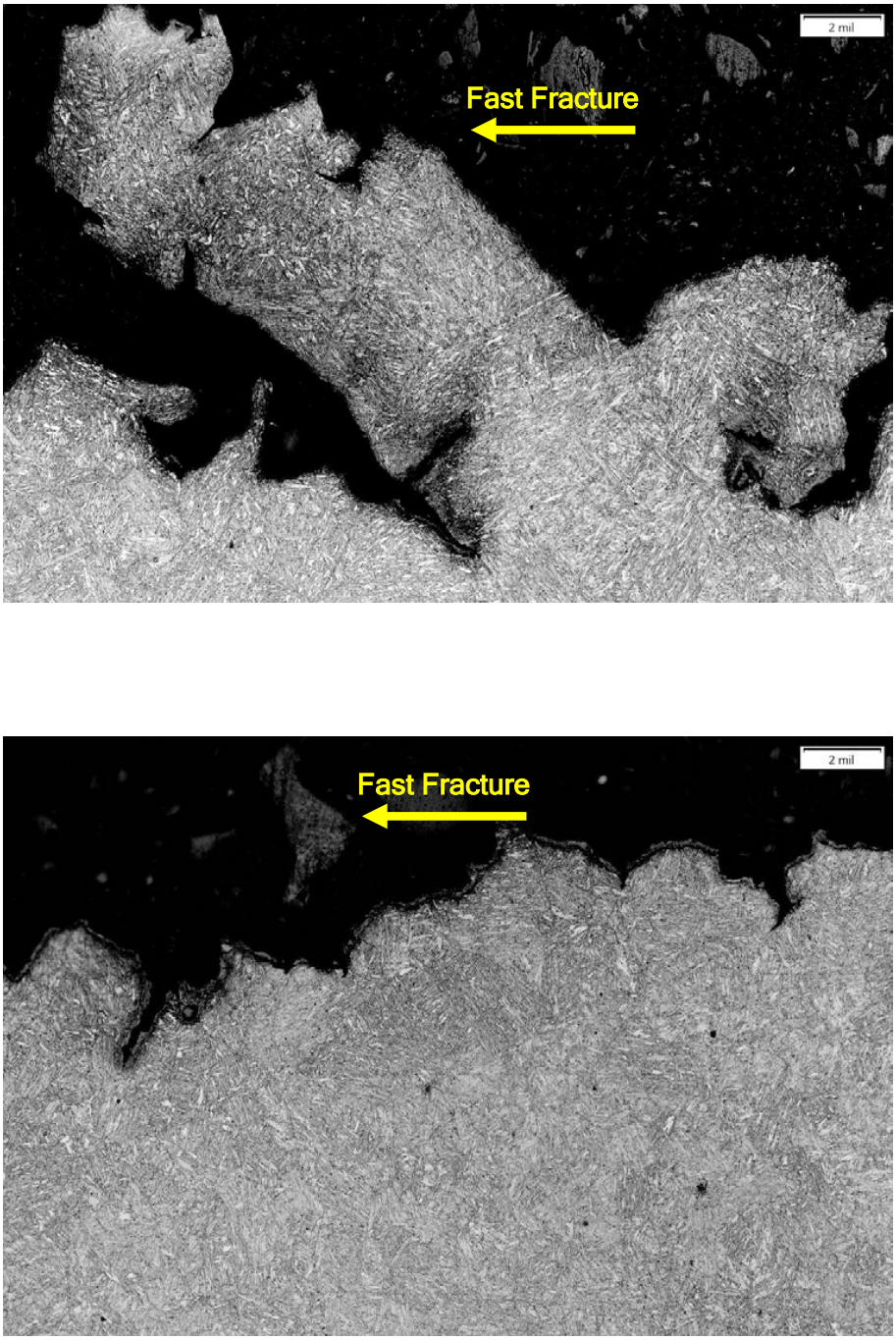

Figure 113. Higher magnification images of features along the crack path shown in Figure 110. (Etchant: Nital)

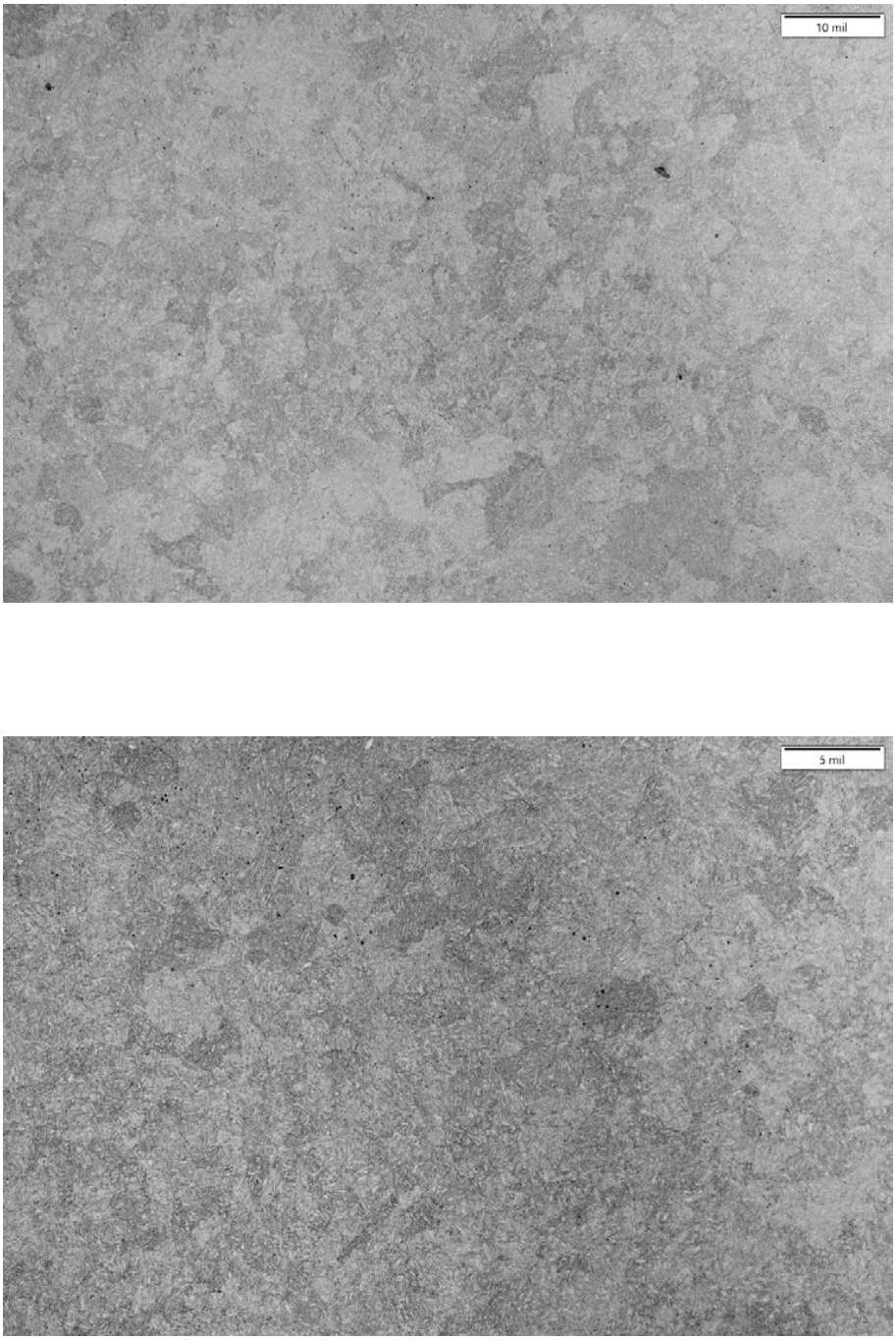

Figure 114. Metallograph images showing the typical retaining ring microstructure. The microstructure consisted of tempered martensite with variable grain size and with scattered nonmetallic inclusions. (Etchant: Nital)

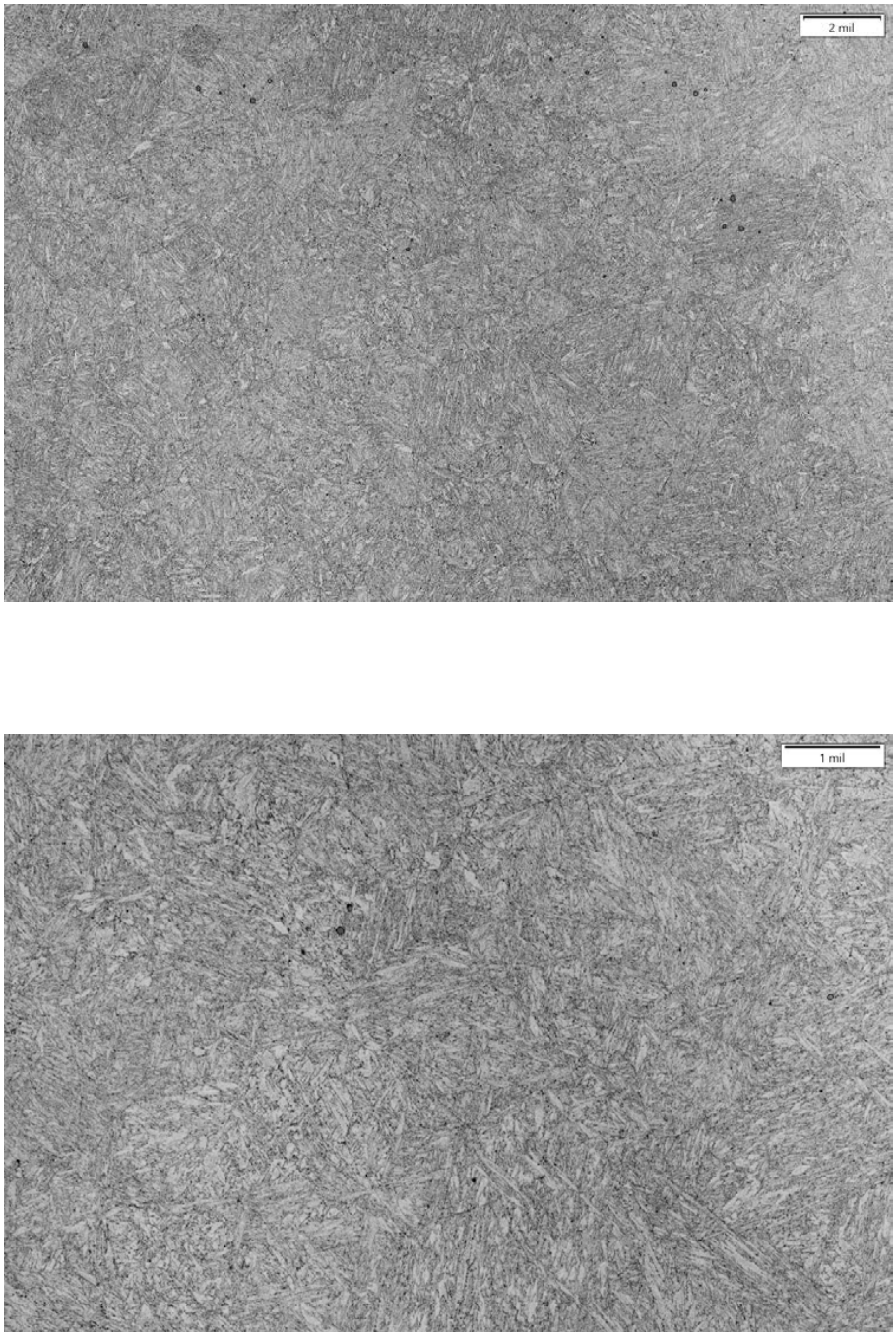

Figure 115. Higher magnification images showing the typical retaining ring microstructure. The microstructure consisted of tempered martensite with variable grain size and with scattered nonmetallic inclusions. (Etchant: Nital)

ATTACHMENT A

2017 HARDNESS TEST RESULTS

Structural Integrity Associates, Inc.®
info@structint.com 1-877-4SI-POWER structint.com

Xcel Energy
RESPONSIBLE BY NATURE

Energy Supply – Technical Services | Reliability Services & Overhaul Management

Brinell Hardness Test Report

Component Description Riverside Unit 7, Turbine end retaining ring

Metallurgy Lab Request Number N/A

Operator Mike Christensen Date 10/5/17

Test Machine & Serial Number Proceq Equo Tip S/N 611.0766

Re-Calibration Due N/A

Test Results					
Reading	Hardness	Reading	Hardness	Reading	Hardness
1 660	42.4 HRC	1 651	41.1 HRC	1	
2 652	41.4 HRC	2 650	41.1 HRC	2	

Average 41.9 HRC Average 41.1 HRC Average _____

Remarks/Component Sketch Including Indent Location

This Test Meets the Requirements of MAP-11 and ASTM E10-14 or ASTM E110-14:

Xcel Energy
RESPONSIBLE BY NATURE

Energy Supply – Technical Services | Reliability Services & Overhaul Management

Brinell Hardness Test Report

Component Description Riverside Unit 7, Exciter end retaining ring

Metallurgy Lab Request Number N/A

Operator Mike Christensen Date 10/5/17

Test Machine & Serial Number Proceq Equo Tip S/N 611.0766

Re-Calibration Due N/A

Test Results					
Reading	Hardness	Reading	Hardness	Reading	Hardness
1 655	41.6 HRC	1 658	42.1 HRC		
2 652	41.4 HRC	2 659	42.1 HRC		
Average	41.5 HRC	Average	42.1 HRC	Average	

Remarks/Component Sketch Including Indent Location

This Test Meets the Requirements of MAP-11 and ASTM E10-14 or ASTM E110-14:

CERTIFICATE OF SERVICE

I, Christine Marquis, hereby certify that I have this day served copies of the foregoing document on the attached list of persons.

xx by depositing a true and correct copy thereof, properly enveloped with postage paid in the United States mail at Minneapolis, Minnesota

xx electronic filing

Docket No. **E002/AA-24-63**
E002/AA-25-63

Dated this 19th day of September 2025

/s/
_____
Christine Marquis
Regulatory Administrator

#	First Name	Last Name	Email	Organization	Agency	Address	Delivery Method	Alternate Delivery Method	View Trade Secret	Service List Name
1	Kevin	Adams	kadams@caprw.org	Community Action Partnership of Ramsey & Washington Counties		450 Syndicate St N Ste 35 Saint Paul MN, 55104 United States	Electronic Service		No	24-63AA-24-63
2	Mara	Ascheman	mara.k.ascheman@xcelenergy.com	Xcel Energy		414 Nicollet Mall Fl 5 Minneapolis MN, 55401 United States	Electronic Service		Yes	24-63AA-24-63
3	Gail	Baranko	gail.baranko@xcelenergy.com	Xcel Energy		414 Nicollet Mall7th Floor Minneapolis MN, 55401 United States	Electronic Service		Yes	24-63AA-24-63
4	Jessica L	Bayles	jessica.bayles@stoel.com	Stoel Rives LLP		1150 18th St NW Ste 325 Washington DC, 20036 United States	Electronic Service		No	24-63AA-24-63
5	Sasha	Bergman	sasha.bergman@state.mn.us		Public Utilities Commission		Electronic Service		No	24-63AA-24-63
6	Elizabeth	Brama	ebrama@taftlaw.com	Taft Stettinius & Hollister LLP		2200 IDS Center 80 South 8th Street Minneapolis MN, 55402 United States	Electronic Service		No	24-63AA-24-63
7	Matthew	Brodin	mbrodin@allete.com	Minnesota Power		30 West Superior Street Duluth MN, 55802 United States	Electronic Service		No	24-63AA-24-63
8	Mike	Bull	mike.bull@state.mn.us		Public Utilities Commission	121 7th Place East, Suite 350 St. Paul MN, 55101 United States	Electronic Service		Yes	24-63AA-24-63
9	James	Canaday	james.canaday@ag.state.mn.us		Office of the Attorney General - Residential Utilities Division	Suite 1400 445 Minnesota St. St. Paul MN, 55101 United States	Electronic Service		No	24-63AA-24-63
10	John	Coffman	john@johncoffman.net	AARP		871 Tuxedo Blvd. St, Louis MO, 63119-2044 United States	Electronic Service		No	24-63AA-24-63
11	Generic	Commerce Attorneys	commerce.attorneys@ag.state.mn.us		Office of the Attorney General - Department of Commerce	445 Minnesota Street Suite 1400 St. Paul MN, 55101 United States	Electronic Service		Yes	24-63AA-24-63
12	George	Crocker	gwillc@nawo.org	North American Water Office		5093 Keats Avenue Lake Elmo MN, 55042 United States	Electronic Service		No	24-63AA-24-63
13	James	Denniston	james.r.denniston@xcelenergy.com	Xcel Energy Services, Inc.		414 Nicollet Mall, 401-8 Minneapolis MN, 55401 United States	Electronic Service		No	24-63AA-24-63

#	First Name	Last Name	Email	Organization	Agency	Address	Delivery Method	Alternate Delivery Method	View Trade Secret	Service List Name
14	Ian M.	Dobson	ian.m.dobson@xcelenergy.com	Xcel Energy		414 Nicollet Mall, 401-8 Minneapolis MN, 55401 United States	Electronic Service		Yes	24-63AA-24-63
15	Richard	Dornfeld	richard.dornfeld@ag.state.mn.us		Office of the Attorney General - Department of Commerce	Minnesota Attorney General's Office 445 Minnesota Street, Suite 1800 Saint Paul MN, 55101 United States	Electronic Service		No	24-63AA-24-63
16	Christopher	Droske	christopher.droske@minneapolismn.gov	Northern States Power Company dba Xcel Energy-Elec		661 5th Ave N Minneapolis MN, 55405 United States	Electronic Service		No	24-63AA-24-63
17	Brian	Edstrom	briane@cubminnesota.org	Citizens Utility Board of Minnesota		332 Minnesota St Ste W1360 Saint Paul MN, 55101 United States	Electronic Service		No	24-63AA-24-63
18	Rebecca	Eilers	rebecca.d.eilers@xcelenergy.com	Xcel Energy		414 Nicollet Mall - 401 7th Floor Minneapolis MN, 55401 United States	Electronic Service		Yes	24-63AA-24-63
19	John	Farrell	jfarrell@ilsr.org	Institute for Local Self-Reliance		2720 E. 22nd St Institute for Local Self-Reliance Minneapolis MN, 55406 United States	Electronic Service		No	24-63AA-24-63
20	Sharon	Ferguson	sharon.ferguson@state.mn.us		Department of Commerce	85 7th Place E Ste 280 Saint Paul MN, 55101-2198 United States	Electronic Service		No	24-63AA-24-63
21	Lucas	Franco	lfranco@liunagroc.com	LIUNA		81 Little Canada Rd E Little Canada MN, 55117 United States	Electronic Service		No	24-63AA-24-63
22	Edward	Garvey	garveyed@aol.com	Residence		32 Lawton St Saint Paul MN, 55102 United States	Electronic Service		No	24-63AA-24-63
23	Allen	Gleckner	agleckner@elpc.org	Environmental Law & Policy Center		35 E. Wacker Drive, Suite 1600 Suite 1600 Chicago IL, 60601 United States	Electronic Service		No	24-63AA-24-63
24	Matthew B	Harris	matt.b.harris@xcelenergy.com	XCEL ENERGY		401 Nicollet Mall FL 8 Minneapolis MN, 55401 United States	Electronic Service		Yes	24-63AA-24-63
25	Shubha	Harris	shubha.m.harris@xcelenergy.com	Xcel Energy		414 Nicollet Mall, 401 - FL 8 Minneapolis MN, 55401 United States	Electronic Service		Yes	24-63AA-24-63

#	First Name	Last Name	Email	Organization	Agency	Address	Delivery Method	Alternate Delivery Method	View Trade Secret	Service List Name
26	Amber	Hedlund	amber.r.hedlund@xcelenergy.com	Northern States Power Company dba Xcel Energy-Elec		414 Nicollet Mall, 401-7 Minneapolis MN, 55401 United States	Electronic Service		No	24-63AA-24-63
27	Adam	Heinen	aheinen@dakotaelectric.com	Dakota Electric Association		4300 220th St W Farmington MN, 55024 United States	Electronic Service		No	24-63AA-24-63
28	Katherine	Hinderlie	katherine.hinderlie@ag.state.mn.us		Office of the Attorney General - Residential Utilities Division	445 Minnesota St Suite 1400 St. Paul MN, 55101-2134 United States	Electronic Service		No	24-63AA-24-63
29	Michael	Hoppe	lu23@ibew23.org	Local Union 23, I.B.E.W.		445 Etna Street Ste. 61 St. Paul MN, 55106 United States	Electronic Service		No	24-63AA-24-63
30	Alan	Jenkins	aj@jenkinsatlaw.com	Jenkins at Law		2950 Yellowtail Ave. Marathon FL, 33050 United States	Electronic Service		No	24-63AA-24-63
31	Richard	Johnson	rick.johnson@lawmoss.com	Moss & Barnett		150 S. 5th Street Suite 1200 Minneapolis MN, 55402 United States	Electronic Service		No	24-63AA-24-63
32	Sarah	Johnson Phillips	sjphillips@stoel.com	Stoel Rives LLP		33 South Sixth Street Suite 4200 Minneapolis MN, 55402 United States	Electronic Service		No	24-63AA-24-63
33	Michael	Krikava	mkrikava@taftlaw.com	Taft Stettinius & Hollister LLP		2200 IDS Center 80 S 8th St Minneapolis MN, 55402 United States	Electronic Service		No	24-63AA-24-63
34	Carmel	Laney	carmel.laney@stoel.com	Stoel Rives LLP		33 South Sixth Street Suite 4200 Minneapolis MN, 55402 United States	Electronic Service		No	24-63AA-24-63
35	Peder	Larson	plarson@larkinhoffman.com	Larkin Hoffman Daly & Lindgren, Ltd.		8300 Norman Center Drive Suite 1000 Bloomington MN, 55437 United States	Electronic Service		No	24-63AA-24-63
36	Annie	Levenson Falk	annielf@cubminnesota.org	Citizens Utility Board of Minnesota		332 Minnesota Street, Suite W1360 St. Paul MN, 55101 United States	Electronic Service		No	24-63AA-24-63
37	Ryan	Long	ryan.j.long@xcelenergy.com			414 Nicollet Mall 401 8th Floor Minneapolis MN, 55401 United States	Electronic Service		Yes	24-63AA-24-63
38	Alice	Madden	alice@communitypowermn.org	Community Power		2720 E 22nd St Minneapolis	Electronic Service		No	24-63AA-24-63

#	First Name	Last Name	Email	Organization	Agency	Address	Delivery Method	Alternate Delivery Method	View Trade Secret	Service List Name
						MN, 55406 United States				
39	Kavita	Maini	kmaini@wi.rr.com	KM Energy Consulting, LLC		961 N Lost Woods Rd Oconomowoc WI, 53066 United States	Electronic Service		No	24-63AA-24-63
40	Christine	Marquis	regulatory.records@xcelenergy.com	Xcel Energy		414 Nicollet Mall MN1180-07-MCA Minneapolis MN, 55401 United States	Electronic Service		Yes	24-63AA-24-63
41	Mary	Martinka	mary.a.martinka@xcelenergy.com	Xcel Energy Inc		414 Nicollet Mall 7th Floor Minneapolis MN, 55401 United States	Electronic Service		Yes	24-63AA-24-63
42	Erica	McConnell	emcconnell@elpc.org	Environmental Law & Policy Center		35 E. Wacker Drive, Suite 1600 Chicago IL, 60601 United States	Electronic Service		No	24-63AA-24-63
43	Stacy	Miller	stacy.miller@minneapolismn.gov	City of Minneapolis		350 S. 5th Street Room M 301 Minneapolis MN, 55415 United States	Electronic Service		No	24-63AA-24-63
44	David	Moeller	dmoeller@allete.com	Minnesota Power			Electronic Service		No	24-63AA-24-63
45	Andrew	Moratzka	andrew.moratzka@stoel.com	Stoel Rives LLP		33 South Sixth St Ste 4200 Minneapolis MN, 55402 United States	Electronic Service		No	24-63AA-24-63
46	Christa	Moseng	christa.moseng@state.mn.us		Office of Administrative Hearings	P.O. Box 64620 Saint Paul MN, 55164-0620 United States	Electronic Service		No	24-63AA-24-63
47	David	Niles	david.niles@avantenergy.com	Minnesota Municipal Power Agency		220 South Sixth Street Suite 1300 Minneapolis MN, 55402 United States	Electronic Service		No	24-63AA-24-63
48	Carol A.	Overland	overland@legalectric.org	Legalectric - Overland Law Office		1110 West Avenue Red Wing MN, 55066 United States	Electronic Service		No	24-63AA-24-63
49	Generic Notice	Residential Utilities Division	residential.utilities@ag.state.mn.us		Office of the Attorney General - Residential Utilities Division	1400 BRM Tower 445 Minnesota St St. Paul MN, 55101-2131 United States	Electronic Service		Yes	24-63AA-24-63
50	Kevin	Reuther	kreuther@mncenter.org	MN Center for Environmental Advocacy		26 E Exchange St, Ste 206 St. Paul MN, 55101-1667 United States	Electronic Service		No	24-63AA-24-63
51	Amanda	Rome	amanda.rome@xcelenergy.com	Xcel Energy		414 Nicollet Mall FL 5 Minneapoli	Electronic Service		Yes	24-63AA-24-63

#	First Name	Last Name	Email	Organization	Agency	Address	Delivery Method	Alternate Delivery Method	View Trade Secret	Service List Name
						MN, 55401 United States				
52	Joseph L	Sathe	jsathe@kennedy-graven.com	Kennedy & Graven, Chartered		150 S 5th St Ste 700 Minneapolis MN, 55402 United States	Electronic Service		No	24-63AA-24-63
53	Elizabeth	Schmiesing	eschmiesing@winthrop.com	Winthrop & Weinstine, P.A.		225 South Sixth Street Suite 3500 Minneapolis MN, 55402 United States	Electronic Service		No	24-63AA-24-63
54	Peter	Scholtz	peter.scholtz@ag.state.mn.us		Office of the Attorney General - Residential Utilities Division	Suite 1400 445 Minnesota Street St. Paul MN, 55101-2131 United States	Electronic Service		No	24-63AA-24-63
55	Janet	Shaddix Elling	jshaddix@janetshaddix.com	Shaddix And Associates		7400 Lyndale Ave S Ste 190 Richfield MN, 55423 United States	Electronic Service		No	24-63AA-24-63
56	Joshua	Smith	joshua.smith@sierraclub.org			85 Second St FL 2 San Francisco CA, 94105 United States	Electronic Service		No	24-63AA-24-63
57	Ken	Smith	ken.smith@districtenergy.com	District Energy St. Paul Inc.		76 W Kellogg Blvd St. Paul MN, 55102 United States	Electronic Service		No	24-63AA-24-63
58	Beth	Soholt	bsoholt@cleangridalliance.org	Clean Grid Alliance		570 Asbury Street Suite 201 St. Paul MN, 55104 United States	Electronic Service		No	24-63AA-24-63
59	Byron E.	Starns	byron.starns@stinson.com	STINSON LLP		50 S 6th St Ste 2600 Minneapolis MN, 55402 United States	Electronic Service		No	24-63AA-24-63
60	Scott	Strand	sstrand@elpc.org	Environmental Law & Policy Center		60 S 6th Street Suite 2800 Minneapolis MN, 55402 United States	Electronic Service		No	24-63AA-24-63
61	James M	Strommen	jstrommen@kennedy-graven.com	Kennedy & Graven, Chartered		150 S 5th St Ste 700 Minneapolis MN, 55402 United States	Electronic Service		No	24-63AA-24-63
62	Carla	Vita	carla.vita@state.mn.us	MN DEED		Great Northern Building 12th Floor 180 East Fifth Street St. Paul MN, 55101 United States	Electronic Service		No	24-63AA-24-63
63	Joseph	Windler	jwindler@winthrop.com	Winthrop & Weinstine		225 South Sixth Street, Suite 3500 Minneapolis MN, 55402 United States	Electronic Service		No	24-63AA-24-63

#	First Name	Last Name	Email	Organization	Agency	Address	Delivery Method	Alternate Delivery Method	View Trade Secret	Service List Name
64	Kurt	Zimmerman	kwz@ibew160.org	Local Union #160, IBEW		2909 Anthony Ln St Anthony Village MN, 55418-3238 United States	Electronic Service		No	24-63AA-24-63
65	Patrick	Zomer	pat.zomer@lawmoss.com	Moss & Barnett PA		150 S 5th St #1200 Minneapolis MN, 55402 United States	Electronic Service		No	24-63AA-24-63

#	First Name	Last Name	Email	Organization	Agency	Address	Delivery Method	Alternate Delivery Method	View Trade Secret	Service List Name
1	Kevin	Adams	kadams@caprw.org	Community Action Partnership of Ramsey & Washington Counties		450 Syndicate St N Ste 35 Saint Paul MN, 55104 United States	Electronic Service		No	AA-25-63
2	Mara	Ascheman	mara.k.ascheman@xcelenergy.com	Xcel Energy		414 Nicollet Mall Fl 5 Minneapolis MN, 55401 United States	Electronic Service		No	AA-25-63
3	Gail	Baranko	gail.baranko@xcelenergy.com	Xcel Energy		414 Nicollet Mall7th Floor Minneapolis MN, 55401 United States	Electronic Service		No	AA-25-63
4	Jessica L	Bayles	jessica.bayles@stoel.com	Stoel Rives LLP		1150 18th St NW Ste 325 Washington DC, 20036 United States	Electronic Service		No	AA-25-63
5	Sasha	Bergman	sasha.bergman@state.mn.us		Public Utilities Commission		Electronic Service		No	AA-25-63
6	Elizabeth	Brama	ebrama@taftlaw.com	Taft Stettinius & Hollister LLP		2200 IDS Center 80 South 8th Street Minneapolis MN, 55402 United States	Electronic Service		No	AA-25-63
7	Matthew	Brodin	mbrodin@allete.com	Minnesota Power		30 West Superior Street Duluth MN, 55802 United States	Electronic Service		No	AA-25-63
8	Mike	Bull	mike.bull@state.mn.us		Public Utilities Commission	121 7th Place East, Suite 350 St. Paul MN, 55101 United States	Electronic Service		Yes	AA-25-63
9	James	Canaday	james.canaday@ag.state.mn.us		Office of the Attorney General - Residential Utilities Division	Suite 1400 445 Minnesota St. St. Paul MN, 55101 United States	Electronic Service		No	AA-25-63
10	John	Coffman	john@johncoffman.net	AARP		871 Tuxedo Blvd. St, Louis MO, 63119-2044 United States	Electronic Service		No	AA-25-63
11	Generic	Commerce Attorneys	commerce.attorneys@ag.state.mn.us		Office of the Attorney General - Department of Commerce	445 Minnesota Street Suite 1400 St. Paul MN, 55101 United States	Electronic Service		Yes	AA-25-63
12	George	Crocker	gwillc@nawo.org	North American Water Office		5093 Keats Avenue Lake Elmo MN, 55042 United States	Electronic Service		No	AA-25-63
13	James	Denniston	james.r.denniston@xcelenergy.com	Xcel Energy Services, Inc.		414 Nicollet Mall, 401-8 Minneapolis MN, 55401 United States	Electronic Service		No	AA-25-63
14	Ian M.	Dobson	ian.m.dobson@xcelenergy.com	Xcel Energy		414 Nicollet Mall, 401-8 Minneapolis	Electronic Service		No	AA-25-63

#	First Name	Last Name	Email	Organization	Agency	Address	Delivery Method	Alternate Delivery Method	View Trade Secret	Service List Name
						MN, 55401 United States				
15	Richard	Dornfeld	richard.dornfeld@ag.state.mn.us		Office of the Attorney General - Department of Commerce	Minnesota Attorney General's Office 445 Minnesota Street, Suite 1800 Saint Paul MN, 55101 United States	Electronic Service		No	AA-25-63
16	Christopher	Droske	christopher.droske@minneapolismn.gov	Northern States Power Company dba Xcel Energy-Elec		661 5th Ave N Minneapolis MN, 55405 United States	Electronic Service		No	AA-25-63
17	Brian	Edstrom	briane@cubminnesota.org	Citizens Utility Board of Minnesota		332 Minnesota St Ste W1360 Saint Paul MN, 55101 United States	Electronic Service		No	AA-25-63
18	Rebecca	Eilers	rebecca.d.eilers@xcelenergy.com	Xcel Energy		414 Nicollet Mall - 401 7th Floor Minneapolis MN, 55401 United States	Electronic Service		Yes	AA-25-63
19	John	Farrell	jfarrell@ilsr.org	Institute for Local Self-Reliance		2720 E. 22nd St Institute for Local Self-Reliance Minneapolis MN, 55406 United States	Electronic Service		No	AA-25-63
20	Sharon	Ferguson	sharon.ferguson@state.mn.us		Department of Commerce	85 7th Place E Ste 280 Saint Paul MN, 55101-2198 United States	Electronic Service		No	AA-25-63
21	Lucas	Franco	lfranco@liunagroc.com	LIUNA		81 Little Canada Rd E Little Canada MN, 55117 United States	Electronic Service		No	AA-25-63
22	Edward	Garvey	garveyed@aol.com	Residence		32 Lawton St Saint Paul MN, 55102 United States	Electronic Service		No	AA-25-63
23	Allen	Gleckner	agleckner@elpc.org	Environmental Law & Policy Center		35 E. Wacker Drive, Suite 1600 Suite 1600 Chicago IL, 60601 United States	Electronic Service		No	AA-25-63
24	Matthew B	Harris	matt.b.harris@xcelenergy.com	XCEL ENERGY		401 Nicollet Mall FL 8 Minneapolis MN, 55401 United States	Electronic Service		No	AA-25-63
25	Shubha	Harris	shubha.m.harris@xcelenergy.com	Xcel Energy		414 Nicollet Mall, 401 - FL 8 Minneapolis MN, 55401 United States	Electronic Service		No	AA-25-63
26	Amber	Hedlund	amber.r.hedlund@xcelenergy.com	Northern States Power Company dba		414 Nicollet Mall, 401-7 Minneapolis	Electronic Service		No	AA-25-63

#	First Name	Last Name	Email	Organization	Agency	Address	Delivery Method	Alternate Delivery Method	View Trade Secret	Service List Name
				Xcel Energy-Elec		MN, 55401 United States				
27	Adam	Heinen	aheinen@dakotaelectric.com	Dakota Electric Association		4300 220th St W Farmington MN, 55024 United States	Electronic Service		No	AA-25-63
28	Katherine	Hinderlie	katherine.hinderlie@ag.state.mn.us		Office of the Attorney General - Residential Utilities Division	445 Minnesota St Suite 1400 St. Paul MN, 55101-2134 United States	Electronic Service		No	AA-25-63
29	Michael	Hoppe	lu23@ibew23.org	Local Union 23, I.B.E.W.		445 Etna Street Ste. 61 St. Paul MN, 55106 United States	Electronic Service		No	AA-25-63
30	Alan	Jenkins	aj@jenkinsatlaw.com	Jenkins at Law		2950 Yellowtail Ave. Marathon FL, 33050 United States	Electronic Service		No	AA-25-63
31	Richard	Johnson	rick.johnson@lawmoss.com	Moss & Barnett		150 S. 5th Street Suite 1200 Minneapolis MN, 55402 United States	Electronic Service		No	AA-25-63
32	Sarah	Johnson Phillips	sjphillips@stoel.com	Stoel Rives LLP		33 South Sixth Street Suite 4200 Minneapolis MN, 55402 United States	Electronic Service		No	AA-25-63
33	Michael	Krikava	mkrikava@taftlaw.com	Taft Stettinius & Hollister LLP		2200 IDS Center 80 S 8th St Minneapolis MN, 55402 United States	Electronic Service		No	AA-25-63
34	Carmel	Laney	carmel.laney@stoel.com	Stoel Rives LLP		33 South Sixth Street Suite 4200 Minneapolis MN, 55402 United States	Electronic Service		No	AA-25-63
35	Peder	Larson	plarson@larkinhoffman.com	Larkin Hoffman Daly & Lindgren, Ltd.		8300 Norman Center Drive Suite 1000 Bloomington MN, 55437 United States	Electronic Service		No	AA-25-63
36	Annie	Levenson Falk	annielf@cubminnesota.org	Citizens Utility Board of Minnesota		332 Minnesota Street, Suite W1360 St. Paul MN, 55101 United States	Electronic Service		No	AA-25-63
37	Ryan	Long	ryan.j.long@xcelenergy.com			414 Nicollet Mall 401 8th Floor Minneapolis MN, 55401 United States	Electronic Service		No	AA-25-63
38	Alice	Madden	alice@communitypowermn.org	Community Power		2720 E 22nd St Minneapolis MN, 55406 United States	Electronic Service		No	AA-25-63

#	First Name	Last Name	Email	Organization	Agency	Address	Delivery Method	Alternate Delivery Method	View Trade Secret	Service List Name
39	Kavita	Maini	kmaini@wi.rr.com	KM Energy Consulting, LLC		961 N Lost Woods Rd Oconomowoc WI, 53066 United States	Electronic Service		No	AA-25-63
40	Christine	Marquis	regulatory.records@xcelenergy.com	Xcel Energy		414 Nicollet Mall MN1180-07-MCA Minneapolis MN, 55401 United States	Electronic Service		Yes	AA-25-63
41	Mary	Martinka	mary.a.martinka@xcelenergy.com	Xcel Energy Inc		414 Nicollet Mall 7th Floor Minneapolis MN, 55401 United States	Electronic Service		No	AA-25-63
42	Erica	McConnell	emcconnell@elpc.org	Environmental Law & Policy Center		35 E. Wacker Drive, Suite 1600 Chicago IL, 60601 United States	Electronic Service		No	AA-25-63
43	Stacy	Miller	stacy.miller@minneapolismn.gov	City of Minneapolis		350 S. 5th Street Room M 301 Minneapolis MN, 55415 United States	Electronic Service		No	AA-25-63
44	David	Moeller	dmoeller@allete.com	Minnesota Power			Electronic Service		No	AA-25-63
45	Andrew	Moratzka	andrew.moratzka@stoel.com	Stoel Rives LLP		33 South Sixth St Ste 4200 Minneapolis MN, 55402 United States	Electronic Service		No	AA-25-63
46	Christa	Moseng	christa.moseng@state.mn.us		Office of Administrative Hearings	P.O. Box 64620 Saint Paul MN, 55164-0620 United States	Electronic Service		No	AA-25-63
47	David	Niles	david.niles@avantenergy.com	Minnesota Municipal Power Agency		220 South Sixth Street Suite 1300 Minneapolis MN, 55402 United States	Electronic Service		No	AA-25-63
48	Carol A.	Overland	overland@legalectric.org	Legalectric - Overland Law Office		1110 West Avenue Red Wing MN, 55066 United States	Electronic Service		No	AA-25-63
49	Generic Notice	Residential Utilities Division	residential.utilities@ag.state.mn.us		Office of the Attorney General - Residential Utilities Division	1400 BRM Tower 445 Minnesota St St. Paul MN, 55101-2131 United States	Electronic Service		Yes	AA-25-63
50	Kevin	Reuther	kreuther@mncenter.org	MN Center for Environmental Advocacy		26 E Exchange St, Ste 206 St. Paul MN, 55101-1667 United States	Electronic Service		No	AA-25-63
51	Amanda	Rome	amanda.rome@xcelenergy.com	Xcel Energy		414 Nicollet Mall FL 5 Minneapoli MN, 55401 United States	Electronic Service		No	AA-25-63

#	First Name	Last Name	Email	Organization	Agency	Address	Delivery Method	Alternate Delivery Method	View Trade Secret	Service List Name
52	Joseph L	Sathe	jsathe@kennedy-graven.com	Kennedy & Graven, Chartered		150 S 5th St Ste 700 Minneapolis MN, 55402 United States	Electronic Service		No	AA-25-63
53	Elizabeth	Schmiesing	eschmiesing@winthrop.com	Winthrop & Weinstine, P.A.		225 South Sixth Street Suite 3500 Minneapolis MN, 55402 United States	Electronic Service		No	AA-25-63
54	Peter	Scholtz	peter.scholtz@ag.state.mn.us		Office of the Attorney General - Residential Utilities Division	Suite 1400 445 Minnesota Street St. Paul MN, 55101-2131 United States	Electronic Service		No	AA-25-63
55	Janet	Shaddix Elling	jshaddix@janetshaddix.com	Shaddix And Associates		7400 Lyndale Ave S Ste 190 Richfield MN, 55423 United States	Electronic Service		No	AA-25-63
56	Joshua	Smith	joshua.smith@sierraclub.org			85 Second St FL 2 San Francisco CA, 94105 United States	Electronic Service		No	AA-25-63
57	Ken	Smith	ken.smith@districtenergy.com	District Energy St. Paul Inc.		76 W Kellogg Blvd St. Paul MN, 55102 United States	Electronic Service		No	AA-25-63
58	Beth	Soholt	bsoholt@cleangridalliance.org	Clean Grid Alliance		570 Asbury Street Suite 201 St. Paul MN, 55104 United States	Electronic Service		No	AA-25-63
59	Byron E.	Starns	byron.starns@stinson.com	STINSON LLP		50 S 6th St Ste 2600 Minneapolis MN, 55402 United States	Electronic Service		No	AA-25-63
60	Scott	Strand	sstrand@elpc.org	Environmental Law & Policy Center		60 S 6th Street Suite 2800 Minneapolis MN, 55402 United States	Electronic Service		No	AA-25-63
61	James M	Strommen	jstrommen@kennedy-graven.com	Kennedy & Graven, Chartered		150 S 5th St Ste 700 Minneapolis MN, 55402 United States	Electronic Service		No	AA-25-63
62	Carla	Vita	carla.vita@state.mn.us	MN DEED		Great Northern Building 12th Floor 180 East Fifth Street St. Paul MN, 55101 United States	Electronic Service		No	AA-25-63
63	Joseph	Windler	jwindler@winthrop.com	Winthrop & Weinstine		225 South Sixth Street, Suite 3500 Minneapolis MN, 55402 United States	Electronic Service		No	AA-25-63
64	Kurt	Zimmerman	kwz@ibew160.org	Local Union #160, IBEW		2909 Anthony Ln	Electronic Service		No	AA-25-63

#	First Name	Last Name	Email	Organization	Agency	Address	Delivery Method	Alternate Delivery Method	View Trade Secret	Service List Name
						St Anthony Village MN, 55418-3238 United States				
65	Patrick	Zomer	pat.zomer@lawmoss.com	Moss & Barnett PA		150 S 5th St #1200 Minneapolis MN, 55402 United States	Electronic Service		No	AA-25-63